An International ICT Journal
Featuring Industry–University–Institute Cooperation and
Indexed in Scopus

ISSN 1673-5188
CN 34-1294/TN

ZTE COMMUNICATIONS

中兴通讯技术(英文版)

http://zte.magtechjournal.com

June 2025, Vol. 23 No. 2

Special Topic:
Digital Twin Online Channel Modeling for 6G and Beyond

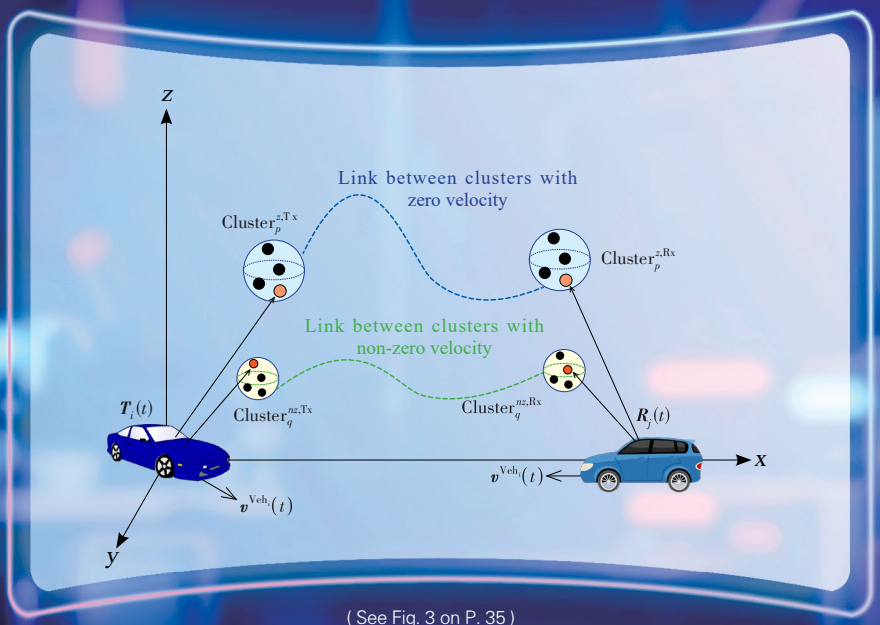

(See Fig. 3 on P. 35)

ISSN 1673-5188
06
9 771673 518253

The 10th Editorial Board of ZTE Communications

Chairman GAO Wen, Peking University (China)

Vice Chairmen XU Ziyang, ZTE Corporation (China) | XU Chengzhong, University of Macau (China)

Members (Surname in Alphabetical Order)

AI Bo	Beijing Jiaotong University (China)
CAO Jiannong	The Hong Kong Polytechnic University (China)
CHEN Chang Wen	The Hong Kong Polytechnic University (China)
CHEN Yan	Northwestern University (USA)
CHI Nan	Fudan University (China)
CUI Shuguang	UC Davis (USA) and The Chinese University of Hong Kong, Shenzhen (China)
GAO Wen	Peking University (China)
GAO Yang	Nanjing University (China)
GAO Yue	Fudan University (China)
FANG Rong	ZTE Corporation (China)
GE Xiaohu	Huazhong University of Science and Technology (China)
HE Yejun	Shenzhen University (China)
Victor C. M. LEUNG	The University of British Columbia (Canada)
LI Xiangyang	University of Science and Technology of China (China)
LIAO Yong	Chongqing University (China)
LIN Xiaodong	ZTE Corporation (China)
LIU Chi	Beijing Institute of Technology (China)
LIU Jian	ZTE Corporation (China)
LIU Yue	Beijing Institute of Technology (China)
MA Jianhua	Hosei University (Japan)
MA Zheng	Southwest Jiaotong University (China)
PAN Yi	Shenzhen University of Advanced Technology, Chinese Academy of Sciences (China)
PENG Mugen	Beijing University of Posts and Telecommunications (China)
REN Fuji	Tokushima University (Japan)
REN Kui	Zhejiang University (China)
SHENG Min	Xidian University (China)
SU Zhou	Xi'an Jiaotong University (China)
SUN Huifang	Pengcheng Laboratory (China)
SUN Zhili	University of Surrey (UK)
TAO Meixia	Shanghai Jiao Tong University (China)
WANG Chengxiang	Southeast University (China)
WANG Haiming	Southeast University (China)
WANG Xiang	ZTE Corporation (China)
WANG Xiyu	ZTE Corporation (China)
WANG Yongjin	Nanjing University of Posts and Telecommunications (China)
XU Chengzhong	University of Macau (China)
XU Ziyang	ZTE Corporation (China)
YANG Kun	University of Essex (UK)
YU Hongfang	University of Electronic Science and Technology of China (China)
YUAN Jinhong	University of New South Wales (Australia)
ZENG Wenjun	Eastern Institute of Technology, Ningbo (China)
ZHANG Honggang	City University of Macau (China)
ZHANG Jianhua	Beijing University of Posts and Telecommunications (China)
ZHANG Rui	The Chinese University of Hong Kong, Shenzhen (China)
ZHANG Wenqiang	Fudan University (China)
ZHANG Yueping	Nanyang Technological University (Singapore)
ZHOU Wanlei	City University of Macau (China)
ZHUANG Weihua	University of Waterloo (Canada)

CONTENTS

ZTE COMMUNICATIONS
June 2025 Vol. 23 No. 2 (Issue 91)

Special Topic ▶

Digital Twin Online Channel Modeling for 6G and Beyond

01 Editorial ····· WANG Chengxiang, HUANG Chen

03 Channel Measurement and Analysis of Human Body Radar Cross Section in 26 GHz ISAC Systems ····· DUAN Hongyu, WANG Mengyang, DUO Hao, HE Danping, MA Yihua, LU Bin, ZHONG Zhangdui

11 Space Network Emulation System Based on a User-Space Network Stack ····· LEI Jianzhe, ZHAO Kanglian, HOU Dongxu, ZHOU Fenlin

20 A Machine Learning-Based Channel Data Enhancement Platform for Digital Twin Channels ····· AI Bo, ZHANG Yuxin, YANG Mi, HE Ruisi, GUO Rongge

31 6G Digital Twin Enabled Channel Modeling for Beijing Central Business District ····· LU Mengyuan, BAI Lu, HAN Zengrui, HUANG Ziwei, LU Shiliang, CHENG Xiang

46 Channel Knowledge Maps for 6G Wireless Networks: Construction, Applications, and Future Challenges ····· LIU Xingchen, SUN Shu, TAO Meixia, Aryan KAUSHIK, YAN Hangsong

60 Air-to-Ground Channel Measurement and Modeling for Low-Altitude UAVs: A Survey ····· CHEN Peng, LIU Yajuan, WEI Wentong, WANG Wei, LI Na

Review ▶

76 Liquid Neural Networks: Next-Generation AI for Telecom from First Principles ····· ZHU Fenghao, WANG Xinquan, ZHU Chen, HUANG Chongwen

85 Overview of Cross-Component In-Loop Filters in Video Coding Standards ····· LI Zhaoyu, MENG Xuewei, ZHANG Jiaqi, HUANG Cheng, JIA Chuanmin, MA Siwei, JIANG Yun

Research Papers ▶

96 GaN-Based Optoelectronic Impact Force Sensor ····· RUAN Junhui, JIANG Chengxiang, XU Shengli, WANG Yongjin, SHI Fan

103 Intelligent AP Clustering and Receiver Design for Uplink Cell-free Networks ····· AN Zhenyu, HE Shiwen, YANG Li, ZHAN Hang, HUANG Yongming

109 Integrated All-Light Network for Air, Space, Land, and Sea ····· LIANG Yingze, WANG Linning, QI Ziqian, LIU Pengzhan, WANG Yongjin

Serial parameters: CN 34–1294/TN*2003*q*16*114*en*P*¥30.00*2200*12* 2025-06

Submission of a manuscript implies that the submitted work has not been published before (except as part of a thesis or lecture note or report or in the form of an abstract); that it is not under consideration for publication elsewhere; that its publication has been approved by all co-authors as well as by the authorities at the institute where the work has been carried out; that, if and when the manuscript is accepted for publication, the authors hand over the transferable copyrights of the accepted manuscript to *ZTE Communications*; and that the manuscript or parts thereof will not be published elsewhere in any language without the consent of the copyright holder. Copyrights include, without spatial or timely limitation, the mechanical, electronic and visual reproduction and distribution; electronic storage and retrieval; and all other forms of electronic publication or any other types of publication including all subsidiary rights.

Responsibility for content rests on authors of signed articles and not on the editorial board of *ZTE Communications* or its sponsors.

Statement

This magazine is a free publication for you. If you do not want to receive it in the future, you can send the "TD unsubscribe" mail to magazine@zte.com.cn. We will not send you this magazine again after receiving your email. Thank you for your support.

ZTE Communications Guidelines for Authors

Remit of Journal

ZTE Communications publishes original theoretical papers, research findings, and surveys on a broad range of communications topics, including communications and information system design, optical fiber and electro-optical engineering, microwave technology, radio wave propagation, antenna engineering, electromagnetics, signal and image processing, and power engineering. The journal is designed to be an integrated forum for university academics and industry researchers from around the world.

Manuscript Preparation

Manuscripts must be typed in English and submitted electronically in MS Word (or compatible) format. The word length is approximately 3 000 to 8 000, and no more than 8 figures or tables should be included. Authors are requested to submit mathematical material and graphics in an editable format.

Abstract and Keywords

Each manuscript must include an abstract of approximately 150 words written as a single paragraph. The abstract should not include mathematics or references and should not be repeated verbatim in the introduction. The abstract should be a self-contained overview of the aims, methods, experimental results, and significance of research outlined in the paper. Three to eight carefully chosen keywords must be provided with the abstract.

References

Manuscripts must be referenced at a level that conforms to international academic standards. All references must be numbered sequentially intext and listed in corresponding order at the end of the paper. References that are not cited in-text should not be included in the reference list. References must be complete and formatted according to *ZTE Communications* Editorial Style. A minimum of 10 references should be provided. Footnotes should be avoided or kept to a minimum.

Copyright and Declaration

Authors are responsible for obtaining permission to reproduce any material for which they do not hold copyright. Permission to reproduce any part of this publication for commercial use must be obtained in advance from the editorial office of *ZTE Communications*. Authors agree that a) the manuscript is a product of research conducted by themselves and the stated co-authors; b) the manuscript has not been published elsewhere in its submitted form; c) the manuscript is not currently being considered for publication elsewhere. If the paper is an adaptation of a speech or presentation, acknowledgement of this is required within the paper. The number of co-authors should not exceed five.

Content and Structure

ZTE Communications seeks to publish original content that may build on existing literature in any field of communications. Authors should not dedicate a disproportionate amount of a paper to fundamental background, historical overviews, or chronologies that may be sufficiently dealt with by references. Authors are also requested to avoid the overuse of bullet points when structuring papers. The conclusion should include a commentary on the significance/future implications of the research as well as an overview of the material presented.

Peer Review and Editing

All manuscripts will be subject to a two-stage anonymous peer review as well as copyediting, and formatting. Authors may be asked to revise parts of a manuscript prior to publication.

Biographical Information

All authors are requested to provide a brief biography (approx. 100 words) that includes email address, educational background, career experience, research interests, awards, and publications.

Acknowledgments and Funding

A manuscript based on funded research must clearly state the program name, funding body, and grant number. Individuals who contributed to the manuscript should be acknowledged in a brief statement.

Address for Submission

http://mc03.manuscriptcentral.com/ztecom

Guest Editorial >>>

Special Topic on Digital Twin Online Channel Modeling for 6G and Beyond

Guest Editors

WANG Chengxiang

HUANG Chen

Channel characterization and modeling are fundamental to communication system design, development, testing, and deployment. As the innate digital twins of wireless channels, channel models replicate real-world channel behaviors, e.g., large-scale/small-scale fading, spatio-temporal-frequency non-stationarity, through mathematical and data-driven methods. This enables simulation-based validation across system development stages—from protocol design to network optimization—without costly physical testing.

In 6G/B6G, new frequency bands (e. g., centimeter wave and millimeter wave) and new scenarios (e.g., integrated sensing and communication (ISAC), unmanned aerial vehicle (UAV) communications) have introduced highly dynamic, complex channel characteristics. The critical task is to conduct channel measurements and modeling for diverse bands/scenarios, challenged by technological advancements: Larger antenna arrays and higher resolution have driven transitions from traditional static measurements to dynamic ones, generating massive datasets. In such cases, AI has become an essential method to process big data, improve model accuracy, and enable real-time channel adaptation, overcoming bottlenecks in high-frequency and dynamic scenario analysis.

In this special issue, a series of articles are presented to address the challenges in channel measurement and modeling for next-generation wireless networks, offering innovative solutions to advancing the field. These articles cover a diverse range of topics, including novel measurement methodologies for complex scenarios, machine learning-enhanced channel data processing technologies, digital twin-enabled modeling frameworks, and applications in emerging 6G use cases such as ISAC and UAV communications. The call for papers of this special issue has received many high-quality submissions, reflecting strong academic and industrial interest in overcoming the technical bottlenecks of channel characterization across frequency bands and scenarios. After two rounds of rigorous peer review, six excellent papers have been selected for publication in this special issue, which are presented as follows.

The first paper, titled "Channel Measurement and Analysis of Human Body Radar Cross Section in 26 GHz ISAC Systems", proposes a systematic approach to characterizing electromagnetic scattering from human bodies in ISAC systems, leveraging multi-angle measurements and ray-tracing analysis to optimize joint communication-sensing performance in urban micro-cellular environments.

The second paper, titled "Space Network Emulation System Based on a User-Space Network Stack", presents a novel user-space network stack (Nos) -based framework to realistically emulate satellite and aerial network channels, enabling validation of space-air-ground integrated communication systems under dynamic propagation conditions and reducing development complexity through technologies like Open vSwitch (OVS) and traffic control (TC).

The third paper, titled "A Machine Learning-Based Channel Data Enhancement Platform for Digital Twin Channels", introduces a generative adversarial network (GAN) -driven platform to address channel data scarcity, demonstrating how AI can generate statistically realistic channel samples from sparse measurements to accelerate digital twin channel devel-

DOI: 10.12142/ZTECOM.202502001
Citation (Format 1): WANG C X, HUANG C. Editorial: digital twin online channel modeling for 6G and beyond [J]. ZTE Communications, 2025, 23 (2): 1–2. DOI: 10.12142/ZTECOM.202502001
Citation (Format 2): C. X. Wang and C. Huang, "Editorial: digital twin online channel modeling for 6G and beyond," *ZTE Communications*, vol. 23, no. 2, pp. 1–2, Jun. 2025. doi: 10.12142/ZTECOM.202502001.

opment for 6G networks.

The fourth paper, titled "6G Digital Twin Enabled Channel Modeling for Beijing Central Business District", proposes a scenario-specific digital twin framework that integrates light detection and ranging (LiDAR) point clouds, RGB images, and crowdsourced data to characterize ultra-dense urban channels, providing insights for network deployment in high-rise commercial zones by mimicking channel non-stationarity and consistency.

The fifth paper, titled "Channel Knowledge Maps for 6G Wireless Networks: Construction, Applications, and Future Challenges", establishes a knowledge graph based architecture to systematically organize channel data, models, and engineering experiences, facilitating intelligent decision-making in multi-band and multi-scenario communication systems through the concept of channel knowledge maps (CKMs).

The sixth paper, titled "Air-to-Ground Channel Measurement and Modeling for Low-Altitude UAVs: A Survey", synthesizes recent advancements in low-altitude UAV air-to-ground channel research, providing a comprehensive overview of measurement campaigns, modeling approaches, and future directions critical to 6G aerial network design, with a focus on millimeter-wave scenarios beyond suburban environments.

In conclusion, we hope this special issue serves as a valuable resource for researchers, practitioners, and students engaged in 6G/B6G channel measurements and modeling. It aims to inspire innovative solutions for dynamic channel challenges and drive advancements in AI-integrated channel modeling. We sincerely thank all authors, reviewers, and editorial staff for their contributions, which are crucial to curating this collection. We trust these articles will offer insightful guidance and foster new perspectives in wireless channel characterization for next-generation networks.

Biographies

WANG Chengxiang received his BS and ME degrees in communication and information systems from Shandong University, China in 1997 and 2000, respectively, and PhD degree in wireless communications from Aalborg University, Denmark in 2004. He was a research assistant with the Hamburg University of Technology, Germany from 2000 to 2001, a visiting researcher with Siemens AG Mobile Phones, Germany in 2004, and a research fellow with the University of Agder, Norway from 2001 to 2005. He was with Heriot-Watt University, UK from 2005 to 2018, where he was promoted to professor in 2011. He has been with Southeast University, China, as a professor since 2018, and he is now the Dean of the School of Information Science and Engineering. He is also a professor with the Pervasive Communication Research Center, Purple Mountain Laboratories, China. He has authored 4 books, 3 book chapters, and over 620 papers in refereed journals and conference proceedings, including 28 highly cited papers. He has also delivered 32 invited keynote speeches/talks and 21 tutorials in international conferences. His current research interests include wireless channel measurements and modeling, 6G wireless communication networks, and electromagnetic information theory. Dr. WANG is a member of the Academia Europaea (The Academy of Europe), a member of the European Academy of Sciences and Arts (EASA), a Fellow of the Royal Society of Edinburgh (FRSE), IEEE, and IET. He was an IEEE Communications Society Distinguished Lecturer in 2019 and 2020, and a highly-cited researcher recognized by Clarivate Analytics in 2017 – 2020. He is currently an Executive Editorial Committee Member of the *IEEE Transactions on Wireless Communications*. He has served as an editor for over sixteen international journals, including the *IEEE Transactions on Wireless Communications*, from 2007 to 2009, the *IEEE Transactions on Vehicular Technology*, from 2011 to 2017, and the *IEEE Transactions on Communications*, from 2015 to 2017. He was a guest editor of the *IEEE Journal on Selected Areas in Communications*, *IEEE Transactions on Big Data*, and *IEEE Transactions on Cognitive Communications and Networking*. He has served as a TPC Chair and General Chair for more than 30 international conferences. He received the IEEE Neal Shepherd Memorial Best Propagation Paper Award in 2024. He also received 19 Best Paper Awards from international conferences.

HUANG Chen received his PhD degree from Beijing Jiaotong University, China in 2021. From 2018 to 2020, he was a visiting scholar with the University of Southern California (USC), USA, and with the Universite Catholique de Louvain (UCLouvain), Belgium. From April 2021 to April 2023, he was a postdoctoral research associate at the Pervasive Communication Research Center, Purple Mountain Laboratories (PML), China, and also at the National Mobile Communications Research Laboratory, School of Information Science and Engineering, Southeast University (SEU), China. Since April 2023, he has been a research associate professor at the Pervasive Communication Research Center, PML, and an extramural supervisor at the National Mobile Communications Research Laboratory, School of Information Science and Engineering, SEU. Dr. HUANG was selected for Young Elite Scientists Sponsorship Program by China Association for Science and Technology, "333" High-Level Talent Program and Outstanding Postdoctoral Fellow Program in Jiangsu, received the Best Paper Awards from IEEE ICC 2025, IEEE/CIC ICCC 2024, IEEE ICCT 2023, WCSP 2018, IEEE/CIC ICCC 2018, and serves as the chair of the AI Channel Modeling subgroup at IEEE P1499 Standard Group, associate editor for *IEEE Transactions on Vehicular Technology* and Technical Program Committee (TPC) member for several conferences, including GlobeCom, ICC, VTC-Fall, VTC-Spring, etc. His research interests include 6G channel measurements, characterization, and modeling, machine learning-based channel prediction, and localization. He has authored/co-authored 1 book chapter, over 70 journal and conference papers, and 17 patents.

Channel Measurement and Analysis of Human Body Radar Cross Section in 26 GHz ISAC Systems

DUAN Hongyu[1,2], WANG Mengyang[2], DUO Hao[3], HE Danping[2], MA Yihua[4], LU Bin[5], ZHONG Zhangdui[2]

(1. State Key Laboratory of Advanced Rail Autonomous Operation, Beijing Jiaotong University, Beijing 100044, China;
2. School of Electronic and Information Engineering, Beijing Jiaotong University, Beijing 100044, China;
3. CTTL Terminal Labs, China Academy of Information and Communication Technology, Beijing 100191, China;
4. State Key Laboratory of Mobile Network and Mobile Multimedia Technology, ZTE Corporation, Shenzhen 518055, China;
5. China Telecom Research Institute, Guangzhou 510630, China)

DOI: 10.12142/ZTECOM.202502002

https://kns.cnki.net/kcms/detail/34.1294.TN.20250517.1809.002.html, published online May 18, 2025

Manuscript received: 2024-12-13

Abstract: Radar cross section (RCS) plays a critical role in modeling target scattering characteristics and enhancing the precision of target detection and localization in integrated sensing and communication (ISAC) systems. This paper investigates the human body RCS at 26 GHz via multi-angle channel measurements under different clothing conditions. Based on calibrated electromagnetic (EM) parameters, the RCS characteristics of the human body in far-field conditions are analyzed using ray-tracing (RT) simulations. Some suggestions for the design of ISAC systems are also discussed. The results provide a solid theoretical foundation and practical reference for the modeling of target scattering characteristics for ISAC channels.

Keywords: channel measurement; human body; radar cross section; integrated sensing and communication; ray-tracing

Citation (Format 1): DUAN H Y, WANG M Y, DUO H, et al. Channel measurement and analysis of human body radar cross section in 26 GHz ISAC systems [J]. ZTE Communications, 2025, 23(2): 3 - 10. DOI: 10.12142/ZTECOM.202502002

Citation (Format 2): H. Y. Duan, M. Y. Wang, H. Duo, et al., "Channel measurement and analysis of human body radar cross section in 26 GHz ISAC systems," *ZTE Communications*, vol. 23, no. 2, pp. 3 - 10, Jun. 2025. doi: 10.12142/ZTECOM.202502002.

1 Introduction

6G technology drives the evolution of integrated sensing and communication (ISAC) systems. With its large bandwidth advantage, a 6G system allows perception functions to be upgraded from basic positioning to high-precision tracking, target recognition, and classification. Accurately perceiving key targets in ISAC channels is essential for achieving high-accuracy positioning and tracking[1].

In the research field of ISAC, the scattering characteristics of the human body as a typical target have attracted significant research attention. As a critical metric for evaluating the reflection characteristics of targets, the radar cross section (RCS) provides a critical reference basis for ISAC systems. With the rapid development of autonomous driving, healthcare, security monitoring, and other fields, the demand for high-precision object detection and recognition technology has surged[2-3]. In healthcare, the detected data can facilitate remote monitoring of vital signs and early detection of health issues, leveraging the advanced communication-sensing capabilities of 6G networks[4]. Furthermore, in search and rescue operations for survivors buried under avalanches, landslides, or collapsed buildings, RCS analysis of the human body can be promptly conducted to assess the situation and locate the trapped individuals. This capability enables precise localization and monitoring, facilitating efficient rescue operations and optimal resource allocation[2]. Other significant applications lie in the field of security, where this technology enables the identification and distinction of potentially dangerous individuals based on anomalous breath patterns or heartbeat patterns[5]. Human body RCS analysis further expands new applications for advanced technologies, such as multiple-input multiple-output (MIMO)[6], reconfigurable intelligent surface (RIS)[7-8], and micro-Doppler signature[9]. While there are ample application prospects and advantages, human body RCS analysis faces significant challenges. The radar simu-

This work was supported by the National Natural Science Foundation of China under Grant No. 62271043, Ministry of Education of China under Grant No. 8091B032123, and Beijing Natural Science Foundation under Grant No. L212029.

lation technique for human motion must be as close to the real radar data as possible; however, it must be easily implementable and computationally efficient at the same time[3].

Currently, most existing human detection radar systems operate in X-band, ultra-high frequency (UHF), and even lower frequency bands[10]. Ref. [11] discusses the findings of an RCS and specific absorption rate (SAR) study of the human head at 0.9 – 2.45 GHz based on full-wave numerical model simulations. The effective RCS of human cardiopulmonary activity is studied for a male subject in supine and prone positions at 2.4 GHz[12]. An experimental setup for complex channel measurement in a non-anechoic environment in the 6 – 10 GHz frequency range is validated in Ref. [13]. With the advancement of wireless communication towards higher frequency bands, such as millimeter-wave (mmWave), terahertz (THz), and visible light bands, an increasing overlap with traditional sensing frequency bands will occur[14]. Specifically, mmWave frequency bands are essential for 6G communication-sensing integration due to their remarkable capabilities, encompassing fine spatial resolution that enables high-precision target localization, speed measurement, and imaging[15]. Among mmWave frequencies, the 26 GHz band is particularly advantageous. It offers an effective balance between propagation characteristics suitable for long-range communications and the wide bandwidth essential for high-resolution sensing. Furthermore, the short wavelength of 26 GHz signals helps reduce interference from other cellular data, thereby enhancing spectrum efficiency.

Despite the recent execution of numerous ISAC channel measurements with human targets, a notable lack of data supporting human body RCS characteristics within the mmWave frequency bands poses a significant challenge for ISAC. Building on the limited existing literature, Ref. [16] presents detailed evaluations of human RCS characteristics. As an extension to prior analyses, it addresses open issues including the influence of different limb postures and clothing types on the 23 – 28 GHz frequency bands. However, precise data regarding the human body within the ISAC frequency band remains severely lacking, and various influential factors have not been comprehensively considered. Firstly, owing to its non-rigid nature, the human body undergoes numerous dynamic motions, leading to significant variations in the RCS depending on individual posture and radar orientation. Secondly, the human body is composed of multiple dielectric layers, which further complicates the RCS analysis. The roughness of skin and clothing surfaces introduces substantial variability in these analyses[17]. Additionally, existing studies often fail to provide direct electromagnetic (EM) material parameters for the human body during the RCS data analysis, thereby limiting the generalizability of research findings to other deterministic studies. Achieving far-field conditions for antenna and target channel measurements poses significant physical challenges. Ray-tracing (RT) techniques can effectively overcome these limitations, enabling precise calculation of RCS. However, current research still lacks RCS modeling in the multi-polarization mode under far-field conditions[18].

To address the above-mentioned demands and challenges, this paper conducts measurements and analyses of the human body within communication channels to provide a reference for implementing sensing functions through the communication systems. The main contributions and novelties of this paper are as follows.

• Channel measurements of the human body at 26 GHz are conducted on individuals wearing different clothing, capturing data from different angles in static situations. Based on these measurements, a comprehensive dataset of the human body is established.

• The EM material parameters related to the human body are calibrated. These parameters can be utilized for generalization simulations, providing a reference for deterministic modeling endeavors.

• The RCS at different azimuth and elevation angles is calculated and analyzed for different multi-polarization combinations. Based on these findings, suggestions for the future design of the ISAC system are discussed.

The rest of this paper is organized as follows. Section 2 describes the measurement system and campaign. Section 3 introduces the RT simulation and calibration of EM parameters. Section 4 presents a detailed RCS calculation and analysis, and Section 5 concludes the paper.

2 Measurement

2.1 Measurement System

In this work, the measurement system comprises a Keysight N5247A vector network analyzer (VNA), a personal computer (PC) control terminal, and two standard gain horn antennas, as depicted in Fig. 1. The VNA, connected to the PC and controlled by specialized programs, generates signals with a bandwidth of 1 GHz and acquires 201 frequency samples. The an-

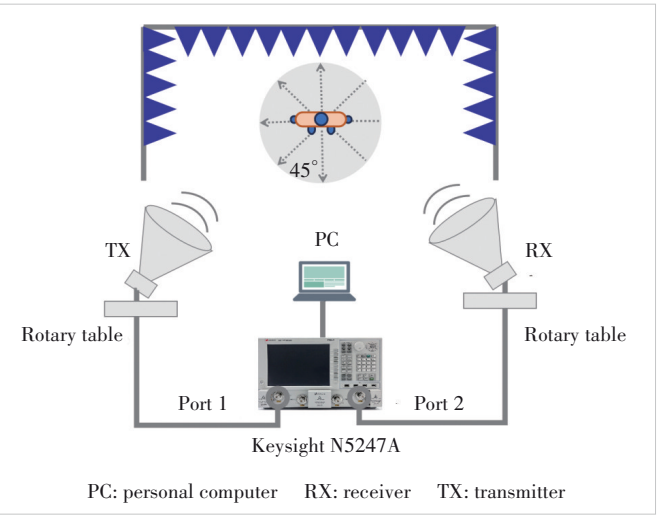

Figure 1. Measurement system

tennas, serving as the transmitter (TX) and receiver (RX), are fixed on separate rotary tables and connected to Port 1 and Port 2 of the VNA, respectively. The system is set up in a semi-dark room with the antennas positioned at ±34° angles toward the human body, maintained at a distance of 1.6 m and a height of 1.01 m above the ground. This configuration ensures that the main lobe of the TX illuminates the human body, while the RX receives the corresponding echo. The configuration parameters of the measurement system are summarized in Table 1.

2.2 Measurement Campaign

The channel measurement of the human body at multiple angles is carried out in a semi-dark room built with absorbing materials. The subject is an adult male (1.78 m in height, 78 kg in weight) wearing two kinds of clothing (short and long clothes), as shown in Fig. 2. The point cloud of the subject's body is obtained by laser scanning. After processing the point cloud and importing it into SketchUp to give the corresponding materials to the human body surface, the human body model used in RT simulation is established.

To obtain the scattering characteristics of the human body at different angles, five rotational positions of the human body relative to the measurement system are set up. The subject stands on a rotary table to control the rotation angle by the scale. The 0° position corresponds to the human body directly facing the measurement system, and the other four positions are set at 45°, 90°, 135°, and 180° in the clockwise direction. The measurement results under different clothing conditions are shown in Figs. 3 and 4. The absorbing material effectively shields the echoes from many environmental objects, and the multipath component (MPC) of the human body is marked.

Table 1. Configuration parameters of the measurement system

Measurement Parameter	Value
Center frequency	26 GHz
Bandwidth	1 GHz
Delay resolution	1 ns
Frequency samples	201
TX and RX heights from the ground	1.01 m
Distance between TX and RX	1.6 m
Antenna rotation angle towards the human body	±34°
Polarization mode	Vertical polarization
Antenna gain	22.4 dBi

RX: receiver TX: transmitter

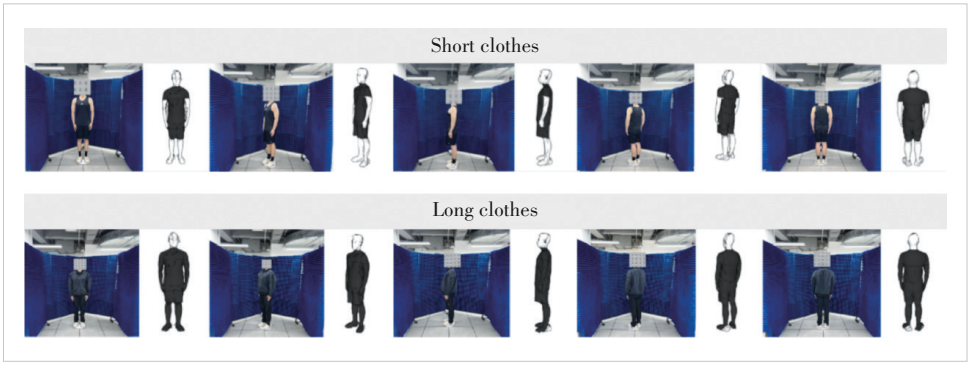

Figure 2. Human body in different types of clothes

The results show that the power of MPC of the human body is the strongest when facing the measurement system and facing away from it, which are rotating at 0° and 180°. In these two cases, the reflection and scattering area of the human body is larger, so the reflected echo energy is larger. The human back approximates a convex surface, resulting in the strongest reflection power. This is because the convex surface concentrates the reflected waves into a smaller area, thereby increasing the power density of the reflected signal in the direction of reflection. Meanwhile, the power of MPC under short clothes is higher than that under long clothes, which can be explained by the fact that human skin is smoother than clothing, and its echo power of reflection and scattering is stronger. However, in the case of rotating at 180°, the back in long clothes is flatter than that in short clothes, so the reflected power is stronger than that under short clothes. Additionally, the body posture observed in this study often has the limbs close to the body, making it challenging to accurately identify different body parts using only the power delay profile (PDP).

3 RT Simulation and Calibration of EM Parameters

3.1 RT Simulation

In this work, the high-performance RT simulation platform developed by the State Key Laboratory of Advanced Rail Autonomous Operation of Beijing Jiaotong University is adopted[19–20]. In ISAC channels, the scattering characteristics of targets are crucial for accurate channel modeling, which is affected by the dominant propagation mechanisms of reflection and scattering. Fresnel reflection and directional scattering[21] are applied in RT.

3.1.1 Reflection

When an object whose volume is much larger than the wavelength of the EM wave is in the path of propagation, the wave cannot diffract through the object and will be reflected at the junction of different media. The wireless signal reflected by the ground or other obstacles reaches the receiver, called the reflected wave. The electric field strength of the reflected wave and transmitted wave depends on the Fresnel reflection coefficient of the incident wave in the medium. The coefficients $r_{\parallel i,k}$ and $r_{\perp i,k}$ are

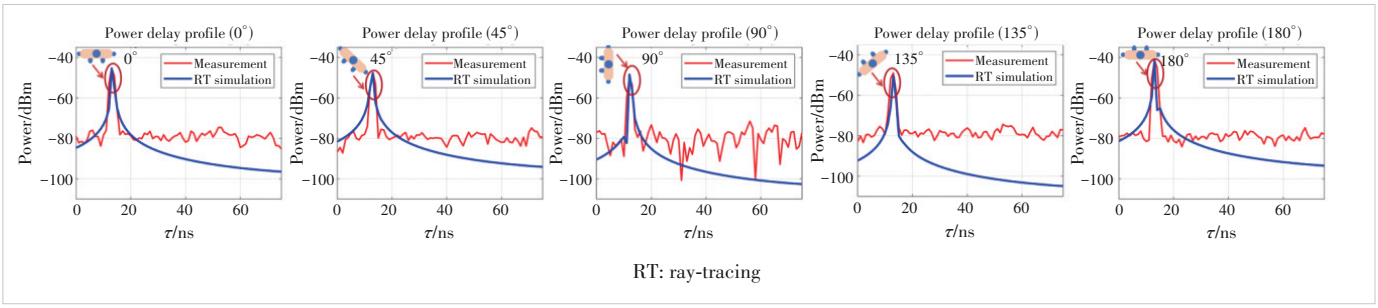

Figure 3. Measurement results of the subject in short clothes

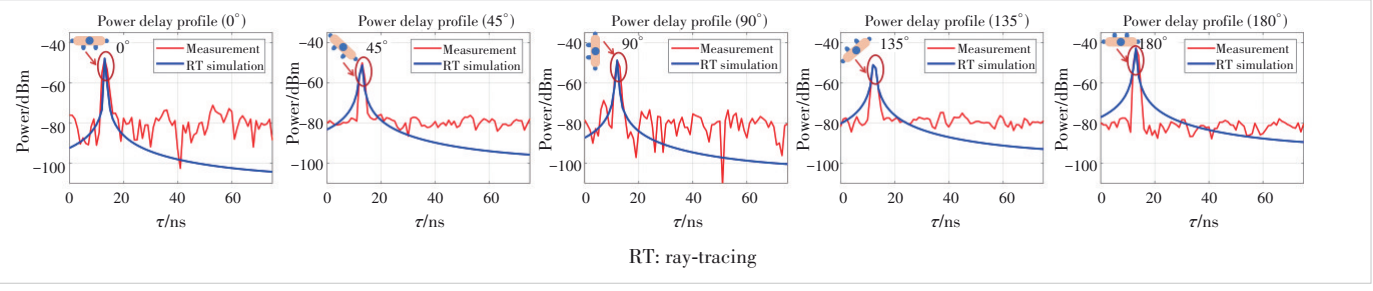

Figure 4. Measurement results of the subject in long clothes

the reflection (scattering) coefficients of the vertical and horizontal components of the k-th multipath component at the i-th reflection (scattering) surface, respectively. For transversal magnetic (TM) polarization, the reflection coefficient is:

$$r_{\parallel i,k} = R_{\mathrm{TM}_{i,k}} = \frac{\sqrt{\frac{\varepsilon_2}{\varepsilon_1}}\cos\delta_{\mathrm{inc}_{i,k}} - \cos\delta_{\mathrm{trans}_{i,k}}}{\sqrt{\frac{\varepsilon_2}{\varepsilon_1}}\cos\delta_{\mathrm{inc}_{i,k}} + \cos\delta_{\mathrm{trans}_{i,k}}} \tag{1}$$

For transversal electric (TE) polarization, the reflection coefficient is:

$$r_{\perp i,k} = R_{\mathrm{TE}_{i,k}} = \frac{\cos\delta_{\mathrm{inc}_{i,k}} - \sqrt{\frac{\varepsilon_2}{\varepsilon_1}}\cos\delta_{\mathrm{trans}_{i,k}}}{\cos\delta_{\mathrm{inc}_{i,k}} + \sqrt{\frac{\varepsilon_2}{\varepsilon_1}}\cos\delta_{\mathrm{trans}_{i,k}}} \tag{2}$$

For the TM case, the magnetic field component is parallel to the reflection (scattering) surface. However, for the TE case, the electric field component is parallel to the reflection (scattering) surface. The angles $\delta_{\mathrm{inc}_{i,k}}$ and $\delta_{\mathrm{trans}_{i,k}}$ are the incidence and transmission angles, respectively, with respect to the normal vector of the surface where reflection (scattering) occurs.

3.1.2 Scattering

There are two kinds of scattering models in wireless communication: the directional scattering and RCS scattering. The former includes the directional single-beam model and the directional double-beam model. The directional single-beam model is mainly introduced here. This model assumes that the scattered lobes reflect in the direction of the mirror surface, and the expression is as follows:

$$\left|E_S\right|^2 = \left|E_{S_0}\right|^2\left(\frac{1+\cos\psi}{2}\right)^{\alpha_R},\ \alpha_R = 1, 2, \cdots, N \tag{3}$$

where ψ denotes the angle formed between the scattering and reflection directions; α_R represents the scattering equivalent roughness, an integer that dictates the width of the scattering lobe, with increasing values resulting in narrower beams; E_S signifies the scattered electric field, measured at an angle ψ from the reflection direction; E_{S_0} signifies the maximum scattered electric field value. When the EM wave is incident on the surface of the material at the incident angle θ_i, E_{S_0} is expressed as follows:

$$\left|E_{S_0}\right|^2 = \left(\frac{SK}{d_t d_r}\right)^2 \frac{\mathrm{dS}\cos\theta_i}{F_{\alpha_R}} \tag{4}$$

Extending the unit area of the material surface dS (the length of the scatterer is l and the width is unit length), we get the final expression of the DS model as follows:

$$\left|E_S\right|^2 = \left|E_{S_0}\right|^2\left(\frac{1+\cos\Psi}{2}\right)^{\alpha_R} = \left(\frac{SK}{d_t d_r}\right)^2 \frac{l\cos\theta_i}{F_{\alpha_R}}\left(\frac{1+\cos\Psi}{2}\right)^{\alpha_R} \tag{5}$$

where l represents the length of the scatterer, K is a constant that depends on the incident power P_t and antenna gain G_t, K =

$\sqrt{60P_tG_t}$, and F_{α_R} is the proportionality factor.

3.2 Calibration of EM Parameters

EM parameters of materials are the foundation of RT, enabling effective representation of the interactions between targets and surroundings. Accurate EM parameters not only enhance the generalization capability of RT across different application scenarios but also improve its predictive accuracy in complex environments. Before calibration of EM parameters, the system and cable losses are measured to ensure accuracy.

Multiple key EM parameters of the human body are calibrated, including the real part of relative permittivity ϵ_{rel}, the loss tangent δ, the scattering gain S, and the effective smoothness α_R. The EM parameters can also describe the body's absorption of radio waves to a certain extent. As shown in Fig. 5, the EM parameters are calibrated based on the power of MPC. The EM parameters of the relevant materials are continuously updated until the error between the simulation power and the measurement power converges. The initialized and calibrated EM parameters are summarized in Table 2.

Table 3 shows the errors between the power of calibrated simulation and measurement, including cases at multiple rotating angles. The calibrated RT can accurately describe the scattering characteristics of the human body at multiple angles with a mean absolute error of 0.82 dB and a standard deviation of 0.89 dB.

4 Analysis of RCS

4.1 Calculation of RCS

RCS plays a key role in target sensing and recognition in ISAC channels, as it directly impacts the reflection and scattering characteristics. The RCS σ can be calculated based on the receiving power P_r of the multipath, as shown in:

$$\sigma = \frac{P_r(4\pi)^3 R^4}{P_t G_t G_r \lambda^2} \quad (6),$$

where P_t is the transmitting power, λ is the wavelength, and R is the range between the target and the measurement system. The gains G_t and G_r represent the transmitting and receiving antenna gains.

Near-field effects arise near the radiating element, where the EM field is incomplete, causing significant inductive and capacitive coupling. Conversely, far-field effects, observed at distances where waves have propagated as plane waves, minimize coupling impacts. However, due to the physical limitations of the measurement systems and environments, it is often difficult to ensure that both the antenna and the target are in the far-field region[22]. When the target and the antenna are in the far field, the EM waves can be approximated as plane waves. This facilitates the calculation and prediction of scattering characteristics, ensuring the stability and consistency of measurement results. If not, near-field effects may significantly degrade measurement accuracy, leading to erroneous analysis outcomes. In such cases, RT, with its flexibility, breaks scenario constraints, making it an effective tool for calculating RCS.

The distance between the human body and RX is 1.80 m. The maximum size of the human body is 1.78 m. According to the equation:

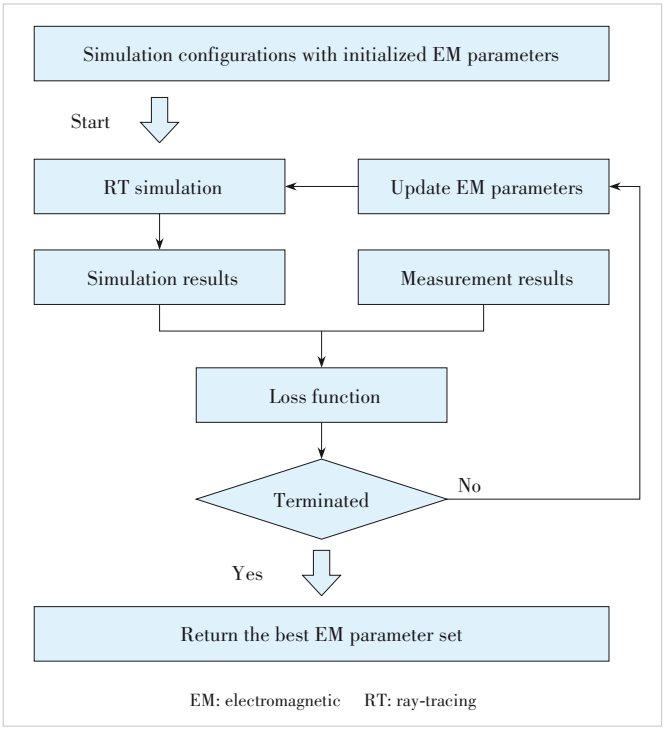

Figure 5. Working flow of calibration of EM parameters

Table 2. Comparison of initialized and calibrated EM parameters.

Material	Initialized				Calibrated			
	ϵ_{rel}	δ	S	α_R	ϵ_{rel}	δ	S	α_R
Skin	1	0.1	1	1	17.7	0.953 1	0.88	16.5
Polyester	1	0.1	1	1	2.1	0.750 0	0.85	15.3
Cotton	1	0.1	1	1	2.8	0.700 0	0.83	14.2

Table 3. Error statistics

Outfit	Angle/(°)	Measurement Power/dBm	Simulation Power/dBm	Absolute Error/dB
Short	0	−45.20	−45.34	0.14
	45	−47.37	−47.70	0.36
	90	−49.85	−48.40	1.45
	135	−49.01	−50.45	1.44
	180	−41.36	−41.52	0.16
Long	0	−48.05	−47.93	0.12
	45	−50.05	−51.30	1.25
	90	−48.71	−48.85	0.14
	135	−51.30	−51.11	0.19
	180	−39.51	−42.44	2.93

$$d_f = 2D^2/\lambda \quad (7),$$

where d_f is the distance of the Fraunhofer region, D is the maximum linear dimension of the antenna, and λ is the wavelength. The far-field distance of the human body is 561.6 m. In the simulation of this work, the distance between the human body and the measurement system is set to 580 m to ensure that both the human body and antennas are in the far field.

In ISAC systems, the variation of RCS at different azimuth angles is essential for describing a target's scattering characteristics. Since RCS represents how a target reflects EM waves, its variation with angle directly influences sensing accuracy and communication channel performance. On the other hand, the research of RCS at different zenith angles is also very important for the deployment of ISAC systems. The TX-RX polarization combinations include horizontal-horizontal (H-H), horizontal-vertical (H-V), vertical-horizontal (V-H), and vertical-vertical (V-V) polarizations. As shown in Figs. 6 and 7, the RCSes of the human body at different horizontal and elevation angles under different clothing are calculated by RT. Table 4 shows the statistics of RCS under different polarization modes.

The findings reveal that the RCS is typically greater when the TX and RX antennas are aligned in the same polarization mode. Furthermore, the RCS for short clothing tends to be slightly higher than that for long clothing in the same polarization mode. Notably, the mean azimuth RCS, when subjected to different polarization modes, experiences a decrease of approximately 16 dBsm compared to that in the same polarization mode. The mean elevation RCS sees a reduction of around 14 dBsm under similar circumstances.

4.2 System Design Discussion

The calculation of RCS indicates that the RCS values are higher when using co-polarized transmit and receive antennas, which can be attributed to the EM scattering characteristics of co-polarization. In a co-polarization configuration, the polarization of the TX and RX antennas is aligned, allowing for more efficient capture of the reflected signals from the target. This alignment enables better matching between the incident wave and the target's scattering properties, particularly for surfaces with geometric regularity or dimensions comparable to the wavelength, resulting in stronger energy coupling and consequently higher RCS values. From an EM theory perspective, the target's

Table 4. Statistics of RCS under different polarization modes

Outfit	Polarization	Mean Azimuth RCS/dBsm	Polarization	Mean Elevation RCS/dBsm
Short	H-H	−2.78	H-H	−7.83
	H-V	−19.3	H-V	−22.21
	V-H	−19.3	V-H	−22.21
	V-V	−2.52	V-V	−7.45
Long	H-H	−3.91	H-H	−8.17
	H-V	−18.82	H-V	−21.91
	V-H	−18.82	V-H	−21.91
	V-V	−3.59	V-V	−7.54

H-H: horizontal-horizontal RCS: radar cross section V-V: vertical-vertical
H-V: horizontal-vertical V-H: vertical-horizontal

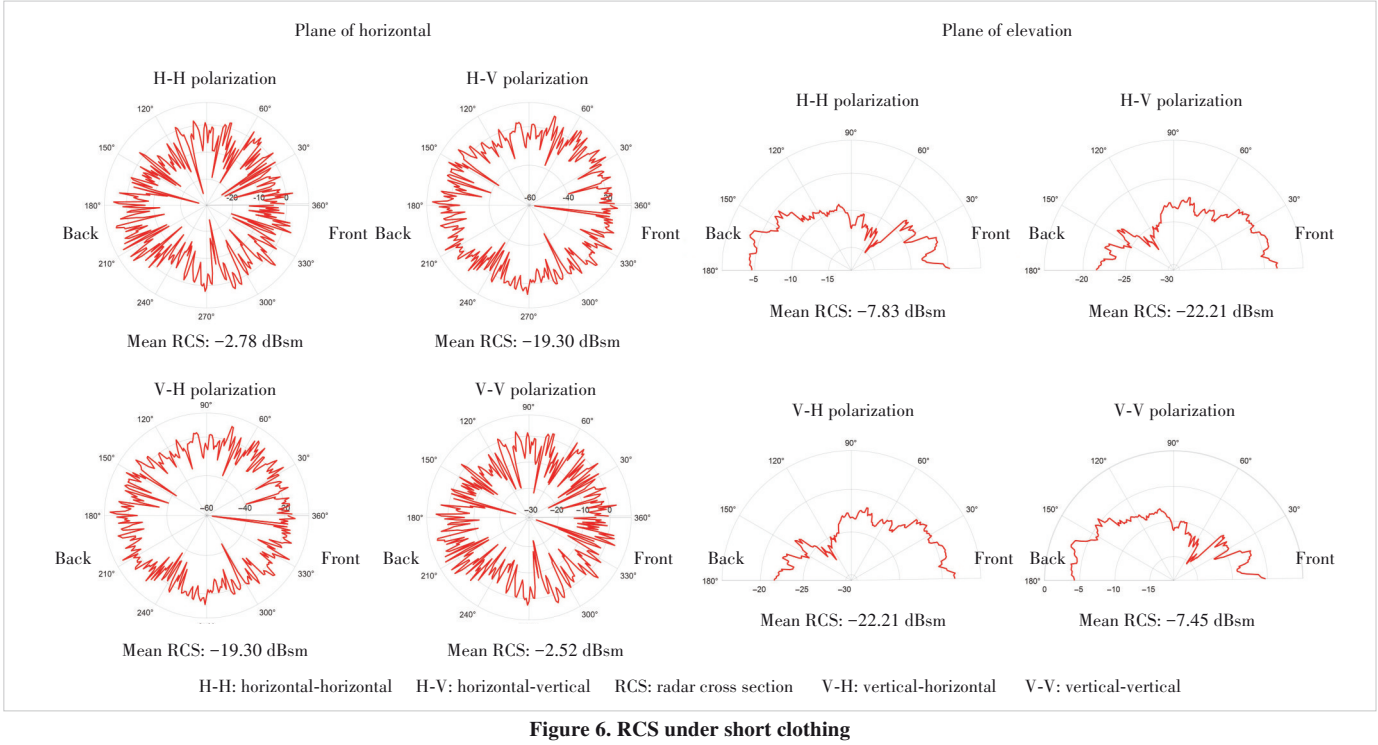

Figure 6. RCS under short clothing

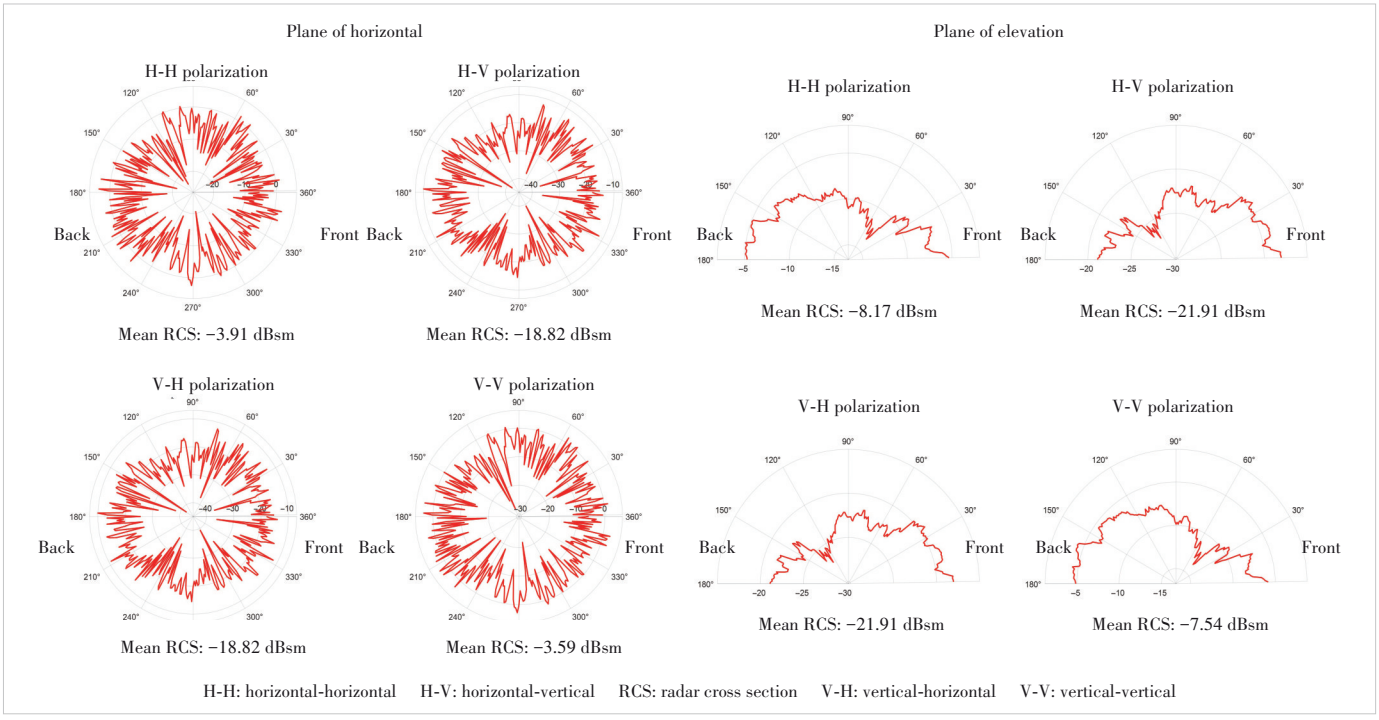

Figure 7. RCS under long clothing

surface induces scattering, reflection, and absorption of the EM waves. Under co-polarized conditions, the reflection coefficient is relatively high. For complex targets such as the human body, various factors, including the surface roughness, material composition, EM parameters, and clothing conditions, can significantly influence RCS. The co-polarization setup enhances the coherence of reflected signals, thereby increasing the strength of the scattered signals. Furthermore, as EM waves undergo multiple reflections on the target's surface, co-polarization tends to facilitate phase addition, further amplifying the magnitude of the received signal.

The research content of this paper aims to analyze the characteristics of the target in the communication channel to realize the sensing function. Therefore, in the design of this kind of ISAC systems, opting for co-polarized TX and RX configurations can effectively enhance the echo signal from the target, improving detection sensitivity. It also enhances the system's resilience to interference and reduces the impact of background noise, thereby improving sensing accuracy and robustness. Such a design is particularly suitable for scenarios requiring high sensitivity and precise sensing, such as long-range target detection and weak scattering characteristic capture.

However, interference may distort the reflected signal, leading to fluctuations or attenuation of the RCS. The movement of a target in a dynamic environment alters its reflective characteristics, causing the RCS to vary with the incident angle. Multipath effects may further exacerbate the impact. In the future, we need to consider measuring in more element-rich scenarios to fully account for these influencing factors.

5 Conclusions

This paper presents multi-angle channel measurements of the human body at 26 GHz under different clothing conditions. Based on the measurement data, the EM parameters of human body materials are calibrated with a mean absolute error of 0.82 dB and a standard deviation of 0.89 dB. The RT simulator is deployed to comprehensively calculate and analyze the RCS of the human body under various polarization configurations, azimuth angles, and elevation angles. The results indicate that co-polarized antennas exhibit higher RCS values across a range of angles compared to cross-polarized configurations. Finally, some suggestions on the design of ISAC systems are given. This work not only highlights the significant impact of polarization on target scattering characteristics but also provides critical insights for target identification and environmental sensing. The data and results presented in this work offer theoretical support and practical guidance for the design of ISAC systems.

References

[1] INCA S, MROZOWSKI A, PRADO-ALVAREZ D, et al. Angular correlation study of sensing and communication channels in V2X scenarios for 6G ISAC usage [C]//Proc. IEEE Globecom Workshops (GC Wkshps). IEEE, 2023: 1189 – 1194. DOI: 10.1109/GCWkshps58843.2023.10465114
[2] DE PASQUALE G, SARRI A, BONOPERA C, et al. RCS of human being physiological movements in the 1 – 10 GHz bandwidth: theory, simulation and measurements [C]//Proc. IEEE Radar Conference. IEEE, 2008: 1 – 6. DOI: 10.1109/RADAR.2008.4720983
[3] ISHAK K, APPENRODT N, DICKMANN J, et al. Advanced radar micro-Doppler simulation environment for human motion applications [C]//Proc.

IEEE Radar Conference (RadarConf). IEEE, 2019: 1 – 6. DOI: 10.1109/RADAR.2019.8835755
[4] KIRIAZI J E, BORIC-LUBECKE O, LUBECKE V M. Radar cross section of human cardiopulmonary activity for recumbent subject [C]//Annual International Conference of the IEEE Engineering in Medicine and Biology Society. IEEE, 2009: 4808 – 4811. DOI: 10.1109/IEMBS.2009.5332634
[5] KIRIAZI J E, BORIC-LUBECKE O, LUBECKE V M. Modeling of human torso time-space characteristics for respiratory effective RCS measurements with Doppler radar [C]//Proc. IEEE MTT-S International Microwave Symposium. IEEE, 2011: 1. DOI: 10.1109/MWSYM.2011.5973284
[6] HONMA N, SASAKAWA D, SHIRAKI N, et al. A state-machine-based approach for human activity classification using MIMO radar [C]//Proceedings of International Symposium on Antennas and Propagation (ISAP). IEEE, 2021: 1 – 2. DOI: 10.23919/ISAP47258.2021.9614433
[7] SHEN Y, OU P, CHEN F K, et al. Reconfigurable intelligent surface-assisted channel characteristics in 5G high-speed railway scenario [J]. Journal of Beijing Jiaotong University, 2023, 47(2): 23 – 35. DOI: 10.11860/j.issn.1673-0291.20220098
[8] HAN F Y, DING J M, FEI D, et al. Channel parameter acquisition and simulation evaluation of RIS-aided wireless communication system [J]. Journal of Beijing Jiaotong University. 2023, 47(5): 63 – 71. DOI: 10.11860/j.issn.1673-0291.20220147
[9] ABADPOUR S, PAULI M, SCHYR C, et al. Angular resolved RCS and Doppler analysis of human body parts in motion [J]. IEEE transactions on microwave theory and techniques, 2023, 71(4): 1761 – 1771. DOI: 10.1109/TMTT.2022.3218304
[10] SINGH A D, RAM S S, VISHWAKARMA S. Simulation of the radar cross-section of dynamic human motions using virtual reality data and ray tracing [C]//Proc. IEEE Radar Conference (RadarConf18). IEEE, 2018: 1555 – 1560. DOI: 10.1109/RADAR.2018.8378798
[11] FANG C H, QIN Y, HU C-F. Numerical study of human head RCS and SAR at 0.9 – 2.45 GHz [C]//2017 International Applied Computational Electromagnetics Society Symposium (ACES). IEEE, 2017: 1 – 2
[12] LEE A, GAO X M, XU J, et al. Effects of respiration depth on human body radar cross section using 2.4 GHz continuous wave radar [C]//Proc. 39th Annual International Conference of the IEEE Engineering in Medicine and Biology Society (EMBC). IEEE, 2017: 4070 – 4073. DOI: 10.1109/EMBC.2017.8037750
[13] TIEN T V, OUVRY L, SIBILLE A. Time domain complex radar cross section of human body for breath-activity monitoring [C]//Proc. 11th European Conference on Antennas and Propagation (EUCAP). IEEE, 2017: 421 – 425. DOI: 10.23919/EuCAP.2017.7928648
[14] YANG B, LIANG X, LIU S N, et al. Intelligent 6G wireless network with multi-dimensional information perception [J]. ZTE communications, 2023, 21(2): 3 – 10. 10.12142/ZTECOM.202302002
[15] LIU H P, ZHANG X Y, ZHOU A F, et al. Indoor environment and human sensing via millimeter wave radio: a review [J]. ZTE communications, 2021, 19(3): 22 – 29. DOI: 10.12142/ZTECOM.202103004
[16] SCHUBERT E, KUNERT M, MENZEL W, et al. Human RCS measurements and dummy requirements for the assessment of radar based active pedestrian safety systems [C]//14th International Radar Symposium (IRS). IEEE, 2013: 752 – 757
[17] ABADPOUR S, MARAHRENS S, PAULI M, et al. Backscattering behavior of vulnerable road users based on high-resolution RCS measurements [J]. IEEE transactions on microwave theory and techniques, 2022, 70(3): 1582 – 1593. DOI: 10.1109/TMTT.2021.3131156
[18] MANFREDI G, RUSSO P, DE LEO A, et al. Efficient simulation tool to characterize the radar cross section of a pedestrian in near field [J]. Progress in electromagnetics research C, 2020, 100: 145 – 159. DOI: 10.2528/pierc19112701
[19] HE D P, AI B, GUAN K, et al. The design and applications of high-performance ray-tracing simulation platform for 5G and beyond wireless communications: a tutorial [J]. IEEE communications surveys & tutorials, 2019, 21(1): 10 – 27. DOI: 10.1109/COMST.2018.2865724
[20] HE D P, GUAN K, YAN D, et al. Physics and AI-based digital twin of multi-spectrum propagation characteristics for communication and sensing in 6G and beyond [J]. IEEE journal on selected areas in communications, 2023, 41(11): 3461 – 3473. DOI: 10.1109/JSAC.2023.3310108
[21] DEGLI-ESPOSTI V, FUSCHINI F, VITUCCI E M, et al. Measurement and modelling of scattering from buildings [J]. IEEE transactions on antennas and propagation, 2007, 55(1): 143 – 153. DOI: 10.1109/TAP.2006.888422
[22] HUANG J H, ZHOU J J, DENG Y. Near-to-far field RCS calculation using correction optimization technique [J]. Electronics, 2023, 12(12): 2711. DOI: 10.3390/electronics12122711

Biographies

DUAN Hongyu received his BE degree in information engineering from the School of Electronic and Information Engineering, Beijing Jiaotong University, China in 2022. He is currently pursuing a PhD degree at the State Key Laboratory of Advanced Rail Autonomous Operation, Beijing Jiaotong University. His research interests include radio wave propagation, wireless channel modeling, and integrated sensing and communication.

WANG Mengyang received his BE degree in communication engineering from University of Jinan, China in 2024. He is pursuing a master's degree at the School of Electronic and Information Engineering, Beijing Jiaotong University, China. His research interests include wireless channel modeling and integrated sensing and communication.

DUO Hao (duohao@caict.ac.cn) is the Deputy Chief Engineer of CTTL-terminal at the China Academy of Information and Communications Technology. He has been engaged in the research of wireless mobile communication technology for a long time. He has extensive experience in mobile terminal standardization work, both domestically and internationally, with a particular focus on mobile terminal device testing technology. He has completed over 30 industry-standard projects in China's mobile terminal industry and published over 10 papers in important domestic journals.

MA Yihua received his BE degree from Southeast University, China in 2015 and MS degree from Peking University, China in 2018. Since 2018, he has been with ZTE Corporation. He is now a senior expert in the Department of Wireless Algorithm of ZTE, and a member of the State Key Laboratory of Mobile Network and Mobile Multimedia Technology, China. His main research interests include integrated sensing and communications, distributed massive MIMO, and grant-free NOMA.

HE Danping is an associate professor with the School of Electronic and Information Engineering, Beijing Jiaotong University, China. Her current research interests include radio propagation and channel modeling, ray-tracing technologies, and wireless communication algorithm design. She received five best paper awards and the 2019 Applied Computational Electromagnetics Society (ACES)-China Young Scientist Award.

LU Bin received his master's and PhD degrees from the Department of Radio Engineering, South China University of Technology, China. He is now a senior engineer at the China Telecom Research Institute. His current research interests include wireless private networks, radio propagation and channel modeling, and wireless mobile digital twin technology.

ZHONG Zhangdui is a professor with the School of Electronic and Information Engineering, Beijing Jiaotong University, China. He is also a director of the Innovative Research Team of the Ministry of Education, China, and a Chief Scientist of the Ministry of Railways of China. He is an executive council member of the Radio Association of China and a deputy director of the Radio Association of Beijing, China. His research interests are wireless communications for railways, control theory and techniques for railways, and the GSM-R system.

Space Network Emulation System Based on a User-Space Network Stack

LEI Jianzhe[1], ZHAO Kanglian[1], HOU Dongxu[2], ZHOU Fenlin[2]
(1. Nanjing University, Nanjing 210023, China;
2. ZTE Corporation, Shenzhen 518057, China)

DOI: 10.12142/ZTECOM.202502003
https://kns.cnki.net/kcms/detail/34.1294.TN.20250514.1835.002.html, published online May 15, 2025
Manuscript received: 2025-02-22

Abstract: This paper presents a space network emulation system based on a user-space network stack named Nos to solve space networks' unique architecture and routing issues and kernel stacks' inefficiency and development complexity. Our low Earth orbit satellite scenario emulation verifies the dynamic routing function of the protocol stack. The proposed system uses technologies like Open vSwitch (OVS) and traffic control (TC) to emulate the space network's highly dynamic topology and time-varying link characteristics. The emulation results demonstrate the system's high reliability, and the user-space network stack reduces development complexity and debugging difficulty, providing convenience for the development of space network protocols and network functions.

Keywords: network emulation; space network; user-space network stack; network function virtualization

Citation (Format 1): LEI J Z, ZHAO K L, HOU D X, et al. Space network emulation system based on a user-space network stack [J]. ZTE Communications, 2025, 23(2): 11 - 19. DOI: 10.12142/ZTECOM.202502003
Citation (Format 2): J. Z. Lei, K. L. Zhao, D. X. Hou, et al., "Space network emulation system based on a user-space network stack," *ZTE Communications*, vol. 23, no. 2, pp. 11 - 19, Jun. 2025. doi: 10.12142/ZTECOM.202502003.

1 Introduction

1.1 Development of Space Network and Its Emulation Methods

In recent years, with the continuous iteration of communication technologies and the growing demands for information perception, satellite telemetry, and global network integration, the traditional terrestrial Internet based on the Open Systems Interconnection (OSI) protocol stack can no longer meet the increasingly diverse and expanding network service needs. As a new network service model, the space Internet offers a broader service coverage while ensuring transmission bandwidth. It effectively overcomes challenges such as user access limitations due to terrestrial factors.

Satellite networks have become indispensable in various fields, including military security, aerospace, civilian networks, and remote sensing exploration. However, a series of emerging and evolving network algorithms, protocol systems, and network management models have also surfaced alongside its rapid development. Implementing a new technology, from theoretical development to practical deployment, requires a series of complex validation processes, such as performance evaluations and network throughput tests. As a communication network deployed in unique environments, the satellite network particularly requires systematic network emulation methods and verification platforms to support technological validation. Network emulation methods are generally categorized into four types: network theoretical model construction, physical platform setup, network simulation, and network emulation[1].

- Network theoretical model construction: This method involves network research through modeling, theoretical analysis, and algorithm design. It provides a theoretical foundation for the design and implementation of network technology.
- Physical platform setup: This approach aims to replicate the network scenario to the greatest extent, offering high authenticity. However, it is challenging to deploy, needs more scalability and reconfigurability, and has high hardware requirements for network equipment, limiting its use for large-scale deployments.
- Network simulation: This software-based method simulates existing network scenarios, protocols, and services, offering relatively simple, cost-effective and easily extendable experimental environment. However, it does not support real traffic loads transmission, leading to less accurate results.
- Network emulation: Combining the advantages of physical platforms and network simulation, network emulation supports

This work was supported by the National Natural Science Foundation of China under Grant No. 62131012 and ZTE Industry-University-Institute Cooperation Funds under Grant No. IA20230712005.

real protocols and data flow transmission. It thus offers high fidelity, flexibility, easy deployability, and scalability.

A network emulation platform is generally constructed through virtualization technology. Virtualization reallocates and isolates physical hardware resources on real physical devices, abstracting resources from computer hardware to the network operating system and network applications, to create an emulation environment. Traditional virtualization technology builds virtual machine managers on the host system, where each virtual unit requires its own operating system. In large-scale satellite network scenarios, where the network applications between nodes are similar, traditional virtualization solutions result in considerable resource redundancy, leading to inefficiency. Therefore, container-based network solutions have been proposed. Based on the host server's operating system, containerized networking implements process-level virtualization, which minimizes emulation node overhead and maximizes the use of the host server's physical resources.

Given the unique structure of the space network, it differs significantly from traditional terrestrial networks in terms of transmission conditions, node deployment, and information compatibility. For instance, network signals are significantly impacted by factors such as cosmic electromagnetic interference and terrestrial atmospheric activity during transmission. This results in high bit error rates or temporary link interruptions. Additionally, due to the large distances between satellite nodes, network signal transmission experiences high latency and time jitter. The high-speed movement of satellites further leads to highly dynamic network topologies, causing periodic changes in link relationships between nodes[2]. These factors restrict satellite network service to some extent. When constructing an emulation system for space network, these characteristics must be considered and incorporated into the design to best replicate the space network environment.

Existing studies have led to the design and implementation of several mature and stable network emulation systems, including NS3, OMNeT++[3], STK[4], and EmuStack[5]. While these tools provide valuable insights into space network behavior, they have notable limitations:

• Limited real-time protocol testing: Many tools focus on theoretical simulations, which limits their ability to validate real-world protocol implementations.

• Inefficiency in handling dynamic topologies: The frequent changes in space network topologies, such as those seen in low Earth orbit (LEO), are not well supported by traditional simulation platforms.

• High computational overhead: Some platforms require significant computational resources, making them less scalable for large-scale emulations.

• Dependence on kernel-based network stacks: These systems often rely on kernel-level networking, leading to inefficiencies due to context-switching and limited real-time performance.

1.2 User-Space Network Stack

The network interface subsystem, as the most complex module in the Linux operating system kernel, has undergone decades of development and evolution, achieving a high level of reliability and stability. However, while the kernel network stack is widely used, it has also faced criticism for its high debugging and development costs, as well as its relatively low packet forwarding speeds[6]. To improve the performance and scalability of the network stack, developers have been looking for ways to abandon the kernel network stack solution and migrate the entire functionality of the network stack to user space. With the continuous development and iteration of high-performance network I/O technologies such as Data Plane Development Kit (DPDK) and Netmap, the user-space network stack can bypass the operating system kernel, thereby directly delivering the received packets from the network interface card to the user space. This avoids the significant overhead caused by frequent context switching, memory copying, and other factors, thus improving the performance of the network stack[7]. Moreover, for network development personnel, a network stack located in user space is more straightforward to debug and maintain, which is beneficial for the development of space network technologies that require extensive validation work. Therefore, the kernel network stack is not well-suited for real-world space network environments.

Building upon existing user-space network stacks (e. g., mTCP[8], IX[9], and Arrakis[10]), this paper introduces a non-open-source, high-performance commercial solution specifically designed for next-generation space network routing technologies. Unlike other user-space network stacks, Nos not only offers exceptional data processing efficiency but also demonstrates excellent topological adaptability. Furthermore, it can be integrated with Docker container technology to operate in lightweight virtual environments. Designing and implementing an emulation system based on Nos allows for more effective debugging and development, thereby providing enhanced space network routing services.

This paper proposes an emulation system based on the user-space network stack Nos. The system overcomes most of the limitations by providing high-performance data processing, better topology adaptability, and scalability in lightweight virtual environments. This approach offers a more efficient platform for validating space network protocols.

2 Design of Space Network Emulation System

2.1 Design of General Emulation System

2.1.1 Node Emulation Solution

As a virtual system, the space network emulation system is built on the virtualization and reallocation of emulation server hardware resources. These resources are then abstracted into independent emulation units. Among these components, the

emulation node serves as the core element of the scenario. In emulation experiments, Docker container technology is commonly used to abstract hardware resources and manage the emulation nodes in a unified manner.

Docker is an open-source application container engine that provides a unified runtime environment for applications. It packages applications and their runtime environments into lightweight, portable container images, which can be deployed on any Linux machine. Meanwhile, Docker containers share the host system's operating system and hardware resources, managed by the Docker engine. This allows for fast startup and execution speeds, as well as high hardware resource utilization, making Docker container technology ideal for the unified orchestration of emulation nodes. It offers potent portability, quick startup, and high resource utilization[11].

The underlying principle of Docker networking is Linux "namespaces", a core mechanism enabling container networking. Namespaces can isolate various resources of a container, such as process IDs (PIDs), filesystem mount points, hostnames, and other system resources. The network namespace, in particular, logically provides independent network functionalities for different containers, including network devices, routing tables, Address Resolution Protocol (ARP) tables, iptables, firewalls, and sockets. Additionally, virtual devices such as veth, a virtual Ethernet device pair, can be used to interconnect containers. Emulation nodes can support different network protocols by deploying and running the corresponding network applications in Docker containers.

2.1.2 Link Emulation Solution

Connection between emulation containers is established through Linux's veth and Open vSwitch (OVS). Specifically, a veth network interface is created between the container and the OVS bridge, with OVS managing the link connectivity between nodes.

The emulation system provides an interface to control the link status. Users can upload a configuration file that stores the link connectivity information, and the main control program will import the relevant data into the MySQL database. Once the emulation experiment starts, the main control program continuously polls the database and, at time points where link events such as link up or down occur, calls the OVS processing function. It adds or deletes the corresponding flow entries in the bridge to represent the occurrence of the link event.

At the start of the emulation experiment, custom network applications run in the containers, while a set of threads are submitted by the main control service. When link characteristics such as delay, packet loss rate, and bandwidth change, these threads read the corresponding link configurations from the database and forward them to the network application in the container. The application then configures the appropriate traffic control (TC) queuing discipline for the container's veth interface to represent the occurrence of this particular link event. Thus, in the emulation experiment, dynamic topology and link characteristics control are abstracted as adding or deleting specific network flow entries in the OVS bridge and configuring TC queuing discipline in the container's virtual network interfaces.

The network applications running in the container can either be custom network programs that perform specific network configuration functions or open-source network programs. For example, after configuring the network topology in the main control program, a Quagga process can be run in the container to calculate the routing rules for the emulation scenario dynamically.

2.1.3 Emulation Architecture Design

The emulation system architecture, as shown in Fig. 1, is designed and implemented. The system can be abstracted from three dimensions: service call, emulation logic, and emulation scenarios.

Service call refers to how developers call the functions of the emulation system. At the engineering implementation level, the emulation system is built as a Maven project integrated with Spring Boot. The frontend page provides a corresponding web graphical user interface (GUI), allowing developers to invoke the system's backend through the relevant interfaces. The frontend program is deployed on an Nginx server, and its GUI provides rich functional interfaces. It also visually displays the topological relationships of the emulation scenarios, supporting complex scenarios consisting of ground stations, LEO satellites, deep space satellites, and lunar exploration probes. The backend server (Center Server) of the system performs operations such as scenario construction, link configuration, and service processing according to specific web requests. The data interaction between the frontend and backend is typically achieved through HTTP requests and responses. The frontend sends requests using JavaScript, and the backend receives and processes these requests and returns JSON data to the frontend. The backend's request processing often involves significant database access, as the database stores all experiment-related information, including experiment status, node configurations, and link details. The database and backend program are deployed on the same server, enabling local and high-speed database access operations. The backend main control program uniformly orchestrates the container nodes and builds a star-shaped topology with an OVS bridge at the center, as defined in the "Emulation Logic" module. As a virtual switch supporting the OpenFlow protocol and flow entry distribution, OVS provides support for dynamic topology control in the emulation system.

From a general perspective, the service call module serves as the interface through which the emulation system directly interacts with the user. User actions are transmitted via frontend requests to the backend, where they undergo a series of processing steps and database interactions. This process ulti-

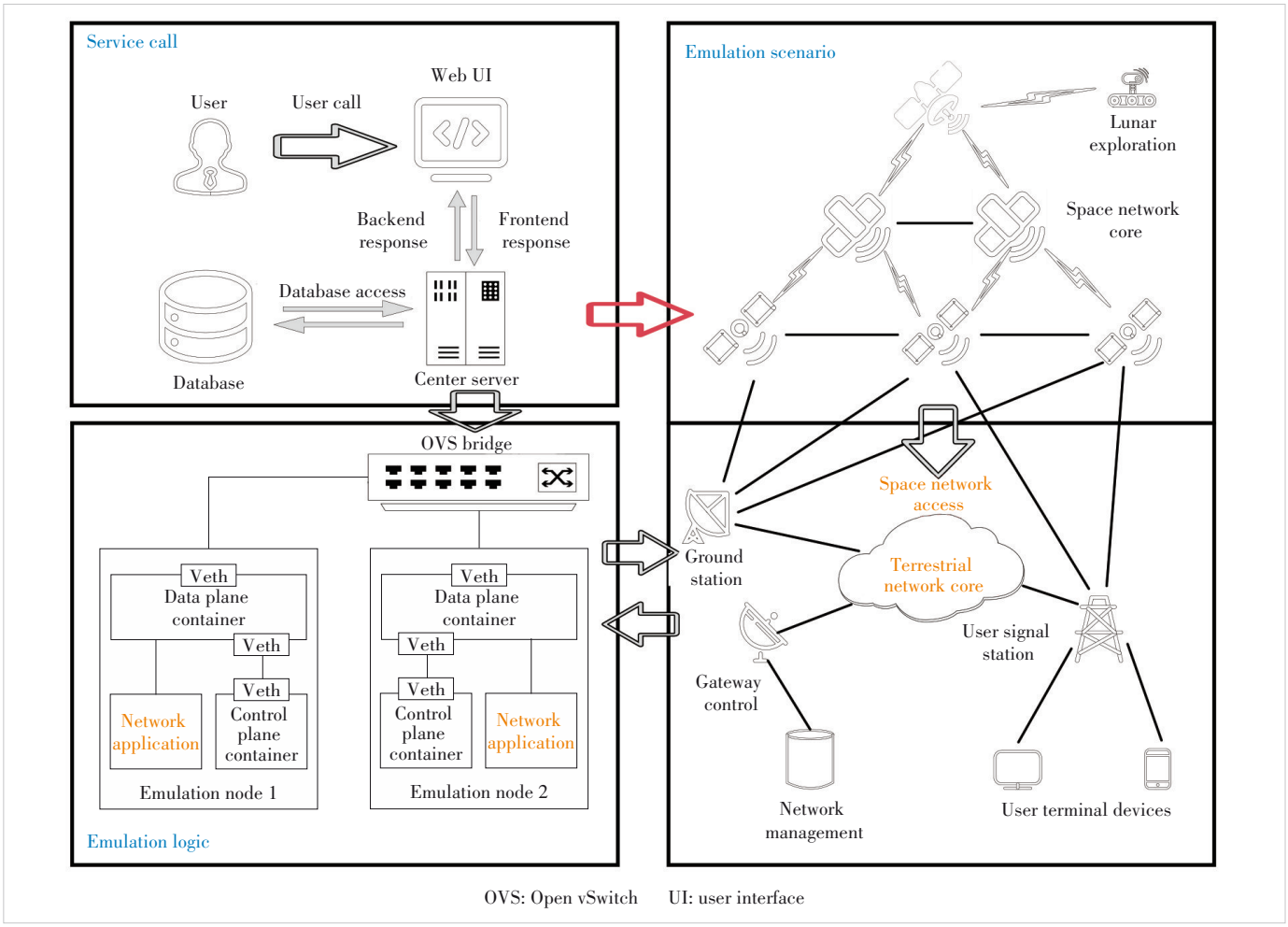

Figure 1. Emulation system architecture

mately constructs the container network as depicted in the Emulation Logic module. The elements in this container network are directly mapped to the corresponding elements in the Emulation Scenario. The Emulation Logic and Emulation Scenario represent two topological frameworks for the emulation experiment: the former reflects the actual network configuration, while the latter serves as an abstract model of the former. These three core modules effectively demonstrate the structure of a general emulation system.

In designing the general network emulation system, it is crucial to consider the platform that best supports the performance and scalability requirements of space network emulation. The system performance is influenced by multiple factors, including network topology dynamics, packet processing efficiency, resource allocation, and system scalability. These factors collectively determine the overall effectiveness of the emulation.

The system is deployed on a general-purpose x86, 64-bit server and utilizes a combination of Nos and Docker containerization to achieve high performance and flexibility. Nos enables efficient packet processing and supports dynamic topology adaptation, while Docker containers provide a lightweight, scalable environment for running emulation nodes.

The use of Docker as the platform ensures efficient resource utilization, minimizing computational overhead and allowing for the emulation of large-scale satellite constellations with high fidelity. This choice of platform addresses the limitations of traditional kernel-based approaches, such as high computational costs and reduced scalability, making it an ideal solution to emulating space networks in a real-time, dynamic environment.

2.2 Integration of Nos

The space network emulation platform described above is designed to integrate Nos. In this design, two Docker containers run in a single emulation node, as shown in Fig. 2. The network control plane functions are consolidated in the routing processor (RP) container, which is responsible for processing routing packets and dynamically calculating routing rules based on the real-time network topology. The network data plane functions are consolidated in the line processor (LP) container, which performs high-performance forwarding based on the routing information table of Nos. The two containers are connected through a veth pair and communicate with each

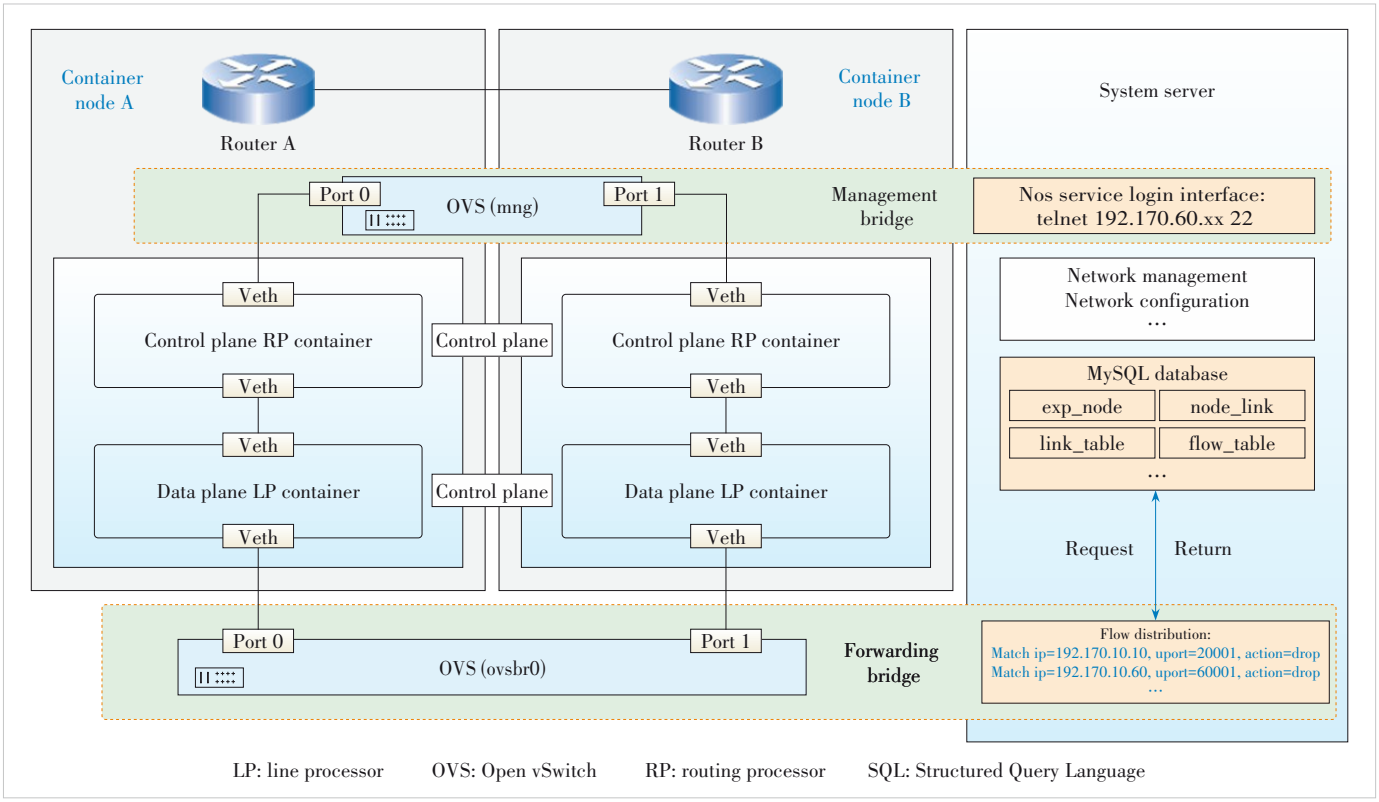

Figure 2. Emulation system architecture with integrated Nos

other directly, collectively forming an emulation node.

Each emulation node's LP container is connected to the OVS bridge "ovsbr0" via a southbound veth interface, with all emulation traffic being exchanged through the ovsbr0 bridge. The RP container of the emulation node is connected to the OVS bridge "mng" via a northbound veth interface. The mng bridge, as a management bridge, ensures communication between the main control server and the emulation node. Developers can log into the RP container's reserved port 22 via this management bridge and access the user management interface of the network stack.

2.3 Soft Forwarding Interface Configuration and Link Mapping

Unlike terrestrial networks, the space network often experiences link interruptions and handovers. For example, in a polar orbit constellation scenario, when a satellite enters the polar region, the link between satellites of adjacent orbits within the same latitude range will be temporarily interrupted and resume once the satellite exits the polar region[12]. Additionally, the satellite connected to a given ground station will change over time. In such high dynamic topologies, a unified emulation strategy is adopted. That is, all possible link resources are reserved during the scenario construction. When a link temporarily fails, the corresponding flow entries are added to the ovsbr0 bridge, matching all packets from the two end nodes of the link and discarding them, thus emulating link up/down and handover events.

However, the apparent disadvantage of this emulation strategy is that reserving resources for all possible links in advance can result in substantial waste, especially in scenarios where link handovers occur frequently, as shown in Fig. 3.

A ground station may only be connected to several satellites at any given time, while the links with all the other potential satellites are temporarily interrupted. These interrupted links,

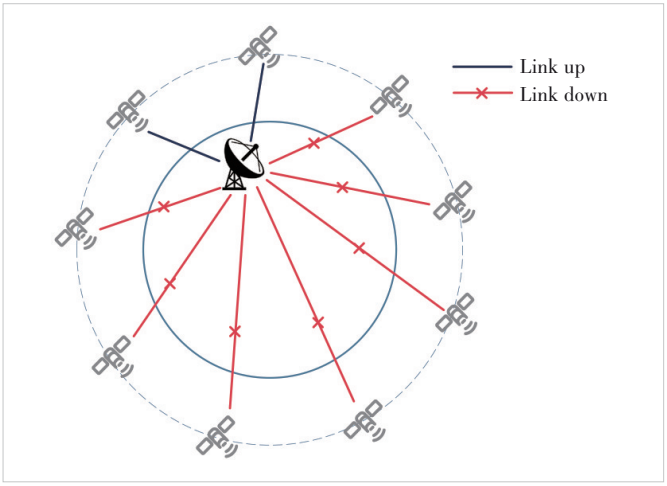

Figure 3. Link handovers occur frequently

however, could take significant system resources. In large-scale constellation scenarios, such scale of resource waste is unacceptable. Nos uses a virtual network interface called "fei" for software forwarding. This interface is implemented in software within the network stack and does not incur additional system resource overhead. All packets forwarded through the fei interface are first handed to the southbound veth interface of the LP container and then forwarded by the ovsbr0 bridge.

The LP container has only one southbound veth interface, and all emulation nodes are connected to the OVS bridge through a single veth interface. All traffic from the emulation node is transmitted through this interface. As shown in Fig. 4, in any given emulation node, the fei interface in the forwarding plane LP container is a virtual interface created in software, existing within the user-space network stack. An IP address needs to be assigned to it for end-to-end forwarding in the emulation experiment. The IP address configured on the veth interface connecting all LP containers to OVS is specified within a particular subnet (such as the subnet 192.170.10.0/24 in Fig. 4). That is, all LP container veth interfaces are in the same subnet.

To ensure that all packets passing through the veth interface are correctly matched with the software forwarding fei interface, a User Datagram Protocol (UDP) port number (uport) is introduced, and a mapping relationship from "veth IP + uport" to "fei IP" is established. Within any given emulation node, the fei IP address maps to the veth IP + uport of the LP container. For all neighboring nodes of a particular node, the link endpoints' fei IP can be mapped as a four-tuple: "IP local, uport local, IP remote, uport remote".

Before the experiment starts, the link mapping relationships between any node and its neighbors are saved in the network stack's startup configuration file "soft_forward.xml". Upon starting, the network stack reads this configuration file to establish local link mappings with all neighbors. On the emulation layer, any packet is forwarded through the fei interface of the LP container after the network stack finishes encapsulating it. However, at the implementation level, when the fei interface receives a packet, it cannot forward it directly. Instead, it must first use the local link mapping information and encapsulate an additional layer, combining the local veth IP address and local UDP port with the corresponding remote veth IP and remote UDP port. The packet is then handed to the southbound veth interface of the LP container and forwarded by the OVS bridge (Fig. 5). When an emulation node receives a packet, the same process occurs: the outer IP and UDP port numbers are decapsulated first, and then the packet is passed to the fei interface for processing.

In the emulation architecture mentioned above, the emulation of link characteristics also requires a corresponding design. First, for the OVS bridge ovsbr0, which is responsible for forwarding all traffic generated by the emulation nodes, flow entries can be added in it to match specific packets and take corresponding actions. For example, when emulating a node failure, a flow entry can be added to match the source or destination IP address of the node's southbound veth interface and drop the packet. This effectively emulates the temporary isolation of that node in the emulation scenario. Simply deleting

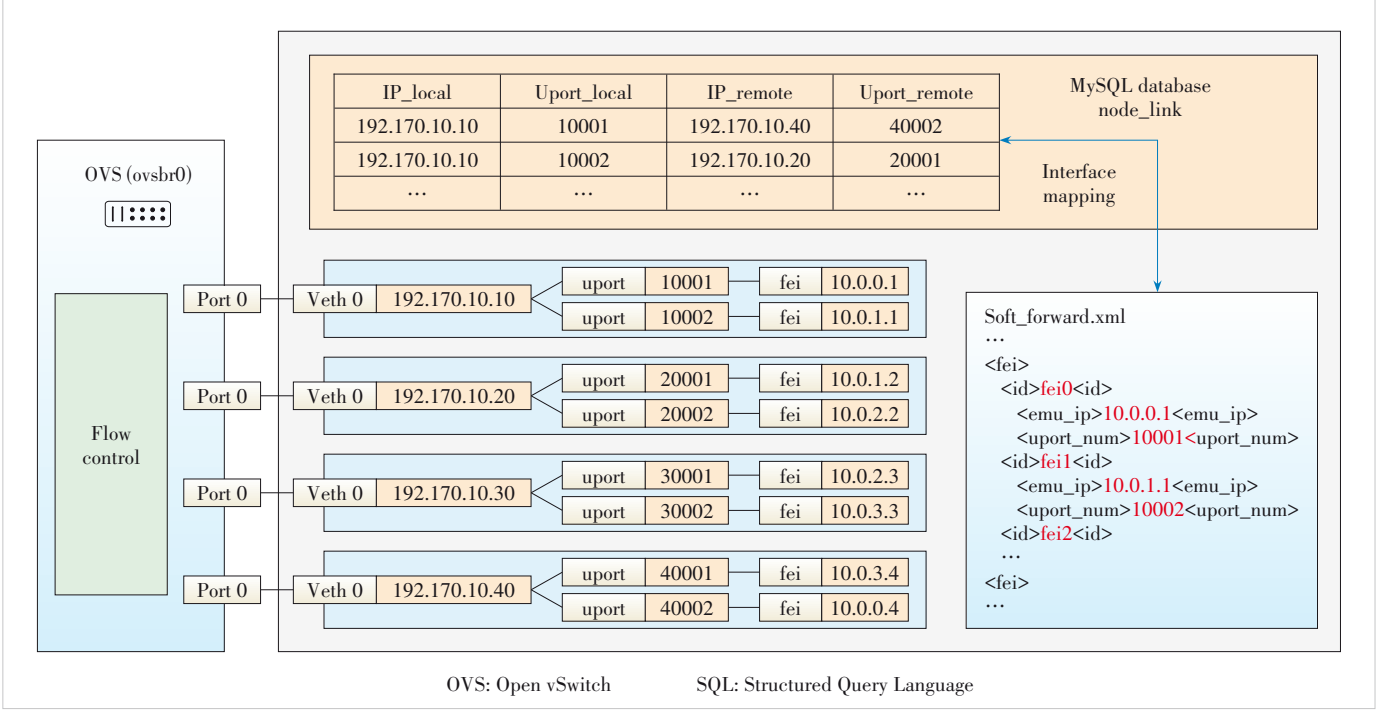

Figure 4. Virtual fei interface configuration for soft forward and its link-mapping rules

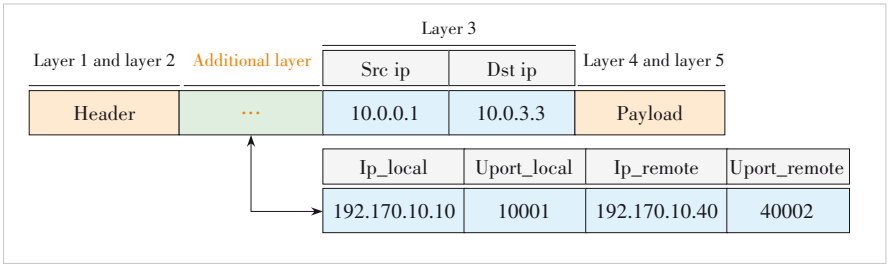

Figure 5. Additional packet encapsulation

the flow entry will suffice to restore the node's state. Similarly, when emulating the failure of a link, a flow entry can be added to match the source IP + UDP port number or the destination IP + UDP port number, and take the "drop" action.

Secondly, link characteristics such as delay and packet loss rate can be emulated by constructing a TC queue discipline tree (Fig. 6) on the southbound veth interface of the LP container. This will enable traffic flowing through the interface to be split. Packets enter the filter from the root queue, and the filter will match the destination IP address and UDP port number of the packets, directing them into different leaf classes[13]. By configuring the appropriate queue settings under the leaf classes, these link characteristics can be emulated.

3 Low Earth Orbit Constellation Emulation

A small LEO constellation scenario, as shown in Fig. 7, is constructed in the emulation system. The scenario consists of two polar satellite orbital planes, each with four satellites, along with two ground station terminals. All ten emulation nodes are created through the frontend GUI interface, and all link configurations are imported.

The satellite motion model used in this experiment is based on real-world orbital dynamics, with satellite positions and movements derived from real-world data exported via Satellite Toolkit (STK). The orbital parameters, such as satellite speed, orbital inclination, and orbital altitude, are extracted from STK's high-fidelity models, ensuring accurate representation of the satellite's behavior in LEO over time. These orbital parameters directly affect link availability and inter-satellite communication.

The link quality is computed based on various factors, including propagation delay, signal strength, and bit error rate. These factors are influenced by the relative distance between satellites, atmospheric conditions, and the satellite's position. The link quality model reflects the real-time variations caused by satellite motion, orbital perturbations, and environmental factors, ensuring that the emulation results accurately represent the dynamic nature of space networks.

After the emulation experiment starts, the RP container within Nos reads the routing protocol configuration file and calculates the routing relationships for the nodes. After a certain period, the routing converges, and all nodes obtain routing entries for all subnets in the emulation scenario.

The threads submitted by the emulation system access the link up/down information in real time and synchronize the control of the emulated links. For example, when a satellite enters the polar region, communication between adjacent-orbital sat-

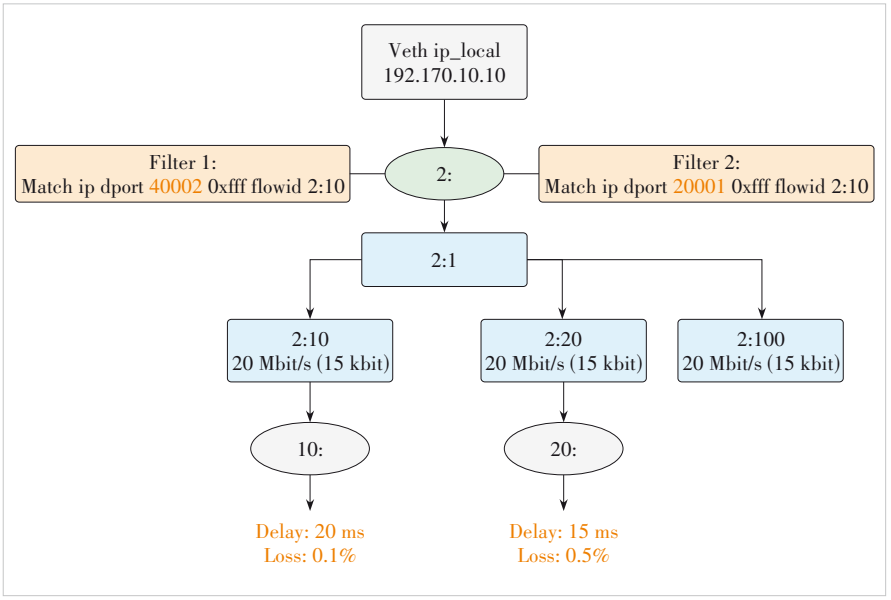

Figure 6. Traffic control (TC) queuing discipline tree

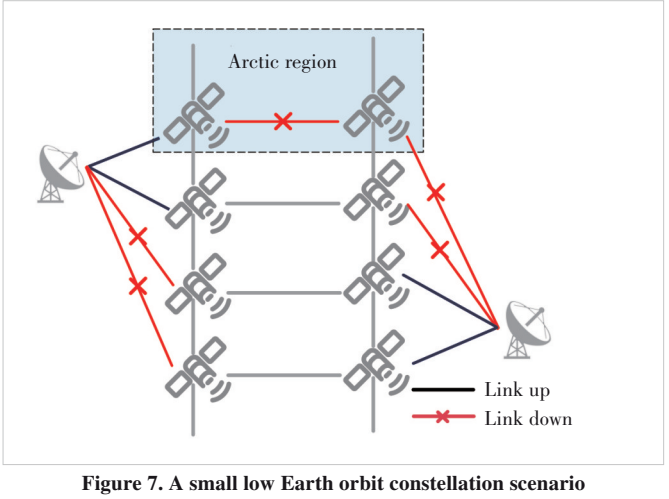

Figure 7. A small low Earth orbit constellation scenario

ellites in the same latitude zone will be temporarily interrupted until the satellite exits this region. When the control plane of Nos detects such network topology changes, it recalculates and updates the routing. The TC thread accesses the database to obtain real-time inter-satellite distances. Using these measurements, it calculates the inter-satellite propagation delay for the current time slice with a fixed duration and subsequently updates the TC queue discipline tree to propagate the delay information.

Fig. 8 shows the changes in delay and packet loss rates between two adjacent-orbital satellites in the same latitude zone. The delay exhibits a certain periodicity over time. When the two satellites move from high-latitude regions to low-latitude regions, the inter-satellite delay gradually increases; when moving from low-latitude regions to high-latitude regions, the inter-satellite delay gradually decreases. When the satellite's latitude becomes too high and it enters the polar region, the inter-satellite link is disconnected. In this case, communication between the two satellites must rely on inter-satellite links with satellites in their respective lower-latitude orbits, resulting in significantly higher delays.

The delay and packet loss rate variations between the two ground station terminals are shown in Fig. 9. At the same time, throughput and bandwidth utilization tests were conducted on a ground station terminal, and the results are shown in Fig. 10. The end-to-end delay remains generally stable, with minor fluctuations caused by satellite movement. Due to the impact of bottleneck links in the satellite network, the throughput of the ground station ranges approximately from 450 kbit/s to 700 kbit/s, with bandwidth utilization reaching over 75%. However, when a link is interrupted or involves a satellite-ground link switch, there is a certain waiting time for the routing information in Nos to converge again. During this time, the two terminals are temporarily unable to communicate.

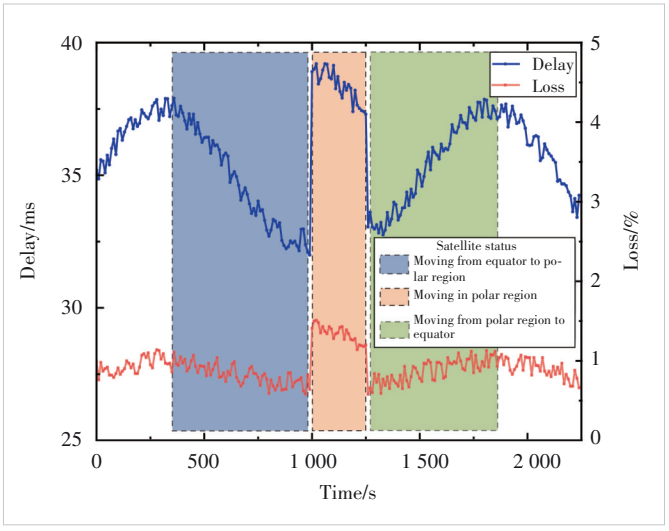

Figure 8. Delay and packet loss between two adjacent-orbital satellites in the same latitude region

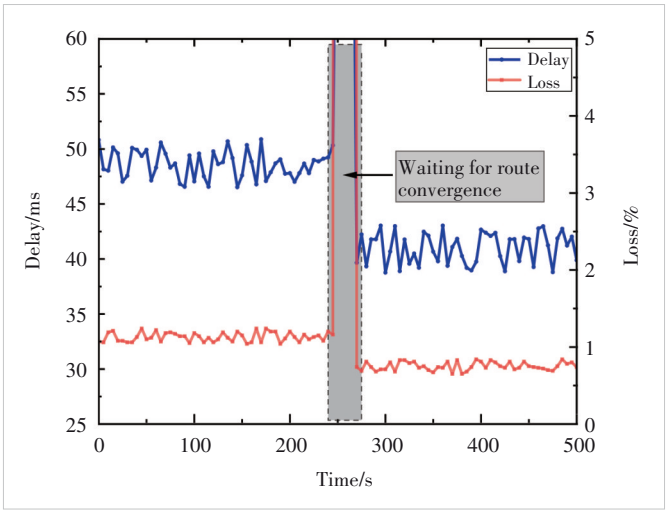

Figure 9. Delay and packet loss between two ground station terminals

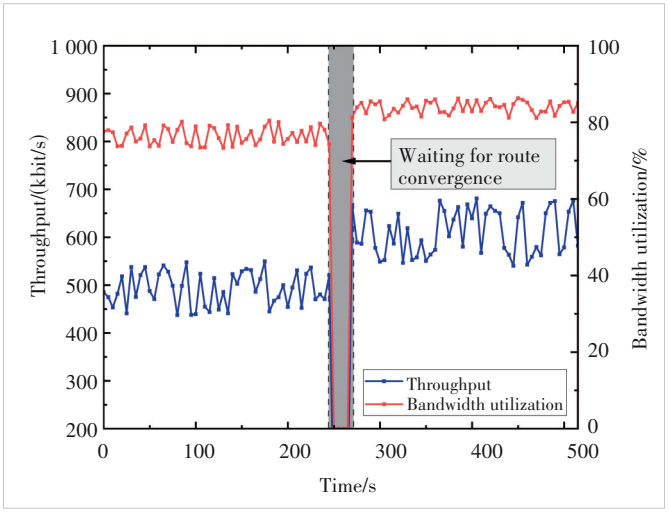

Figure 10. Throughput and bandwidth utilization of one ground station terminal

4 Conclusions

The construction of a space network emulation system is more complex than that of a ground network. We propose a space network emulation system based on Nos, a high-performance user-space network stack, in this paper. This emulation system facilitates the development and debugging of protocol systems and network functions. The separation of control and forwarding in the Nos architecture improves the overall stability of the emulation system. By constructing an LEO satellite constellation scenario, the routing and forwarding functions of Nos are validated, and the dynamic topology and time-varying link characteristics of the satellite network are realistically and reliably emulated. Nos has a rich set of functionalities. Therefore, this emulation system provides a reliable means for applying many network concepts and technologies to space communication.

There are still some areas in the space network emulation

that need to be fully considered. For example, inter-satellite or satellite-ground link delays are determined not only by distance, but also by many other factors such as atmospheric cloud cover. Moreover, the protocol model provided by Nos is primarily designed for the terrestrial network, and when emulating deep-space communication scenarios, protocols like Delay-Tolerant Network (DTN) are not supported. Future iterations and optimizations of the emulation platform should focus on enhancing system realism, stability, and network functionality completeness.

References

[1] ZHOU L W. Research on simulation and evaluation platform of large-scale satellite network based on container technology [D]. Xi'an: Xidian University, 2022. DOI: 10.27389/d.cnki.gxadu.2022.000914
[2] LI H W, WU Q, XU K, et al. Progress and tendency of space and earth integrated network [J]. Science & technology review, 2016, 34(14): 95 – 106. DOI: 10.3981/j.issn.1000-7857.2016.14.011
[3] VARGA A, HORNIG R. An overview of the OMNeT++ simulation environment [C]//Proc. 1st International Conference on Simulation Tools and Techniques for Communications, Networks and Systems & Workshops. ICST, 2008: 1 – 10
[4] COOK P, SCAVONE G. The synthesis ToolKit (STK) [EB/OL]. [2024-09-30]. http://hdl.handle.net/2027/spo.bbp2372.1999.366
[5] LI H F, ZHOU H C, ZHANG H K, et al. EmuStack: an openstack-based DTN network emulation platform [C]//Proc. International Conference on Networking and Network Applications (NaNA). IEEE, 2016: 387 – 392. DOI: 10.1109/NaNA.2016.24
[6] MARINOS I, WATSON R N M, HANDLEY M. Network stack specialization for performance [J]. ACM SIGCOMM computer communication review, 2015, 44(4): 175 – 186. DOI: 10.1145/2740070.2626311
[7] RIZZO L. Revisiting network I/O APIs: the netmap framework [J]. Communications of the ACM, 2012, 55(3): 45 – 51. DOI: 10.1145/2093548.2093565
[8] JEONG E Y, WOO S, JAMSHED M, et al. MTCP: a highly scalable user-level TCP stack for multicore systems [C]//11th USENIX Symposium on Networked Systems Design and Implementation. USENIX, 2014: 489 – 502
[9] BELAY A, PREKAS G, KLIMOVIC A, et al. IX: a protected dataplane operating system for high throughput and low latency [C]//11th USENIX Symposium on Networked Systems Design and Implementation. USENIX, 2014: 49 – 65
[10] PETER S, LI J, ZHANG I, et al. Arrakis: the operating system is the control plane [J]. ACM transactions on computer systems (TOCS), 2016, 33 (4): 1 – 30. DOI: 10.1145/2812806
[11] POTDAR A M, NARAYAN D G, KENGOND S, et al. Performance evaluation of docker container and virtual machine [J]. Procedia computer science, 2020, 171: 1419 – 1428. DOI: 10.1016/j.procs.2020.04.152
[12] FOSSA C E, RAINES R A, GUNSCH G H, et al. An overview of the IRIDIUM (R) low Earth orbit (LEO) satellite system [C]//Proc. IEEE 1998 National Aerospace and Electronics Conference. IEEE, 1998: 152 – 159. DOI: 10.1109/NAECON.1998.710110
[13] ALMESBERGER W. Linux network traffic control—implementation overview [EB/OL]. (1999-4-23) [2024-09-30]. https://www.almesberger.net/cv/papers/tcio8.pdf

Biographies

LEI Jianzhe is a student at the School of Electronic Science and Engineering, Nanjing University, China. His research focuses on space network emulation and network forwarding technologies.

ZHAO Kanglian (zhaokanglian@nju.edu.cn) received his PhD degree from Nanjing University, China. He is currently working at Nanjing University as a professor and doctoral supervisor. His main research interests include space intelligent information networks and 6G integrated terrestrial and space networks.

HOU Dongxu received his PhD degree from the School of Electronic Science and Engineering, Nanjing University, China in 2022. He is working at ZTE Corporation. His research interests include satellite network routing technologies and bearer networks.

ZHOU Fenlin is a Chief Engineer for Future Network Research at ZTE Corporation. His research directions include computing networks, deterministic networks, intelligent computing networks, non-terrestrial networks, and future network architectures.

A Machine Learning-Based Channel Data Enhancement Platform for Digital Twin Channels

AI Bo[1], ZHANG Yuxin[1], YANG Mi[1], HE Ruisi[1], GUO Rongge[2]

(1. School of Electronic and Information Engineering, Beijing Jiaotong University, Beijing 100044, China;
2. School of Traffic and Transportation, Beijing Jiaotong University, Beijing 100044, China)

DOI: 10.12142/ZTECOM.202502004

https://kns.cnki.net/kcms/detail/34.1294.TN.20250523.1012.002.html, published online May 23, 2025

Manuscript received: 2025-03-17

Abstract: Reliable channel data helps characterize the limitations and performance boundaries of communication technologies accurately. However, channel measurement is highly costly and time-consuming, and taking actual measurement as the only channel data source may reduce efficiency because of the constraints of high testing difficulty and limited data volume. Although existing standard channel models can generate channel data, their authenticity and diversity cannot be guaranteed. To address this, we use deep learning methods to learn the attributes of limited measured data and propose a generative model based on generative adversarial networks to rapidly synthesize data. A software simulation platform is also established to verify that the proposed model can generate data that are statistically similar to the measured data while maintaining necessary randomness. The proposed algorithm and platform can be applied to channel data enhancement and serve channel modeling and algorithm evaluation applications with urgent needs for data.

Keywords: channel measurement; channel modeling; deep learning; data enhancement

Citation (Format 1): AI B, ZHANG Y X, YANG M, et al. A machine learning-based channel data enhancement platform for digital twin channels [J]. ZTE Communications, 2025, 23(2): 20 - 30. DOI: 10.12142/ZTECOM.202502004

Citation (Format 2): B. Ai, Y. X. Zhang, M. Yang, et al., "A machine learning-based channel data enhancement platform for digital twin channels," *ZTE Communications*, vol. 23, no. 2, pp. 20 - 30, Jun. 2025. doi: 10.12142/ZTECOM.202502004.

1 Introduction

In recent years, the 6G wireless communication technology has attracted widespread attention, and many institutes have officially started the 6G research[1]. With the expansion of 6G to full-scenario, multi-frequency, and wide-coverage applications, the demands for 6G mobile communications are becoming more diversified and complicated. As a signal transmission medium, wireless channels are an indispensable part of communication links, and their characteristics determine the upper limit of communication system performance. A channel model is a mathematical description of the key channel characteristics, so channel modeling is a basis for the design, simulation, and planning of wireless communication systems.

The goal of channel research is to provide a model that can generate channel parameters according to the input parameter set. This model can be a mathematical model based on statistical fitting, such as the common empirical statistical model[2] and the geometric stochastic model[3]. For example, Ref. [4] conducted statistical modeling of features such as arrival time and power of multipath components, ensuring they conform to specific distributions. Ref. [5] introduced a geometric multiple-input multiple-output (MIMO) channel model for millimeter-wave (mmWave) mobile-to-mobile (M2M) applications, using a few clusters placed on two rings centered on the transmitter and receiver. In addition, the deterministic model based on numerical analysis and simulation is another channel modeling idea[6]. For example, the classic Longly-Rice model[7] uses a two-ray interference approach from geometric optics to predict radio wave propagation characteristics within the line-of-sight region. Ref. [8] investigated the channel characteristics of massive MIMO systems in the 26 GHz mmWave band for indoor scenarios using ray-tracing (RT). The simulation results are consistent with the measured results. With the

This work was supported by the National Key R&D Program of China under Grant No. 2023YFB2904802 , National Natural Science Foundation of China under Grant Nos. 62301022, 62221001, 62431003, and 62101507, Young Elite Scientists Sponsorship Program by CAST under Grant No. 2022QNRC001, and Program for Science & Technology R&D Plan Joint Fund of Henan Province under Grant No. 225200810112.

The corresponding author is YANG Mi.

expansion and application of artificial intelligence (AI) methods such as deep learning, researchers have proposed some AI-based channel models that use neural networks instead of traditional mathematical formulas and numerical simulations to generate channel parameters. Typical examples are found in Refs. [9 – 11]. Specifically, Ref. [9] used the convolutional autoencoder to extract 3D-building information to assist path loss prediction in street canyon scenarios. Ref. [10] employed convolutional neural networks to predict channel path loss using receiver-centric satellite maps as environmental features. Ref. [11] used a multilayer perceptron and long short-term memory (LSTM) to estimate real-time channel attenuation at Q-band. For a further overview of the existing classical modeling methods, please refer to Refs. [12 – 14].

No matter what the specific modeling method is, a consensus is that the channel model is essentially a mapping relationship. Although the model input attributes can be heterogeneous data such as scene category labels, antenna heights, three-dimensional models, and satellite images, the mapping relationship is generally between the environment and the corresponding channel parameters. The question worth considering here is whether these channel models, which we can collectively call environment-driven models, are the only solutions to channel research, in other words, whether these models can solve all the demands for channel data at present. For most application requirements, such as network deployment and coverage prediction, it is meaningful to input the necessary environmental characteristics to get the channel parameters of the corresponding input scene. However, it should not be forgotten that channel data are not only applied to environment-related applications. In other words, the existence of environment input should not be a prerequisite for generating channel data. For example, after obtaining some measured channel data through expensive and time-consuming actual measurement, researchers want to get more data under the same conditions conveniently. Another similar situation is that an algorithm needs to use a lot of real channel data to evaluate its performance, but the existing data are insufficient. The above two hypothetical situations are real cases in research and engineering practice. At the moment, the classic environment-driven model cannot meet all the requirements. Faced with these situations, researchers may need a so-called data-driven channel model, which can learn the characteristics of a small number of existing data and output a large number of similar data. Alternatively, it can be interpreted as a digital twin model, which constructs a virtual copy of the real physical channel, and this "copy" has the same statistical characteristics as the original data. In a word, this data-based modeling process, which does not depend on environmental input, can be called Channel Data Enhancement. It has significant practical value in some application scenarios.

At present, there have been several studies on data-driven channel models. As the groundbreaking work, Ref. [15] introduced the use of generative adversarial networks (GAN) to address autonomous channel modeling. Building on this, the GAN model was utilized to learn the distribution of additive white Gaussian noise channels. Ref. [16] developed a link-level MIMO channel generation method named ChannelGAN to support deep learning-based channel state information (CSI) feedback research. For different scenarios, Ref. [17] proposed a GAN-based channel data augmentation algorithm for communication systems in industrial Internet of Things (IIoT) scenarios to address the issue of insufficient data. Ref. [18] performed the GAN model to generate channel responses to address the issue of inadequate channel estimation performance in high-speed train scenarios. However, despite these efforts, some shortcomings still exist. Most studies rely on idealized simulated channel data, whereas measured data can more accurately capture various interference factors presented in real-world environments. Developing channel models based on measurement can enhance their credibility. Additionally, whether the channel characteristics described by these models are consistent with real data has not yet been comprehensively validated. Therefore, this paper proposes a channel data enhancement platform, the core capability of which is to quickly generate a large number of simulation data with similar characteristics based on a small number of data. Specifically, the platform consists of three subsystems: the channel measurement subsystem, which is used to collect the measured data and construct the basic data set; the data enhancement algorithm, which provides a model that can learn the characteristics of the data set and output the simulation data; the application software, which integrates the algorithm and necessary control functions to provide a convenient interface for users.

The rest of this paper is organized as follows. Section 2 describes the proposed channel data enhancement platform design and architecture. Section 3 is about the subsystems related to channel measurement and the data set in the platform. Following that, we explain the proposed data enhancement algorithm in Section 4. The algorithm verification and application software are described in Section 5. Finally, Section 6 concludes the paper.

2 Platform Design and Architecture

In this paper, a channel data enhancement platform is implemented, which can complete channel measurement in a high dynamic scene and then use the proposed algorithm to learn and measure channel characteristics, greatly expanding the number of channel data. The overall design and architecture of the proposed platform are shown in Fig. 1.

The platform is divided into three subsystems:

1) Channel measurement subsystem

Based on the software-defined radio instrument, this subsystem realizes broadband channel sounding. The subsystem can be applied to dynamic scenarios covering the sub-6 GHz frequency band. The measurement subsystem contains a sepa-

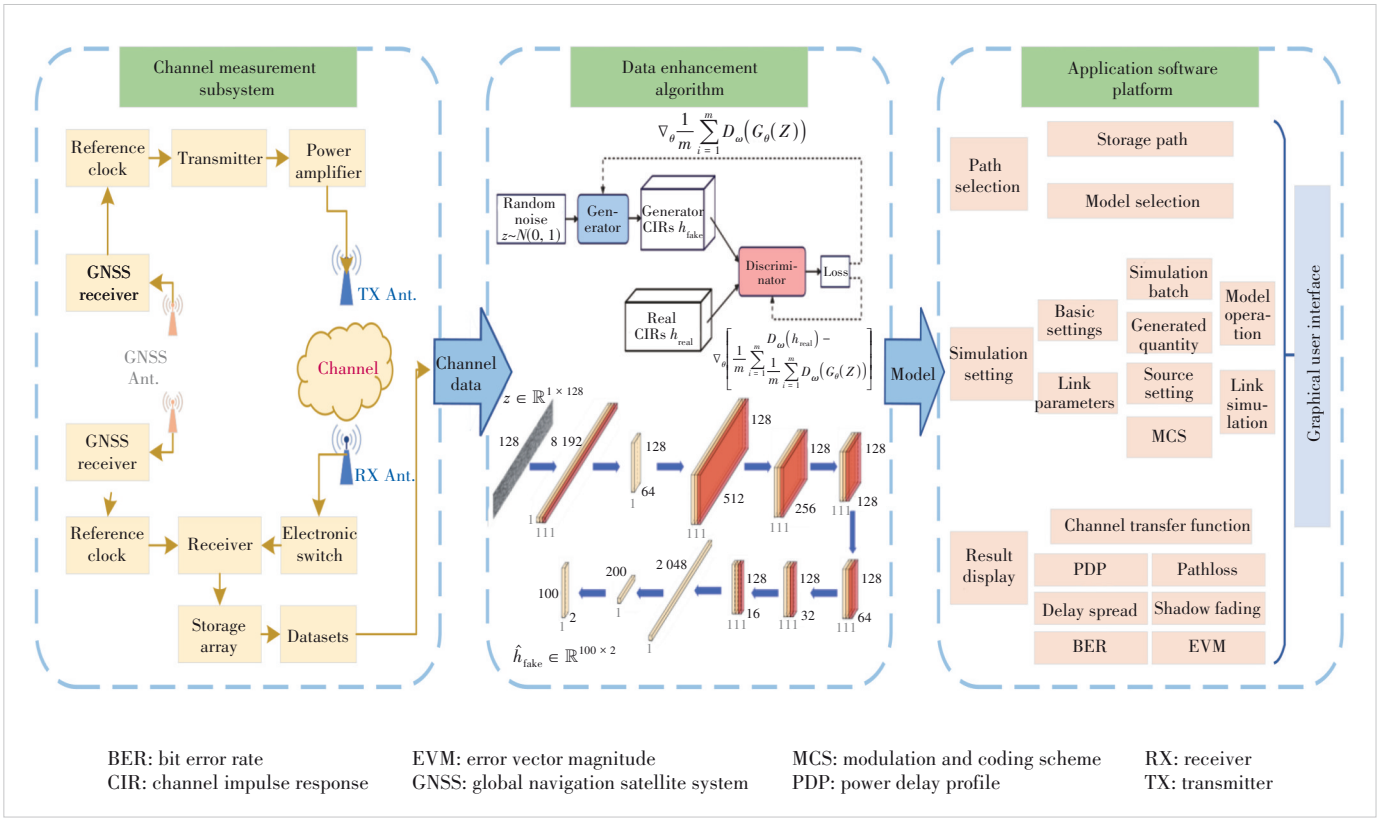

BER: bit error rate
CIR: channel impulse response
EVM: error vector magnitude
GNSS: global navigation satellite system
MCS: modulation and coding scheme
PDP: power delay profile
RX: receiver
TX: transmitter

Figure 1. Proposed channel data enhancement platform architecture

rate transmitter and a receiver, which can process and display the collected signals in real time. In the dynamic scene, the back-to-back calibration can eliminate the influence of system response errors of cables and transceivers.

Due to the diversity of measurement scenarios, the core functional indicators of the measurement subsystem need to be defined by software. This can be scalable enough to meet the needs of different measurement environments. Specifically, the subsystem transmitter needs to complete baseband signal generation, power amplification, signal processing, and visual display. The receiver needs to complete signal reception, baseband signal processing, channel coefficient extraction, channel parameter analysis, visual display, and others. The overall structural design is complex and needs to be adapted to the cooperation on different hardware devices. Therefore, the software and hardware design and development of the measurement subsystem is one of the main difficulties in the whole platform implementation process. The measurement system program is flexible and can be migrated to different SDR hardware. The hardware configuration can be flexibly combined according to the requirements of the actual environment.

2) Data enhancement algorithm

The data enhancement algorithm needs to use the measured channel impulse response (CIR) obtained by the measurement subsystem. Then, the channel simulator based on GAN is trained to learn the intrinsic characteristics of measured data. The proposed method reduces the complexity of channel simulation and can quickly generate channel data by using the trained model. In addition, the accuracy of generated channel data is verified by channel high-order statistical characteristics, such as power delay profile, shadow fading, and delay spread.

The key point of subsystem algorithm design is to learn the characteristics of measured data. However, with the increase of measurement bandwidth, the time delay resolution of data becomes higher. In addition, CIRs are composed of multiple ray clusters, which contain a lot of noise signals. Therefore, the prime difficulty in data preprocessing is to denoise and reduce the dimension of the CIR matrix while retaining effective information as much as possible. Furthermore, the model network structure includes the number and types of networks, the logical relationship between networks, and others. These architectures directly affect the complexity and, more importantly, the accuracy. In addition, the appropriate training algorithm should be carefully selected for the specific network structure. Architecture and training are the key control factors of model performance.

3) Application software

After verifying the channel simulation ability of the model through experiments, the focus shifts to building a convenient software platform. This paper designs an easy-to-operate simulation application program based on MATLAB, which can complete the functions of model loading, simulation data gen-

eration, real-time verification, display, and data storage. In addition, a visual interface is designed.

3 Channel Measurement and Datasets

The broadband wireless channel measurement subsystem includes a separate transmitter and a separate receiver. The transmitter consists of a baseband signal source, a local oscillator, an up-converter, a power amplifier, a filter, a signal processing unit, and an antenna. The receiver is composed of a baseband signal source, a local oscillator, a down-converter, a low noise amplifier, an electronic switch, a data storage unit, and an antenna[19]. The transmitter sends a signal at a specific carrier frequency to act as a sounding signal, and the receiver can identify and detect the signal after channel attenuation and distortion.

The channel measurement subsystem uses multi-carrier signals as sounding signals, as shown in Eq. (1).

$$s_k = \sum_{i=0}^{L-1} d_i \exp\left(\frac{j2i\pi k}{L}\right) \quad (0 \leqslant k \leqslant L-1) \tag{1},$$

where L represents the number of subcarriers and d_i represents the symbol of each subcarrier. The out-of-band power is reduced by rectangular window function filtering. At the receiver, the received signal is shown in Eq. (2).

$$Y(f) = X(f)H_{\mathrm{TX}}(f)H(f)H_{\mathrm{RX}}(f) \tag{2},$$

where $X(f)$ and $Y(f)$ represent the transmitted and received signals in the frequency domain respectively. $H(f)$ represents the channel transfer function, and $H_{\mathrm{TX}}(f)$ and $H_{\mathrm{RX}}(f)$ are the transfer functions of equipment and cables at the transmitter and receiver respectively. The transmitter and receiver are directly connected by cables for back-to-back calibration, so the influence of equipment and cables on the measurement results can be eliminated.

The measurement subsystem takes the signal transceiver based on software-defined radio (SDR) as core hardware. The transmitter implements the loading and generation of baseband sounding signals and the up-conversion of the baseband signals through secondary frequency conversion (baseband to intermediate frequency and intermediate frequency to radio frequency). The receiver samples and down-converts the signals captured by the antennas to obtain the baseband signals and stores them in the local disk. This subsystem realizes hardware device driving and signal processing, and finally obtains key channel parameters and displays them visually. The receiver and transmitter of this subsystem use a rubidium atomic clock calibrated by the global navigation satellite system (GNSS) as the reference clock source to ensure the consistency of the 10 MHz reference clock[20]. Main parameters of the subsystem are shown in Table 1, and the equipment is shown in Fig. 2.

Table 1. Parameters of measurement subsystem

Parameter	Value
Carrier frequency	5.9 GHz
Bandwidth	Max to 160 MHz
Transmit power	Max to 55 dBm
Transmit signal type	Multi-carrier signals
Transmit signal samples	1 024
Snapshot interval	6.4 μs

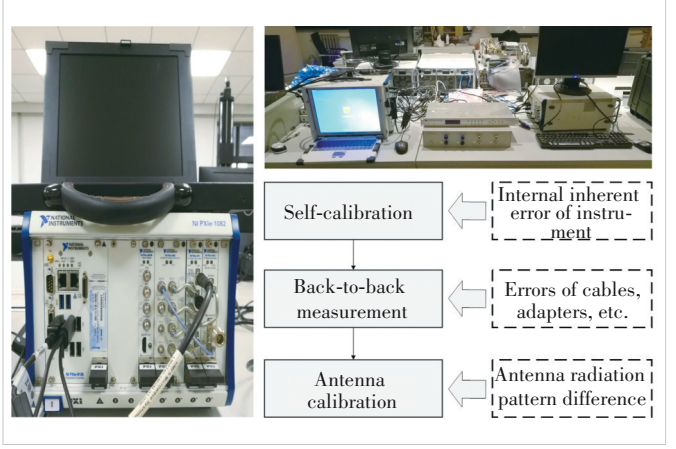

Figure 2. Vector signal transceiver equipment

The software of the channel measurement subsystem is developed based on LabVIEW. LabVIEW is a program development environment developed by National Instruments (NI), which is well compatible with SDR-based signal transceivers used in subsystems and can also easily establish a visual interface. The main purpose of subsystem software is to drive and control the hardware. The software design should be able to call the hardware equipment, configure the measurement parameters such as frequency, bandwidth, clock, and sampling rate of the equipment, and ensure that the received signal data can be stored[21].

The subsystem also provides a visual user interface for testers, as shown in Fig. 3. The interface includes the configuration of various parameters, system running state detection, and error reporting. To observe the channel state in real time during the measurement process, the subsystem also processes some collected data in real time and gets typical channel parameters. In Fig. 3, the receiver interface shows the CIR at the current time. Besides CIR, the current time domain waveform chart and frequency spectrum chart can be displayed in real time.

The original response obtained by the subsystem includes the channel response, the inherent response of the measurement system, and the antenna radiation characteristics. Therefore, system calibration verification is needed to eliminate the errors caused by these factors. As shown in Fig. 2, the calibration verification of the subsystem is divided into three parts:

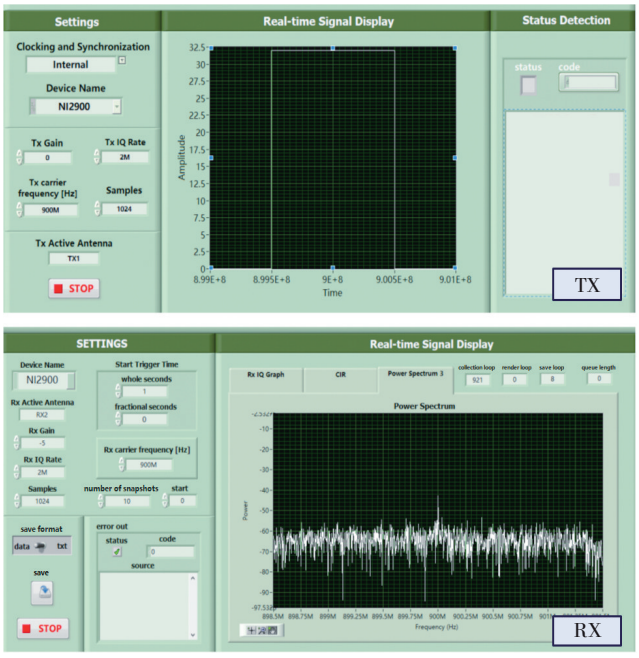

RX: receiver TX: transmitter

Figure 3. Visual interface of channel measurement subsystem

instrument self-calibration, back-to-back measurement calibration, and antenna system calibration.

The purpose of instrument self-calibration is to make the performance and output of the instrument conform to the nominal value. The transmitter used in this paper has a self-calibration function, and subsequent measurements can only be started after the self-calibration has passed before each measurement. Back-to-back measurement can eliminate the errors caused by cables and adapters. The specific method can be summarized as follows. The reference measurement is conducted when the channel response is known by connecting the attenuator directly between the transmitter and the receiver. Thus, the system's inherent response is obtained. During the actual measurement data processing, the collected data are processed using these reference measurement results to eliminate the inherent response of the system and then get the accurate channel response. Antenna calibration refers to the measurement of antenna gain in all propagation directions in an anechoic chamber, which is an important prerequisite to ensure the accuracy of test results. The measurement error from antenna radiation can be eliminated when processing the received data.

The experimental study on channel measurement in this paper was carried out in Beijing, China. During the field measurements, the transmitter and receiver vehicles moved in the same direction and kept an interval of 20 – 40 m. During the measurement period, the maximum vehicle speed was no more than 70 km/h, and the system acquired 16-channel snapshots per second. To reduce the influence of random backscatters, measurement routes were restricted to empty road sections. Both the transmitting and receiving antennas were installed on the roof, and the antenna heights were about 1.8 m. The total number of measured channel snapshots was about 7 000 groups.

4 Proposed Data Enhancement Algorithm

4.1 GAN-Based Algorithm

GAN is a kind of deep generation model, which can implicitly learn the probability distribution of input images to generate identically distributed images. Initially developed for image generation, GAN is not a simple method for copying or imitating reality, nor does it merely blend or average multiple real samples. Instead, it uses two game-theoretic neural networks, namely the generator (G-network) and the discriminator (D-network), to learn intrinsic statistical patterns of real data, without direct objective functions.

G-network is used to learn the distribution of real data to generate identically distributed data, and D-network judges the probability whether its input data comes from reality or generation. Through training, the purpose of the generator is to gradually generate realistic data to deceive the discriminator. Discriminators want to always be able to distinguish between real and generated data. Therefore, the essence of GAN is to make the generator learn the approximate value of real data distribution through antagonistic learning.

GAN usually has some problems in training, such as mode collapse, unstable optimization, gradient disappearance, and non-convergence. To avoid the above problems, this paper uses Wasserstein GAN with gradient penalty (WGAN-GP) as the network framework, which is an improved version of GAN. Wasserstein distance, also known as the Earth-Mover (EM) distance, is used to evaluate the similarity between two distributions, which can provide a relatively stable gradient relative to Jensen-Shannon (JS) divergence. GP can avoid the problem of gradient disappearance caused by large model weights. Therefore, WGAN-GP is more stable and converges faster in training and can significantly improve the training speed and address the slow convergence issue in original WGAN.

4.2 Algorithm-Based Model Design

4.2.1 Generator Design

Fig. 4 illustrates the network architecture and detailed parameters of the generator in this algorithm. The model takes noise vector as input and generates CIR through the generator that uses one-dimensional convolution to extract features. The convolution layer can create a convolution kernel, and the input of this layer is rolled up in a single space (or time) dimension to produce the output. The convolution kernel size in the generator is set to 3. Subsequently, the batch normalization layer is added behind each convolution layer, which acceler-

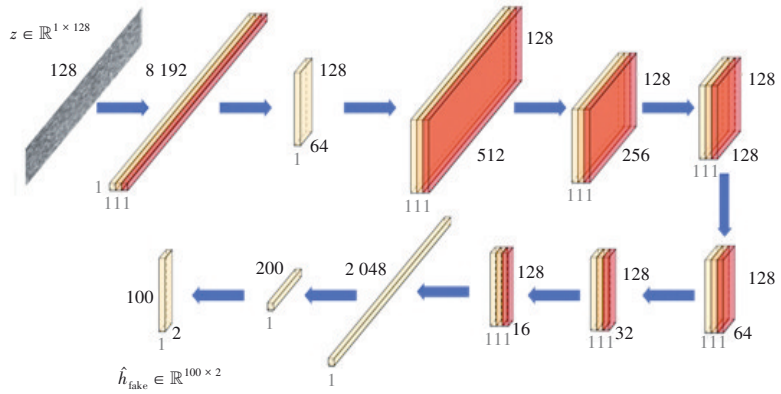

Layer Type	Output Shape
Input layer	(128, 1)
Dense & batche normalization & LeakyReLU	(8 192, 1)
Reshape	(128, 64)
Conv ID & batche normalization & LeakyReLU	(128, 512)
Conv ID & batche normalization & LeakyReLU	(128, 256)
Conv ID & batche normalization & LeakyReLU	(128,128)
Conv ID & batche normalization & LeakyReLU	(128, 64)
Conv ID & batche normalization & LeakyReLU	(128, 32)
Conv ID & batche normalization & LeakyReLU	(128, 16)
Flatten	(2 048, 1)
Dense	(200, 1)
Reshape	(100, 2)

LeakyReLU: Leaky Rectified Linear Unit

Figure 4. Generator network design and detailed parameters

ates the convergence speed of model training. It also makes the model training process more stable to avoid gradient explosion or gradient disappearance. In addition, this paper chooses Leaky Rectified Linear Unit (LeakyReLU) as the activation function to alleviate the problem of gradient disappearance. The expression of LeakyReLU is shown in Eq. (3).

$$\text{LeakyReLU}(x) = \begin{cases} x, & x \geqslant 0 \\ \alpha \cdot x, & \text{otherwise} \end{cases} \tag{3},$$

where x is the input of LeakyReLU. When $x < 0$, LeakyReLU gives x a slope α. Parameter α is an adjustable superparameter, and the value set in this paper is 0.2. Because Tanh can limit the output to $[-1, 1]$, the generated CIR better matches with the real CIR amplitude. Therefore, Tanh is selected as the activation function after the last convolution layer, and its expression is shown in Eq. (4).

$$\text{Tanh}(x) = \frac{e^{x} - e^{-x}}{e^{x} + e^{-x}} \tag{4},$$

where x is the input of Tanh. When the input noise passes through six convolution layers, it will pass through the Flatten layer, and the result will be mapped into a separable space in combination with the fully connected layer. The fully connected layer maps the learned features to the sample label space. Since the generator finally outputs the CIR, it is necessary to reshape the samples passing through the fully connected layer.

4.2.2 Discriminator Design

Fig. 5 shows the network architecture and detailed configuration of the discriminator. The input of the discriminator is the CIR sample generated by the generator or the real CIR sample. The input channel samples are first zero-padded to facilitate the subsequent convolution process. Similar to the generator, the discriminator mainly uses one-dimensional convolution and LeakyReLU activation function. The convolution kernel size of the one-dimensional convolution is 5. Finally, it is output through the Flatten and fully connected layers. The output of the discriminator is the probability while the input is a

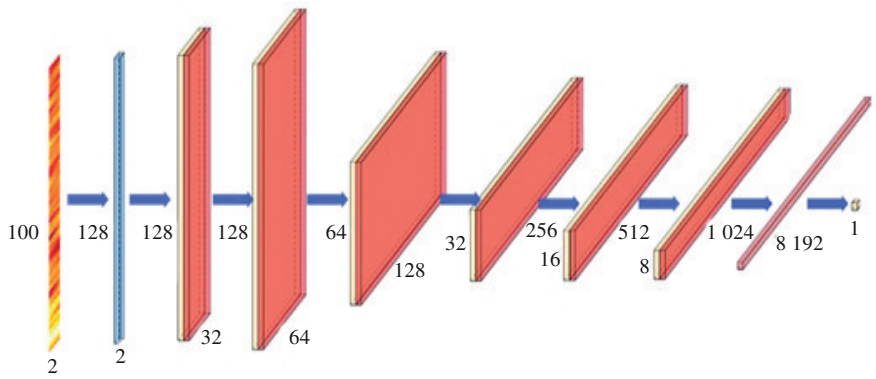

Layer Type	Output Shape
Input layer	(100, 2)
Zero padding ID	(128, 2)
Conv ID & LeakyReLU	(128, 32)
Conv ID & LeakyReLU	(128, 64)
Conv ID & LeakyReLU	(64,128)
Conv ID & LeakyReLU	(32, 256)
Conv ID & LeakyReLU	(16, 512)
Conv ID & LeakyReLU	(8, 1 024)
Flatten	8 192
Dense	1

LeakyReLU: Leaky Rectified Linear Unit

Figure 5. Discriminator network design and detailed parameters

real channel sample or a generated channel sample.

5 Algorithm Verification and Application Software

5.1 Algorithm Verification

Algorithm implementation consists of model design, model training, and CIR sample generation. The training process follows an alternating scheme, where the discriminator is updated multiple times per generator update to ensure stable convergence. The Adam optimization algorithm is employed to update the parameters of the GAN network with a learning rate of 0.000 05. Upon completing 2 500 training epochs, the trained model is saved. Then, in the generation process, the saved model is used to generate CIR by inputting the desired number of CIR samples along with a 128-dimensional random noise vector.

In this section, the similarity between the real and generated channels is demonstrated by comparing the distribution performance of the power delay profile (PDP), path loss, and root mean square (RMS) delay spread between the measurement and generated data. To facilitate accurate evaluation against real channels, this paper generates channel samples equal in number to the real ones.

Figs. 6a and 6b illustrate the channel PDP obtained through actual measurements and GAN generation, respectively. It can be seen that GAN-generated PDP closely matches the measured data in terms of morphology, especially aligning with the peak positions in the delay domain observed in the measurements. Additionally, the generated channels preserve the diversity, randomness, and noise-affected characteristics of real channels, demonstrating high fidelity. Fig. 6c presents a comparison of the averaged PDP. Specifically, when calculating the PDP, the samples are averaged according to the number of samples, as shown in Eq. (5).

$$\mathrm{PDP} = \frac{1}{N}\sum_{N}\left|h(n,\tau)\right|^2 \tag{5},$$

where N is the total number of channel samples, h represents the measured or generated CIR, n is the sample index corresponding to the number of delay points, and τ refers to the delay points.

For the real channel, the average PDP is depicted by the black curve in Fig. 6c. The average PDP of the channels generated by the AI model after 2 500 training iterations is shown by the blue dashed line with square markers. For comparison, channels generated by the model after training for 20 epochs are included, with PDP illustrated by the purple solid line

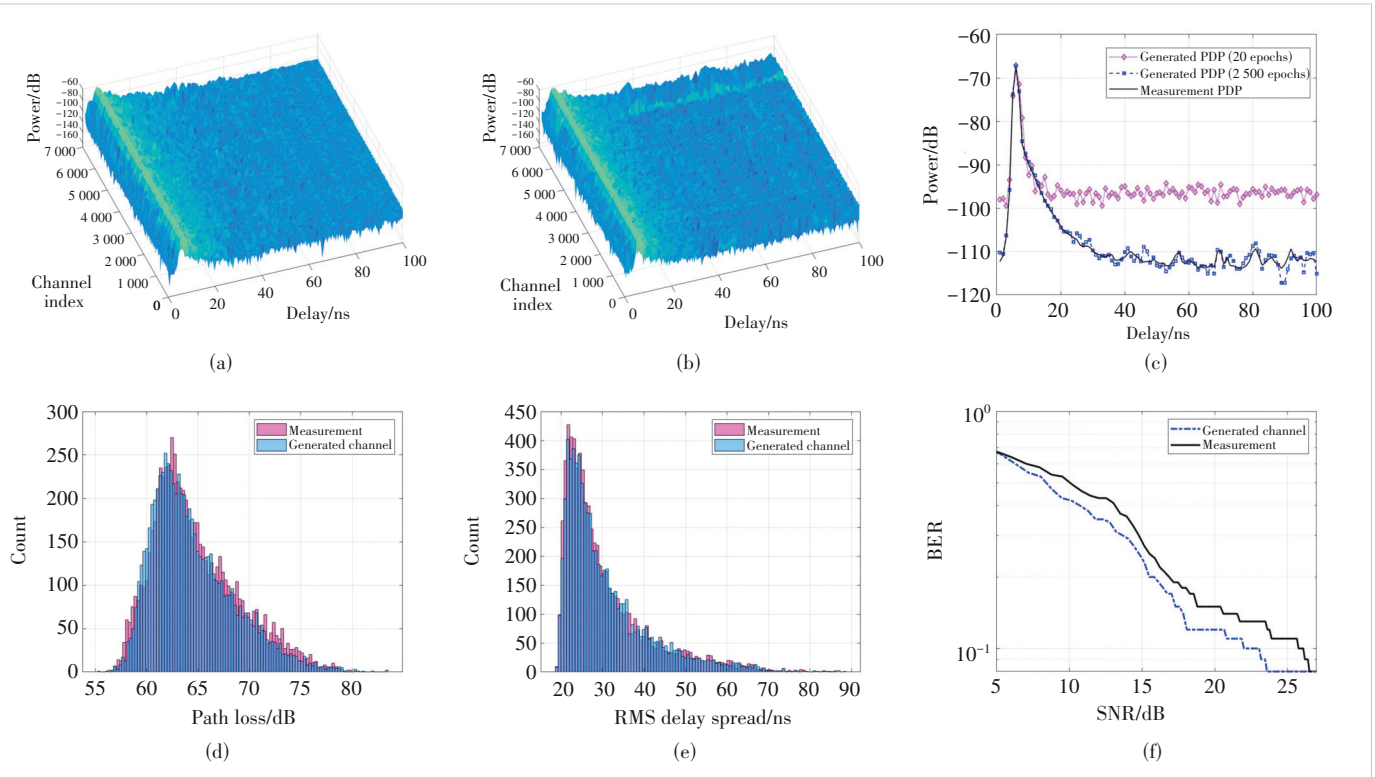

Figure 6. Algorithm verification results: (a) measured PDP; (b) generated PDP; (c) PDP comparison; (d) path loss; (e) RMS delay spread; (f) BER performance

with diamond markers in Fig. 6c. It can be observed that the channel power distribution generated by the model trained for 20 epochs ranges in [−100 dB, −60 dB], whereas the power distribution of both the real channel and the channel generated by the model trained for 2 500 epochs spans from −120 dB to −60 dB. This discrepancy arises from insufficient training, which prevents the model from fully capturing channel characteristics and distribution. As a result, the generated channel data lack multipath details and exhibit higher noise power. Channels generated by a high-performing GAN model closely resemble the real channels, including the transition of the PDP from peak values to a gradual stabilization.

Further validating the distribution of channel parameters is crucial for evaluating model performance. Path loss is used to characterize the power loss that occurs during signal transmission, which is an important parameter for evaluating signal coverage area and quality in wireless communication systems. It can be calculated using PDP, as shown in Eq. (6).

$$\mathrm{PL} = \frac{1}{N_\tau}\left(\sum_{N_\tau}\left|h(n,\tau)\right|^2\right) \tag{6},$$

where N_τ denotes the number of delay points, and h represents the measured or generated channel. Fig. 6d illustrates the path loss distributions for both the measured and generated data. It is evident that the generated data (blue histogram) exhibits a high degree of overlap with the measurement (red histogram) in terms of path loss. Meanwhile the mean path loss values for the measured and generated channels are 64.80 dB and 64.47 dB, further demonstrating the high similarity between the generated and real channels.

RMS delay spread is used to describe the degree of delay dispersion in a channel, which reflects the impact of the delay distribution of each propagation path on the received signal in a multipath propagation environment. RMS delay spread can be calculated as follows:

$$\tau_{\mathrm{RMS}}(n) = \sqrt{\frac{\sum_{\tau_N}\tau(n)^2\mathrm{PDP}(n,\tau)}{\sum_{\tau_N}\mathrm{PDP}(n,\tau)} - \overline{\tau}(n)^2} \tag{7},$$

where τ_N represents the delay component of the N-th channel sample, $\overline{\tau}(n)$ refers to the average delay. $\overline{\tau}(n)$ is calculated as:

$$\overline{\tau}(n) = \frac{\sum_{\tau_N}\tau(n)\mathrm{PDP}(n,\tau)}{\sum_{\tau_N}\mathrm{PDP}(n,\tau)} \tag{8}.$$

Comparing the histograms displaying the RMS delay spread distributions of the measured and GAN-generated channels, Fig. 6e shows that both channels exhibit a high degree of consistency in their distribution shapes and ranges. Additionally, the mean RMS delay spreads for the measured and the generated channels are 30.65 ns and 30.74 ns, further validating the similarity between the two channel distributions. This also confirms the strong performance of the GAN model in capturing the channel delay characteristics.

Furthermore, the generation performance of the standard GAN model is further compared and evaluated. Figs. 7a and 7b present the statistical distributions of path loss and RMS delay spread from the generated channel by the GAN model. By comparing these results with the WGAN-GP performance in Fig. 6, it is evident that WGAN-GP achieves better alignment between the statistical characteristics of the generated channel data and those of the measured channel. Fig. 7c provides a quantitative assessment of the fidelity of the generated channel data using the Frechet Inception Distance (FID) metric. The results indicate that the WGAN-GP model achieves significantly lower FID scores (0.114 3 for path loss and 0.106 for RMS delay spread) compared to the standard GAN model

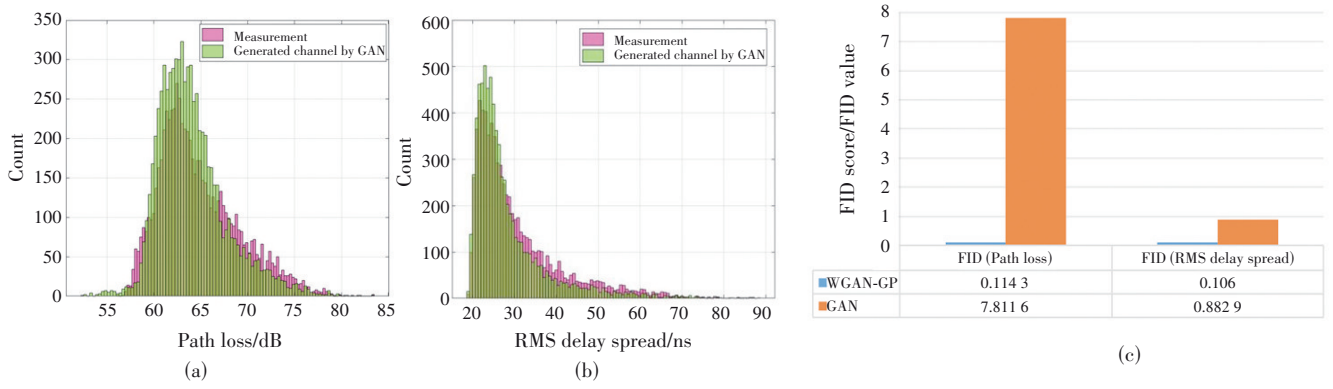

FID: Frechet Inception Distance GAN: generative adversarial network RMS: root mean square WGAN-GP: Wasserstein GAN with gradient penalty

Figure 7. Standard GAN model generation performance: (a) path loss; (b) RMS delay spread; (c) FID comparison

(7.811 6 and 0.882 9, respectively). This demonstrates that WGAN-GP is capable of generating channel data with higher fidelity, ensuring a closer match to the statistical characteristics of measurements.

To validate the effectiveness of GAN-generated channels, a simplified link-level simulation was conducted for evaluation, which employed phase shift keying (PSK) modulation with 100 transmitted bits and a modulation order set to 16. Fig. 6f compares the bit error rate (BER) of the real channel with that of the GAN-generated channel, where the BER curves of the real and GAN-generated channel are highly consistent, exhibiting similar BER trends under different signal-to-noise ratio (SNR) conditions. This high level of similarity indicates that the GAN-generated channel can effectively simulate the real channel in terms of error performance.

5.2 Application Software

The main function of the application software is to generate channels by using the previous algorithm, and the visual interface is shown in Fig. 8. The software can be divided into two sub-functions: one-time channel generation and uninterrupted real-time channel generation. The former can generate a specified number of channel data at one time. In addition, the software can track the duration record generated by the channel. When generating channels in real time, the function of selecting generation batches is added. If the generation batch is selected, the channel can be generated in real time according to the batch size, and the dynamic generation process of the channel and the dynamic distribution of the channel parameters can also be seen on the visualization panel. After the dynamic generation of the channel is completed, the software will detect the end of the generation and turn the indicator light green as a prompt.

Fig. 9 shows the operation flow of the software. First, the path needs to be set, including selecting measurement data and generating models. The path to store the generated channel data should also be configured. Next, the options of link simulation are configured. The modulation mode can be PSK or quadrature amplitude modulation (QAM), and the modulation order can be 4 or 16. In link simulation, we can choose

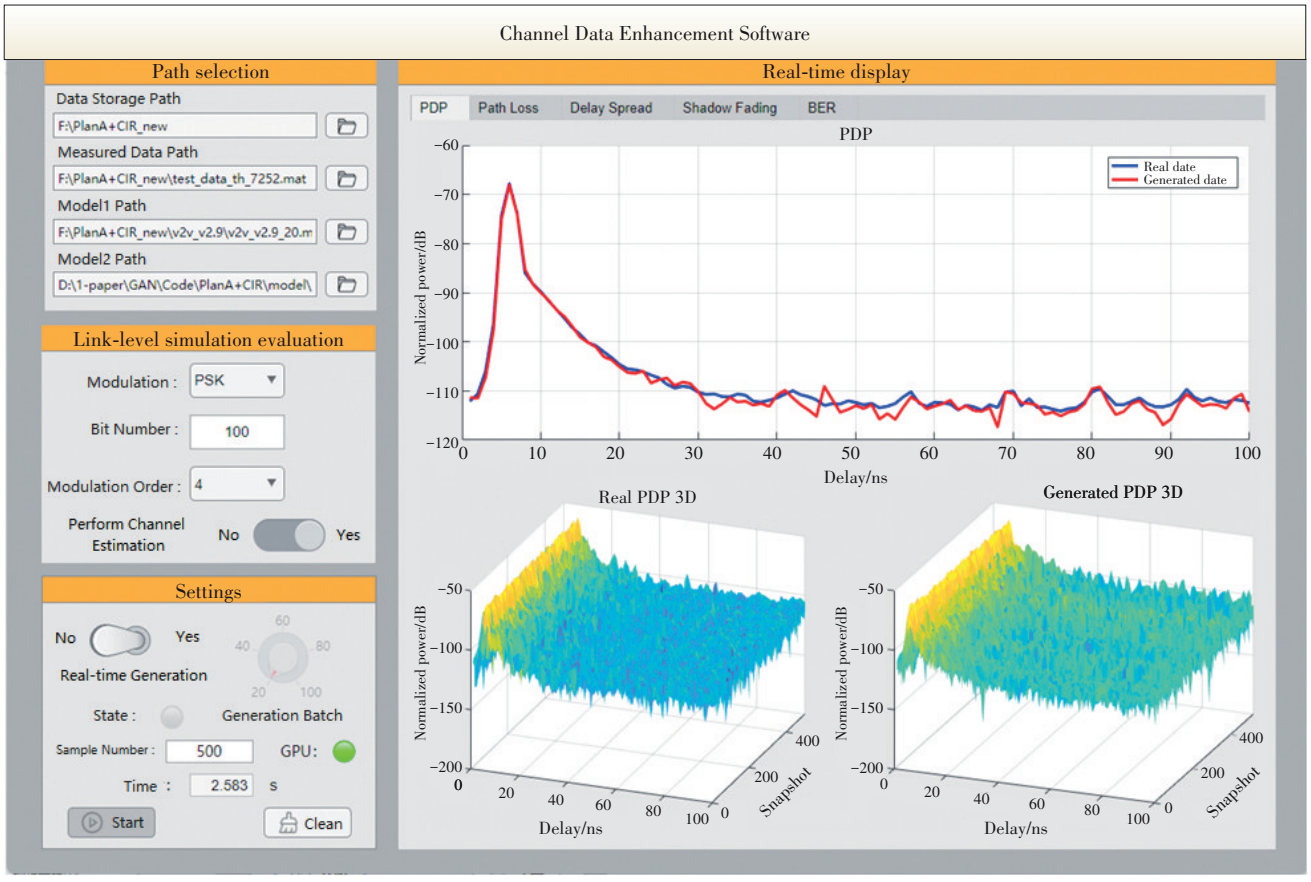

BER: bit error rate PDP: power delay profile

Figure 8. Channel data enhancement application software interface

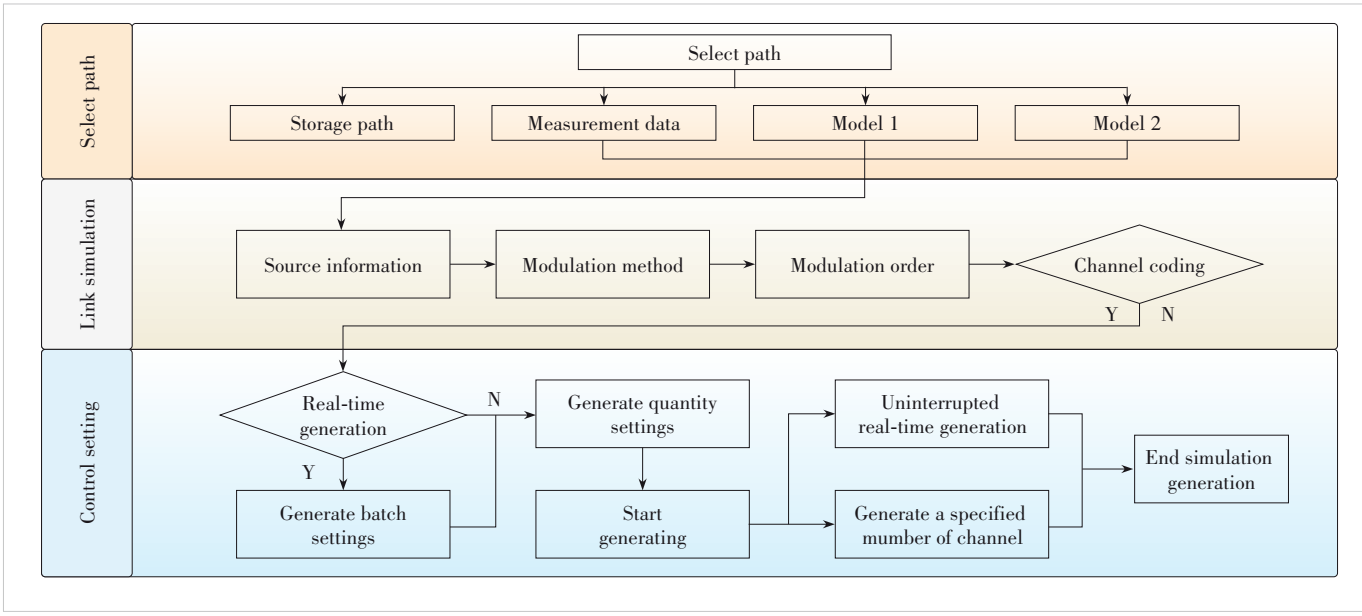

Figure 9. Operation flow chart of channel enhancement software

whether to perform channel estimation or not. Then, we should choose whether to generate channels in real time in the basic settings. If not, the software will generate all the channel data with the set number of channels at one time. If it is real-time generation, we need to further set the generation batch; the software will subsequently generate channel data according to the set generation batch, and the display window will dynamically display the whole channel generation process. Finally, after clicking the Start button, the software will initiate the generation of channel data based on the specified configuration. Clicking the Clear button will then clear the contents of the display window, allowing the settings to be reset for generating channel data under the new configuration.

6 Conclusions

Channel characteristics and models are the basis of communication system design and evaluation. Meanwhile, it has been a consensus that channel data is the support of channel research and modeling. To address the current issue of challenging channel data acquisition, this paper proposes a channel data enhancement platform based on the idea of a digital twin channel. The platform includes three key subsystems: channel measurement, enhancement algorithm, and application software. The measurement subsystem is a broadband dynamic channel measurement system based on the SDR architecture, which can complete channel data acquisition in the sub-6 GHz frequency. The channel enhancement algorithm, the core of the proposed platform, is a neural network based on the GAN architecture. It can learn the intrinsic characteristics of real channel data and quickly generate a large number of highly similar simulation channels. We verify and evaluate the generated channel under the high-order characteristics of power delay profile, path loss, shadow fading, and root mean square delay spread. The results show that the generated channel is similar to the original channel in statistical characteristics and has sufficient randomness. Finally, the platform includes integrated software for engineers and researchers, which can call the above algorithm and generate channel data in real time. The result of this paper is a potential channel modeling and simulation methodology.

References

[1] LU K, HAN B M, ZHOU X S. Smart urban transit systems: from integrated framework to interdisciplinary perspective [J]. Urban rail transit, 2018, 4(2): 49 – 67. DOI: 10.1007/s40864-018-0080-x
[2] HATA M. Empirical formula for propagation loss in land mobile radio services [J]. IEEE transactions on vehicular technology, 1980, 29(3): 317 – 325. DOI: 10.1109/T-VT.1980.23859
[3] ZAJIC A G, STUBER G L, PRATT T G, et al. Wideband MIMO mobile-to-mobile channels: geometry-based statistical modeling with experimental verification [J]. IEEE transactions on vehicular technology, 2009, 58(2): 517 – 534. DOI: 10.1109/TVT.2008.928001
[4] SALEH A A M, VALENZUELA R. A statistical model for indoor multipath propagation [J]. IEEE journal on selected areas in communications, 1987, 5(2): 128 – 137. DOI: 10.1109/JSAC.1987.1146527
[5] HE R S, AI B, STÜBER G L, et al. Geometrical-based modeling for millimeter-wave MIMO mobile-to-mobile channels [J]. IEEE transactions on vehicular technology, 2018, 67(4): 2848 – 2863. DOI: 10.1109/TVT.2017.2774808
[6] PANG L H, ZHANG J, ZHANG Y, et al. Investigation and comparison of 5G channel models: from QuaDRiGa, NYUSIM, and MG5G perspectives [J]. Chinese journal of electronics, 2022, 31(1): 1 – 17. DOI: 10.1049/cje.2021.00.103
[7] WEINER M. Use of the Longley-Rice and Johnson-Gierhart tropospheric radio propagation programs: 0.02 – 20 GHz [J]. IEEE journal on selected

areas in communications, 1986, 4(2): 297 – 307. DOI: 10.1109/JSAC.1986.1146313
[8] AI B, GUAN K, HE R S, et al. On indoor millimeter wave massive MIMO channels: measurement and simulation [J]. IEEE journal on selected areas in communications, 2017, 35(7): 1678 – 1690. DOI: 10.1109/JSAC.2017.2698780
[9] GUPTA A, DU J F, CHIZHIK D, et al. Machine learning-based urban canyon path loss prediction using 28 GHz Manhattan measurements [J]. IEEE transactions on antennas and propagation, 2022, 70(6): 4096 – 4111. DOI: 10.1109/TAP.2022.3152776
[10] THRANE J, ARTUSO M, ZIBAR D, et al. Drive test minimization using deep learning with Bayesian approximation [C]//Proc. IEEE 88th Vehicular Technology Conference (VTC-Fall). IEEE, 2018: 1 – 5. DOI: 10.1109/VTCFall.2018.8690911
[11] BAI L, XU Q, HUANG Z W, et al. An atmospheric data-driven Q-band satellite channel model with feature selection [J]. IEEE transactions on antennas and propagation, 2022, 70(6): 4002 – 4013. DOI: 10.1109/TAP.2021.3137285
[12] YANG M, AI B, HE R S, et al. Dynamic V2V channel measurement and modeling at street intersection scenarios [J]. IEEE transactions on antennas and propagation, 2023, 71(5): 4417 – 4432. DOI: 10.1109/TAP.2023.3249101
[13] HUANG C, HE R S, AI B, et al. Artificial intelligence enabled radio propagation for communications—part II: scenario identification and channel modeling [J]. IEEE transactions on antennas and propagation, 2022, 70(6): 3955 – 3969. DOI: 10.1109/TAP.2022.3149665
[14] WANG C L, AI B, HE R S, et al. Channel path loss prediction using satellite images: a deep learning approach [J]. IEEE transactions on machine learning in communications and networking, 2024, 2: 1357 – 1368
[15] YANG Y, LI Y, ZHANG W X, et al. Generative-adversarial-network-based wireless channel modeling: challenges and opportunities [J]. IEEE communications magazine, 2019, 57(3): 22 – 27. DOI: 10.1109/MCOM.2019.1800635
[16] XIAO H, TIAN W Q, LIU W D, et al. ChannelGAN: deep learning-based channel modeling and generating [J]. IEEE wireless communications letters, 2022, 11(3): 650 – 654. DOI: 10.1109/LWC.2021.3140102
[17] LIANG X, LIU Z Y, CHANG H R, et al. Wireless channel data augmentation for artificial intelligence of things in industrial environment using generative adversarial networks [C]//Proc. IEEE 18th International Conference on Industrial Informatics (INDIN). IEEE, 2020, 1: 502 – 507. DOI: 10.1109/indin45582.2020.9442206
[18] ZHANG D Y, ZHAO J H, YANG L H, et al. Generative adversarial network-based channel estimation in high-speed mobile scenarios [C]// Proc. 13th International Conference on Wireless Communications and Signal Processing (WCSP). IEEE, 2021: 1 – 5. DOI: 10.1109/WCSP52459.2021.9613362
[19] ZHAO H, LYU Q, LIU Y C, et al. Wireless channel measurements and modeling of LTE broadband system for high-speed railway scenarios [J]. Chinese journal of electronics, 2018, 27(5): 1092 – 1097
[20] ZHANG Z Y, HE R S, AI B, et al. A cluster-based statistical channel model for integrated sensing and communication channels [J]. IEEE transactions on wireless communications, 2024, 23(9): 11597 – 11611. DOI: 10.1109/TWC.2024.3383594
[21] YANG M, AI B, HE R S, et al. Measurements and cluster-based modeling of vehicle-to-vehicle channels with large vehicle obstructions [J]. IEEE transactions on wireless communications, 2020, 19(9): 5860 – 5874. DOI: 10.1109/TWC.2020.2997808

Biographies

AI Bo received his MS and PhD degrees from Xidian University, China in 2002 and 2004, respectively. He was an Excellent Postdoctoral Research Fellow with Tsinghua University, China in 2007. He is currently a professor with the State Key Laboratory of Advanced Rail Autonomous Operation and School of Electronic and Information Engineering, Beijing Jiaotong University, China. He has authored or co-authored eight books and published over 300 academic research papers. His five papers have been recognized as ESI highly cited papers. His research interests include channel measurement and channel modeling, and dedicated mobile communications for rail traffic systems.

ZHANG Yuxin received her MS degree in information and communication engineering from Beijing Jiaotong University (BJTU), China in 2024. She is currently pursuing a PhD degree at the School of Electronics and Information Engineering, BJTU. Her current research focuses on artificial intelligence-based wireless channel modeling.

YANG Mi (myang@bjtu.edu.cn) received his MS and PhD degrees from Beijing Jiaotong University, China in 2017 and 2021, respectively. He is currently an associate professor with the State Key Laboratory of Advanced Rail Autonomous Operation and the School of Electronic and Information Engineering, Beijing Jiaotong University. His research interests include wireless channel measurement and modeling.

HE Ruisi received his BE and PhD degrees from Beijing Jiaotong University (BJTU), China in 2009 and 2015, respectively. He is currently a professor with the School of Electronics and Information Engineering, BJTU. He has been a visiting scholar at Georgia Institute of Technology, USA, University of Southern California, USA, and Université Catholique de Louvain (UCLouvain), Belgium. His research interests include wireless propagation channels, 5G, and 6G communications. He has authored/co-authored eight books, five book chapters, more than 200 journal and conference papers, and several patents.

GUO Rongge received her BS degree from Sun Yat-sen University, China in 2014, and MS and PhD degrees from Beijing Jiaotong University, China in 2017 and 2021, respectively. She is currently a lecturer with the School of Traffic and Transportation, Beijing Jiaotong University. Her research interests include public transport, intelligent transport systems (ITS), transport planning, transport management, and traffic control.

6G Digital Twin Enabled Channel Modeling for Beijing Central Business District

LU Mengyuan[1,2], BAI Lu[1,3,4], HAN Zengrui[5], HUANG Ziwei[5], LU Shiliang[1,2], CHENG Xiang[5]

(1. Joint SDU-NTU Centre for Artificial Intelligence Research (C-FAIR), Shandong University, Jinan 250101, China;
2. School of Software, Shandong University, Jinan 250101, China;
3. National Mobile Communications Research Laboratory, Southeast University, Nanjing 214135, China;
4. Shandong Research Institute of Industrial Technology, Jinan 250100, China;
5. School of Electronics, Peking University, Beijing 100871, China)

DOI: 10.12142/ZTECOM.202502005

https://kns.cnki.net/kcms/detail/34.1294.TN.20250521.0912.002.html, published online May 21, 2025

Manuscript received: 2025-01-20

Abstract: A novel digital twin (DT) enabled channel model for 6G vehicular communications in Beijing Central Business District (Beijing CBD) is proposed, which can support the design of intelligent transportation systems (ITSs). A DT space for Beijing CBD is constructed, and two typical transportation periods, i.e., peak and off-peak hours, are considered to characterize the vehicular communication channel better. Based on the constructed DT space, a DT-enabled vehicular communication dataset is developed, including light detection and ranging (LiDAR) point clouds, RGB images, and channel information. With the assistance of LiDAR point clouds and RGB images, the scatterer parameters, including number, distance, angle, power, and velocity, are analyzed under different transportation periods. The channel non-stationarity and consistency are mimicked in the proposed model. The key channel statistical properties are derived and simulated. Compared to ray-tracing (RT) results, the accuracy of the proposed model is verified.

Keywords: DT; channel modeling; 6G vehicular communications; Beijing CBD; DT-enabled vehicular communication dataset

Citation (Format 1): LU M Y, BAI L, HAN Z R, et al. 6G digital twin enabled channel modeling for Beijing central business district [J]. ZTE Communications, 2025, 23(2): 31 - 45. DOI: 10.12142/ZTECOM.202502005
Citation (Format 2): M. Y. Lu, L. Bai, Z. R. Han, et al., "6G digital twin enabled channel modeling for Beijing central business district," *ZTE Communications*, vol. 23, no. 2, pp. 31 - 45, Jun. 2025. doi: 10.12142/ZTECOM.202502005.

1 Introduction

With the development of 6G wireless networks, the demands for high-performance communications are increasing, particularly in densely populated and built-up areas such as central business districts (CBDs). As the core business hub of China's capital, Beijing CBD faces exceptionally high wireless communication demands. The unique architecture and dense traffic flow in this area have a significant impact on wireless channel characteristics. 6G networks are expected to meet these challenges by providing wider coverage, higher data rates, and lower latency. Intelligent transportation systems (ITSs), as a key technology to enhance traffic management and transportation efficiency, promote traffic safety and efficiency through the application of information technology, communication equipment, computing technology, and artificial intelligence (AI). Vehicular communication is an important part of ITS, which significantly improves road safety via real-time communications between vehicles[1]. However, in high-density and high-traffic urban environments like Beijing CBD, vehicular communications are challenged by complex and dynamic wireless channel conditions. Accurate channel modeling is essential to ensure the reliability and efficiency of vehicular communications. Furthermore, traffic density differs significantly between peak and off-peak hours. As a result, more accurate channel models are essentially required to depict the wireless communication environment and to

This work was supported in part by the National Natural Science Foundation of China under Grant Nos. 62371273, 62125101 and 62341101; the Taishan Scholars Program under Grant No. tsqn202312307; the Young Elite Scientists Sponsorship Program by CAST under Grant No. YESS20230372; the Shandong Natural Science Foundation under Grant No. ZR2023YQ058; the New Cornerstone Science Foundation through the Xplorer Prize; the Xiaomi Young Talents Program; the open research fund of National Mobile Communications Research Laboratory, Southeast University under Grant No. 2025D04; the China National Postdoctoral Program for Innovative Talents under Grant No. BX20240007; the China Postdoctoral Science Foundation under Grant No. 2024M760111; the Beijing Natural Science Foundation under Grant No. 4254067.

guide a more precise design of the communication system.

Digital twin (DT) is a digital reconstruction of physical entities and can be utilized as an efficient method to characterize, simulate, and visualize physical entities[2]. DT has advantages in representing physical entities that are difficult to model and replicate. DT enables the creation of a virtual replica of the real-world environment, which allows the dynamics of the channel to be accurately modeled.

Recent studies have integrated DT with wireless communication systems. DT is utilized to construct virtual models that simulate the real world and facilitate data acquisition based on the constructed models. A platform for DT was proposed in Ref. [3], along with a synthetic dataset combining the data obtained through the real world and those obtained through virtual copies. This approach reduces the burden of collecting real-world channel data and significantly decreases the system overhead. DT can also reduce the data acquisition overhead of the communication system and improve the system accuracy. In Ref. [4], the authors introduced a ray-tracing (RT) oriented approach for DT demonstration of radio propagation in multiple frequency bands from microwave to visible light. Furthermore, a super-resolution modeling method was developed by fusing RT and AI algorithms to improve the stability and accuracy of communications. The authors in Ref. [5] utilized site-specific DT models to train deep learning (DL) models. The proposed DT-based method generates site-specific synthetic channel state information (CSI) data through 3D modeling and RT methods, enabling effective training of DL models while reducing the overhead of real-world data collection. To further improve model performance, an online data selection approach is used to refine the DL model training with a small real-world CSI dataset. Since DT can contribute to balancing the overhead and the accuracy of communication systems, it has been widely adopted in various communication scenarios, such as UAV and vehicular communication systems. A framework for DT-based UAV applications was proposed in Ref. [6], where a task manager orchestrated interactions between the DT system and physical UAVs. DT can assist UAVs to achieve more efficient flight paths and reduce energy consumption, which improves the efficiency of UAV communication systems. For vehicular communication systems, a city-model-aware DL algorithm for dynamic channel estimation in urban vehicular environments was proposed in Ref. [7]. The proposed model gained a balance between accuracy and timeliness. In summary, DT effectively reduces the overhead of data acquisition and significantly improves system accuracy by reflecting the dynamic changes of the environment in real time. DTs have been applied to a variety of typical communication scenarios. However, accurate comprehension and modeling of the environment are essential to further enhance system security and reliability.

To accurately depict the communication environment, the channel characteristics between the transmitter (TX) and the receiver (RX) need to be precisely characterized. Therefore, channel modeling is the cornerstone of communication systems, and more accurate channel models are essential to further improve the efficiency of communication systems. Conventional channel modeling approaches, including stochastic and deterministic models, have significantly contributed to wireless communication systems. However, the methods have limitations when applied to complex and dynamic urban environments. For example, stochastic models depend on predefined assumptions, which may not accurately capture variations in specific scenarios[8]. Deterministic models, such as RT methods, provide better accuracy with high computational overhead and the difficulty of real-time adjustment[9].

DT provides a new paradigm for channel modeling as it enables accurate physical-virtual world mapping. By precisely modeling and dynamically updating the virtual environment, DT can capture the changing characteristics in the environment in real time. When integrated with machine learning (ML) algorithms, DT can also extract key characteristics from complex scenarios and realize high-precision modeling of diverse channel characteristics. In Ref. [10], the authors proposed a channel modeling approach based on generative adversarial networks for DT environments, which can generate channel data with a statistical distribution that closely matches the measured channel. A data-driven continuous trajectory modeling method for a user equipment with a DT channel was proposed in Ref. [11]. This method generates channel models whose spatial and temporal characteristics match the real-world wireless channels. Nevertheless, current studies on DT-based channel modeling are still at the preliminary stage, particularly on high-precision modeling in dynamic environments. Most existing DT-based channel models cannot handle high-mobility vehicular communication scenarios. Therefore, there is an urgent need to explore DT-based methods for improving the accuracy of vehicular communication channel modeling.

To fill this gap, we explore the application of DT to channel modeling and select a typical urban communication scenario, i.e., vehicular communications within Beijing CBD. We propose a new method of channel modeling based on DT for complex urban environments. The main contributions and novelties of this paper are summarized as follows.

1) A new reliable DT space for Beijing CBD is constructed, where the physical and electromagnetic spaces are precisely aligned by AirSim and Wireless InSite. It provides a highly accurate virtual environment for channel modeling.

2) A DT-based dataset is constructed for Beijing CBD for the first time, which includes sensory data, i.e., light detection and ranging (LiDAR) point clouds, RGB images, and channel data. The dataset is constructed in complex and dynamic scenarios and comprehensively captures the unique characteristics of vehicular communications in ur-

ban environments.

3) A DT-enabled vehicular communication channel model for Beijing CBD is developed, which models and analyzes the channel characteristics of peak and off-peak hours in Beijing CBD for the first time. Furthermore, the channel parameters, e.g., number, distance, angle, and power of scatterers with different velocities, are developed under different transportation periods.

4) Based on the proposed channel model for Beijing CBD, key channel statistical properties, i.e., time-frequency correlation function (TF-CF) and Doppler power spectral density (DPSD), are derived and simulated. According to the simulation results, the effect of different transportation periods on the channel statistical properties is investigated. Simulation results are consistent with the experimental results based on RT, which verifies the accuracy and practicability of the channel model based on DT.

The remainder of this paper is organized as follows. Section 2 describes the DT space for Beijing CBD. Section 3 proposes a novel DT-enabled vehicular communication channel model for Beijing CBD. Section 4 presents the statistical properties of the vehicular communication channel and compares the simulation results with those based on RT. Finally, Section 5 concludes the paper.

2 DT Space for Beijing CBD

Beijing CBD provides a unique scenario for ITS applications with its high-density buildings, complex transportation networks, and diverse communication requirements. However, conventional channel modeling methods face several challenges in complex urban scenarios, particularly in modeling multipath propagation and dynamic changes. DT technology enables the construction of digital spaces that match the real world to accurately reflect real-time environmental changes. Therefore, a DT space for Beijing CBD is constructed to achieve accurate modeling of the physical environment and dynamic traffic characteristics of the area. This DT space provides a robust platform for channel modeling, which can support the research of high-precision vehicular communication systems.

2.1 Construction of DT Space for Beijing CBD

In Beijing CBD, the diversity of building distribution and types has a significant impact on the signal propagation characteristics. The CBD, as the core business district of the capital, features high building density with numerous high-rise and modern office buildings. The different heights, shapes, layouts, and building materials of these buildings significantly influence wireless signal propagation. As for transportation, the traffic volume in Beijing CBD peaks during rush hours, and vehicle quantity and density directly affect wireless signal transmission.

To construct a DT space that can match the real environment well, we first use Blender, a 3D modeling tool, to establish a scenario identical to Beijing CBD, leveraging satellite maps and 3D models of the buildings. To ensure the accuracy of the constructed scenario, the heights, sizes, and inter-building distances are strictly consistent with the real world. Then we utilize Wireless InSite in Ref. [12] to build the electromagnetic space. The process involves importing the constructed 3D model into Wireless InSite. Then the propagation parameters are set with a frequency of 5.9 GHz, a bandwidth of 20 MHz, and an omnidirectional antenna for transceivers. Parameters related to electromagnetic phenomena, such as reflections and dispersions, are configured in Wireless InSite to simulate channel characteristics in specific frequency bands. Meanwhile, the influence of buildings, vehicles, and other obstacles in radio propagation is ensured to be effectively reflected. Two scenarios are constructed for investigating the effect of peak and off-peak traffic conditions on channel characteristics. The objects in the two scenarios remain identical except for the number of vehicles. Vehicles are 57 during peak hours and 34 during off-peak hours. After establishing the electromagnetic environment model, the model exported from Wireless InSite is imported into the AirSim platform for detailed visualization, which provides a simulation of the visual and dynamic environment similar to Ref. [13]. Each vehicle in AirSim is equipped with sensory devices, i.e., RGB cameras and LiDAR devices. The dynamic vehicular trajectories simulated in AirSim remains identical to those in Wireless InSite. With the precisely aligned scenarios in Wireless InSite and AirSim, the real-world physical environment is accurately replicated in the virtual space. The environment consistency across different platforms is maintained and dynamically updated, facilitating the construction of a highly reproducible DT space.

2.2 Data Collection and Processing in DT Space

Beijing CBD scenarios in Wireless InSite and AirSim are presented in Fig. 1. To construct the DT-based Beijing CBD vehicular communication dataset, a simulation setup in Wireless InSite and AirSim is required. The number of simulation snapshots is set to 300 with a time interval of 0.01 s. The batch generation of the scenarios is set up through MATLAB scripts in Wireless InSite, and the position of the vehicles is simulated through Python scripts set up by frame in AirSim. The vehicular trajectories during off-peak hours are shown in Fig. 2. Sensory data (LiDAR point clouds and RGB images) and communication data are collected. Simultaneously, the moving vehicles establish the Beijing CBD vehicle communication dataset based on DT. The communication links simulated in both transportation periods are identical, as shown in Fig. 2. The constructed dataset consists of 10 800 LiDAR point clouds, 10 800 RGB images, and 9 000 communication link data.

The high mobility of multiple transceivers and scatterers

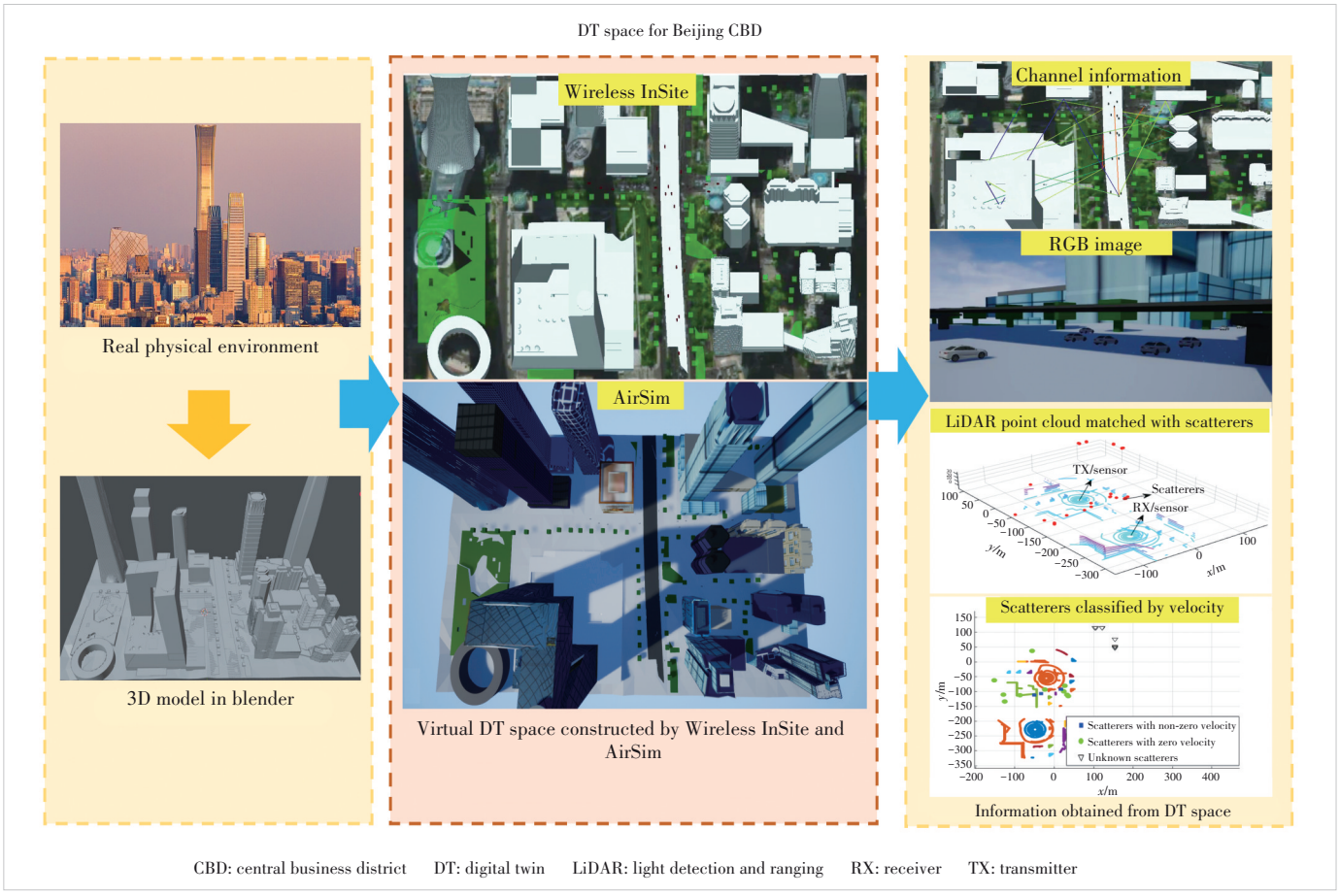

Figure 1. DT space for Beijing CBD vehicular communication scenarios

results in complex characterization. Therefore, the detection of the velocity properties of scatterers is extremely significant. With the support of sensing data (LiDAR point clouds and RGB data), zero velocity scatterers (ZVSes) and non-zero velocity scatterers (NVSes) can be detected and matched to static objects and dynamic vehicles. The LiDAR point clouds, combined with the clustering algorithm and RGB images, can effectively distinguish between the ZVS and those with non-zero velocity. The point cloud data are preprocessed and then clustered using the density-based spatial clustering of applications with noise (DBSCAN) clustering algorithm in Ref. [14], a typical ML algorithm for grouping the point clouds. ZVS sets usually correspond to static objects such as buildings, which remain stable over multiple time frames, while NVS sets correspond to dynamic objects (vehicles), whose positions change over time. The two types of scatterers can be accurately distinguished by matching point cloud clusters in different time frames and combining them with velocity estimation methods. Some scatterers cannot correspond to any object due to exceeding the detection range of the LiDAR sensor. Since unknown scatterers are usually far away from the transceiver and the received power via them is very small, they can be ignored in the channel realization. Fig. 1 characterizes the scatterers extracted from the RT-based wireless channel data.

3 DT Enabled Channel Modeling

Based on the constructed DT space, a DT-enabled vehicular communication channel model for the Beijing CBD area is proposed, which considers the impact of different traffic densities for peak and off-peak hour periods. Moreover, to parameterize the proposed model more accurately, the scatterer properties, i.e., number, distance, angle, and power of scatterers with different velocities, are modeled and analyzed. Furthermore, the channel non-stationarity and consistency in the time domains are studied.

3.1 Framework of DT-Enabled Channel Model for Beijing CBD

The channel impulse response (CIR) of the vehicular communication channel $h(t,\tau)$, i.e., the CIR of the transmission link from the i-th vehicle to the j-th vehicle, can be represented as:

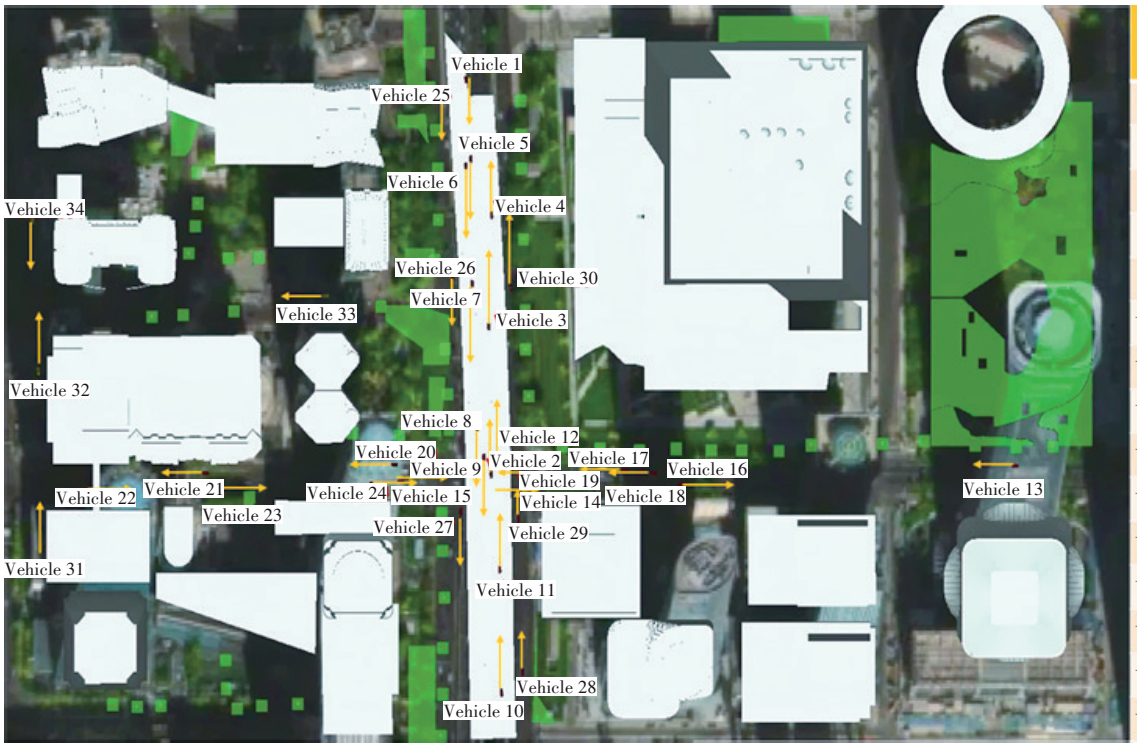

Communication links	
Vehicle 5	Vehicle 9
Vehicle 5	Vehicle 10
Vehicle 8	Vehicle 12
Vehicle 8	Vehicle 15
Vehicle 8	Vehicle 32
Vehicle 17	Vehicle 16
Vehicle 17	Vehicle 19
Vehicle 24	Vehicle 15
Vehicle 24	Vehicle 17
Vehicle 30	Vehicle 11
Vehicle 30	Vehicle 14
Vehicle 33	Vehicle 9
Vehicle 33	Vehicle 23
Vehicle 33	Vehicle 27
Vehicle 33	Vehicle 28

Figure 2. Vehicular trajectories and communication links under off-peak DT-enabled Beijing CBD scenarios

$$h(t,\tau)=\underbrace{\sqrt{\frac{\Omega(t)}{\Omega(t)+1}}h^{\mathrm{LoS}}(t)\delta\left(\tau-\tau^{\mathrm{LoS}}(t)\right)}_{\mathrm{LoS}}+\underbrace{\sqrt{\frac{\eta^{\mathrm{GR}}(t)}{\Omega(t)+1}}h^{\mathrm{GR}}(t)\delta\left(\tau-\tau^{\mathrm{GR}}(t)\right)}_{\mathrm{Ground\ Reflection}}+\underbrace{\sum_{p=1}^{N_c^z(t)}\sum_{n_p=1}^{N_s^z(t)}\sqrt{\frac{\eta^{z}(t)}{\Omega(t)+1}}h^{z}_{p,n_p}(t)\delta\left(\tau-\tau^{z}_{p,n_p}(t)\right)+\sum_{q=1}^{N_c^{nz}(t)}\sum_{n_q=1}^{N_s^{nz}(t)}\sqrt{\frac{\eta^{\mathrm{nz}}(t)}{\Omega(t)+1}}h^{nz}_{q,n_q}(t)\delta\left(\tau-\tau^{nz}_{q,n_q}(t)\right)}_{\mathrm{NLoS}},\quad(1),$$

where $\Omega(t)$ represents the Ricean factor of the transmission link from the i-th vehicle to the j-th vehicle. $\eta^{\mathrm{GR}}(t)$, $\eta^{z}(t)$, and $\eta^{nz}(t)$ are the power ratios of the ground reflection component, component via clusters with zero velocity, and component via clusters with non-zero velocity in the transmission link from the i-th vehicle to the j-th vehicle; they satisfy $\eta^{\mathrm{GR}}(t)+\eta^{z}(t)+\eta^{nz}(t)=1$. The representation of the proposed DT-enabled vehicular communication channel model for Beijing CBD is depicted in Fig. 3. The distance between transceivers is $D_{i,j}(t_0)$.

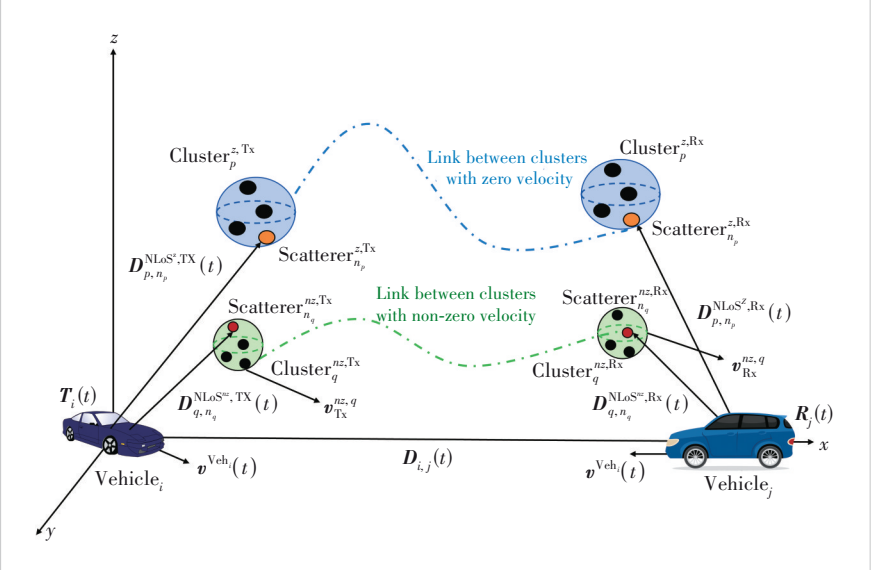

Figure 3. Geometry of the proposed DT-enabled vehicular communication channel model for Beijing CBD

3.1.1 Ground Reflection Component

The ground reflection component complex channel gain of the transmission link from the i-th vehicle to the j-th vehicle can be represented as

$$h^{\mathrm{GR}}(t) = Q(t)\sqrt{P^{\mathrm{GR}}(t)} \times \exp\left\{j2\pi\left[\int_{t_0}^{t} f^{\mathrm{GR},V_i}(t)\mathrm{d}t + \int_{t_0}^{t} f^{\mathrm{GR},V_j}(t)\mathrm{d}t\right] + j\varphi^{\mathrm{GR}}(t)\right\} \quad (2),$$

where $Q(t)$ is a rectangular window function[15]; it equals 1 when $t_0 \le t \le T_0$ (where T_0 means the observation time interval), otherwise equals 0. $P^{\mathrm{GR}}(t)$, $f^{\mathrm{GR},V_i/V_j}(t)$, $\varphi^{\mathrm{GR}}(t)$, and $\tau^{\mathrm{GR}}(t)$ denote power, Doppler frequency at the i/j-th vehicle, phase, and delay of the ground reflection component from the i-th vehicle to the j-th vehicle, respectively. The Doppler frequency $f^{\mathrm{GR},V_i/V_j}(t)$ is expressed as

$$f^{\mathrm{GR},V_i/V_j}(t) = \frac{1}{\lambda}\frac{\left\langle \boldsymbol{D}^{\mathrm{GR},V_i/V_j}(t), \boldsymbol{v}^{V_i/V_j}(t)\right\rangle}{\left\| \boldsymbol{D}^{\mathrm{GR},V_i/V_j}(t)\right\|} \quad (3),$$

where $\boldsymbol{D}^{\mathrm{GR},V_i/V_j}(t)$ is the distance vector from the i/j-th vehicle to the reflection point on the ground. The phase of the ground reflection component from the i-th vehicle to the j-th vehicle can be computed as

$$\varphi^{\mathrm{GR}}(t) = \varphi_0 + \frac{2\pi}{\lambda}\left(\left\| \boldsymbol{D}^{\mathrm{GR},V_i}(t)\right\| + \left\| \boldsymbol{D}^{\mathrm{GR},V_j}(t)\right\|\right) \quad (4),$$

where φ_0 is the initial phase shift.

The delay of the ground reflection component from the i-th vehicle to the j-th vehicle, $\tau^{\mathrm{GR}}(t)$, can be computed as

$$\tau^{\mathrm{GR}}(t) = \frac{\left\| \boldsymbol{D}^{\mathrm{GR},V_i}(t)\right\| + \left\| \boldsymbol{D}^{\mathrm{GR},V_j}(t)\right\|}{c} \quad (5).$$

The calculation of distance vectors $\boldsymbol{D}^{\mathrm{GR},V_i}(t)$ and $\boldsymbol{D}^{\mathrm{GR},V_j}(t)$ is expressed below. The azimuth distance between the TX (the i-th vehicle) and the ground reflection point is $d_{V_i}(t)$, which is derived from $d_{V_i}(t) = \frac{\left\| \boldsymbol{D}^{V_i,V_j}(t)\right\| h_{V_i}(t)}{h_{V_i}(t) + h_{V_j}(t)}$; $h_{V_i}(t)$ and $h_{V_j}(t)$ are the ground clearances of the i-th vehicle and the j-th vehicle. With the geometrical relationship, the distance between the i/j-th vehicle and ground reflection point can be computed as $\| \boldsymbol{D}^{\mathrm{GR},V_i}(t)\| = \sqrt{d_{V_i}^2(t) + h_{V_i}^2(t)}$ and $\left\| \boldsymbol{D}^{\mathrm{GR},V_j}(t)\right\| = \sqrt{\left\| \boldsymbol{D}^{V_i,V_j}(t)\right\|^2 + h_{V_i}^2(t) + h_{V_j}^2} - \left\| \boldsymbol{D}^{\mathrm{GR},V_i}(t)\right\|$. The corresponding distance vectors can be expressed as

$$\boldsymbol{D}^{\mathrm{GR},V_i/V_j} = \left\| \boldsymbol{D}^{\mathrm{GR},V_i/V_j}\right\| \times \begin{bmatrix} \cos\alpha^{\mathrm{GR},V_i/V_j}(t)\cos\beta^{\mathrm{GR},V_i/V_j}(t) \\ \sin\alpha^{\mathrm{GR},V_i/V_j}(t)\cos\beta^{\mathrm{GR},V_i/V_j}(t) \\ \sin\beta^{\mathrm{GR},V_i/V_j}(t) \end{bmatrix} \quad (6),$$

where $\alpha^{\mathrm{GR},V_i/V_j}$ and $\beta^{\mathrm{GR},V_i/V_j}$ are the azimuth and elevation angles of the distance vector $\boldsymbol{D}^{\mathrm{GR},V_i/V_j}$. As the azimuth angle of the ground reflection path matches that of the line-of-sight (LoS) path and the combined power of the LoS and ground reflection paths remains constant, only the elevation angle of the ground reflection path needs to be taken into account similar to Ref [16]. $\beta^{\mathrm{GR},V_i/V_j}$ is computed as $\beta^{\mathrm{GR},V_i/V_j} = \arctan\frac{h_{V_j}}{d_{V_j}(t)}$.

3.1.2 LoS Component

The LoS complex channel gain of the transmission link from the i-th vehicle to the j-th vehicle can be represented as

$$h^{\mathrm{LoS}}(t) = Q(t)\exp\left[j2\pi\int_{t_0}^{t} f^{\mathrm{LoS}}(t)\mathrm{d}t + j\varphi^{\mathrm{LoS}}(t)\right] \quad (7).$$

The Doppler frequency, phase shift, and delay of the LoS component of the transmission link from the i-th vehicle to the j-th vehicle are obtained by

$$f^{\mathrm{LoS}}(t) = \frac{1}{\lambda}\frac{\left\langle \boldsymbol{D}^{\mathrm{LoS}}(t), \boldsymbol{v}^{V_j}(t) - \boldsymbol{v}^{V_i}(t)\right\rangle}{\left\| \boldsymbol{D}^{\mathrm{LoS}}(t)\right\|} \quad (8),$$

$$\varphi^{\mathrm{LoS}}(t) = \varphi_0 + \frac{2\pi}{\lambda}\left\| \boldsymbol{D}^{\mathrm{LoS}}(t)\right\| \quad (9),$$

$$\tau^{\mathrm{LoS}}(t) = \frac{\left\| \boldsymbol{D}^{\mathrm{LoS}}(t)\right\|}{c} \quad (10),$$

where $\langle\cdot,\cdot\rangle$, φ_0, and λ are the inner product, initial phase shift, and carrier wavelength; $\boldsymbol{v}^{V_i}(t)$ and $\boldsymbol{v}^{V_j}(t)$ are the velocity vectors of the i-th vehicle and the j-th vehicle. Meanwhile, the distance vector for the i-th vehicle and the j-th vehicle $\boldsymbol{D}^{\mathrm{LoS}}(t)$ is obtained by

$$\boldsymbol{D}^{\mathrm{LoS}}(t) = \boldsymbol{D}^{\mathrm{LoS}}(t_0) + \int_{t_0}^{t}\boldsymbol{v}^{V_j}(t)\mathrm{d}t - \int_{t_0}^{t}\boldsymbol{v}^{V_i}(t)\mathrm{d}t \quad (11).$$

3.1.3 Non-LoS Component

Vehicular communication's high mobility causes real-time changes in the communication environment. To characterize the non-line-of-sight (NLoS) component of the channel gain, it is essential to separately model the characteristics of scatterers according to their velocities. To compute the NLoS component's complex channel gain, we separately calculate

the complex channel gains of clusters with zero and non-zero velocities. Using LiDAR point clouds and RGB images, the scatterers are classified by velocity (zero/non-zero). Meanwhile, the scatterer parameters with different velocities will be analyzed and utilized for channel modeling, detailed in the next subsection. To depict the NLoS complex channel gain more clearly, we define clusters with centroids closer to TX/RX as TX/RX clusters, which are then randomly shuffled and paired to create twin clusters. The p-th TX/RX cluster with zero velocity and the q-th TX/RX cluster with non-zero velocity are represented as $C_{\mathrm{TX/RX}}^{z,p}$ and $C_{\mathrm{TX/RX}}^{nz,q}$. The velocity vector $\boldsymbol{v}_{\mathrm{TX/RX}}^{nz,q}$ is utilized to depict the q-th TX/RX cluster with non-zero velocity.

The NLoS component's complex channel gain from the i-th vehicle and the j-th vehicle via the n_p-th scatterer in the p-th twin cluster with zero velocity, i.e., $h_{p,n_p}^{\mathrm{NLoS}^z}(t)$, is calculated by

$$h_{p,n_p}^{\mathrm{NLoS}^z}(t)=Q(t)\sqrt{P_{p,n_p}^{\mathrm{NLoS}^z}(t)}\times\exp\left\{j2\pi\left[\int_{t_0}^{t}f_{p,n_p}^{\mathrm{NLoS}^z,\mathrm{TX}}(t)\mathrm{d}t+\int_{t_0}^{t}f_{p,n_p}^{\mathrm{NLoS}^z,\mathrm{RX}}(t)\mathrm{d}t\right]+j\varphi_{p,n_p}^{\mathrm{NLoS}^z}(t)\right\} \tag{12},$$

where $P_{p,n_p}^{\mathrm{NLoS}^z}(t)$ is the normalized power of ZVS, $f_{p,n_p}^{\mathrm{NLoS}^z,\mathrm{TX/RX}}(t)$ is the Doppler frequency of the clusters with zero velocity at TX/RX, and $\varphi_{p,n_p}^{\mathrm{NLoS}^z}(t)$ is the phase shift. $f_{p,n_p}^{\mathrm{NLoS}^z,\mathrm{TX/RX}}$ is computed by

$$f_{p,n_p}^{\mathrm{NLoS}^z,\mathrm{TX}}(t)=\frac{1}{\lambda}\frac{\left\langle\boldsymbol{D}_{p,n_p}^{\mathrm{NLoS}^z,\mathrm{TX}}(t),\boldsymbol{v}^{\mathrm{TX}}(t)\right\rangle}{\left\|\boldsymbol{D}_{p,n_p}^{\mathrm{NLoS}^z,\mathrm{TX}}(t)\right\|} \tag{13},$$

$$f_{p,n_p}^{\mathrm{NLoS}^z,\mathrm{RX}}(t)=\frac{1}{\lambda}\frac{\left\langle\boldsymbol{D}_{p,n_p}^{\mathrm{NLoS}^z,\mathrm{RX}}(t),\boldsymbol{v}^{\mathrm{RX}}(t)\right\rangle}{\left\|\boldsymbol{D}_{p,n_p}^{\mathrm{NLoS}^z,\mathrm{RX}}(t)\right\|} \tag{14},$$

where $\boldsymbol{D}_{p,n_p}^{\mathrm{NLoS}^z,\mathrm{TX/RX}}(t)$ represents the distance between the TX/RX and the n_p-th scatterer in the p-th twin cluster $C_{\mathrm{TX/RX}}^{z,p}$. The distance $\boldsymbol{D}_{p,n_p}^{\mathrm{NLoS}^z,\mathrm{TX/RX}}(t)$ is given by

$$\boldsymbol{D}_{p,n_p}^{\mathrm{NLoS}^z,\mathrm{TX/RX}}(t)=D_{p,n_p}^{\mathrm{NLoS}^z,\mathrm{TX/RX}}(t)\begin{pmatrix}\cos\alpha_{p,n_p}^{\mathrm{NLoS}^z,\mathrm{TX/RX}}(t)\cos\beta_{p,n_p}^{\mathrm{NLoS}^z,\mathrm{TX/RX}}(t)\\ \sin\alpha_{p,n_p}^{\mathrm{NLoS}^z,\mathrm{TX/RX}}(t)\cos\beta_{p,n_p}^{\mathrm{NLoS}^z,\mathrm{TX/RX}}(t)\\ \sin\beta_{p,n_p}^{\mathrm{NLoS}^z,\mathrm{TX/RX}}(t)\end{pmatrix} \tag{15}.$$

The phase shift is computed by

$$\varphi_{p,n_p}^{\mathrm{NLoS}^z}(t)=\varphi_0+\frac{2\pi}{\lambda}\left[\left\|\boldsymbol{D}_{p,n_p}^{\mathrm{NLoS}^z,\mathrm{TX}}(t)\right\|+\left\|\boldsymbol{D}_{p,n_p}^{\mathrm{NLoS}^z,\mathrm{RX}}(t)\right\|+c\tilde{\tau}^{z,p}(t)\right] \tag{16},$$

where $\tilde{\tau}^{z,p}(t)$ represents the delay of the virtual link between the twin clusters $C_{\mathrm{TX/RX}}^{z,p}$, which obeys the Exponential distribution. Moreover, the delay via clusters with zero velocity at TX/RX is computed by

$$\tau_{p,n_p}^{\mathrm{NLoS}^z}(t)=\frac{\left\|\boldsymbol{D}_{p,n_p}^{\mathrm{NLoS}^z,\mathrm{TX}}(t)\right\|+\left\|\boldsymbol{D}_{p,n_p}^{\mathrm{NLoS}^z,\mathrm{RX}}(t)\right\|}{c}+\tilde{\tau}^{z,p}(t) \tag{17}.$$

Similarly, the NLoS complex channel gain from the i-th vehicle and the j-th vehicle via the n_q-th scatterer in the q-th twin cluster with non-zero velocity, i.e., $h_{q,n_q}^{\mathrm{NLoS}^{nz}}(t)$, is calculated by

$$h_{q,n_q}^{\mathrm{NLoS}^{nz}}(t)=Q(t)\sqrt{P_{q,n_q}^{\mathrm{NLoS}^{nz}}(t)}\times\exp\left\{j2\pi\left[\int_{t_0}^{t}f_{q,n_q}^{\mathrm{NLoS}^{nz},\mathrm{TX}}(t)\mathrm{d}t+\int_{t_0}^{t}f_{q,n_q}^{\mathrm{NLoS}^{nz},\mathrm{RX}}(t)\mathrm{d}t\right]+j\varphi_{q,n_q}^{\mathrm{NLoS}^{nz}}(t)\right\} \tag{18},$$

where $P_{q,n_q}^{\mathrm{NLoS}^{nz}}(t)$ is the normalized power of NVS, $f_{q,n_q}^{\mathrm{NLoS}^{nz},\mathrm{TX/RX}}(t)$ is the Doppler frequency of the clusters with non-zero velocity at TX/RX, and $\varphi_{q,n_q}^{\mathrm{NLoS}^{nz}}(t)$ is the phase shift. $f_{q,n_q}^{\mathrm{NLoS}^{nz},\mathrm{TX/RX}}$ is computed by

$$f_{q,n_q}^{\mathrm{NLoS}^{nz},\mathrm{TX}}(t)=\frac{1}{\lambda}\frac{\left\langle\boldsymbol{D}_{q,n_q}^{\mathrm{NLoS}^{nz},\mathrm{TX}}(t),\boldsymbol{v}^{\mathrm{TX}}(t)\right\rangle}{\left\|\boldsymbol{D}_{q,n_q}^{\mathrm{NLoS}^{nz},\mathrm{TX}}(t)\right\|} \tag{19},$$

$$f_{q,n_q}^{\mathrm{NLoS}^{nz},\mathrm{RX}}(t)=\frac{1}{\lambda}\frac{\left\langle\boldsymbol{D}_{q,n_q}^{\mathrm{NLoS}^{nz},\mathrm{RX}}(t),\boldsymbol{v}^{\mathrm{RX}}(t)\right\rangle}{\left\|\boldsymbol{D}_{q,n_q}^{\mathrm{NLoS}^{nz},\mathrm{RX}}(t)\right\|} \tag{20},$$

where $\boldsymbol{D}_{q,n_q}^{\mathrm{NLoS}^{nz},\mathrm{TX/RX}}(t)$ represents the distance between the TX/RX and the n_q-th scatterer in the q-th twin cluster $C_{\mathrm{TX/RX}}^{nz,q}$. The distance $\boldsymbol{D}_{p,n_p}^{\mathrm{NLoS}^z,\mathrm{TX/RX}}(t)$ is given by

$$\boldsymbol{D}_{q,n_q}^{\mathrm{NLoS}^{nz},\mathrm{TX/RX}}(t)=D_{q,n_q}^{\mathrm{NLoS}^{nz},\mathrm{TX/RX}}(t)\begin{pmatrix}\cos\alpha_{q,n_q}^{\mathrm{NLoS}^{nz},\mathrm{TX/RX}}(t)\cos\beta_{q,n_q}^{\mathrm{NLoS}^{nz},\mathrm{TX/RX}}(t)\\ \sin\alpha_{q,n_q}^{\mathrm{NLoS}^{nz},\mathrm{TX/RX}}(t)\cos\beta_{q,n_q}^{\mathrm{NLoS}^{nz},\mathrm{TX/RX}}(t)\\ \sin\beta_{q,n_q}^{\mathrm{NLoS}^{nz},\mathrm{TX/RX}}(t)\end{pmatrix} \tag{21}.$$

The phase shift is computed by

$$\varphi_{q,n_q}^{\mathrm{NLoS}^{nz}}(t)=\varphi_0+\frac{2\pi}{\lambda}\left[\left\|\boldsymbol{D}_{q,n_q}^{\mathrm{NLoS}^{nz},\mathrm{TX}}(t)\right\|+\left\|\boldsymbol{D}_{q,n_q}^{\mathrm{NLoS}^{nz},\mathrm{RX}}(t)\right\|+c\tilde{\tau}^{nz,q}(t)\right] \quad (22),$$

where $\tilde{\tau}^{nz}(t)$ represents the delay of the virtual link between the twin clusters $C_{\mathrm{TX/RX}}^{nz,q}$, which also obeys the Exponential distribution. Moreover, the delay via clusters with non-zero velocity at TX/RX is computed by

$$\tau_{q,n_q}^{\mathrm{NLoS}^{nz}}(t)=\frac{\left\|\boldsymbol{D}_{q,n_q}^{\mathrm{NLoS}^{nz},\mathrm{TX}}(t)\right\|+\left\|\boldsymbol{D}_{q,n_q}^{\mathrm{NLoS}^{nz},\mathrm{RX}}(t)\right\|}{c}+\tilde{\tau}^{nz,q}(t) \quad (23).$$

The power parameter $P_{p/q,n_{p/q}}^{\mathrm{NLoS}^{z/nz}}(t)$, distance parameter $D_{p/q,n_{p/q}}^{\mathrm{NLoS}^{z/nz},\mathrm{TX/RX}}(t)$, and angle parameters $\alpha_{p/q,n_{p/q}}^{\mathrm{NLoS}^{z/nz},\mathrm{TX/RX}}(t)$ and $\beta_{p/q,n_{p/q}}^{\mathrm{NLoS}^{z/nz},\mathrm{TX/RX}}(t)$ obey different statistical distributions, which are analyzed in the following subsection.

3.2 Parameters for Channel Realization

Based on the constructed DT-based Beijing CBD vehicular communication dataset, we use statistical approaches to compute the distribution of parameters related to scatterers with different velocities.

Accurately characterizing and modeling the number of scatterers and clusters is crucial for channel models[17]. However, the statistical properties of the corresponding scatterers/clusters are not depicted in the current standardized models for scatterers with different velocities[18-19]. To comprehensively characterize vehicular communication channels in Beijing CBD, the quantities of scatterers/clusters with zero/non-zero velocities are explored. The numbers of ZVS and NVS in the transmission link from the i-th vehicle (TX) to the j-th vehicle (RX) are denoted as $N_{s_{i,j}}^{z}(t)$ and $N_{s_{i,j}}^{nz}(t)$. Since the distance between the transceivers affects the evaluation of the scatterer number, the parameters controlling scatterer numbers are defined as $Y_{i,j}^{z}$ and $Y_{i,j}^{nz}$, which can be represented as

$$Y_{i,j}^{z}(t)=\frac{N_{s_{i,j}}^{z}(t)}{\|\boldsymbol{T}_i(t)-\boldsymbol{R}_j(t)\|} \quad (24),$$

$$Y_{i,j}^{nz}(t)=\frac{N_{s_{i,j}}^{nz}(t)}{\|\boldsymbol{T}_i(t)-\boldsymbol{R}_j(t)\|} \quad (25),$$

where $\boldsymbol{T}_i(t)$and $\boldsymbol{R}_j(t)$ are the locations of the i-th and j-th vehicles. Moreover, based on the constructed DT-based Beijing CBD vehicular communication dataset, the number ratios of ZVS and NVS for each communication link per snapshot across peak and off-peak traffic periods are calculated and analyzed. Fig. 4 presents the cumulative distribution functions (CDFs) of the velocity-based ratio related to the scatterer number during peak and off-peak hours. These CDFs fit well with the Gaussian mixture model (GMM), which can be represented as

$$F_Y^{z/nz}(x)=\sum_{k=1}^{K^{z/nz}}\pi_k^{z/nz}\mathcal{F}_{Y,k}^{z/nz}(x) \quad (26),$$

where $\mathcal{F}_{Y,k}^{z/nz}(x)$ and $\pi_k^{z/nz}$ are the CDF and weight of the k-th Gaussian distribution, respectively. $\mathcal{F}_{Y,k}^{z/nz}(x)$ can be given by $\mathcal{F}_{Y,k}^{z/nz}(x)=\Phi_{Y,k}^{z/nz}\left(\frac{x-\mu_{Y,k}^{z/nz}}{\sigma_{Y,k}^{z/nz}}\right)$, where $\Phi_{Y,k}^{z/nz}$ is the CDF of the standard normal distribution; $\mu_{Y,k}^{z/nz}$ and $\sigma_{Y,k}^{z/nz}$ are the mean and standard deviations of the k-th Gaussian distribution. The ratios related to scatterer numbers can be obtained from the simulations using the constructed DT-based Beijing CBD vehicular communication dataset. The number of Gaussian distributions k is 3. During off-peak hours, the simulation parameters for the ZVS are $\pi_k^z=[0.395\,2;\,0.466\,6;\,0.138\,2]$, $\mu_{Y,k}^z=[0.156\,5;\,0.026\,3;\,0.617\,9]$, and $\sigma_{Y,k}^z=[0.008\,2;\,3.63\times10^{-4};\,0.191\,2]$, while those for the NVS are $\pi_k^{nz}=[0.114\,8;\,0.317\,5;\,0.567\,7]$, $\mu_{Y,k}^{nz}=[0.116\,4;\,0.049\,2;\,0.010\,7]$and $\sigma_{Y,k}^{nz}=[0.001\,6;\,5.14\times10^{-4};\,3.21\times10^{-5}]$. Meanwhile, during peak hours, the simulation parameters for the ZVS are $\pi_k^z=[0.350\,4;\,0.281\,9;\,0.367\,7]$, $\mu_{Y,k}^z=[1.167\,3;\,0.426\,3;\,0.072\,3]$, and $\sigma_{Y,k}^z=[0.254\,2;\,0.022\,2;\,0.002\,9]$, while those for the NVS are $\pi_k^{nz}=[0.603\,4;\,0.378\,4;\,0.018\,2]$, $\mu_{Y,k}^{nz}=[0.011\,5;\,0.055\,8;\,0.273\,5]$, and $\sigma_{Y,k}^{nz}=[2.94\times10^{-5};\,3.86\times10^{-4};\,0.008\,9]$. Fig. 4 shows that both the mean and variance of the number-related parameters for the NVS are greater during peak hours than during off-peak hours. This is because there are more dynamic vehicles around the transceiver during peak

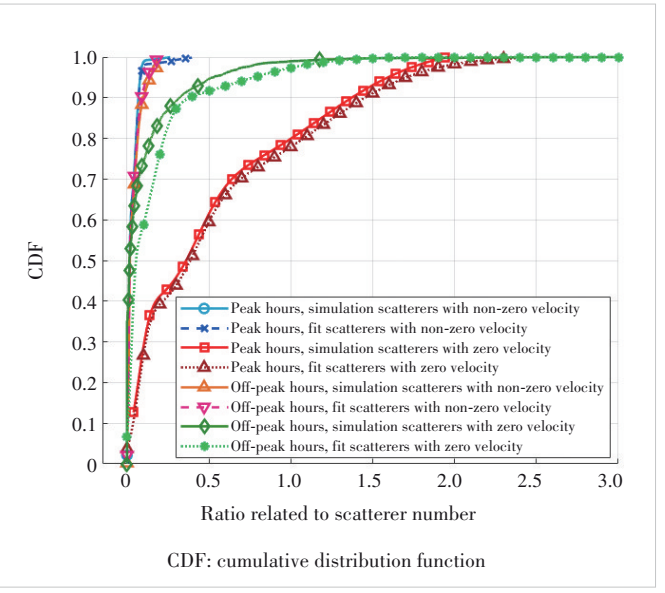

CDF: cumulative distribution function

Figure 4. GMM-fitted CDFs of velocity-based ratios related to scatterer numbers during peak and off-peak hours

hours, which increases the number of NVS. For the ZVS, the mean and variance are also greater during peak hours than during off-peak hours. This is due to the fact that the environment tends to be rich scattering during peak hours, resulting in more propagation paths.

To investigate vehicular channel characteristics in Beijing CBD in detail, the scatterers are clustered to analyze cluster population statistics. Therefore, the parameters of zero-velocity and non-zero-velocity clusters in the transmission link from the i-th vehicle (TX) to the j-th vehicle (RX) are denoted as $U_{i,j}^{z}$ and $U_{i,j}^{nz}$. For each communication link per snapshot, we denote the velocity-based cluster-number parameters across peak and off-peak hours. The CDFs of velocity-based ratios related to cluster numbers follow GMM distributions, which can be expressed as

$$F_{U}^{z/nz}(x)=\sum_{k=1}^{K^{z/nz}}\pi_{k}^{z/nz}\mathcal{F}_{U,k}^{z/nz}(x) \tag{27}$$

where $\mathcal{F}_{U,k}^{z/nz}(x)$, the CDF of the k-th Gaussian distribution, can be given by $\mathcal{F}_{U,k}^{z/nz}(x)=\Phi_{U,k}^{z/nz}\left(\frac{x-\mu_{U,k}^{z/nz}}{\sigma_{U,k}^{z/nz}}\right)$, where $\Phi_{U,k}^{z/nz}$ is the CDF of the standard normal distribution, while $\mu_{U,k}^{z/nz}$ and $\sigma_{U,k}^{z/nz}$ are the mean and standard deviations of the k-th Gaussian distribution. The number of Gaussian distributions k is also 3. For the clusters with zero velocity during off-peak hours, the simulation parameters are $\pi_{k}^{z}=[0.254\,3;0.631\,5;0.114\,2]$, $\mu_{U,k}^{z}=[0.040\,9;0.010\,3;0.101\,7]$, and $\sigma_{U,k}^{z}=[2.97\times10^{-4};4.76\times10^{-5};0.002]$. As for the clusters with non-zero velocity during off-peak hours, the parameters are $\pi_{k}^{nz}=[0.298\,4;0.606\,8;0.094\,8]$, $\mu_{U,k}^{nz}=[0.551\,5;0.011\,7;0.109\,7]$, and $\sigma_{U,k}^{nz}=[2.36\times10^{-4};3.05\times10^{-5};0.001\,7]$. Meanwhile, for the clusters with zero velocity during peak hours, the simulation parameters are $\pi_{k}^{z}=[0.340\,6;0.401\,9;0.257\,5]$, $\mu_{U,k}^{z}=[0.085\,2;0.020\,0;0.212\,0]$ and $\sigma_{U,k}^{z}=[6.96\times10^{-4};1.17\times10^{-4};0.005\,5]$. For the clusters with non-zero velocity during peak hours, the parameters are $\pi_{k}^{nz}=[0.195\,2;0.778\,5;0.026\,3]$, $\mu_{U,k}^{nz}=[0.033\,3;0.010\,9;0.065\,6]$, and $\sigma_{U,k}^{nz}=[2.01\times10^{-5};3.01\times10^{-5};1.07\times10^{-5}]$. Fig. 5 presents the CDFs of the velocity-based ratios related to cluster numbers during peak and off-peak hours. The parameters related to the cluster number show similar trends to those related to the scatterer number with different velocities during peak and off-peak hours.

Distance distribution of scatterers is important for stochastic channel modeling. The distance parameters of scatterers are assumed to follow the Exponential distribution in Ref. [20]. However, scatterer velocity variations and traffic density differences during peak and off-peak hours are ignored. Based on the constructed DT-based Beijing CBD vehicular communication dataset, distance characteristics of the scatterers with different velocities are explored. The distance parameters for the m-th scatterer with zero velocity and the n-th scatterer with non-zero velocity from the transceiver, i.e., the i-th vehicle and the j-th vehicle, are represented as

$$D_{i,j}^{z,m}(t)=\frac{\|\boldsymbol{T}_{i}(t)-\boldsymbol{S}_{i,j}^{z,m}(t)\|+\|\boldsymbol{R}_{j}(t)-\boldsymbol{S}_{i,j}^{z,m}(t)\|-\|\boldsymbol{T}_{i}(t)-\boldsymbol{R}_{j}(t)\|}{\|\boldsymbol{T}_{i}(t)-\boldsymbol{R}_{j}(t)\|} \tag{28}$$

$$D_{i,j}^{nz,n}(t)=\frac{\|\boldsymbol{T}_{i}(t)-\boldsymbol{S}_{i,j}^{nz,n}(t)\|+\|\boldsymbol{R}_{j}(t)-\boldsymbol{S}_{i,j}^{nz,n}(t)\|-\|\boldsymbol{T}_{i}(t)-\boldsymbol{R}_{j}(t)\|}{\|\boldsymbol{T}_{i}(t)-\boldsymbol{R}_{j}(t)\|} \tag{29}$$

where $\boldsymbol{S}_{i,j}^{z,m}(t)$ and $\boldsymbol{S}_{i,j}^{nz,n}(t)$ are the locations of the m-th scatterer with zero velocity and the n-th scatterer with non-zero velocity in the transmission link between the i-th vehicle and the j-th vehicle; $\|\cdot\|$ denotes the calculation of the Frobenius norm. We compute the distance parameters of scatterers with different velocities during peak and off-peak hours for each communication link per snapshot. The CDFs of distance parameters with different velocities also fit well with the GMM distribution, which is represented as

$$F_{D}^{z/nz}(x)=\sum_{k=1}^{K^{z/nz}}\pi_{k}^{z/nz}\mathcal{F}_{D,k}^{z/nz}(x) \tag{30}$$

where $\mathcal{F}_{D,k}^{z/nz}(x)$, the CDF of the k-th Gaussian distribution, can be given by $\mathcal{F}_{D,k}^{z/nz}(x)=\Phi_{D,k}^{z/nz}\left(\frac{x-\mu_{D,k}^{z/nz}}{\sigma_{D,k}^{z/nz}}\right)$, where $\Phi_{D,k}^{z/nz}$ is the CDF of the standard normal distribution, and $\mu_{D,k}^{z/nz}$ and $\sigma_{D,k}^{z/nz}$

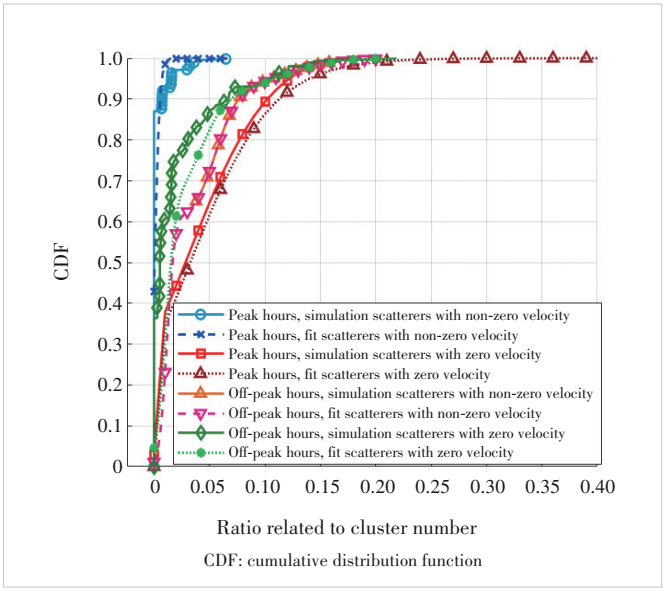

Figure 5. GMM-fitted CDFs of velocity-based ratios related to cluster numbers during peak and off-peak hours

are the mean and standard deviations of the k-th Gaussian distribution. The number of Gaussian distributions k is still 3. During off-peak hours, the simulation parameters for ZVS are $\pi_k^z = [0.312\,9;\ 0.547\,4;\ 0.139\,7]$, $\mu_{D,k}^z = [7.724\,0;\ 0.653\,0;\ 20.991\,6]$, and $\sigma_{\mathrm{ND},k}^z = [9.628\,3;\ 0.316\,4;\ 102.07]$, while the parameters for the NVS are $\pi_k^{nz} = [0.674\,2;\ 0.239\,2;\ 0.068\,8]$, $\mu_{D,k}^{nz} = [0.710\,5;\ 6.879\,5;\ 20.943\,5]$, and $\sigma_{D,k}^{nz} = [0.512\,7;\ 10.750\,7;\ 93.229\,4]$. On the other hand, during peak hours, the simulation parameters for the ZVS are $\pi_k^z = [0.623\,1;\ 0.126\,7;\ 0.250\,2]$, $\mu_{D,k}^z = [0.689\,8;\ 27.995\,2;\ 7.395\,6]$, and $\sigma_{D,k}^z = [0.443\,7;\ 110.228\,6;\ 6.673\,4]$, while the parameters for the NVS are $\pi_k^{nz} = [0.736\,0;\ 0.012\,5;\ 0.251\,5]$, $\mu_{D,k}^{nz} = [0.519\,9;\ 4.989\,4;\ -0.093\,2]$ and $\sigma_{D,k}^{nz} = [0.037\,3;\ 0.003\,0;\ 0.001\,5]$. Fig. 6 shows the CDFs of all distance parameters of the scatterers with different velocities during peak and off-peak hours. The distance parameter of ZVS is larger than that of NVS during peak and off-peak hours, as ZVSes are mainly tall buildings and trees, while NVSes are dynamic vehicles. Dynamic vehicles are generally closer to the TX and RX, which leads to a shorter distance. The variance of the distance parameter is smaller at peak hours than that at off-peak hours since the scatterer distribution is more centered as vehicles around the transceiver increase.

The angle parameters related to scatterers are also crucial for analyzing and constructing channel models for DT-enabled vehicular communication within Beijing CBD. These parameters, including azimuth angle of departure (AAoD), azimuth angle of arrival (AAoA), elevation angle of departure (EAoD), and elevation angle of arrival (EAoA), are analyzed for the scatterers with different velocities under different traffic densities during peak and off-peak hours. AAoA ratios for the m-th scatterer with zero velocity and the n-th scatterer with non-zero velocity from the transceiver, i.e., the i-th vehicle and the j-th vehicle, are expressed as

$$\alpha_{i,j}^{z,m}(t) = \frac{\gamma_{i,j}^{z,m}(t)}{\| \boldsymbol{T}_i(t) - \boldsymbol{R}_i(t) \|} \tag{31},$$

$$\alpha_{i,j}^{nz,n}(t) = \frac{\gamma_{i,j}^{nz,n}(t)}{\| \boldsymbol{T}_i(t) - \boldsymbol{R}_i(t) \|} \tag{32},$$

where $\gamma_{i,j}^{z,m}(t)$ and $\gamma_{i,j}^{nz,n}(t)$ represent the AAoAs of the m-th scatterer with zero velocity and the n-th scatterer with non-zero velocity from the transceiver. Furthermore, based on the DT-based Beijing CBD vehicular communication dataset, the AAoAs of scatterers with different velocities in each communication link per snapshot are analyzed. Fig. 7 shows the CDFs of all AAoAs of the scatterers with different velocities under different traffic densities during peak and off-peak hours, which fit well with the Gaussian distribution. The CDF of the Gaussian distribution for AAoAs related to scatterers with different velocities can be represented by

$$F_{\mathrm{AAoA}}^z(x) = \frac{1}{2}\left[1 + \mathrm{erf}\left(\frac{x - \mu_{\mathrm{AAoA}}^z}{\sigma_{\mathrm{AAoA}}^z\sqrt{2}}\right)\right] \tag{33},$$

$$F_{\mathrm{AAoA}}^{nz}(x) = \frac{1}{2}\left[1 + \mathrm{erf}\left(\frac{x - \mu_{\mathrm{AAoA}}^{nz}}{\sigma_{\mathrm{AAoA}}^{nz}\sqrt{2}}\right)\right] \tag{34},$$

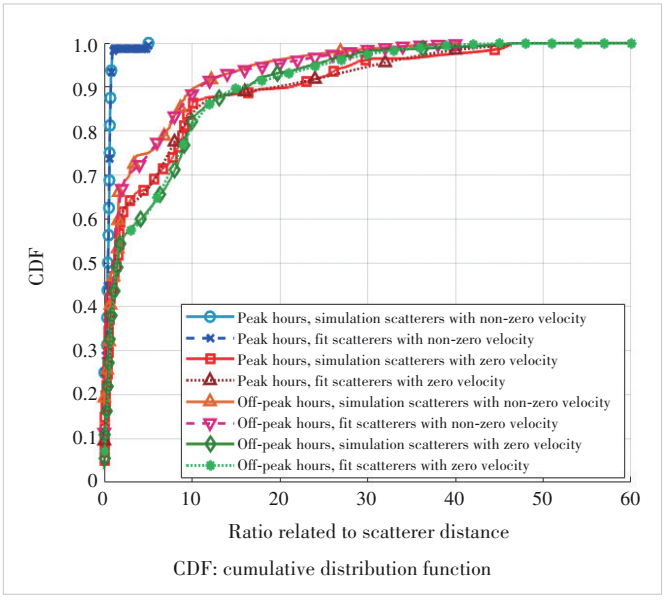

Figure 6. GMM-fitted CDFs of distance parameters during peak and off-peak hours

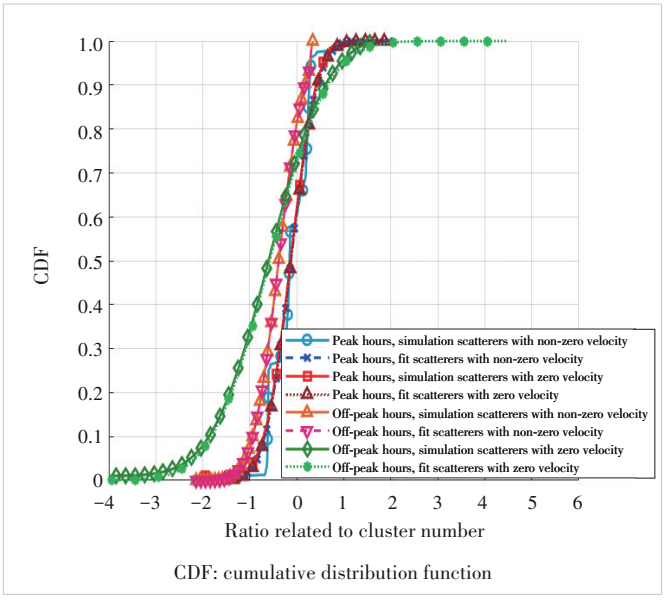

Figure 7. Gaussian-fitted CDFs of azimuth angle of departure (AAoD) during peak and off-peak hours

where $\mu_{\mathrm{AAoA}}^{z/nz}$ and $\sigma_{\mathrm{AAoA}}^{z/nz}$ denote the mean value and standard deviation of the Gaussian distribution for AAoAs related to scatterers with different velocities; erf(·) is the error function. Similarly, AAoD $\theta_{i,j}^{z/nz,\,m/n}(t)$, EAoA $\beta_{i,j}^{z/nz,\,m/n}(t)$, and EAoD $\phi_{i,j}^{z/nz,\,m/n}(t)$ are calculated and also obey the Gaussian distribution. The distance parameters of the simulation during off-peak hours are $\mu_{\mathrm{AAoA}}^{z/nz} = -0.576\,9/-0.385\,2$, $\sigma_{\mathrm{AAoA}}^{z/nz} = 1.065/0.433\,5$; $\mu_{\mathrm{AAoD}}^{z/nz} = -0.146\,4/0.296\,8$, $\sigma_{\mathrm{AAoD}}^{z/nz} = 1.297\,4/0.900\,8$; $\mu_{\mathrm{EAoA}}^{z/nz} = -0.129\,4/-0.029\,3$, $\sigma_{\mathrm{EAoA}}^{z/nz} = 0.153\,9/0.036\,7$; $\mu_{\mathrm{EAoD}}^{z/nz} = -0.157\,9/-0.052\,3$, $\sigma_{\mathrm{EAoD}}^{z/nz} = 0.289\,0/0.066\,4$, while the distance parameters during peak hours are $\mu_{\mathrm{AAoA}}^{z/nz} = -0.548\,1/-0.122\,1$, $\sigma_{\mathrm{AAoA}}^{z/nz} = 1.081\,1/0.434\,9$; $\mu_{\mathrm{AAoD}}^{z/nz} = -0.164\,0/0.212\,6$, $\sigma_{\mathrm{AAoD}}^{z/nz} = 1.237\,2/0.891\,0$; $\mu_{\mathrm{EAoA}}^{z/nz} = -0.146\,8/-0.069\,8$, $\sigma_{\mathrm{EAoA}}^{z/nz} = 0.165\,5/0.103\,8$; $\mu_{\mathrm{EAoD}}^{z/nz} = -0.226\,7/-0.190\,1$, $\sigma_{\mathrm{EAoD}}^{z/nz} = 0.481\,0/0.630\,1$. As shown in Fig. 7 and according to the angle parameters of the statistical distributions above, NVS have a smaller azimuth angle variance than those with zero velocity. This is because the NVS mainly come from dynamic vehicles, which have less variation in heights. Moreover, the angle parameter variance is larger during peak hours than during off-peak hours. This is due to the more complex and variable environment during peak hours, causing greater angle variations.

In addition, path power and delay characteristics are significant in channel realization. The path power is an exponential function of the path delay[21]. Using the DT-based Beijing CBD vehicular communication dataset, we separate the path power into power via ZVS and that via NVS. The path power from the i-th vehicle to the j-th vehicle via the m-th scatterer with zero velocity and the n-th scatterer with non-zero velocity is expressed by

$$P^{z,\,m}(t) = \exp\left(-\xi^{z}\tau^{z,\,m}(t) - \eta^{z}\right)10^{-\frac{Z^{z}}{10}} \tag{35},$$

$$P^{nz,\,n}(t) = \exp\left(-\xi^{nz}\tau^{nz,\,n}(t) - \eta^{nz}\right)10^{-\frac{Z^{nz}}{10}} \tag{36},$$

where $\xi^{z/nz}$ and $\eta^{z/nz}$ are the delay-related parameters of scatterers with different velocities; $\tau^{z/nz,m/n}$ is the delay of the path via the m-th scatterer with zero velocity and the n-th scatterer with non-zero velocity; $Z^{z/nz}$ follows the Gaussian distribution $\mathcal{N}\left(0,\left(\sigma_{\mathrm{E}}^{z/nz}\right)^{2}\right)$. For accurate linear fitting, Eqs. (35) and (36) are transformed as

$$-\ln P^{z,\,m}(t) = \xi^{z}\tau^{z,\,m}(t) + \eta^{z} + \frac{\ln 10}{10}Z^{z} \tag{37},$$

$$-\ln P^{nz,\,n}(t) = \xi^{nz}\tau^{nz,\,n}(t) + \eta^{nz} + \frac{\ln 10}{10}Z^{nz} \tag{38}.$$

The power and delay of each path via each scatterer with different velocities per snapshot are calculated. Fig. 8 presents the fitting results under different traffic densities during peak and off-peak hours. The parameters related to power and delay during off-peak hours are $\xi^{z/nz} = 3.726\,4 \times 10^{6}/2.763\,6 \times 10^{6}$, $\eta^{z/nz} = 28.065\,8/28.876\,9$, and $\sigma_{\mathrm{E}}^{z/nz} = 7.971\,6/7.005\,9$, while those during peak hours are $\xi^{z/nz} = 4.029\,4 \times 10^{6}/2.613\,3 \times 10^{6}$, $\eta^{z/nz} = 27.443\,8/29.404\,1$, and $\sigma_{\mathrm{E}}^{z/nz} = 8.482\,8/7.514\,2$. Fig. 8 shows that the power of NVS is more sensitive to delay changes than that of ZVS. Therefore, an increase in the delay of NVS notably reduces their power.

Consequently, the parameters related to scatterers with different velocities can be generated by the statistical distribution obtained from the aforementioned analysis.

3.3 Capturing of DT-Enabled Channel Non-Stationarity and Consistency

We depict channel non-stationarity and consistency based on the proposed DT-enabled Beijing CBD vehicular communication channel model. The environment is constantly changing with the continuous movement of the vehicle, which leads to continuous changes in LiDAR point clouds and RGB images captured by sensors. Meanwhile, the scatterers in communication links are not effective as they move away from the transceiver. In the transmission links related to different vehicles, the sets of effective clusters are different as well, which leads to the non-stationarity of clusters in the time domain in the DT-enabled Beijing CBD vehicular communication channel. In addition, given the temporal continuity of the communication environment, scatterers exhibit smooth transitions in appearance and disappearance across time and space. This maintains the scatterer consistency in both time and space domains of the DT-enabled Beijing CBD

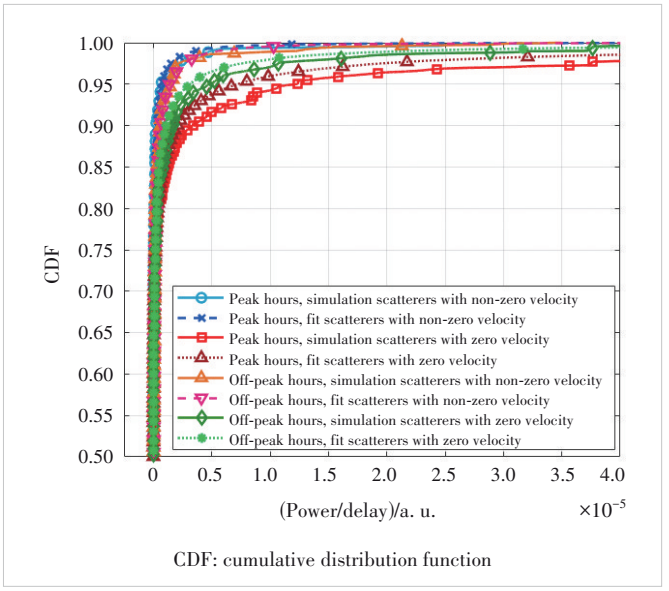

Figure 8. Scatterer power-delay CDFs with Exponential fit during peak and off-peak hours

vehicular communication channel.

To accurately and simultaneously model the channel non-stationarity and consistency in the time domain, a new visibility region (VR)-based method is proposed, which considers the generation of scatterers with different velocities. In the VR methods in Ref. [22], clusters located within the VR range have an impact on the channel realization. As the VR and cluster positions move, the set of visible clusters evolves smoothly, which reflects the channel non-stationarity and consistency in the time domain. To depict smooth cluster time evolution in channels for DT-enabled Beijing CBD vehicular communication, a VR-based method is proposed based on the statistical parameter distribution for different traffic densities during peak and off-peak hours. The scatterers in the environment are initialized, and their parameters, including velocities for peak and off-peak hours, are generated according to the distribution obtained in Section 3.2. The number of scatterers with different velocities between the i-th vehicle and the j-th vehicle at the initial time t_0 and the distances are both generated according to the GMM distribution. The departure and arrival angles (AAoDs, AAoAs, EAoDs, and EAoAs) are generated following the Gaussian distribution. Based on the generated distances and angles for each scatterer, the initial positions of these scatterers at time t_0 are determined. Moreover, the generated scatterers with different velocities are clustered using the K-means algorithm. Each vehicle's VR is modeled as a semi-sphere centered at the vehicle. The VR radius R_i/R_j of the i/j-th vehicle is the maximum distance between the vehicle and initially generated velocity-varying clusters at the initial time. The clusters within R_i/R_j at time t are defined as visible clusters. Since the distance between the cluster and TX/RX at time $t_0 + \Delta t$ is still shorter than the radii of VRs, the cluster is still in the VRs and affects the channel. The number of surviving clusters with different velocities between the i-th and j-th vehicles at time $t_0 + \Delta t$ is given as $U_{i,j}^{z,\mathrm{sur}}(t_0 + \Delta t)/U_{i,j}^{nz,\mathrm{sur}}(t_0 + \Delta t)$. In addition to the surviving clusters, there are some newly generated clusters with different velocities at time $t_0 + \Delta t$. For a certain distance between the i-th and j-th vehicles at time $t_0 + \Delta t$, the number parameter $U_{i,j}^{z,\mathrm{GMM}}(t_0 + \Delta t)/U_{i,j}^{nz,\mathrm{GMM}}(t_0 + \Delta t)$ related to clusters with different velocities is randomly generated according to the GMM distribution. The number of newly generated clusters is computed by

$$U_{i,j}^{z/nz,\,\mathrm{new}}(t) = U_{i,j}^{z/nz,\,\mathrm{GMM}}(t) - U_{i,j}^{z/nz,\,\mathrm{sur}}(t) \tag{39},$$

where $U_{i,j}^{z/nz,\,\mathrm{GMM}}(t)$ is greater than $U_{i,j}^{z/nz,\mathrm{sur}}(t)$ and there are $U_{i,j}^{z/nz}(t) = U_{i,j}^{z/nz,\,\mathrm{GMM}}(t)$ clusters with different velocities that contribute to channel realization. However, if $U_{i,j}^{z/nz,\,\mathrm{GMM}}(t)$ is less than $U_{i,j}^{z/nz,\mathrm{sur}}(t)$, the number of newly generated clusters is $U_{i,j}^{z/nz,\,\mathrm{new}}(t) = 0$. In this case, there are $U_{i,j}^{z/nz}(t) = U_{i,j}^{z/nz,\mathrm{sur}}(t)$ clusters with different velocities that contribute to channel realization.

4 Channel Statistical Properties

In this section, the key statistical properties for the proposed DT-enabled Beijing CBD vehicular communication channel are derived, including the TF-CF and DPSD.

4.1 TF-CF

The TF-CF of the transmission from the i-th vehicle to the j-th vehicle can be calculated as

$$\Pi(t,f;\Delta t,\Delta f) = \mathbb{E}\left[h^*(t,f)h\ (t+\Delta t,f+\Delta f)\right] \tag{40},$$

where $\mathbb{E}[\cdot]$ and $(\cdot)^*$ represent the expectation operation and complex conjugate operation similar to Ref. [23]. As the TF-CFs of the LoS component, ground reflection component, and NLoS component can be assumed as independent, the TF-CF can be obtained by

$$\Pi(t,f;\Delta t,\Delta f) = \Pi^{\mathrm{LoS}}(t,f;\Delta t,\Delta f) + \Pi^{\mathrm{GR}}(t,f;\Delta t,\Delta f) + \Pi^{\mathrm{NLoS}^z}(t,f;\Delta t,\Delta f) + \Pi^{\mathrm{NLoS}^{nz}}(t,f;\Delta t,\Delta f) \tag{41}.$$

The TF-CFs of the LoS component, ground reflection component, and NLoS component can be computed by

$$\Pi^{\mathrm{LoS}}\left(t,f;\Delta t,\Delta f\right) = \sqrt{\frac{\Omega(t)\Omega(t+\Delta t)}{(\Omega(t)+1)(\Omega(t+\Delta t)+1)}}\,h^{\mathrm{LoS}*}(t)h^{\mathrm{LoS}}(t+\Delta t)\exp\left[j2\pi f\tau^{\mathrm{LoS}}(t)-(f+\Delta f)\tau^{\mathrm{LoS}}(t+\Delta t)\right] \tag{42},$$

$$\Pi^{\mathrm{GR}}\left(t,f;\Delta t,\Delta f\right) = \sqrt{\frac{\eta^{\mathrm{GR}}(t)\eta^{\mathrm{GR}}(t+\Delta t)}{(\Omega(t)+1)(\Omega(t+\Delta t)+1)}}\,h^{\mathrm{GR}*}(t)h^{\mathrm{GR}}(t+\Delta t)\exp\left[j2\pi f\tau^{\mathrm{GR}}(t)-(f+\Delta f)\tau^{\mathrm{GR}}(t+\Delta t)\right] \tag{43},$$

$$\Pi^{\mathrm{NLoS}^{z/nz}}(t,f;\Delta t,\Delta f) = \sqrt{\frac{\eta^{z/nz}(t)\eta^{z/nz}(t+\Delta t)}{(\Omega(t)+1)(\Omega(t+\Delta t)+1)}} \times \mathbb{E}\left[\sum_{p/q=1}^{N_s^{z/nz}(t)}\sum_{p'/q'=1}^{N_e^{z/nz}(t+\Delta t)}\sum_{n_{p/q}=1}^{N_s^{z/nz}(t)}\sum_{n'_{p/q}=1}^{N_s^{z/nz}(t+\Delta t)} h_{p/q,n_{p/q}}^{z/nz}(t)h_{p'/q',n'_{p/q}}^{z/nz}(t+\Delta t)\times \exp\left(j2\pi\tau_{p/q,n_{p/q}}^{z/nz}(t)f-(f+\Delta f)\tau_{p'/q',n'_{p/q}}^{z/nz}(t+\Delta t)\right)\right] \tag{44}.$$

Therefore, the time auto-correlation function (TACF) and the frequency correlation function (FCF) can be obtained by setting $\Delta f = 0$ and $\Delta t = 0$, respectively.

4.2 DPSD

The DPSD can be obtained by the Fourier transform of the TACF, which is computed by

$$\Psi(t;f_{\mathrm{D}})=\int_{-\infty}^{+\infty}\Pi(t;\Delta t)e^{-j2\pi f_{\mathrm{D}}\Delta t}\mathrm{d}(\Delta t) \quad (45),$$

where f_{D} and $\Pi(t;\Delta t)$ are the Doppler frequency and TACF. The time-varying DPSD depicts the time-varying characteristic of the proposed DT-enabled Beijing CBD vehicular communication channel model.

4.3 Simulation Results and Analysis

The computational complexity of channel modeling mainly focuses on the generation of the CIR matrix. The primary source of computational complexity comes from the calculation of physical environment parameters. Specifically, the time complexity of generating the CIR matrix is $\mathcal{O}(N_t \cdot N_r)$, where N_t and N_r represent the numbers of TXes and RXes, respectively. The time complexity of processing the LiDAR point cloud is $\mathcal{O}(P)$, where P is the number of points in the point clouds. The time complexity of RGB can be considered to be constants in a snapshot of data processing, i.e., $\mathcal{O}(1)$. Therefore, the overall complexity is $\mathcal{O}(N_t \cdot N_r + P)$. The time consumption of the computation mainly depends on the simulation setting.

Key statistical channel properties are simulated and compared with the accurate RT-based results. The parameters remain unchanged unless otherwise stated. The carrier frequency is f_c = 5.9 GHz with 20 MHz communication bandwidth. Delays of virtual links $\tau_i(t)$ and $\tau_j(t)$ obey the Exponential distribution with the mean and variance of 80 ns and 15 ns to imitate the complex transmission between twin clusters.

Fig. 9 shows the absolute normalized TACFs during peak and off-peak hours at t = 0 s and t = 5 s. The TACFs depend on time instants and time separations. Moreover, time non-stationarity is depicted. The TACF decreases as the traffic density increases, demonstrating that the TACF is lower during peak hours than that during off-peak hours. This is because, as the number of vehicles increases, the channel becomes more variable and the temporal correlation decreases.

The RT-based CIRs are collected in Wireless InSite within the DT space shown in Fig. 1. DPSD is derived based on the CIR data compared with the simulated DPSD during peak and off-peak hours. As shown in Fig. 10, the RT-based DPSD is much closer to the simulated DPSD during peak and off-peak hours, which demonstrates the validity of the proposed model. The DPSD is flatter during peak hours than during off-peak hours, because vehicles are denser during peak hours and the vehicular communication channels are more complex. Therefore, the comparison of different traffic densities during peak and off-peak hours is significant for the proposed DT-enabled vehicular communication channel model.

The effectiveness of the proposed DT-enabled vehicular communication channel model is demonstrated by comparing the TACF and DPSD of the proposed model with the RT-based TACF and DPSD. In the future, we can analyze more channel characteristics, e. g., angular/delay power spectral densities (PSDs) and root mean square (RMS) angular/Doppler/delay spreads, similar to Ref. [24], to further evaluate the performance of the proposed DT-enabled vehicular communication channel model. Meanwhile, we intend to further

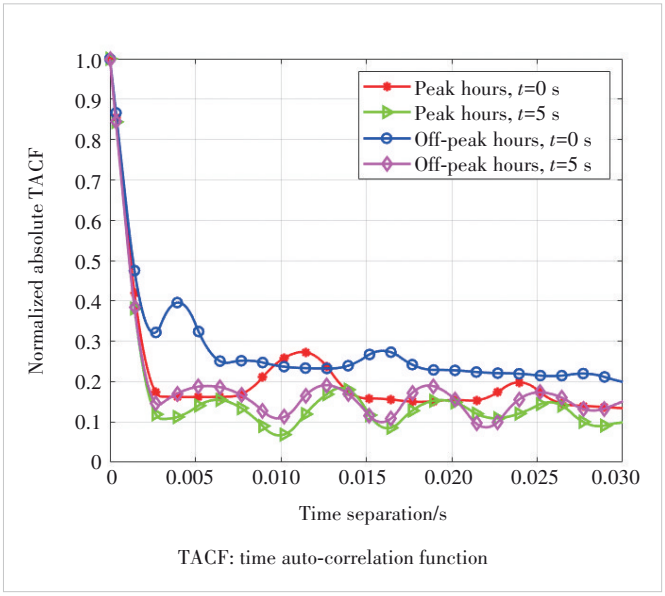

Figure 9. TACFs with varying time instants during peak and off-peak hours

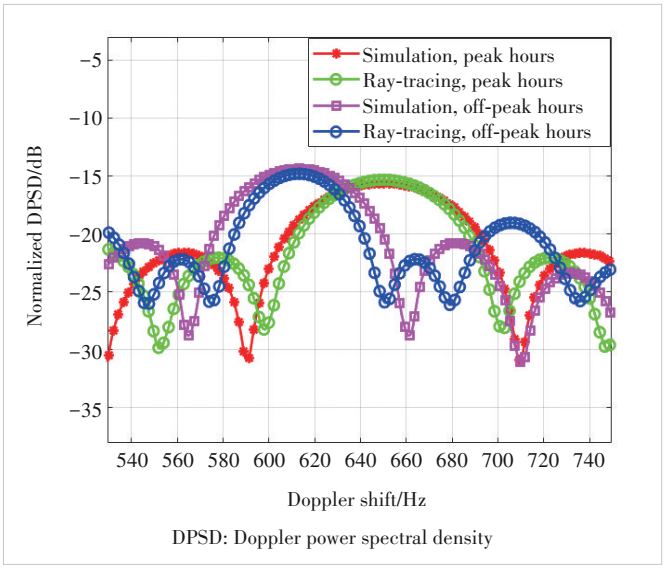

Figure 10. Comparison of simulated DPSDs and RT-based DPSDs during peak and off-peak hours

validate the effectiveness and universality of the proposed DT-based channel model with real-world measurements. Specifically, we aim to collect synchronized multi-modal sensing data and channel data in dense urban scenarios, e.g., Beijing CBD. This will enable us to refine the proposed model under real-world dynamic conditions and increase its real-world deployment value.

5 Conclusions

This paper introduces a novel DT-enabled channel model for vehicular communications in Beijing CBD. The proposed model effectively integrates LiDAR point clouds, RGB images, and channel data to enhance the precision of channel modeling in complex urban environments. A reliable DT space for the Beijing CBD area has been constructed, which has provided a high-fidelity virtual environment for simulating vehicular communication channels. The developed model captures the dynamic characteristics of scatterers during peak and off-peak hours in consideration of their number, distance, angle, power, and velocity. Key channel statistical properties (TF-CF and DPSD) have been derived and simulated during different transportation periods. Simulation results show that the proposed model accurately captures channel non-stationarity and consistency, closely aligning with RT-based experimental data. Therefore, the potential of DT technology for improving vehicular communication channel modeling in urban environments is demonstrated, which can provide a reliable foundation for the design of ITSs and advanced vehicular networks.

References

[1] CHENG X, DUAN D L, GAO S J, et al. Integrated sensing and communications (ISAC) for vehicular communication networks (VCN) [J]. IEEE internet of things journal, 2022, 9(23): 23441 – 23451. DOI: 10.1109/JIOT.2022.3191386
[2] LIN X Q, KUNDU L, DICK C, et al. 6G digital twin networks: from theory to practice [J]. IEEE communications magazine, 2023, 61(11): 72 – 78. DOI: 10.1109/MCOM.001.2200830
[3] ALKHATEEB A, JIANG S F, CHARAN G. Real-time digital twins: vision and research directions for 6G and beyond [J]. IEEE communications magazine, 2023, 61(11): 128 – 134. DOI: 10.1109/MCOM.001.2200866
[4] HE D P, GUAN K, YAN D, et al. Physics and AI-based digital twin of multi-spectrum propagation characteristics for communication and sensing in 6G and beyond [J]. IEEE journal on selected areas in communications, 2023, 41(11): 3461 – 3473. DOI: 10.1109/JSAC.2023.3310108
[5] JIANG S F, ALKHATEEB A. Digital twin aided massive MIMO: CSI compression and feedback [C]//Proc. IEEE International Conference on Communications (ICC). IEEE, 2024: 3586 – 3591. DOI: 10.1109/icc51166.2024.10622316
[6] XIE W L, QI F, LIU L, et al. Radar imaging based UAV digital twin for wireless channel modeling in mobile networks [J]. IEEE journal on selected areas in communications, 2023, 41(11): 3702 – 3710. DOI: 10.1109/JSAC.2023.3310085
[7] DING C, HO I W. Digital-twin-enabled city-model-aware deep learning for dynamic channel estimation in urban vehicular environments [J]. IEEE transactions on green communications and networking, 2022, 6(3): 1604 – 1612. DOI: 10.1109/TGCN.2022.3173414
[8] ALOBAIDY H A H, JIT SINGH M, BEHJATI M, et al. Wireless transmissions, propagation and channel modelling for IoT technologies: applications and challenges [J]. IEEE access, 2022, 10: 24095 – 24131. DOI: 10.1109/access.2022.3151967
[9] CHEN Y, LI Y B, HAN C, et al. Channel measurement and ray-tracing-statistical hybrid modeling for low-terahertz indoor communications [J]. IEEE transactions on wireless communications, 2021, 20(12): 8163 – 8176. DOI: 10.1109/TWC.2021.3090781
[10] ZHANG Y X, HE R S, AI B, et al. Generative adversarial networks based digital twin channel modeling for intelligent communication networks [J]. China communications, 2023, 20(8): 32 – 43
[11] YU Z H, LV X Z, RUI H, et al. Digital twin channel: a data-driven continuous trajectory modeling [C]//Proc. IEEE 1st International Conference on Digital Twins and Parallel Intelligence (DTPI). IEEE, 2021: 302 – 305. DOI: 10.1109/dtpi52967.2021.9540134
[12] REMCOM. Wireless InSite [EB/OL]. (2017-01-01)[2024-02-01]. https://www.remcom.com/wireless-insite-em-propagation-software
[13] SHAH S, DEY D, LOVETT C, et al. AirSim: high-fidelity visual and physical simulation for autonomous vehicles [M]//Field and service robotics. Cham, Switzerland: Springer International Publishing, 2017: 621 – 635. DOI: 10.1007/978-3-319-67361-5_40
[14] SCHUBERT E, SANDER J, ESTER M, et al. DBSCAN revisited, revisited: why and how you should (still) use DBSCAN [J]. ACM transactions on database systems, 2017, 42(3): 1 – 21. DOI: 10.1145/3068335
[15] GUTIERREZ C A, PATZOLD M, DAHECH W, et al. A non-WSSUS mobile-to-mobile channel model assuming velocity variations of the mobile stations [C]//Proc. IEEE Wireless Communications and Networking Conference (WCNC). IEEE, 2017: 1 – 6. DOI: 10.1109/WCNC.2017.7925795
[16] JAECKEL S, RASCHKOWSKI L, WU S B, et al. An explicit ground reflection model for mm-wave channels [C]//Proc. IEEE Wireless Communications and Networking Conference Workshops (WCNCW). IEEE, 2017: 1 – 5. DOI: 10.1109/WCNCW.2017.7919093
[17] BAI L, HUANG Z W, DU H H, et al. A 3-D nonstationary wideband V2V GBSM with UPAs for massive MIMO wireless communication systems [J]. IEEE Internet of Things journal, 2021, 8(24): 17622 – 17638. DOI: 10.1109/JIOT.2021.3081816
[18] International Telecommunication Union. Guidelines for evaluation of radio interface technologies for IMT-2020, preliminary draft new report ITU-R M, document R15-WP5D-170613-TD-0332 [R]. 2017
[19] HANEDA K, NGUYEN S L H, KARTTUNEN A. Measurement results and final mmMAGIC channel models, Rep. H2020-ICT-671650-mmMAGIC/D2.2 [R]. 2017
[20] BAI L, HUANG Z W, LI Y R, et al. A 3D cluster-based channel model for 5G and beyond vehicle-to-vehicle massive MIMO channels [J]. IEEE transactions on vehicular technology, 2021, 70(9): 8401 – 8414. DOI: 10.1109/TVT.2021.3100389
[21] KYOSTI P, MEINILA J, HENTILA L, et al. WINNER II channel models, version 1.1 [R]. 2007.
[22] MARTÍNEZ À O, EGGERS P, DE CARVALHO E. Geometry-based stochastic channel models for 5G: extending key features for massive MIMO [C]//Proc. IEEE 27th Annual International Symposium on Personal, Indoor, and Mobile Radio Communications (PIMRC). IEEE, 2016: 1 – 6. DOI: 10.1109/PIMRC.2016.7794648
[23] PÄTZOLD M. Mobile radio channels [M]. 2nd ed. Chichester, UK: Wiley, 2012
[24] WANG C-X, LV Z, CHEN Y, et al. A complete study of space-time-frequency statistical properties of the 6G pervasive channel model [J]. IEEE transactions on communications, 2023, 71(12): 7273 – 7287. DOI: 10.1109/TCOMM.2023.3307144

Biographies

LU Mengyuan received her BS degree in engineering from the School of Software, Shandong University, China in 2024. She is currently pursuing her master's degree at the same institution. Her research interests focus on AI-based 6G vehicular communications.

BAI Lu (lubai@sdu.edu.cn) received her PhD degree in information and communication engineering from Shandong University, China in 2019. From 2017 to 2019, she was a visiting PhD student with Heriot-Watt University, UK. From 2019 to 2022, she was a post-doctoral researcher with Beihang University, China. She is currently a professor with Shandong University. Her general research interests are in areas of wireless communications and artificial intelligence, subject on which she has published more than 50 journal and conference papers and 2 books, held 5 patents, and participated in formulating 5 Chinese standards. She has received IEEE VR Best Paper Award, Science and Technology Progress Award of China Transport and Logistics Association, and TaiShan Scholar Award. She was a recipient of the Young Elite Scientist Sponsorship Program by China Association for Science and Technology. She has served as a member of the Technical Program Committee and session chair for several international conferences. She is currently an associate editor of *IET Communications* and a member of the IEEE P1944 Standard Group.

HAN Zengrui received his BS degree in information and communication engineering from the School of Information and Communication Engineering, University of Electronic Science and Technology of China in 2024. He is currently pursuing a PhD degree at the School of Electronics, Peking University, China. His current research interest is Al-based channel modeling.

HUANG Ziwei received his BS degree in communication engineering from Chongqing University, China in 2019 and PhD degree from the School of Electronics, Peking University, China. His current research interests include wireless communication channel measurements and modeling, including vehicular channel measurements and modeling, UAV channel modeling, and AI-based channel modeling. He was a co-recipient of IET Communications Best Paper Award: Premium Award.

LU Shiliang is pursuing his master's degree at the School of Software, Shandong University, China. His research interest focuses on MIMO channel modeling.

CHENG Xiang received his joint PhD degree from Heriot-Watt University and The University of Edinburgh, UK in 2009. He is currently a Boya Distinguished Professor with Peking University, China. His research interests include channel modeling, wireless communications, and data analytics, the subjects on which he has published more than 280 journal articles and conference papers, nine books, and held 26 patents. He was a recipient of the IEEE Asia-Pacific Outstanding Young Researcher Award in 2015 and the Xplorer Prize in 2023. He is a subject editor of the *IET Communications* and an associate editor of the *IEEE Transactions on Wireless Communications*, *IEEE Transactions on Intelligent Transportation Systems*, and *IEEE Wireless Communications Letter*. He has been a highly cited Chinese researcher since 2020. In 2021 and 2023, he was selected into two world scientist lists: the World's Top 2% Scientists released by Stanford University and the top computer science scientists released by Guide2Research.

Channel Knowledge Maps for 6G Wireless Networks: Construction, Applications, and Future Challenges

LIU Xingchen[1], SUN Shu[1], TAO Meixia[1], Aryan KAUSHIK[2], YAN Hangsong[3]

(1. School of Information Science and Electronic Engineering, Shanghai Jiao Tong University, Shanghai 200240, China;
2. Department of Computing and Mathematics, Manchester Metropolitan University, Manchester M1 5GD, UK;
3. Hangzhou Institute of Technology, Xidian University, Hangzhou 311231, China)

DOI: 10.12142/ZTECOM.202502006

https://kns.cnki.net/kcms/detail/34.1294.TN.20250517.1809.002.html, published online May 18, 2025

Manuscript received: 2025-04-09

Abstract: The advent of 6G wireless networks promises unprecedented connectivity, supporting ultra-high data rates, low latency, and massive device connectivity. However, these ambitious goals introduce significant challenges, particularly in channel estimation due to complex and dynamic propagation environments. This paper explores the concept of channel knowledge maps (CKMs) as a solution to these challenges. CKMs enable environment-aware communications by providing location-specific channel information, reducing reliance on real-time pilot measurements. We categorize CKM construction techniques into measurement-based, model-based, and hybrid methods, and examine their key applications in integrated sensing and communication (ISAC) systems, beamforming, trajectory optimization of unmanned aerial vehicles (UAVs), base station (BS) placement, and resource allocation. Furthermore, we discuss open challenges and propose future research directions to enhance the robustness, accuracy, and scalability of CKM-based systems in the evolving 6G landscape.

Keywords: channel knowledge map; channel modeling; wireless communication; 6G

Citation (Format 1): LIU X C, SUN S, TAO M X, et al. Channel knowledge maps for 6G wireless networks: construction, applications, and future challenges [J]. ZTE Communications, 2025, 23(2): 46 - 59. DOI: 10.12142/ZTECOM.202502006

Citation ((Format 2): X. C. Liu, S. Sun, M. X. Tao, et al., "Channel knowledge maps for 6G wireless networks: construction, applications, and future challenges," *ZTE Communications*, vol. 23, no. 2, pp. 46 - 59, Jun. 2025. doi: 10.12142/ZTECOM.202502006.

1 Introduction

The advent of 6G wireless networks promises to revolutionize connectivity by enabling ultra-high data rates, ultra-low latency, massive device connectivity, and pervasive intelligence[1-3]. However, these ambitious performance targets come with significant challenges. The increasing density of devices and network nodes[4], along with the deployment of large-scale antenna arrays[5] and the utilization of higher frequency bands[6], such as millimeter wave (mmWave) and terahertz (THz), leads to highly complex propagation environments. In such scenarios, traditional channel estimation methods, primarily based on extensive pilot training, are rapidly becoming inefficient, as they struggle to cope with the increased channel dimensions and dynamic variability in the environment[7]. At the same time, the wealth of diverse environmental data and the rapid evolution of artificial intelligence techniques offer unprecedented opportunities to rethink how wireless channels are characterized and managed[8].

To address these challenges, researchers have proposed novel approaches that leverage both environmental information and advanced data analytics to enhance channel state information acquisition. One promising paradigm first introduced in Ref. [9] is the channel knowledge map (CKM), a site-specific database that links geographical locations to detailed channel parameters. By exploiting the spatial consistency inherent in wireless propagation, CKMs enable networks to infer channel characteristics based on location data, thereby reducing the dependency on real-time, high-overhead pilot measurements[10-11]. This innovative concept not only promises to alleviate the challenges posed by dense and dynamic 6G environments but also paves the way for proactive and predictive communication strategies that can significantly enhance network performance.

This work was supported by the National Natural Science Foundation of China under Grants Nos. 62431014 and 62271310, and the Fundamental Research Funds for the Central Universities of China.
The corresponding author is SUN Shu.

A CKM can be classified into different types based on the scope and granularity of channel knowledge it provides. Some CKMs focus on large-scale channel characteristics, such as path loss and shadowing, which are primarily influenced by terrain and urban structures. Others capture small-scale fading properties, including multipath effects characterized by parameters like the angle of arrival (AoA), the angle of departure (AoD), time delay, and the Doppler shift. Additionally, CKMs can be categorized based on their coverage range, such as BS-to-any (B2X) CKM, which maps the channel characteristics from a given BS to any receiver within a coverage area, and any-to-any (X2X) CKM, which generalizes channel relationships among arbitrary locations.

The construction of CKMs generally falls into three broad approaches: measurement-based methods, model-based methods, and hybrid data-model approaches. Measurement-based methods rely on empirical measurements and employ spatial interpolation techniques, including the nearest-neighbor interpolation[12] and geostatistical methods like Kriging[13]. In contrast, model-based methods use well-established propagation models, including empirical formulas (e.g., COST-231 Hata[14]) and deterministic ray tracing[15]. To address the limitations of both approaches, hybrid methods combine model predictions with real-world measurements, often leveraging advanced machine learning techniques such as deep neural networks and generative adversarial networks (GANs) to enhance CKM accuracy and adaptability.

Based on the provided image, the key idea behind CKM is not just about specific applications but rather a paradigm shift in wireless communication towards environment-aware communications. Fig. 1 illustrates this transformation based on two examples from Ref. [9], by comparing conventional location-based or probabilistic channel modeling with environment knowledge. In Fig. 1a, CKM enables improved path loss prediction by considering environmental obstructions, rather than relying solely on distance-based models. In Fig. 1b, it enhances beamforming by incorporating environment knowledge, allowing for more accurate signal directionality and avoiding obstacles that would otherwise degrade communication performance.

This article is structured as follows. Section 2 introduces the fundamental concepts of CKMs, including their definitions, core principles, and roles in enabling environment-aware communications in 6G networks. Section 3 discusses CKM construction techniques, categorized into measurement-based, model-based, and hybrid data-model approaches, highlighting their methodologies and trade-offs. Section 4 explores key applications of CKMs, such as localization and sensing systems, trajectory optimization, beamforming and BS placement. Section 5 discusses open challenges and outlines future research directions and the transformative potential of CKMs in next-generation wireless systems. Section 6 concludes this article with a summary of the current state of CKM research, emphasizing its potential to revolutionize wireless communications by enabling proactive, environment-aware systems and addressing the challenges that lie ahead in the rapidly evolving 6G landscape.

2 Fundamental Concepts of Channel Knowledge Map

A CKM is a channel knowledge database associated with specific geographical locations, which is constructed to provide region-specific or location-specific channel information, thereby enhancing the understanding of the wireless propagation environment. Mathematically, a CKM can be defined as a function that maps a location vector $\boldsymbol{q} \in R^D$ to a channel knowledge vector $\boldsymbol{z} \in C^J$, where $\boldsymbol{q}$ represents the location of the transmitter and/or receiver, and $\boldsymbol{z}$ the relevant channel knowledge.

$$M: R^D \rightarrow C^J \tag{1}$$

This knowledge may include, but is not limited to, path gain, multipath propagation parameters (such as AoA, AoD,

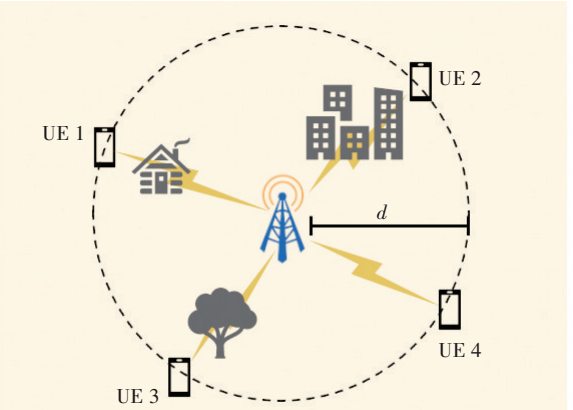

(a)

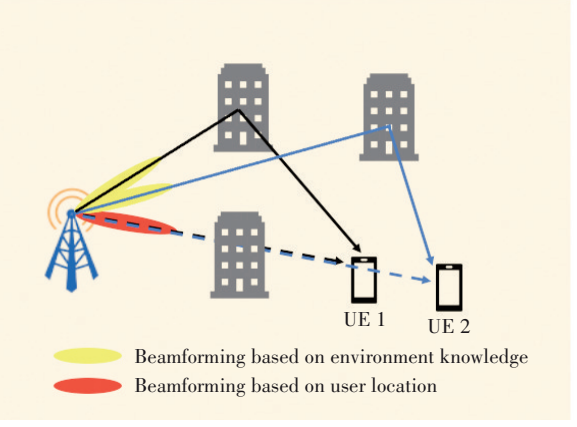

(b)

Figure 1. Illustration of environment knowledge enabled by channel knowledge map[9]: (a) path loss prediction and (b) beamforming

delay, and Doppler shifts), and the complete channel impulse response.

Intuitively, the environmental awareness capability of CKM is derived from the fundamental observation that when a device revisits a previously accessed location, it experiences a wireless propagation environment that is highly similar to the past. By fully utilizing the trajectory information of devices and surrounding environmental data, CKM can significantly reduce channel uncertainty, thereby enabling more accurate channel inference and effective communication strategies.

2.1 Channel Modeling in a Given Region

In a specific geographical area, the wireless propagation channel $z(t)$ is fundamentally a function of the device's position $\boldsymbol{q}(t)$ and the surrounding wireless environment $E(t)$:

$$z(t) = f\left(\boldsymbol{q}(t), E(t)\right) \tag{2},$$

where $E(t)$ represents the propagation environment, which consists of both static and dynamic components. The static environment includes terrain, building structures, and material properties, while the dynamic environment accounts for moving objects such as vehicles and pedestrians. However, due to the complex interactions between electromagnetic waves and the surrounding environment, deriving the function $f(\cdot,\cdot)$ analytically is extremely difficult. Additionally, representing the environment $E(t)$ in a mathematically tractable form is non-trivial due to its high-dimensional and dynamic nature.

To overcome these challenges, CKM leverages historical data to model channel knowledge without requiring an explicit expression of the function $f(\cdot,\cdot)$ or the environmental representation $E(t)$. In a quasi-static environment, where $E(t) \approx E$, the channel can be rewritten as:

$$z(t) = f\left(\boldsymbol{q}(t), E\right) \tag{3}.$$

By collecting a set of historical location data $\{\boldsymbol{q}_1, \boldsymbol{q}_2, \cdots, \boldsymbol{q}_Q\}$ and their corresponding channel knowledge $\{z_1, z_2, \cdots, z_Q\}$, CKM can model the environment as:

$$E = g\left(\boldsymbol{q}_{i=1,\cdots,Q}, z_{i=1,\cdots,Q}\right) \tag{4},$$

which enables the inference of location-specific channel knowledge based on prior measurements.

Fig. 2 illustrates CKM construction for a specific geographic area, using the calculation result of Wireless Insite, a widely used ray tracing simulation software. Fig. 2a shows the root mean square (RMS) delay spread, which reflects how obstacles, for example, buildings, influence multipath propagation. In areas with dense buildings or structures, the signal experiences multiple reflections and scattering, leading to higher delay spread. Conversely, open areas with fewer obstructions result in lower delay spread, indicating less interference and multipath. These variations in delay spread are primarily due to the distribution and density of obstacles, which affect how signals propagate across the area. Fig. 2b presents the received power distribution, demonstrating how environmental factors contribute to signal attenuation. Regions with dense buildings show higher attenuation due to diffraction and reflection, leading to lower received power. On the other hand, open areas with fewer obstacles allow the signal to propagate more freely, resulting in higher received power. Together,

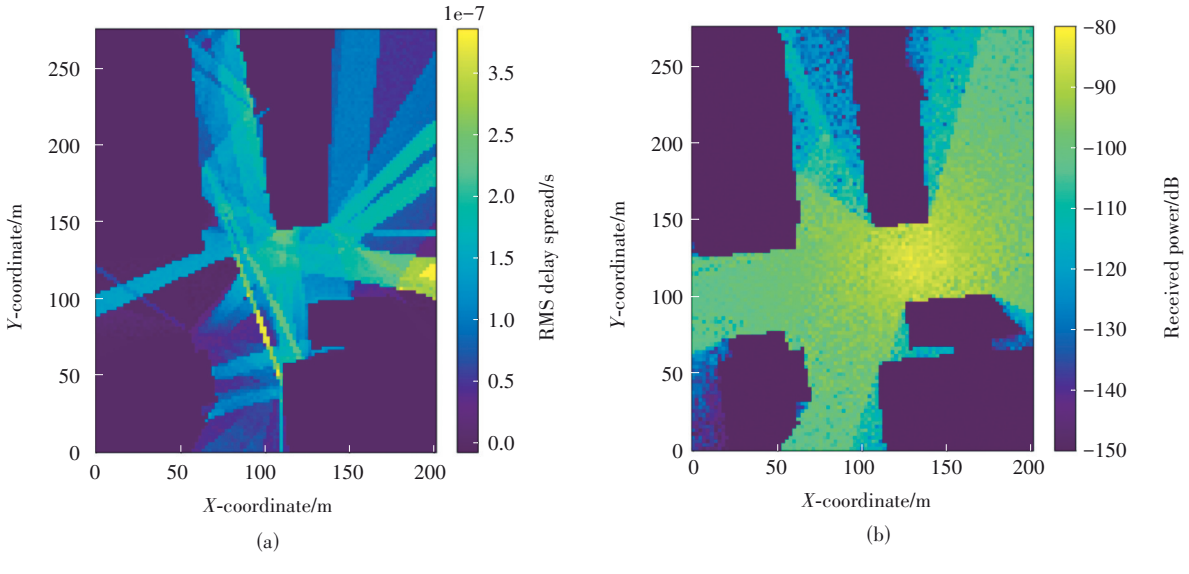

RMS: root mean square

Figure 2. Example of channel knowledge map representation in a given region: (a) RMS delay spread map and (b) received power map

these visualizations highlight how the distribution and arrangement of obstacles significantly affect both the delay spread and received power, illustrating the spatial consistency of wireless channels.

2.2 Advantages and Challenges of CKM over Traditional Communication Methods

Compared with conventional environment-agnostic communications, CKM offers several advantages by providing location-aware channel knowledge. Firstly, by leveraging prestored historical data, CKM significantly reduces the reliance on real-time channel estimation, minimizing training overhead and improving spectral efficiency. Also, by integrating both location and environmental information, CKM improves the accuracy of channel knowledge inference, particularly in complex propagation environments and ultra-dense network deployments. Furthermore, CKM enhances network robustness and adaptability by enabling proactive communication strategies. Traditional wireless systems reacting to real-time channel variations often lead to inefficiencies in mobility management and resource allocation. In contrast, CKM allows networks to anticipate channel conditions based on environmental awareness, facilitating preemptive beam adjustments, intelligent handovers, and optimized power control.

However, it is important to note that the effectiveness of CKM in mobile scenarios depends on its ability to continuously update and adapt to real-time conditions. Although CKM reduces the need for frequent real-time pilot measurements, it still requires periodic updates to maintain its accuracy, especially in highly dynamic environments with rapid device movement. This introduces the challenge of balancing the trade-off between maintaining real-time accuracy and reducing the overhead associated with constant updates. In some cases, the accuracy of CKM may be lower than that of traditional real-time channel estimation, particularly in rapidly changing environments where instantaneous channel state information is crucial. Therefore, while CKM improves efficiency by reducing the reliance on frequent channel estimations, its accuracy may not always surpass that of traditional systems, especially when the propagation environment undergoes significant and rapid changes.

Nevertheless, CKM can outperform traditional real-time channel estimation in scenarios where efficiency and resource optimization are critical, such as in large-scale networks or in environments where real-time measurements are expensive or impractical. Moreover, integrating CKM with real-time data through adaptive learning mechanisms or sensor fusion techniques could enhance its accuracy, allowing it to approach the performance of real-time estimation in dynamic environments.

2.3 Role of CKM in 6G Environment-Aware Communications

In summary, CKM leverages spatial consistency and historical channel knowledge to provide an efficient and scalable solution to 6G wireless communications. Transitioning from environment-agnostic communication to environment-aware communication, CKM represents a paradigm shift in how channel knowledge is acquired and utilized. This novel approach lays the foundation for proactive and predictive communication strategies, ultimately improving the efficiency and robustness of next-generation wireless systems.

3 CKM Construction

3.1 Measurement-Based CKM Construction

Measurement-based methods for CKM construction rely entirely on empirical measurements to estimate channel characteristics across a given region. These methods utilize interpolation and regression techniques to infer the channel parameters at unmeasured locations, assuming spatial correlation in the wireless propagation environment. By avoiding explicit propagation models, these approaches capture real-world channel variations more effectively. For instance, Kriging interpolation has been widely used to create channel maps by incorporating spatial correlations in measurement data[13]. Similarly, k-nearest neighbor (KNN) methods have been applied to estimate channel conditions at unmeasured points based on the nearest available measurements[16].

Relying on real-world data rather than theoretical models, measurement-based CKMs can more accurately reflect actual conditions in a given environment. However, the success of these systems depends on the density and quality of measurement data, as well as the ability to effectively interpolate or extrapolate that data to areas not directly measured. Some studies have demonstrated the effectiveness of these methods in urban and rural environments, but challenges remain in areas with sparse or highly variable data[13].

1) KNN interpolation

KNN interpolation is a simple yet effective approach to estimating unknown channel values in a CKM. Given a target location $\boldsymbol{q}_0$, the estimated channel knowledge $f\left(\boldsymbol{q}_0\right)$ is computed as a weighted average of the k-nearest known measurements z_k: $f\left(\boldsymbol{q}_0\right)=\sum k\in\mathcal{N}\left(\boldsymbol{q}_0\right)w_k z_k$, where $\mathcal{N}\left(\boldsymbol{q}_0\right)$ is the set of k nearest measurements based on the smallest Euclidean distance $\left|\boldsymbol{q}_0-\boldsymbol{q}_i\right|$, and w_k is the weight assigned to each measurement. The weight can be determined using the inverse distance weighting (IDW) rule, where closer measurements contribute more significantly to the estimate. Alternatively, a kernel function can be used to define w_k, such as the Gaussian kernel: $w\left(\boldsymbol{q}_0,\boldsymbol{q}_k\right)=c\cdot\exp\left(-\left|\boldsymbol{q}_0-\boldsymbol{q}_k\right|/\sigma\right)$, or the Laplacian kernel: $w\left(q_0,q_k\right)=c\cdot\exp\left(-\left|q_0-q_k\right|/\sigma\right)$. These kernel functions ensure a smooth interpolation by emphasizing the influence of nearby measurements while reducing the contribution of distant points.

2) Kriging interpolation

Kriging is a geostatistical interpolation method that esti-

mates unknown channel values based on spatially correlated measurements[13, 17], providing an optimal linear unbiased prediction. Unlike simple interpolation techniques, Kriging leverages the spatial structure of the data through the semivariogram, which describes the degree of correlation between two points as a function of their separation distance. Given a set of known measurement locations $\{\boldsymbol{q}_i, z_i\}$, Kriging estimates the channel value at an unknown location $\boldsymbol{q}$ as: $\hat{f}(\boldsymbol{q}) = \sum_{i=1}^{N} \lambda_i z_i + \lambda_0$, where λ_i is the interpolation weights chosen to minimize the mean squared error (MSE), and λ_0 is a bias term to account for the mean of the underlying random process. The weights are computed by solving a linear system derived from the semivariogram function: $\gamma(\boldsymbol{q}_i, \boldsymbol{q}_j) = \frac{1}{2} E\left[\left(z_i - z_j\right)^2\right]$, which captures how the variance of channel measurements evolves with distances. This enables Kriging to make statistically sound predictions with quantified uncertainty.

Kriging is widely applied in CKM construction to develop interference maps[18], which capture spatial variations in interference power. By interpolating interference measurements from multiple devices, these maps support interference-aware resource allocation, allowing networks to optimize transmission parameters and minimize co-channel interference. Similarly, shadowing maps generated via Kriging[19] model large-scale signal fluctuations caused by environmental obstructions. In cognitive radio networks, they help secondary users estimate interference from primary users for efficient spectrum access. In heterogeneous networks, they aid coverage prediction and power control, improving communication reliability. Through these applications, Kriging enhances environment-aware CKM construction, enabling more adaptive and intelligent wireless systems.

3) Matrix completion

Matrix and tensor completion techniques are powerful tools for constructing CKMs when channel measurements are sparse or incomplete[20 - 22]. These methods leverage the low-rank structure of wireless channel data to infer missing values, reducing the need for extensive measurements while maintaining accuracy. In CKM construction, the channel knowledge across a region can be represented as a matrix $\boldsymbol{Z} \in R^{M \times N}$, where missing entries are estimated using matrix completion methods like nuclear norm minimization and alternating least squares. When extended to multi-dimensional data, tensor completion methods (for example, tensor nuclear norm minimization) incorporate additional factors such as frequency and time, enhancing CKM's predictive capabilities. These techniques enable efficient CKM updates, dynamic channel estimation, and resource allocation, making them valuable for real-world wireless systems with limited measurement availability.

4) Other methods

Radial basis function (RBF) interpolation[23] is a widely applied technique that estimates unknown channel values by fitting a smooth function to known measurements, ensuring spatial continuity in CKM. Gaussian process regression models the channel as a Gaussian process with a spatial covariance function[24 - 25], providing both predictions and uncertainty quantification, which makes it particularly useful for adaptive measurement strategies. Thin plate splines interpolation is another effective approach that minimizes bending energy to produce smooth surface reconstructions[26], capturing gradual variations in channel characteristics. These methods enhance the accuracy of CKM, especially in cases where channel measurements are spatially correlated but unevenly distributed.

Fig. 3 compares the performance of several measurement-driven methods for constructing CKMs, using the received power map shown in Fig. 2b as an example, which is generated by Wireless Insite. The comparison is based on the root mean square error (RMSE) between the predicted CKM and the ground truth values. The methods evaluated include the k-nearest neighbor, Kriging, matrix completion using alternating least squares and nuclear norm minimization, radial basis function, thin plate splines, and Gaussian process regression. The x-axis represents the sampling rate, which influences the amount of data used for interpolation, while the y-axis shows the RMSE, indicating prediction accuracy.

KNN and Kriging are intuitive and widely used but may suf-

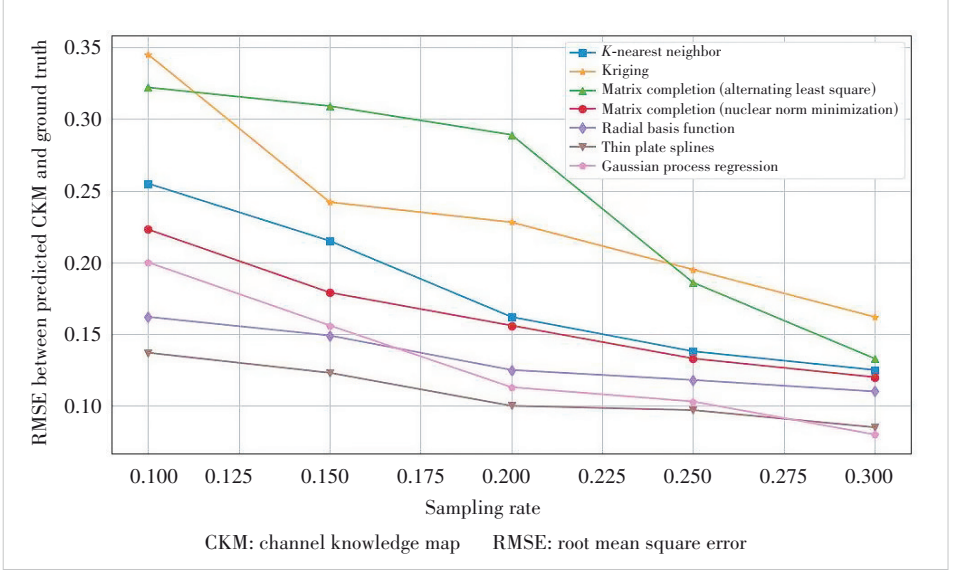

CKM: channel knowledge map RMSE: root mean square error

Figure 3. Comparison of measurement-driven CKM construction methods

fer from limited accuracy when measurement data are sparse or highly variable. Matrix completion methods effectively handle missing data but rely on low-rank assumptions that may not always hold. RBF and thin plate splines offer smooth interpolation, with the latter showing consistently low RMSE across sampling rates in Fig. 3. Gaussian process regression provides accurate predictions with uncertainty estimates but is computationally more demanding. The choice of interpolation and regression methods should consider both accuracy requirements and computational cost in practical CKM applications.

It is important to note that these results are based on a specific example case, and the performance of these methods may vary depending on various factors, such as the type of CKM, the environmental conditions (e.g., the distribution of buildings), and the specific locations of transmitters and receivers. Therefore, the selection of the appropriate method should be carefully considered based on the particular characteristics of the environment and network setup in practice.

3.2 Model-Based CKM Construction

Model-based CKM construction utilizes established propagation models to derive channel characteristics from environmental and systematic parameters. Unlike measurement-driven approaches that require extensive measurements, model-based methods use theoretical formulations to predict channel conditions at different locations. These methods can be broadly categorized into statistical and deterministic channel models, with the latter primarily relying on ray tracing techniques.

1) Statistical model

Statistical channel models describe the wireless channel using probabilistic distributions derived from empirical observations and theoretical analysis. These models capture large-scale and small-scale fading effects, allowing CKM construction based on generalizable statistical properties rather than site-specific measurements.

For large-scale channel variations, path loss models, such as the COST-231 Hata[14] and Okumura models[27], estimate the average signal attenuation as a function of distance, frequency, and environmental factors. These models provide a coarse representation of CKM, making them suitable for initial coverage predictions in urban and suburban environments. Shadowing models, e.g., the log-normal shadowing model[28], account for signal fluctuations due to obstructions, incorporating randomness into path loss predictions.

More advanced models consider the distribution of environmental factors, such as building density, height, and urban layout, to refine path loss predictions. The Walfisch-Bertoni model[29] incorporates diffraction and reflection effects in dense urban environments, adjusting signal attenuation parameters based on the presence of obstacles. Similarly, recent studies have introduced geometry-based stochastic models, which approximate line-of-sight (LoS) and non-line-of-sight (NLoS) probability in urban environments by considering the statistical distribution of buildings and their impact on signal propagation[30]. These models reveal that the density and spatial distribution of buildings significantly impact signal behavior. Another approach extends stochastic probability models to air-to-ground (A2G) communications, analyzing LoS, ground specular, and building-scattering paths based on urban topology[31]. Furthermore, sub-terahertz statistical models have been developed to study spatial channel characteristics in urban microcells, focusing on spatial clustering and power distributions at high frequencies[32].

For small-scale fading, Rayleigh and Rician fading models describe the rapid variations in received signal strength caused by multipath propagation[33–34]. Rayleigh fading is commonly used in rich-scattering environments with no dominant LoS component, while Rician fading accounts for a strong LoS path. These models enable CKM construction that reflects the statistical behavior of fading effects, which is crucial for evaluating signal reliability in dynamic wireless environments.

While statistical models provide a computationally efficient means of CKM construction, they lack site-specific accuracy, as they rely on general assumptions rather than precise environmental information. As a result, they are often complemented by deterministic models that incorporate real-world physical conditions.

2) Deterministic model

Deterministic models predict wireless channel characteristics based on the physics of electromagnetic wave propagation, making them inherently environment-aware. These models incorporate detailed environmental features such as building layouts, vegetation, and material properties to accurately capture wave interactions, including reflection, diffraction, and scattering. Prominent deterministic approaches include ray tracing[15] and finite-difference time-domain (FDTD) simulations[35], both of which approximate solutions to Maxwell's equations. Ray tracing is commonly used due to its high-frequency approximation capabilities, whereas FDTD provides more precise but computationally intensive solutions based on discretized Maxwell's equations[36].

The distribution of buildings within a given environment significantly influences the accuracy of these deterministic models. For instance, ray tracing simulates the paths of electromagnetic waves by modeling interactions with environmental features. The placement, density, and geometry of buildings directly affect the reflection, diffraction, and scattering events considered in ray tracing simulations. Variations in building distribution can lead to significant differences in predicted signal paths, affecting the reliability of communication systems.

By leveraging precise environmental and electromagnetic characteristics, deterministic models offer highly accurate path loss predictions[37–39]. Recent advancements, such as improved geometric and material characterization techniques[40],

have further enhanced model accuracy by reducing discrepancies between simulations and real-world measurements. However, a key challenge of deterministic models is their computational complexity, which makes large-scale, real-time applications difficult.

Several ray-based simulation methods have been developed to improve efficiency, including shooting and bouncing ray (SBR)[41] and vertical-plane-launch (VPL)[42]. Additionally, advanced techniques like intelligent ray tracing (IRT)[43] provide further acceleration, making deterministic modeling more feasible for CKM construction. Despite their computational demands, these models remain crucial for site-specific, high-accuracy channel prediction in next-generation wireless networks.

3.3 Measurement-Model Hybrid CKM Construction

Hybrid CKM construction methods integrate measurement-driven techniques and theoretical propagation models to improve accuracy and efficiency. These approaches leverage the strengths of both paradigms. Measurement-driven methods utilize machine learning to extract patterns from measurements, while model-based methods incorporate physical constraints to ensure consistency with wireless propagation principles. Recent research in this field has focused on two primary strategies for hybrid CKM construction.

1) Computer vision approach

One major trend in hybrid CKM construction is leveraging computer-vision-based deep neural networks to process environmental and sparse measurement data as multi-channel inputs, treating CKM construction as an image-to-image translation task. This approach enables the extraction of spatial features from diverse data sources, including transmitter-receiver locations, building distributions, and limited channel measurements.

Computer-vision-based approach integrates 3D building maps, environmental features, and sparse channel measurements as multi-channel inputs into neural networks, allowing models to infer missing channel information and construct accurate CKMs. A widely used framework is RadioUNet[44], which extends the U-Net architecture by incorporating measurement-assisted inputs alongside environmental maps, improving prediction accuracy. Similarly, models such as EME-Net[45] and ACT-GAN[46] refine CKM predictions by leveraging deep neural networks trained on transmitter positions and building layouts. These architectures enhance generalization by learning structural patterns in radio maps while adapting to different urban environments. Subregional learning techniques[47] offer additional benefits by segmenting the channel gain map into subregions and applying specialized models to each, which is particularly effective in complex environments where traditional models struggle. These techniques allow for more accurate predictions by addressing regional propagation characteristics more effectively.

GAN-based models, such as SS-GAN[48] and RME-GAN[49], have also demonstrated significant improvement in CKM construction by generating realistic channel maps from incomplete data. For instance, the two-stage framework[50] first uses a radio map prediction GAN (RMP-GAN) to generate coarse radio maps based on environmental data, which are then refined with sparse measurement data through a correction GAN (RMC-GAN). This approach is highly relevant for CKM construction as it corrects predictions based on real-time measurements, reducing inaccuracies typically found in traditional models. These adversarial learning techniques effectively enhance CKM accuracy, even in scenarios where building information is incomplete or transmitter locations are unknown.

Additionally, hybrid architectures incorporating variance prediction and uncertainty modeling have gained traction. A notable example is the dual-UNet framework[51], where two separate but identical U-Net models are trained in parallel: one to estimate received signal strength (RSS) values and the other to predict variance maps that quantify uncertainty. This design allows CKM construction to incorporate confidence levels in its predictions, making it more robust to missing or inaccurate input data. Studies on Gaussian-based modeling[52–53] further highlight the importance of integrating statistical uncertainty into deep learning-based CKMs, particularly for urban and indoor wireless environments.

Overall, computer vision-driven CKM construction methods shown in Table 1 provide flexible, data-efficient alternatives to conventional interpolation and model-based techniques. By integrating spatial, spectral, and temporal information, these architectures enable highly accurate, scalable, and real-time CKM generation, paving the way for intelligent wireless network optimization.

2) Calibrated ray tracing

Calibration using real-world measurements has become a key research focus to improve ray tracing performance, since the precise environmental parameters, such as material permittivity, reflection coefficients, and scattering effects, are difficult to obtain. Several techniques have been developed to refine material properties, incorporate diffuse scattering effects, and adjust propagation parameters based on empirical data.

One common calibration strategy is tuning material properties using real-world measurements. In Ref. [54], the relative permittivity of materials in urban microcell (UMi) environments at 28 GHz was fine-tuned, reducing errors in path loss estimation. Similarly, a linear interpolation approach was used in Ref. [55] to estimate the dielectric constant of concrete at 28 GHz based on measured values at 5.2 GHz and 60 GHz, ensuring more accurate reflection loss modeling. Additionally, empirical ray tracing models have been validated against 73 GHz street canyon measurements, refining reflection loss calculations based on the incident angle[56].

Another key challenge in ray tracing is capturing diffuse scattering effects, which become significant at mmWave and THz frequencies. Calibration against 28 GHz urban directional chan-

Table 1. Overview of computer vision based CKM construction models

Model Name	CKM Type	Key Approach	Main Features
RadioUNet[44]	CGM	U-Net (CNN-based)	• Uses city map and transmitter location as input to estimate radio maps • Incorporates physical simulation data for training • Utilizes transfer learning to adapt simulated data to real-life scenarios
EME-Net[45]	Indoor RF-EMF exposure Map	U-Net (CNN-based)	• Four input channels (red, green, blue, alpha) representing received power intensity • Trained on Wi-Fi access points in realistic indoor environments
ACT-GAN[46]	CGM	GAN (with ACT block, CBA module and T-Conv block)	• Three input channels representing 3D building maps, transmitter locations, and environmental features • Trained on sparse channel measurements and environmental data from urban areas • Robust performance in scenarios with sparse discrete observations and unknown emission sources
Subregional learning-based CGM[47]	CGM	MCNN-1D	• Divides the map into subregions using a measurement -driven clustering approach • Input channels: spatial coordinates of BS and sample points, and channel gain • Trained on simulated channel data from a target area
SS-GAN[48]	RF coverage and interference map	GAN	• Two input channels: RF coverage data and geographic data (elevation and building height) • Trained on 4G LTE real-world data • Uses sparsely self-supervised learning for weak supervision
RME-GAN[49]	CGM	cGAN	• Two-phase framework: Phase 1 integrates radio propagation models, Phase 2 captures local shadowing effects • Trained on sparse RF measurements from 700 radio maps, including data from various urban regions like Ankara, Berlin, and Tel Aviv • Inputs: sparse observations, transmitter locations, and urban maps
FPTC-GANs[50]	CGM	RMP-GAN, RMC-GAN	• Training data comes from real-world measurements and environmental information (e.g., transmitter positions, obstacle heights, etc.) • Inputs: transmitter positions, obstacle top views, and empirical radio map • First-predict-then-correct approach (RMP-GAN for initial prediction, RMC-GAN for correction)
GAN-CRME[51]	CGM	cGAN	• Inputs: distributed RSS samples and geographical map • Trained on a dataset with RSS samples and geographical map information
SSSP[52]	CGM	U-Net	• Inputs: signal strength measurements, 3D map of the environment (urban) • Training data: signal strength data generated using wireless InSite ray-tracing software from simulated environments (45 urban environments) • The model does not require transmitter location or statistical channel models
REM-U-Net[53]	CGM	U-Net	• Inputs: building height maps, building layout maps, and LoS maps • Trained on the RadioMap3DSeer dataset with simulated data from 701 city maps • Uses LoS maps as additional input to improve prediction accuracy

ACT: aggregated contextual transformation
CBA: convolutional block attention
cGAN: conditional generative adversarial network
CGM: channel gain map
CKM: channel knowledge map
CNN: convolutional neural network
CRME: cooperative radio map estimation
EMF: electromagnetic field
FPTC: first-predict-then-correct
GAN: generative adversarial network
LoS: line-of-sight
MCNN: modular convolutional neural network
REM: radio environment map
RMC: measurement data correction
RME: radio map estimation
RMP: radio map prediction
SSSP: spatial signal strength prediction

nel measurements in Ref. [57] involved adjusting scattering coefficients and incorporating an angular spread correction factor, improving received power predictions. At THz frequencies, extensive indoor ultra-broadband measurements were conducted in Ref. [58], leading to the development of a frequency-dependent scattering model that reduced errors in delay spread estimation. In an office setting at 60 GHz, multipath component gains were analyzed and adjusted to improve model reliability[59]. The NYURay ray tracing calibration method simplified the process by assuming angle-independent reflection, enabling a closed-form least squares optimization to align simulated multipath power with real-world measurements[60]. Instead of iterative tuning, the method directly optimizes reflection and penetration losses on a logarithmic scale, improving efficiency while maintaining accuracy.

In recent years, research has investigated the integration of neural networks with traditional ray tracing frameworks. In Ref. [61], the authors applied neural networks to the interaction calculation module, utilizing neural networks to predict the output direction and losses of each interaction. The architecture consists of two main components: the Spatial Network and the Material Network. The Spatial Network processes the spatial characteristics of the ray's path, while the Material Network accounts for the material properties influencing the ray's behavior. However, this framework does not consider high frequency in future communication applications, which

limits its effectiveness within certain application ranges. Apart from this, Ref. [62] proposed a learnable wireless digital twin, which, similar to ray tracing frameworks, integrates neural networks. This framework uses a single entity representing each object within the environment, constructing a neural network to encode its electromagnetic property one by one, which results in improved accuracy for channel modeling. However, the design of neural networks in large-scale systems also increases complexity and the requirement for computational resources.

3.4 Summary of Advantages and Disadvantages of CKM Construction Methods

The various CKM construction methods each have their unique advantages and limitations. Measurement-based methods, such as KNN and Kriging, are highly effective when sufficient real-world measurement data are available, providing high-level accuracy. However, their performance heavily relies on the density and quality of the data. In cases where data are sparse or irregular, their effectiveness can be reduced. Model-based methods, including statistical models and ray tracing, are useful when measurement data are limited, as they rely on theoretical models. While they can be efficient, their accuracy may be lower in complex or rapidly changing environments, and may fail to capture fine-grained variations.

Hybrid methods that combine measurement-driven approaches with theoretical models strike a balance between accuracy and efficiency. These methods can offer improved performance in dynamic environments by leveraging both empirical data and physical models, but they are computationally more demanding. The choice of method largely depends on available data, computational resources, and the complexity of the environment, with measurement-based methods often being preferred for high-accuracy scenarios and model-based methods being more suited for situations with limited measurements.

4 Applications of CKM

4.1 Integrated Sensing and Communication

CKM plays a critical role in integrated sensing and communication (ISAC) systems, where it bridges the gap between sensing and communication systems. By providing detailed, location-specific channel information, CKM not only enhances localization but also improves communication performance in dynamic environments. Unlike traditional methods that rely solely on measurements like RSS, CKM offers additional features such as time of arrival (ToA) and AoA, which are crucial for localization and beamforming optimization[63 – 64]. In terms of communication, CKM helps in adjusting the communication links between BSs and mobile users by integrating sensing data, like dynamic environmental changes, into the channel model[65]. This integration allows for more efficient resource allocation, interference management, and adaptive beamforming. For example, in unmanned aerial vehicle (UAV) systems, CKM can simultaneously support both the localization of UAVs and the optimization of their communication links with ground stations by using real-time channel state information[66]. Additionally, CKM allows for dynamic sensing of moving objects, such as vehicles and pedestrians, and enables real-time updates of the communication network based on the sensed data, optimizing the overall system performance[67].

Fig. 4 illustrates the application of CGMs in ISAC systems, specifically within the fingerprint localization algorithm. In this approach, the user's signal characteristics are collected and matched against multiple CGMs stored in a Finger Database. The algorithm processes this data to estimate the user's location based on the similarity of the measured signal to the stored CGMs. This example highlights how CKMs, including various types beyond CGMs, can enhance both the sensing and communication capabilities in ISAC systems, offering a more accurate and efficient means for location tracking in complex environments.

4.2 UAV Trajectory Optimization

CKM plays a critical role in enhancing UAV trajectory optimization in 6G networks, both for cellular-connected UAVs and UAV-assisted communication systems. By utilizing rich, location-specific channel data, CKM helps construct real-time signal-to-interference plus noise ratio (SINR) maps that account for both channel gain and interference. In the cellular-connected UAV scenario, CKM aids in constructing SINR

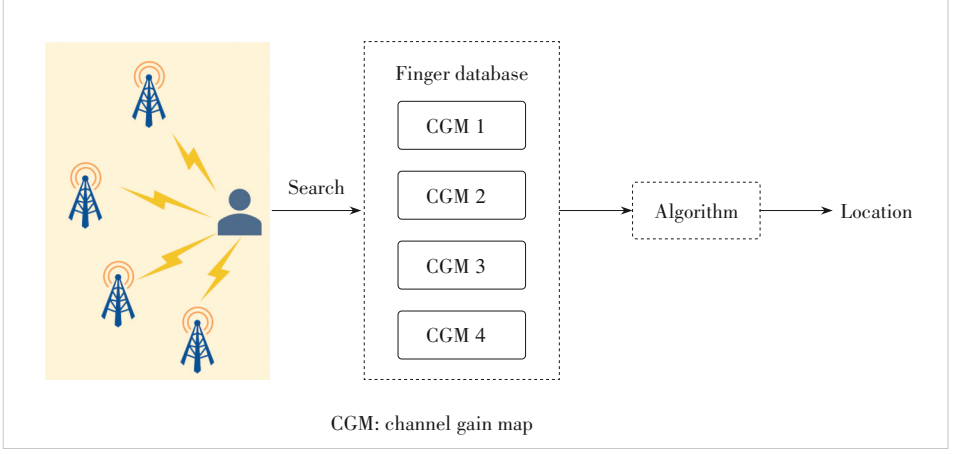

Figure 4. Fingerprint localization using CGM in integrated sensing and communication systems

maps based on channel gain and interference, allowing for the design of flight paths that minimize outage probability and mission latency while ensuring continuous communication with ground BSs. Unlike traditional methods based on deterministic LoS or stochastic channel models, which fail to account for LoS blockages, CKM enables the UAV to navigate areas with high interference or blockages while maintaining a reliable SINR throughout the path[68]. In UAV-assisted systems, where a UAV serves multiple users, CKM helps optimize the trajectory by identifying paths with strong A2G channels, thus enhancing overall system performance. This method ensures better coverage for all users, compared with conventional designs that focus on a single user's location. Additionally, combining reinforcement learning with CKM allows the UAV to dynamically adjust its trajectory based on real-time user distribution and channel quality data, improving communication efficiency across the system[69–70].

4.3 Hybrid Beamforming

CKM significantly enhances hybrid beamforming for mmWave massive multiple-input multiple-output (MIMO) systems, offering a more efficient approach to reducing the complexity and overhead typically associated with traditional training-based channel estimation[71–72]. In these systems, hybrid analog-digital beamforming uses a combination of analog and digital beamforming techniques at both the transmitter and receiver to manage multiple data streams effectively. Traditional beamforming approaches often rely on extensive channel state information and require significant training to estimate the full MIMO channel matrix, which becomes more challenging as the number of antennas increases. With the integration of CKM, such as the channel angle map (CAM) and beamforming indicator map (BIM), the need for extensive training is minimized, as the system can use location-specific channel information, including AoA, AoD, and path loss, that is directly derived from the environment. This enables training-free or light-training beamforming, where the accuracy of these designs depends on the precision of user location and environmental factors like scatterer movement. While limited training may still be beneficial to refine the system, CKM improves beamforming efficiency, particularly in dynamic environments with multiple users or interference, optimizing data throughput and SINR over large antenna arrays.

4.4 BS Placement

In BS deployment, CKM applications assist in optimizing BS placement strategies to enhance network coverage and performance. By constructing detailed CKMs, one can accurately assess signal strength, interference levels, and coverage areas at various locations, thereby determining optimal BS positions and configurations. For instance, in low-altitude environments, methods for deploying multiple aerial BS utilize binary CKMs to optimize BS layouts to meet the communication needs of different areas[73]. Additionally, principles for deploying ultra-wideband (UWB) indoor positioning system BS emphasize the importance of CKMs. By analyzing indoor channel characteristics, reasonable BS placement can improve positioning accuracy and system performance[74]. In summary, CKM applications in BS deployment support more intelligent BS placement decisions by providing precise channel information, enhancing network coverage and service quality.

4.5 Resource Allocation

In 6G networks, particularly for ultra-reliable low-latency communication (URLLC) in mission-critical Internet of Things (IoT) systems, CKMs can be used to optimize resource allocation by adapting transmission control policies. These policies aim to meet the stringent quality of service (QoS) requirements of URLLC while minimizing the transmit power. By utilizing CKMs, which provide channel gain statistics for various locations within a target area, transmission control can be optimized without the need for real-time, costly channel state information. A notable approach, including power scaling based on CKM data, was proposed[75], where location-specific transmission parameters are adjusted to maintain a target delay violation probability across all devices. This method ensures that devices in varying conditions can still operate within the desired reliability and latency constraints. Additionally, meta-reinforcement learning techniques have been employed to further enhance adaptability, enabling rapid policy adjustment across different environments with minimal retraining. This combination of CKM-driven power scaling and meta-learning offers a scalable solution to resource allocation in URLLC systems.

5 Open Problems and Future Directions

5.1 Localization Accuracy and Robustness of CKM

One major challenge for CKM-based systems is the dependence on high-precision localization data. Since CKMs rely on accurate location information to construct location-specific channel knowledge, errors in localization can directly affect the performance and robustness of the system. Inaccurate positioning data, such as from the Global Positioning System (GPS) or environmental obstructions, can distort the generated channel map, leading to suboptimal outcomes in applications like localization, beamforming, and interference management. To address this issue, future research must focus on maintaining CKM robustness in the presence of localization inaccuracies. This may involve using machine learning techniques to compensate for errors or applying sensor fusion methods to combine various positioning sources. Additionally, techniques such as spatial smoothing or interpolation can help mitigate the impact of small localization errors, ensuring CKM construction remains reliable even with less precise location data.

5.2 Incorporating Material Properties for Enhanced CKM Accuracy

Another significant challenge for CKM-based systems is efficiently incorporating detailed environmental information, particularly the impact of various material properties on CKM. While most existing methods primarily rely on geometric information, such as building shapes or the layout of obstacles, they often overlook how the materials of these objects (e.g., walls, windows, or furniture) affect the propagation of radio waves. Different materials, with varying electromagnetic properties, can significantly influence path loss, reflection, and scattering, which in turn affect the accuracy of the CKM. To address this, future research should focus on integrating material-specific data with CKM construction. This may involve leveraging detailed environmental sensing, such as materials' electromagnetic characteristics, or using machine learning to predict the impact of materials on the channel. Combining geometric and material information will improve the fidelity of CKMs, making them more reflective of real-world conditions and enhancing applications such as beamforming and localization in complex environments.

5.3 Improving Generalization with Efficient Neural Network Architectures for CKM Construction

A third key challenge is enhancing the generalization ability of CKM construction, particularly when using neural network-based methods. Currently, most neural network models require training on a large variety of scenarios to achieve robust performance. However, this process can be time-consuming and computationally expensive. The ability to design more efficient neural network architectures that can be trained on fewer scenarios while maintaining strong performance across a wide range of environments is crucial. To tackle this, future research should focus on developing models that require minimal training data, perhaps by using transfer learning, domain adaptation, or few-shot learning techniques. These approaches may enable neural networks to generalize better and perform well across different deployment scenarios, making CKM-based systems more scalable and effective for real-world applications, even with limited training data.

5.4 Continuous CKM Updates with Real-Time Data

A crucial challenge for CKM-based systems is how to continuously update the CKM with new data, ensuring its accuracy and relevance over time. In dynamic environments, the wireless channel is constantly changing due to factors like mobility, environmental alterations, and user behavior. To maintain an up-to-date CKM, it is essential to integrate new measurements and real-time data effectively. This could be achieved through techniques such as incremental learning and online learning, where the CKM model is continuously updated as new data are acquired, without the need to retrain from scratch. Additionally, sensor fusion methods can be employed to combine data from different sources, such as measurement devices, UAVs, and sensors for IoT, providing a more comprehensive and accurate representation of the environment. By incorporating these approaches, CKM systems can adapt in real time to changing conditions, ensuring that they remain accurate and reliable for various applications.

5.5 CKM in 6G for Robotics

In the future, the application of CKMs in robotics will play a crucial role in advancing 6G technologies. As robotics continues to evolve, key aspects such as accurate channel modeling, enhanced localization accuracy, and efficient sensing capabilities will become increasingly important. CKMs can significantly contribute to these areas by providing detailed, environment-aware channel information, enabling robots to navigate and interact more effectively in dynamic environments[76]. Through the integration of CKMs with 6G networks, robots can benefit from more reliable localization and real-time sensing, improving their ability to adapt to changing conditions and interact with both humans and other devices seamlessly. Efficient use of the communication channel will also be vital for optimizing robot performance, ensuring low latency and high throughput for tasks such as autonomous control, monitoring, and remote operation.

6 Conclusions

This paper has provided an in-depth overview of CKMs and their transformative role in 6G wireless networks. CKMs represent a paradigm shift from environment-agnostic communication to environment-aware communication, allowing for more efficient channel estimation and resource allocation. Through various CKM construction methods from measurement-based and model-based techniques to hybrid approaches, researchers have demonstrated the potential to improve channel knowledge accuracy, particularly in complex environments. The applications of CKMs, including ISAC systems, beamforming, UAV trajectory optimization, BS placement and resource allocation, highlight their broad influence on network performance and optimization.

As 6G technologies evolve, the integration of CKMs with advanced systems such as reconfigurable intelligent surfaces (RIS), mmWave communications, and machine learning-based adaptive resource management holds great promise. Combining CKMs with these technologies can dynamically optimize the communication environment, improve coverage in challenging areas, and enable real-time adaptation to network changes, further enhancing system efficiency and reliability. However, despite their promising applications, several challenges remain in the development and deployment of CKM systems. Future research should focus on improving CKM robustness in scenarios with imprecise localization data, better integrating material-specific environmental information and enhancing the generalization capabilities of neural network

models. Moreover, continuously updating CKMs with real-time data will be crucial for maintaining their relevance and accuracy in dynamic environments.

References

[1] JIANG W, HAN B, HABIBI M A, et al. The road towards 6G: a comprehensive survey [J]. IEEE open journal of the communications society, 2021, 2: 334 – 366
[2] WANG C X, YOU X H, GAO X Q, et al. On the road to 6G: visions, requirements, key technologies, and testbeds [J]. IEEE communications surveys & tutorials, 2023, 25(2): 905 – 974. DOI: 10.1109/COMST.2023.3249835
[3] SINGH R, KAUSHIK A, SHIN W, et al. Towards 6G evolution: three enhancements, three innovations, and three major challenges [EB/OL]. (2024-02-16) [2025-03-25]. https://arxiv.org/abs/2402.10781v1
[4] ALSABAH M, NASER M A, MAHMMOD B M, et al. 6G wireless communications networks: a comprehensive survey [J]. IEEE access, 2021, 9: 148191 – 148243
[5] WANG Z, ZHANG J Y, DU H Y, et al. A tutorial on extremely large-scale MIMO for 6G: fundamentals, signal processing, and applications [J]. IEEE communications surveys & tutorials, 2024, 26(3): 1560 – 1605. DOI: 10.1109/COMST.2023.3349276
[6] WANG J, WANG C X, HUANG J, et al. 6G THz propagation channel characteristics and modeling: recent developments and future challenges [J]. IEEE communications magazine, 2024, 62(2): 56 – 62. DOI: 10.1109/MCOM.001.2200403
[7] SERGHIOU D, KHALILY M, BROWN T W C, et al. Terahertz channel propagation phenomena, measurement techniques and modeling for 6G wireless communication applications: a survey, open challenges and future research directions [J]. IEEE communications surveys & tutorials, 2022, 24 (4): 1957 – 1996
[8] MAHMOOD M R, MATIN M A, SARIGIANNIDIS P, et al. A comprehensive review on artificial intelligence/machine learning algorithms for empowering the future IoT toward 6G era [J]. IEEE access, 2022, 10: 87535 – 87562
[9] ZENG Y, XU X. Toward environment-aware 6G communications via channel knowledge map [J]. IEEE wireless communications, 2021, 28(3): 84 – 91. DOI: 10.1109/MWC.001.2000327
[10] GIORDANI M, POLESE M, ROY A, et al. A tutorial on beam management for 3GPP NR at mmWave frequencies [J]. IEEE communications surveys and tutorials, 2019, 21(1): 173 – 196. DOI: 10.1109/COMST.2018.2869411
[11] ALKHATEEB A, EL AYACH O, LEUS G, et al. Channel estimation and hybrid precoding for millimeter wave cellular systems [J]. IEEE journal of selected topics in signal processing, 2014, 8(5): 831 – 846. DOI: 10.1109/JSTSP.2014.2334278
[12] NI K S, NGUYEN T Q. An adaptable *k*-nearest neighbors algorithm for MMSE image interpolation [J]. IEEE transactions on image processing, 2009, 18(9): 1976 – 1987. DOI: 10.1109/TIP.2009.2023706
[13] DALL'ANESE E, KIM S J, GIANNAKIS G B. Channel gain map tracking via distributed Kriging [J]. IEEE transactions on vehicular technology, 2011, 60(3): 1205 – 1211
[14] AKHPASHEV R V, ANDREEV A V. COST 231 Hata adaptation model for urban conditions in LTE networks [C]//The 17th International Conference of Young Specialists on Micro/Nanotechnologies and Electron Devices (EDM). IEEE, 2016: 64 – 66. DOI: 10.1109/EDM.2016.7538693
[15] YUN Z Q, ISKANDER M F. Ray tracing for radio propagation modeling: principles and applications [J]. IEEE access, 2015, 3: 1089 – 1100
[16] XU Z D, HUANG B Q, JIA B. An efficient radio map learning scheme based on kernel density function [J]. IEEE transactions on vehicular technology, 2021, 70(12): 13315 – 13324. DOI: 10.1109/TVT.2021.3121470
[17] KIM S J, DALL'ANESE E, GIANNAKIS G B. Cooperative spectrum sensing for cognitive radios using Kriged Kalman filtering [J]. IEEE journal of selected topics in signal processing, 2011, 5(1): 24 – 36. DOI: 10.1109/JSTSP.2010.2053016
[18] GUTIERREZ-ESTEVEZ D M, AKYILDIZ I F, FADEL E A. Spatial coverage cross-tier correlation analysis for heterogeneous cellular networks [J]. IEEE transactions on vehicular technology, 2014, 63(8): 3917 – 3926. DOI: 10.1109/TVT.2014.2306260
[19] JAYAWICKRAMA B A, DUTKIEWICZ E, FANG G, et al. Downlink power allocation algorithm for licence-exempt LTE systems using Kriging and compressive sensing based spectrum cartography [C]//Global Communications Conference (GLOBECOM). IEEE, 2013: 3766 – 3771. DOI: 10.1109/GLOCOM.2013.6831659
[20] SUN H, CHEN J T. Propagation map reconstruction via interpolation assisted matrix completion [J]. IEEE transactions on signal processing, 2022, 70: 6154 – 6169. DOI: 10.1109/TSP.2022.3230332
[21] ZHANG G Y, FU X, WANG J, et al. Spectrum cartography via coupled block-term tensor decomposition [J]. IEEE transactions on signal processing, 2020, 68: 3660 – 3675. DOI: 10.1109/TSP.2020.2993530
[22] SUN H, CHEN J T. Grid optimization for matrix-based source localization under inhomogeneous sensor topology [C]//IEEE International Conference on Acoustics, Speech and Signal Processing (ICASSP). IEEE, 2021: 5110 – 5114. DOI: 10.1109/ICASSP39728.2021.9414100
[23] MAJDISOVA Z, SKALA V. Radial basis function approximations: comparison and applications [J]. Applied mathematical modelling, 2017, 51: 728 – 743. DOI: 10.1016/j.apm.2017.07.033
[24] JANG K J, PARK S, KIM J, et al. Path loss model based on machine learning using multi-dimensional Gaussian process regression [J]. IEEE access, 2022, 10: 115061 – 115073
[25] WANG X Y, WANG X Y, MAO S W, et al. DeepMap: deep Gaussian process for indoor radio map construction and location estimation [C]//Global Communications Conference (GLOBECOM). IEEE, 2018: 1 – 7. DOI: 10.1109/GLOCOM.2018.8647266
[26] KELLER W, BORKOWSKI A. Thin plate spline interpolation [J]. Journal of geodesy, 2019, 93(9): 1251 – 1269. DOI: 10.1007/s00190-019-01240-2
[27] SHAKIR Z, AL-THAEDAN A, ALSABAH R, et al. Performance evaluation for RF propagation models based on data measurement for LTE networks [J]. International journal of information technology, 2022, 14(5): 2423 – 2428. DOI: 10.1007/s41870-022-01006-8
[28] BLASZCZYSZYN B, KARRAY M K. Quality of service in wireless cellular networks subject to log-normal shadowing [J]. IEEE transactions on communications, 2013, 61(2): 781 – 791. DOI: 10.1109/TCOMM.2012.120512.110673
[29] YAMADA W, SASAKI M, KITA N. Extended Walfisch-Bertoni propagation model to cover short range and millimeter-wave bands [J]. Radio science, 2021, 56(3): e2020RS007161. DOI: 10.1029/2020RS007161
[30] KIM K W, KWON H, PARK S. Line-of-sight probability in urban environments representing deterministic grids [J]. IEEE transactions on antennas and propagation, 2025, 73(3): 1792 – 1804. DOI: 10.1109/TAP.2024.3513540
[31] SABOOR A, CUI Z Z, VINOGRADOV E, et al. Air-to-ground channel model for pedestrian and vehicle users in general urban environments [J]. IEEE antennas and wireless propagation letters, 2025, 24(1): 227 – 231. DOI: 10.1109/LAWP.2024.3492507
[32] JU S H, RAPPAPORT T S. Sub-terahertz spatial statistical MIMO channel model for urban microcells at 142 GHz [C]//Global Communications Conference (GLOBECOM). IEEE, 2021: 1 – 6. DOI: 10.1109/GLOBECOM46510.2021.9685929
[33] ZHENG Y R, XIAO C S. Simulation models with correct statistical properties for Rayleigh fading channels [J]. IEEE transactions on communications, 2003, 51(6): 920 – 928. DOI: 10.1109/TCOMM.2003.813259
[34] PATZOLD M, KILLAT U, LAUE F, et al. On the statistical properties of deterministic simulation models for mobile fading channels [J]. IEEE

transactions on vehicular technology, 1998, 47(1): 254 – 269. DOI: 10.1109/25.661052
[35] HAGNESS S C, TAFLOVE A, GEDNEY S D. Finite-difference time-domain methods [M]//Numerical methods in electromagnetics. Amsterdam: Elsevier, 2005: 199 – 315. DOI: 10.1016/s1570-8659(04)13003-2
[36] SARKAR T K, JI Z, KIM K, et al. A survey of various propagation models for mobile communication [J]. IEEE antennas and propagation magazine, 2003, 45(3): 51 – 82. DOI: 10.1109/MAP.2003.1232163
[37] ZHANG X, SHU X J, ZHANG B W, et al. Cellular network radio propagation modeling with deep convolutional neural networks [C]//The 26th ACM SIGKDD International Conference on Knowledge Discovery & Data Mining. ACM, 2020: 2378-2386. DOI: 10.1145/3394486.3403287
[38] SARKAR S, MANSHAEI M H, KRUNZ M. RADIANCE: radio-frequency adversarial deep-learning inference for automated network coverage estimation [C]//IEEE Global Communications Conference. IEEE, 2023: 832 – 837. DOI: 10.1109/GLOBECOM54140.2023.10437767
[39] JAENSCH F, CAIRE G, DEMIR B, et al. Radio map estimation: an open dataset with directive transmitter antennas and initial experiments [EB/OL]. (2024-01-12) [2025-03-25]. https://arxiv.org/abs/2402.00878v1
[40] ZHANG F B, ZHOU C, BRENNAN C, et al. A radio wave propagation modeling method based on high-precision 3-D mapping in urban scenarios [J]. IEEE transactions on antennas and propagation, 2024, 72(3): 2712 – 2722. DOI: 10.1109/TAP.2024.3355502
[41] LING H, CHOU R C, LEE S W. Shooting and bouncing rays: calculating the RCS of an arbitrarily shaped cavity [J]. IEEE transactions on antennas and propagation, 1989, 37(2): 194 – 205. DOI: 10.1109/8.18706
[42] LIANG G, BERTONI H L. A new approach to 3-D ray tracing for propagation prediction in cities [J]. IEEE transactions on antennas and propagation, 1998, 46(6): 853 – 863. DOI: 10.1109/8.686774
[43] HOPPE R, WÖLFLE G, LANDSTORFER F. Fast 3D ray tracing for the planning of microcells by intelligent preprocessing of the database [C]// The 3rd European Personal and Mobile Communications Conference (EPMCC), 1999
[44] LEVIE R, YAPAR Ç, KUTYNIOK G, et al. RadioUNet: fast radio map estimation with convolutional neural networks [J]. IEEE transactions on wireless communications, 2021, 20(6): 4001 – 4015. DOI: 10.1109/TWC.2021.3054977
[45] MALLIK M, KHARBECH S, MAZLOUM T, et al. EME-net: a U-net-based indoor EMF exposure map reconstruction method [C]//The 16th European Conference on Antennas and Propagation (EuCAP). IEEE, 2022: 1 – 5
[46] CHEN Q, YANG J J, HUANG M, et al. ACT-GAN: radio map construction based on generative adversarial networks with ACT blocks [J]. IET communications, 2024, 18(19): 1541 – 1550. DOI: 10.1049/cmu2.12846
[47] CHEN J Y, GAO R F, WANG J, et al. Channel gain map construction based on subregional learning and prediction [J]. IEEE transactions on vehicular technology, 2025, (99): 1 – 6. DOI: 10.1109/TVT.2025.3542581
[48] LI Z, CAO J N, WANG H W, et al. Sparsely self-supervised generative adversarial nets for radio frequency estimation [J]. IEEE journal on selected areas in communications, 2019, 37(11): 2428 – 2442. DOI: 10.1109/JSAC.2019.2933779
[49] ZHANG S Y, WIJESINGHE A, DING Z. RME-GAN: a learning framework for radio map estimation based on conditional generative adversarial network [J]. IEEE Internet of Things journal, 2023, 10(20): 18016 – 18027. DOI: 10.1109/JIOT.2023.3278235
[50] WANG Y F, SUN S, LIU N, et al. Two-stage radio map construction with real environments and sparse measurements [J]. IEEE wireless communications letters, 2025, 14(4): 969 – 973. DOI: 10.1109/LWC.2025.3528512
[51] ZHANG Z Z, ZHU G X, CHEN J T, et al. Fast and accurate cooperative radio map estimation enabled by GAN [EB/OL]. [2025-03-25]. https://arxiv.org/abs/2402.02729v1
[52] KRIJESTORAC E, HANNA S, CABRIC D. Spatial signal strength prediction using 3D maps and deep learning [C]//International Conference on Communications. IEEE, 2021: 1 – 6. DOI: 10.1109/ICC42927.2021.9500970
[53] SALLOUHA H, SARKAR S, KRIJESTORAC E, et al. REM-U-Net: deep learning based agile REM prediction with energy-efficient cell-free use case [J]. IEEE open journal of signal processing, 2024, 5: 750 – 765
[54] LEE J H, CHOI J S, KIM S C. Cell coverage analysis of 28 GHz millimeter wave in urban microcell environment using 3-D ray tracing [J]. IEEE transactions on antennas and propagation, 2018, 66(3): 1479 – 1487. DOI: 10.1109/TAP.2018.2797531
[55] HUR S, BAEK S, KIM B, et al. Proposal on millimeter-wave channel modeling for 5G cellular system [J]. IEEE journal of selected topics in signal processing, 2016, 10(3): 454 – 469. DOI: 10.1109/JSTSP.2016.2527364
[56] NGUYEN H C, MACCARTNEY G R, THOMAS T, et al. Evaluation of empirical ray-tracing model for an urban outdoor scenario at 73 GHz E-band [C]//The 80th Vehicular Technology Conference (VTC2014-Fall). IEEE, 2014: 1 – 6. DOI: 10.1109/VTCFall.2014.6965971
[57] CHARBONNIER R, LAI C, TENOUX T, et al. Calibration of ray-tracing with diffuse scattering against 28-GHz directional urban channel measurements [J]. IEEE transactions on vehicular technology, 2020, 69(12): 14264 – 14276. DOI: 10.1109/TVT.2020.3038620
[58] PRIEBE S, KANNICHT M, JACOB M, et al. Ultra-broadband indoor channel measurements and calibrated ray tracing propagation modeling at THz frequencies [J]. Journal of communications and networks, 2013, 15(6): 547 – 558
[59] ZHOU A D, HUANG J, SUN J, et al. 60 GHz channel measurements and ray tracing modeling in an indoor environment [C]//The 9th International Conference on Wireless Communications and Signal Processing (WCSP). IEEE, 2017: 1 – 6. DOI: 10.1109/WCSP.2017.8170934
[60] KANHERE O, PODDAR H, RAPPAPORT T S. Calibration of NYURay for ray tracing using 28, 73, and 142 GHz channel measurements conducted in indoor, outdoor, and factory scenarios [J]. IEEE transactions on antennas and propagation, 2025, 73(1): 405 – 420
[61] OREKONDY T, KUMAR P, KADAMBI S, et al. Winert: towards neural ray tracing for wireless channel modelling and differentiable simulations [EB/OL]. [2025-03-02]. https://openreview.net/pdf?id=tPKKXeW33YU
[62] JIANG S F, QU Q, PAN X Q, et al. Learnable wireless digital twins: Reconstructing electromagnetic field with neural representations [EB/OL]. (2024-09-04) [2025-03-02]. https://arxiv.org/abs/2409.02564v2
[63] QI Y H, KOBAYASHI H, SUDA H. Analysis of wireless geolocation in a non-line-of-sight environment [J]. IEEE transactions on wireless communications, 2006, 5(3): 672 – 681. DOI: 10.1109/TWC.2006.1611097
[64] KAUSHIK A, SINGH R, DAYARATHNA S, et al. Toward integrated sensing and communications for 6G: key enabling technologies, standardization, and challenges [J]. IEEE communications standards magazine, 2024, 8(2): 52 – 59. DOI: 10.1109/MCOMSTD.0007.2300043
[65] YAPAR Ç, LEVIE R, KUTYNIOK G, et al. Real-time localization using radio maps [EB/OL]. (2020-06-09) [2025-03-02]. https://arxiv. org/abs/2006.05397v1
[66] ZENG S Q, XU X L, ZENG Y, et al. CKM-assisted LoS identification and predictive beamforming for cellular-connected UAV [C]//International Conference on Communications. IEEE, 2023: 2877 – 2882. DOI: 10.1109/ICC45041.2023.10278702
[67] ZHANG B T, CHEN J T. Constructing radio maps for UAV communications via dynamic resolution virtual obstacle maps [C]//The 21st International Workshop on Signal Processing Advances in Wireless Communications (SPAWC). IEEE, 2020: 1 – 5. DOI: 10.1109/SPAWC48557.2020.9154223
[68] ZHANG S W, ZHANG R. Radio map-based 3D path planning for cellular-connected UAV [J]. IEEE transactions on wireless communications, 2021, 20(3): 1975 – 1989. DOI: 10.1109/TWC.2020.3037916
[69] HUANG Y W, MO X P, XU J, et al. Online maneuver design for UAV-enabled NOMA systems via reinforcement learning [C]//Wireless Commu-

nications and Networking Conference (WCNC). IEEE, 2020: 1 – 6. DOI: 10.1109/WCNC45663.2020.9120492
[70] ZENG Y, XU X L, JIN S, et al. Simultaneous navigation and radio mapping for cellular-connected UAV with deep reinforcement learning [J]. IEEE transactions on wireless communications, 2021, 20(7): 4205 – 4220. DOI: 10.1109/TWC.2021.3056573
[71] WU D, ZENG Y, JIN S, et al. Environment-aware hybrid beamforming by leveraging channel knowledge map [J]. IEEE transactions on wireless communications, 2024, 23(5): 4990 – 5005. DOI: 10.1109/TWC.2023.3323941
[72] YANG B, WANG W, ZHANG W. Cell-free massive MIMO beamforming based on radio map [C]//International Conference on Communications. IEEE, 2024: 4506 – 4511. DOI: 10.1109/ICC51166.2024.10622568
[73] XIA X C, XU K, XIE W, et al. Multiple aerial base station deployment and user association based on binary radio map [J]. IEEE Internet of Things journal, 2023, 10(19): 17206 – 17219. DOI: 10.1109/JIOT.2023.3272555
[74] GANAME H, LIU Y Z, GHAZZAI H, et al. 5G base station deployment perspectives in millimeter wave frequencies using meta-heuristic algorithms [J]. Electronics, 2019, 8(11): 1318. DOI: 10.3390/electronics8111318
[75] PENG H S, KALLEHAUGE T, TAO M X, et al. Fast transmission control adaptation for URLLC via channel knowledge map and meta-learning [J]. IEEE Internet of Things journal, 2025, 12(9): 13097 – 13111. DOI: 10.1109/JIOT.2025.3552413
[76] KAUSHIK A, SINGH R, et al. Empowering robotic systems with integrated sensing and communications in the 6G era [EB/OL]. (2025-02-11) [2025-03-25]. https://www.techrxiv.org/doi/full/10.36227/techrxiv.173929717.76503413/v1

Biographies

LIU Xingchen received his BS degree in information engineering from Southeast University, China in 2022, and MS degree in information and communication engineering from Shanghai Jiao Tong University, China in 2025. His research interests include ray tracing, channel modeling, and the application of artificial intelligence in wireless communications.

SUN Shu (shusun@sjtu.edu.cn) obtained her BS degree in applied physics from Shanghai Jiao Tong University (SJTU), China in 2012, and PhD degree in electrical engineering from New York University, USA in 2018, and held summer internship positions at Nokia Bell Labs, USA in 2014 and 2015. She worked as a system engineer at Intel Corporation, USA from 2018 to 2021. She is currently a tenure-track associate professor at SJTU. Her current research interests include channel modeling, millimeter-wave communications, integrated sensing and communication, and holographic MIMO. She received multiple international academic awards including the 2023 and 2017 IEEE Neil Shepherd Memorial Best Propagation Paper Awards, the 2017 Marconi Society Young Scholar Award, the IEEE VTC2016-Spring Best Paper Award, and the 2015 IEEE Donald G. Fink Award. She is an editor for various international journals.

TAO Meixia received her BS degree in electronic engineering from Fudan University, China in 1999, and PhD degree in electrical and electronic engineering from Hong Kong University of Science and Technology, China in 2003. She is currently a distinguished professor with the School of Information Science and Electronic Engineering at Shanghai Jiao Tong University, China. Her research interests include wireless edge learning, semantic communications, integrated communication-computing-sensing, and AI-based channel modeling and beamforming. She received the 2019 IEEE Marconi Prize Paper Award, the 2013 IEEE Heinrich Hertz Award for Best Communications Letters, the IEEE/CIC International Conference on Communications in China (ICCC) 2015 Best Paper Award, the International Conference on Wireless Communications and Signal Processing (WCSP) 2012 and 2022 Best Paper Awards, and the 2009 IEEE ComSoc Asia-Pacific Outstanding Young Researcher Award. She is an editor for various international journals.

Aryan KAUSHIK has been an associate professor with Manchester Metropolitan University, UK since 2024. He is a core member of the IEEE P1955 Standard on 6G-Empowering Robotics, Chair of the IEEE ComSoc ETI on ESIT, Co-Chair of the IEEE SIG on AITNTN, and an editor of 5 books published by Elsevier and Wiley. He also serves as an editor for several journals, such as *IEEE Transactions on Communications*, *IEEE Transactions on Mobile Computing*, *IEEE Communications Surveys and Tutorials*, *IEEE OJCOMS* (2023 and 2024 Best Editor Award), *IEEE Communications Letters* (2023 and 2024 Exemplary Editor), *IEEE IoT Magazine*, and *IEEE CTN*. He has delivered invited talks, keynote speeches, and tutorials at over 110 academic and industry events and conferences globally, including IEEE ICC 2024-2025, IEEE GLOBECOM 2023-2024. Additionally, he has served as the General Chair for over 30 workshops and special sessions, such as those at IEEE ICC 2024-2025 and IEEE GLOBECOM 2023-2025.

YAN Hangsong received his PhD degree in electrical engineering from New York University, USA in 2021. From 2021 to 2024, he was a senior research engineer with Huawei Technologies Co., Ltd, China, where he received various awards including the Company Future Star Award and the President's Award in 5G & LTE FDD domain. He is currently an associate researcher with Hangzhou Institute of Technology, Xidian University, China. His research interests include massive MIMO related theories and applications, and satellite communications. He serves as a reviewer for multiple international journals and conferences, and has been recognized as an exemplary reviewer for *IEEE Transactions on Communications* and *IEEE Wireless Communications Letters*.

Air-to-Ground Channel Measurement and Modeling for Low-Altitude UAVs: A Survey

CHEN Peng, LIU Yajuan, WEI Wentong,

WANG Wei, LI Na

(School of Information Engineering, Chang'an University, Xi'an 710064, China)

DOI: 10.12142/ZTECOM.202502007

https://kns.cnki.net/kcms/detail/34.1294.TN.20250529.1048.002.html, published online May 29, 2025

Manuscript received: 2025-02-20

Abstract: As important infrastructure for airborne communication platforms, unmanned aerial vehicles (UAVs) are expected to become a key part of 6G wireless networks. Thus, modeling low- and medium-altitude propagation channels has attracted much attention. Air-to-ground (A2G) propagation channel models vary in different scenarios, requiring accurate models for designing and evaluating UAV communication links. Unlike terrestrial models, A2G channel models lack detailed investigation. Therefore, this paper provides an overview of existing A2G channel measurement campaigns, different types of A2G channel models for various environments, and future research directions for UAV air-land channel modeling. This study focuses on the potential of millimeter-wave technology for UAV A2G channel modeling and highlights non-suburban scenarios requiring consideration in future modeling efforts.

Keywords: unmanned aerial vehicle (UAV); air-to-ground (A2G); channel measurement; channel modeling; small-scale and large-scale fading

Citation (Format 1): CHEN P, LIU Y J, WEI W T, et al. Air-to-ground channel measurement and modeling for low-altitude UAVs: a survey [J]. ZTE Communications, 2025, 23(2): 60 - 75. DOI: 10.12142/ZTECOM.202502007

Citation (Format 2): P. Chen, Y. J. Liu, W. T. Wei, et al., "Air-to-ground channel measurement and modeling for low-altitude UAVs: a survey," *ZTE Communications*, vol. 23, no. 2, pp. 60 - 75, Jun. 2025. doi: 10.12142/ZTECOM.202502007.

1 Introduction

Drones were developed more than a century ago and initially served military purposes. At present, unmanned aerial vehicles (UAVs) are also widely used in civil applications in many countries, including power line inspection, pesticide spraying, aerial surveying and mapping, wildlife protection, meteorological monitoring, special weather tracking, disaster rescue, and search and rescue of stranded people. These applications demonstrate remarkable effectiveness compared with traditional manpower, particularly in high-risk and time-critical operations[1]. All these are enabled by UAV-based wireless communication systems with low cost, simple operation, and flexible configuration[2 - 4].

In the 5G era, artificial intelligence (AI) and other emerging technologies are providing strong impetus to the drone industry. These technology combinations are creating secondary markets for drone applications. Examples include the emergence of advanced military drones such as the Predator and the Global Hawk. Wireless connectivity to drones is key for enabling the integration of drones into national airspace and expanding the scenarios in which drones can be used.

In contrast to conventional terrestrial communication systems such as cellular and vehicular networks, UAV communication systems exhibit unique three-dimensional (3D) characteristics, including 3D scattering environments, 3D flight trajectories, and 3D antenna arrays. These features significantly influence the propagation characteristics of UAV communication systems. UAVs can operate at various flight altitudes, causing the signal propagation to transition from a simple line of sight (LoS) path to more complex paths involving ground reflections and scatterings from obstacles. This results in strong randomness of the received signal and rapid changes in the received signal envelope. Additionally, UAVs can maneuver freely in real environments, where obstacles are inevitable. Unlike traditional air-to-ground (A2G) systems that assume aircraft can avoid ground obstacles, UAVs often face challenges in obstacle avoidance, further complicating the propagation environment. The mobility of both the transmitter and receiver also impacts the fading characteristics of the signals. In particular, the high flight speeds of UAVs can lead to significant Doppler shifts in bands with large carrier frequencies. To address these complexities and enhance modeling accuracy, researchers have proposed advanced channel models.

This work was supported by the National Natural Science Foundation of China under Grant No. 42176190, Fundamental Research Funds for the Central Universities, CHD under Grant Nos. 300102243401 and 300102244203, and Research Funds for the Interdisciplinary Projects, CHU under Grant Nos. 300104240912 and 300104240922.

For instance, Ref. [5] introduced a non-stationary ray-tracing (RT) channel model that incorporates 3D scattering environments, 3D flight trajectories, and 3D antenna arrays. This model combines deterministic methods for computing inter-path parameters based on geometric configurations with stochastic approaches for generating intra-path parameters, thereby improving computational efficiency and reducing complexity. Furthermore, Ref. [6] developed a 3D non-stationary geometry-based stochastic model (GBSM) that accounts for UAV body orientations. By introducing time-varying 3D attitude matrices, this model characterizes UAV attitude dynamics and analyzes their effects on channel statistical properties, such as temporal autocorrelation functions and spatial cross-correlation functions. These studies collectively highlight that UAV attitude variations are critical factors influencing channel characteristics and must be explicitly incorporated into channel modeling frameworks.

UAV operating environments and scenarios pose technical challenges for communication between the control point and the UAV, and these technical issues have attracted many researchers to investigate them. For instance, Ericsson researchers have shown that mobile networks can provide wide-area, high-speed, and secure wireless connectivity to enhance the control and safety of UAV operations[7], and Nokia Bell Labs researchers have proposed that UAVs connected to cellular network path loss and shadowing parameters must follow highly correlated models[8]. Typically, A2G channels are considered free-space channels or two-ray channels, which add reflections from the Earth's surface to the LoS parameter. Traditionally, A2G channel measurements and modeling have been carried out at high altitude with large aircraft[9].

For public safety reasons, however, some countries including Japan, Ireland and the Philippines limit the application of UAVs to low-altitude flight (below 150 m) under LoS[10] conditions. However, the A2G propagation channel model used for high-altitude aerial communications is usually not directly applicable to low-altitude UAV communications, as low-altitude communications are strongly influenced by a variety of factors, such as the vehicle, terrain, and weather. For example, in terms of vehicle selection, small UAVs of different manufacturers and models do not have uniform and fixed structures or flight characteristics. In terms of the environment, it is technically challenging to provide continuous coverage for low-altitude communications in obstructed environments such as hilly terrains, mountain forests, rivers, and high buildings.

Compared with terrestrial propagation channels, UAV A2G propagation channels have not yet attracted widespread attention. There are few studies on the characteristics of A2G propagation channels, with Ref. [11] being an exception. To encourage more research on UAV A2G propagation channels, this paper summarizes the basics and characteristics of UAV A2G propagation channels, presents an overview of UAV A2G channel measurement methodologies, and outlines future research directions in this field.

The rest of the paper is organized as follows. Section 2 describes the basics and characteristics of UAV A2G channels based on the literature. Section 3 overviews important UAV A2G channel measurement campaigns. Section 4 classifies UAV A2G channel models for diversified scenarios. Section 5 presents future research directions for UAV A2G channel measurement and modeling, and Section 6 concludes the paper.

2 Basic Information and Characteristics of Air-to-Ground Channels

2.1 Introduction to Air-to-Ground Communication

A2G communication generally refers to the communication between ground command institutions and aerial vehicles. Such systems use aerial platforms to carry communication payloads via air-based relaying or mobile switching, and integrate with multiple ground platforms (stations) to achieve information interaction of wireless communication systems. A2G communication essentially aims to increase the height of ground-based communication equipment, converting over-the-horizon communication into LoS communication. This enables long communication distances, large coverage areas, wide transmission bandwidths, and easy network deployment. Additionally, it is highly mobile and flexible[12].

According to the lifting altitude of the air platform, the coverage radius of wireless communication can range from tens to hundreds of kilometers. Current propagation models for fading in A2G wireless channels can be divided into three main categories: free-space transmission, shadow fading, and propagation models for multipath fading. Among them, free-space transmission and shadow fading are generally classified as large-scale fading, because they primarily cause changes in received power over long distances with their impact on wireless signals unfolding relatively slow (also termed slow fading). In contrast, multipath fading is often referred to as small-scale fading or fast fading. This is because the signals from the mobile station near scattering bodies (such as terrain, features, and moving objects) undergo multipath propagation. As a result, the received signal experiences rapid rises and falls due to the superposition of multiple paths at the receiving point.

2.2 Large-Scale Decay

Statistical models of A2G communication channels are divided into large-scale and small-scale models. Large-scale models typically include path loss and shadow fading models. Large-scale fading mainly includes path loss (PL) and shadow fading (SF). PL refers to the signal fading over long distances, while SF occurs when the signal encounters obstacles or uneven terrain. SF is characterized by its dependence on the topography of the radio propagation and the distribution and

heights of obstacles. In most of the literature, the well-known ground-based logarithmic distance PL model is used as:

$$\mathrm{PL}(d) = \mathrm{PL}(d_0) + 10\gamma \log_{10}\frac{d}{d_0} + X_\sigma \quad (1),$$

where $\mathrm{PL}(d)$ denotes the path loss in dB when the spacing between transceiver devices is d; $\mathrm{PL}(d_0)$ represents the reference path loss measured at a reference distance d_0 (typically 1 m, derived from actual measurement); γ is the path loss exponent (PLE) obtained through a best-fit minimum mean square error method, which quantifies the rate at which the path loss increases with distance. Theoretically, γ should equal 2 in free space. However, Table 1 shows that the measured PLE γ is approximately 1.5 – 4[13 – 20]. In Eq. (1), X_σ is a normal random variable with a standard deviation of sigma, which is used to account for the variations in shadowing or in the linear fit in the LoS channel. A large body of literature shows that shadow fading obeys a zero-mean lognormal distribution[21]:

$$f(m) = \frac{1}{\sqrt{2\pi\sigma^2}} e^{\frac{-(\ln m - \mu)^2}{2\sigma^2}} \quad (2),$$

where μ is the mean value, and σ is the standard deviation. UAV A2G channels tend to be more dispersed than mobile radio channels, producing greater ground shadow attenuation and faster variations. Channel factors typically include reflection, scattering, diffraction, and shading effects in the direct view path. However, in most LoS A2G channels, large-scale fading occurs only when the LoS path between the UAV and the ground station (GS) is obstructed by an object with a large relative wavelength. Several models have been developed for this fading condition (e.g., terrain diffraction and tree shading). Many large-scale fading models for UAV A2G channels in the literature cover both PL and SF. For example, Ref. [13] conducted comprehensive measurements of path loss in the L-band and C-band in different propagation scenarios, and two primary conclusions were obtained. 1) The PLE varied slightly but was usually close to the free space value for urban, suburban, hilly, and water scenarios; 2) the standard deviation of the linear fit was usually less than 3 dB. Table 1 summarizes the literature on large-scale A2G propagation and its path loss parameters, with the log-distance PL model being the most common model. The PL estimates are given via the logarithmic model[15, 17, 22 – 23]. Other PL models consider the shadowing of non-line of sight (NLoS) paths, as well as additional losses due to other obstacles[9, 19]. In Ref. [19], shadowing losses are considered in the modeling and evaluated as a function of the elevation angle of the NLoS path.

Table 1. Research on large-scale A2G propagation and its path loss parameters in existing literature

Ref.	Scenario	Propagation Path	Model	PLE γ
[13]	Urban/ suburban	LoS	Log-distance path loss model, two-ray model	L-band: 1.7, C-band: 1.5 – 2
[14]	Urban/ open field	LoS	Free space path loss model	
[15]	Urban/ rural	LoS	Log-distance path loss model	4.1
[16]	Open field	LoS	Log-distance path loss model	2.01
[17]	Aerial	LoS	Log-distance path loss model	2.32
[18]	Water	LoS	Log-distance path loss model	1.9
[19]	Urban/ suburban	LoS, NLoS	Free space path loss model	
[20]	Urban	LoS, NLoS	Free space path loss model	

A2G: air-to-ground LoS: line of sight NLoS: non-line of sight
PLE: path loss exponent

2.3 Small-Scale Decay

Small-scale modeling of the UAV A2G channel relies on the multipath fading characteristics of the channel and the Doppler power spectrum. Small-scale fading models are applicable to narrowband channels or individual multipath components (MPCs). Stochastic fading models are usually obtained from empirical data or geometric analysis and simulation[24 – 29]. PL, including shadowing, was reported in Refs. [15, 30 – 32], where we note that in the case of LoS without real obstacles in the first Fresnel zone, it is not actually shadowing that causes the PL to change, but rather small-scale effects.

Ref. [31] noted that the PL and its associated shadows are attributed to buildings only when the UAV is flying near the ground, whereas when the UAV is flying higher, actual shadows do not exist, but changes in small-scale fading still occur. Table 2 summarizes the fading characteristics of small-scale A2G propagation channels in the literature[15, 30 – 34].

Table 2. Fading characteristics of small-scale air-to-ground propagation channels in the literature

Ref.	Frequency/ GHz	Fading Distribution	K-factor/dB	Scenario
[33]	3.1 – 5.3	Nakagami		Suburban/ open field
[15]	2	Rayleigh, Ricean		Urban/suburban
[30]	5.75	Ricean	−5 – 10	Urban/suburban
[32]	0.968 – 2.06	Ricean	12 – 27.4	Urban/suburban
[34]	8 – 18	Ricean, Nakagami	2 – 5	Forest
[31]	2	Ricean		Urban/suburban

2.3.1 Multipath Components

Small-scale multipath fading refers to rapid fluctuations in the amplitude, phase, or multipath delay of a wireless signal over short time intervals or distances (typically within half a wavelength). This fading results from the mutual interference of multipath components originating from the same transmitted signal, which propagate through different paths and arrive at the receiver with varying time delays. HUANG et al.[35] considered a time-varying approach to model the propagation between a GS and a UAV. They proposed a method based on MPC distances to track the evolution of MPC during UAV flight to obtain MPC trajectories that were modeled with straight-line segments. To describe the evolutionary trend of the MPC, several properties (including survival length, initial position spacing, initial relative delay, and relative slope) were also defined and statistically characterized for each flight trajectory. The model serves as a basis for modeling time-varying radio propagation channels between a low-altitude UAV and a ground base station.

Notably, in UAV A2G channel modeling, multipath fading can also come from the UAV itself, albeit usually weak and with minimal relative delays. The main propagation paths for A2G communications include the direct propagation path between the UAV and GS and a cluster of reflected, delayed propagation paths; thus, for statistical analysis, the channel model usually includes the LoS component and a cluster of NLoS components that comprise multiple reflected paths with varying delays.

2.3.2 Doppler Shift

The Doppler effect is caused by the mutual motion between the mobile station and the base station or by the motion of other objects in the propagation environment. In UAV communications, this effect is influenced by the UAV's speed, geometry, and operational wavelength. If the UAV flies too rapidly, it may generate a large Doppler shift, potentially causing issues due to higher Doppler frequencies. In addition, since the frequency and wavelength of electromagnetic waves are inversely proportional, the lower the operating frequency band, the smaller the Doppler shift for high-speed UAVs. However, the spectrum resources in the lower frequency bands are very tight, so the Doppler shift caused by high-speed movement of UAVs is a major challenge for the UAV data chain. Doppler shift introduces a carrier frequency shift and inter-carrier interference. Doppler shift modeling in A2G scenarios has long been studied[30, 36–39]. Ref. [30] investigated the Doppler shift and its impact on channel performance in different flight phases (parking and taxiing, in-flight, take-off, and landing) through simulation. The Doppler shift for the realization of orthogonal frequency division multiplexing (OFDM) systems in multipath environments was considered in Ref. [39], where different frequency offsets were observed for the arriving multiple components.

In Ref. [40], the Doppler frequency profile (DFP) of a vehicle in different states was analyzed, as shown in Fig. 1, and the Doppler shift equation was given:

$$f_D = f_{D_{\max}} \cos\left[\alpha_L + \mu(\alpha_H - \alpha_L)\right] \tag{3},$$

where $\mu \in [0, 1]$ is a uniformly distributed random variable, and α_H and α_L are the maximum and minimum angles of arrival under navigation, respectively. The statistical model proposed by ELNOUBI et al.[41] characterizes UAV-to-ground propagation based on transmission coefficients and performs a Doppler spectral analysis of the scattered MPCs. ZAMAN et al.[42] proposed a model with both LoS and NLoS components, describing the Doppler shift as a random process and using an unmodulated 118 MHz carrier as the input to the channel. They observed that the output signal's amplitude spectrum deviated from the carrier frequency. LI et al.[43] presented a simulation model for high-altitude UAV communication scenarios, in which statistics such as temporal correlation and Doppler spectrum were investigated. CHENG et al.[44] proposed a 3D nonstationary geometric model for wideband UAV channels. The Doppler shift induced by the UAV's high-speed motion is determined by the analyzed correlation and Doppler properties. However, the scenarios considered in previous studies typically exclude the presence of nearby scatterers. This limitation restricts the applicability of these studies to broader multi-antenna UAV scenarios that may involve various altitudes.

2.4 Typical Scenario of UAV Air-to-Ground Channel Propagation

The first step in UAV communication research is modeling the communication channel. However, A2G propagation channel models developed for both traditional terrestrial and high-altitude aerial communication systems are not directly applicable to low-altitude UAV communications. UAV communication systems operate in more complex and variable environments, often influenced by terrain, obstacles, and self-

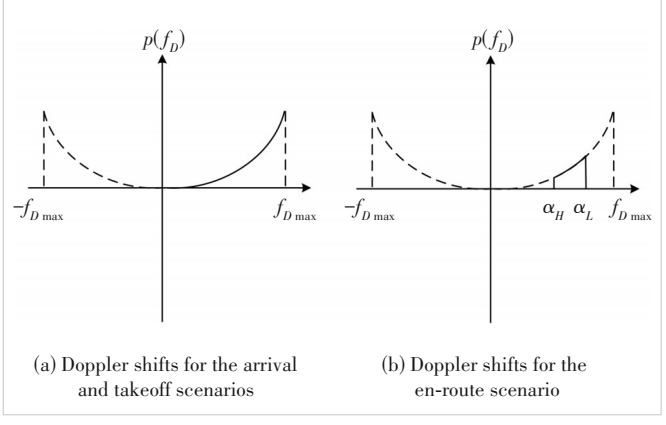

(a) Doppler shifts for the arrival and takeoff scenarios

(b) Doppler shifts for the en-route scenario

Figure 1. Doppler shifts in different states of the aircraft

occlusion caused by the UAV itself. These factors make LoS connections infeasible in all scenarios, which needs to be considered in UAV communication research. Fig. 2 illustrates a common A2G propagation scenario with ground obstacles, often referred to as scatterers.

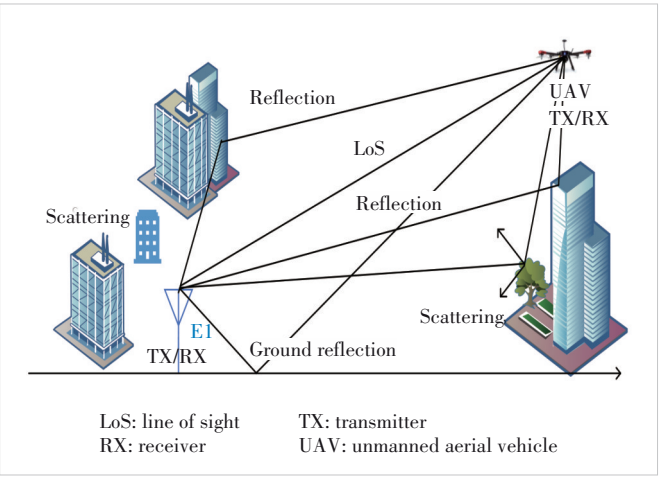

Figure 2. A typical scenario of UAV air-to-ground channel propagation

3 UAV Air-to-Ground Channel Model

3.1 Channel Modeling Based on Measured Data

UAV channel measurements have received increasing attention over the past decade. Table 3 summarizes the literature on channel measurements via small rotor UAVs[8, 10, 16 - 17, 22, 33, 35, 45 - 56]. In Ref. [45], the channel measurement system consists of a six-rotor UAV, a cylindrical antenna, a Universal Software Radio Peripheral (USRP), and a

Table 3. Summary of important A2G channel measurement research in the literature

Ref.	Frequency	Bandwidth/ MHz	UAV	Maximum Flight Altitude/m	Scenario	Antenna	Characteristics
[33]	3.1 - 5.3 GHz	2 200	Quadcopter	16	Open field, suburban	Dipole SISO	PL, SF, TOA, PDP, CDF, RMS, BC
[45]	2.585 GHz	18	Hexacopter	100	Suburban, campus	Quasi-omnidirectional-discone, SISO	PL, SF, K-factor, DPP
[46]	2.585 GHz	18	Hexacopter	300	Suburban, campus	Omni-directional, SISO	PDP, RMS, CDF, K-factor
[47]	1 - 24 GHz	—	Hexacopter	24	Semi Urban	Monopole, SISO	PL, SF
[48]	1.2 - 4.2 GHz	—	Hexacopter	100	Semi Urban	MIMO	PL, K-factor
[8]	800 MHz	—	Hexacopter	120	Suburban	Dipole, SISO	PL, SF
[49]	5.8 GHz	20	Octocopter	165	Uptown, montane	MIMO	RMS, DC, CDF
[35]	2.5 GHz	9	Hexacopter	105	Suburban	Omni-directional, SISO	MPC
[50]	2.5 GHz	15.36	Hexacopter	105	Suburban	SISO	PL, SF, DPP
[22]	2.4 GHz	—	Quadcopter	120	Open field, campus	SISO	PL, AO
[16]	5.24 GHz	—	Quadcopter	110	Open field	Dipole MIMO	PL, PAS, UDP, CDF
[51]	0.915 GHz	—	Quadcopter	—	Urban, open field	Omni-directional, SISO	PL, RSSI
[17]	2.4 GHz	—	Hexacopter	20	—	Inverted-FSISO	RSSI
[52]	5.76 GHz, 1.817 GHz	13.5	Hexacopter	50	Suburban	Three-leaf antenna, SISO	PL, SF, PDP, K-factor, RMS, CDF
[53]	2.4 GHz	—	Fixed wing	75	—	Omni-directional, MIMO	AC
[54]	2.4 GHz	—	Hexacopter	40	Laboratory, outdoors	Omni-directional, MIMO	PL, PAS, K-factor, PDF
[55]	900 MHz	—	Fixed wing	—	Rural	SISO	Pr
[56]	850 MHz	—	Quadcopter	120	Suburban	SISO	PL, SF
[10]	909 MHz	—	Quadcopter	100	Open field	Dipole, SISO	PL

A2G: air-to-ground
AC: antenna correlation
AO: antenna orientation
BC: bandwidth-coherence
CDF: cumulative distribution function
DC: direct current
DPP: Doppler power profile
FSISO: full-duplex single input single output
MIMO: multiple-input multiple-output
MPC: multipath component
PAS: power angle spectrum
PDP: power delay profile
PL: path loss
Pr: power-received
RMS: root mean square -delay spread
RSSI: received signal strength indicator
SF: shadow fading
SISO: signal input signal output
TOA: time-of-arrival
UAV: unmanned aerial vehicle
UDP: user datagram protocol

laptop for controlling the USRP and connecting the laptop to a router. Measurements of five horizontal flights at different altitudes and five ascending flights at different horizontal distances to the base station were carried out in the 2.585 GHz band, as shown in Fig. 2. This is a common experiment for UAV air-to-ground channel measurements.

In Ref. [46], a new channel modeling method was proposed based on a feature selection algorithm, an effective and fundamental method for big data analysis. The measurement was conducted via a USRP-based channel sounder by transmitting a frequency modulated (FM) continuous wave with a center frequency of 5 760 MHz and a bandwidth of 16 MHz. Refs. [17, 22, 33] also provided propagation measurement examples performed by a rotorcraft during both flight and hovering. These A2G propagation measurements were conducted at different UAV altitudes ranging from 16 m to 120 m.

However, the effect of UAV hovering on the received signal was not considered in these measurements. Ref. [47] investigated the multi-frequency A2G propagation channel of a low-altitude UAV flying vertically. The basic parameters of large-scale and small-scale channels, including path loss, autocorrelation, shadowing and small-scale fading characteristics, were comprehensively analyzed and modeled. Moreover, Ref. [48] studied the variation in the propagation channel over the flight range of a small- to medium-sized UAV.

Measurements of different routes in a semi-urban complex environment have been carried out to obtain data at different locations. Analysis of the measurement results reveals that small-scale fading is more strongly influenced by the flight altitude than by the elevation angle or distance. In Refs. [35, 50], a height-dependent model was proposed for path loss and shadowing parameters. Measurements in Ref. [51] were conducted in open terrain to explore the feasibility of fixed cellular networks for UAV telemetry and control, focusing on radio propagation, which is shorter in the air than on the ground. In addition to conventional A2G channel detection, such measurements can also leverage fixed cellular networks using the IEEE 802.11 standards with different protocol versions for indirect UAV A2G channel measurements[13, 17, 22]. Specifically, Ref. [13] used a tracking algorithm based on multipath component distances and proposed a dynamic model that could describe the time-varying radio propagation channel between a low-altitude UAV and a ground base station from identified time-varying trajectories.

Ref. [7] proposed a flyby communication scenario using an airborne UAV connected to a cellular network. The study tested several scenarios with different altitudes, orientations, and distances, and analyzed the performance of LTE networks in dynamic 3D environments. Simple extensions to the communication system are proposed to achieve quasi-isotropic radiation to provide uniform 3D connectivity.

Antennas are also key components that cannot be ignored in A2G communications. The number, type and orientation of antennas are all factors that affect the performance of an A2G link. Most A2G channel measurements use a standalone (single) antenna, and a multiple-input multiple-output (MIMO) antenna configuration is available in the literature for A2G propagation measurements[48, 53 – 54]. Antennas can be classified into two types based on their directionality: directional antennas and omnidirectional antennas. Directional antennas, which provide significant gain in a specific direction, are suitable for long-distance communication. However, their performance is poor during movement due to their limited angular coverage. In contrast, omnidirectional antennas offer superior performance during movement because of their wide coverage area. This makes them particularly popular in vehicle communications.

The omnidirectional or directional orientation of the antenna affects the received signal strength and system throughput. Ref. [12] reported that the PLE of IEEE 802.11 communication varies during UAV hovering and moving due to the different orientations of vehicle-mounted antennas. Compared with the vertical-vertical orientation, the horizontal-horizontal orientation exhibits better throughput performance in Ref. [57]. In Ref. [58], the horizontal antenna orientation helps overcome the difference in yaw; similarly, the vertical orientation performs better during UAV tilting. Therefore, antenna orientation maps may affect the true channel path loss characteristics, but eliminating their effects is not always easy.

Ref. [25] suggested the use of MIMO systems to improve the channel capacity of A2G propagation channels. Different values of MIMO channel capacity are obtained by varying the circular antenna array diameter and UAV flight altitude[59]. Omnidirectional antennas are usually more suitable for UAVs than directional antennas due to the high maneuverability of UAVs during flight. In addition, the generated PL model is still useful for the particular UAV configuration used. However, owing to arbitrary mobility patterns and different types of communication applications[60], UAV A2G communications face many other challenges.

3.2 Geometry-Based Random Channel Model

In recent years, geometry-based stochastic channel models have been widely used. They offer higher accuracy than statistical models and better integration with MIMO techniques, while requiring less computational effort than deterministic models. Any geometry-based model is determined by the position of the scatterer. In deterministic geometric methods (e.g., RT), the position of the scatterer is set in a database. In contrast, the geometry-based stochastic channel model (GBSCM) generates the scatterer positions randomly according to a specific probability distribution. The GBSCM can be further classified into a regular-shaped GBSCM and an irregular-shaped GBSCM. For the former, the scatterer distribution, such as an ellipsoid, a cylinder, or a sphere, is ideal.

Overall, the main difference among regular-shaped GB-

SCMs is the locations and statistical distributions of scatterers, which leads to variability in the calculation results of 2D angular parameters. Table 4 presents the Angle-of-Arrival (AOA) distributions of common GBSCMs and compares different shape models[27, 44, 57, 61 – 65]. Among them, cylindrical and spherical channel models are currently the primary methods for UAV-based geometrically stochastic A2G channel modeling. With the application of MIMO technology, an increasing number of stochastic channel models have incorporated MIMO capabilities. For example, Ref. [61] proposed a 3D hemispherical GBSM for UAV MIMO channels, which takes into account the non-smooth propagation environment due to the fast movement of UAVs and scattering clusters.

Ref. [66] modeled UAV rotation as a sinusoidal process and investigated the effect of UAV rotation on the MIMO channel characteristics of air-to-ground communication systems by considering the effective scatterers within the main flap of the directional antenna. Ref. [67] introduced a Gauss-Markov mobility model to describe the 3D arbitrary trajectories of UAVs and proposed a 3D cylindrical GBSM for UAVs with broadband unsteady channels. Considering a uniform and two different propagation scenarios with variable speeds, the numerical results reveal that under the uniform speed condition, the vertical motion of the UAV has a greater effect on the time correlation function than does the horizontal motion. In contrast, when the UAV moves at a variable speed, the effect of the UAV on the correlation function at a constant speed disappears due to the randomness of maneuvering.

Ref. [64], with the same assumption as Ref. [24], proposed a 3D columned GBSM for UAV-MIMO Rayleigh channels, as shown in Fig. 3, and investigated the effects of several UAV-related parameters on the GBSM. The numerical results reveal that both the UAV's direction of motion and its position strongly influence the obtained correlations. They indicate that to maintain a stable UAV link, the UAV should move toward the ground mobile users, whereas for reliable MIMO performance, the UAV should move horizontally. Ref. [68] proposed a stochastic model for A2G channels based on 3D geometry. Moreover, a Gauss-Markov mobility model was used to generate dynamic trajectories. According to different scattering environments, a reference model and a statistical simulation model of the A2G channel were developed. The dynamic motion scenarios generated by the Gauss-Markov process were analyzed, along with their effects on the correlation of the A2G channel. Notably, the authors developed a statistical simulation model

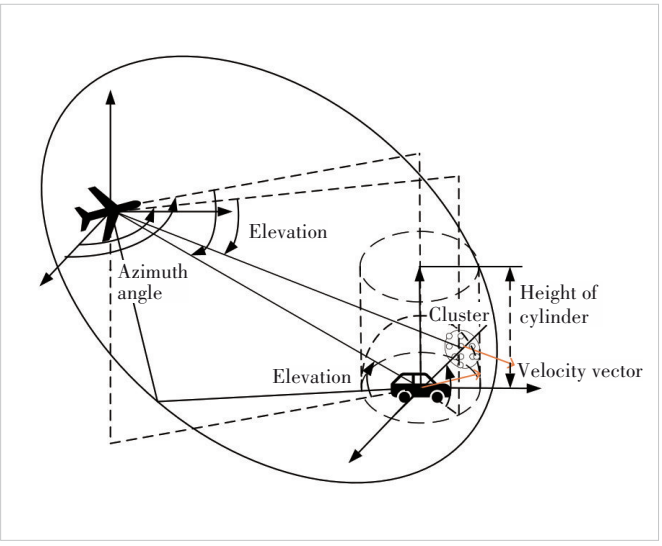

Figure 3. MIMO air-to-ground channel model of a UAV

Table 4. Comparison of geometry-based stochastic channel models

Model	Ref.	Angle Distribution Function	Scenario
Cylindroid	[27, 62]	AOA: $f_{\alpha_{\mathrm{rx},n,m}^{-1}}(\alpha)=\frac{e^{k\cos(\alpha-\alpha_{\mathrm{rx},n}^{-1})}}{2\pi I_0(k)}$ EOA: $f_{\beta_{\mathrm{rx},n,m}^{-S}}(\beta)=\frac{\pi}{4\lvert\beta_{R_m}\rvert}\cos\left(\frac{\pi}{2}\frac{\beta-\beta_{\mathrm{tx},n,m}^{-S}}{\beta_{R_m}}\right)$	Highly accurate, but relies on geographic information and high computational complexity
Sphere	[61 – 63]	AOA: $P_{\alpha_{\mathrm{rx},n,m}^{-S},\beta_{\mathrm{rx},n,m}^{-S}}^{-S}(\alpha,\beta)=\frac{e^{k\left(\cos\beta\cos\beta_{\mathrm{rx},n}^{-S}\cos\left(\alpha-\alpha_{\mathrm{rx},n}^{-S}\right)+\sin\beta\sin\beta_{\mathrm{rx},n}^{-S}\right)}}{\left(k^{-\frac{1}{2}}\right)(2\pi)^{\frac{3}{2}}I_{\frac{1}{2}}(k)}$	Angular parameters can be abstracted to specific mathematical distributions, which can greatly simplify calculations
Cylinder	[57] (R=3 km, H_C =300 m); [64] (R=100 m); [44] (R=500 m); [65] (R=50 m, H_C=700 m)	AOA: $f_{\alpha_{\mathrm{rx},n,m}^{-1}}(\alpha)=\frac{e^{k\cos(\alpha-\alpha_{\mathrm{rx},n}^{-1})}}{2\pi I_0(k)}$ EOA: $f_{\beta_{\mathrm{rx},n,m}^{-S}}(\beta)=\frac{\pi}{4\lvert\beta_{R_m}\rvert}\cos\left(\frac{\pi}{2}\frac{\beta-\beta_{\mathrm{tx},n,m}^{-S}}{\beta_{R_m}}\right)$	

AOA: Angle of Arrival EOA: Elevation over Angle

to reduce computational complexity. This is relatively rare.

3.3 UAV Channel Modeling Across Different Frequency Bands and Bandwidths

UAV communication systems are being explored across diverse frequency bands and bandwidths to meet varied application requirements.

1) Sub-6 GHz frequency band

At sub-6 GHz frequencies, UAV channels exhibit characteristics similar to terrestrial channels, but feature enhanced 3D scattering and multipath effects due to the aerial nature of UAVs. Path loss and shadowing are significant, and the impact of terrain and urban structures on signal propagation must be carefully modeled. For instance, in urban environments, signal reflections from buildings and the ground create complex multipath scenarios. Studies including Ref. [69] show that traditional PL models need adaptation for the higher elevation angles typical in UAV communications.

2) Millimeter-wave (mmWave) frequency band

The mmWave frequency band offers large bandwidths for high data rate communications but suffers from higher path loss and sensitivity to blockage. UAV channels in this band are highly dependent on LoS conditions. The narrow beamforming used in mmWave communications requires precise alignment between the UAV and GS, which is challenging due to the mobility of UAVs. Research in Ref. [70] indicates that unique 3D flight trajectories of UAVs necessitate advanced beam management and tracking algorithms to maintain reliable connections.

3) Terahertz (THz) frequency band

The THz band promises ultra-high data rates and ultra-low latency, making it attractive for future 6G applications. However, signal propagation in this band is severely affected by atmospheric absorption and scattering, leading to significant path loss. UAV channel modeling in the THz band must incorporate the effects of weather conditions and molecular absorption. As highlighted in Ref. [71], the integration of ultra-massive MIMO techniques is crucial to compensate for propagation losses in this band.

4) Impact of bandwidth on channel modeling

The increasing use of large bandwidths in higher frequency bands poses new challenges for channel modeling. Frequency-selective fading and Doppler spread become more pronounced, requiring more sophisticated models to capture the dynamic nature of UAV channels. For example, in mmWave and THz bands, the channel model must account for the rapid changes in channel characteristics due to the high mobility of UAVs and the narrow beam widths used.

3.4 RT-Based Channel Model

In the A2G propagation channel of a UAV, MPCs appear due to reflections from the Earth's surface, from ground objects, and sometimes from the body of the UAV itself. The characteristics of the channel depend on the material, shape and size of the scattering object. In A2G propagation scenarios, the strongest MPCs other than the LoS component are usually single reflections from the Earth's surface. This gives rise to the well-known two-ray model shown in Fig. 4. Table 5 summarizes the two-ray model for selected A2G channels[13, 15, 17, 23, 32–33, 59, 72–74]. In two-ray PL modeling, there is a clear peak in the PL variation with distance due to the superposition of the dominant and surface-reflected components. In most of the PL models, PL variation is approximated as a log-normal random variable. This variation may be due to shadows from the UAV airframe or MPC from ground scatterers such as buildings[13, 19, 27, 72]. Ref. [73] presented path loss and shadow

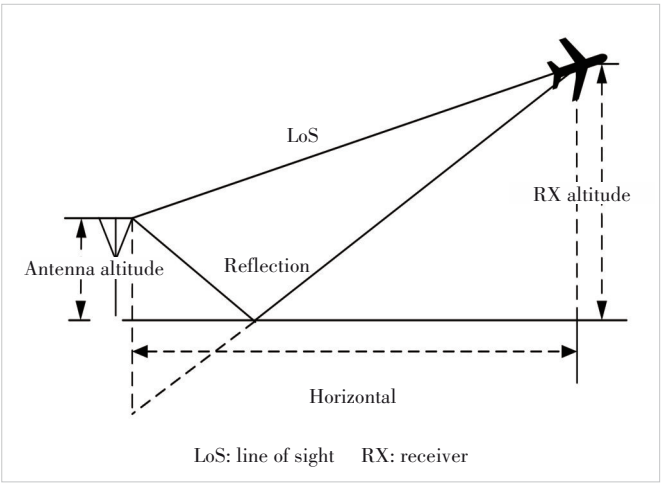

Figure 4. Two-ray model

Table 5. Two-ray model for selected A2G channels

Ref.	Frequency	Bandwidth	Transmit Power/dBm	Channel Characteristics
[13, 23, 32, 72]	0.968 GHz, 5.06 GHz	5 MHz, 50 MHz	40	PL, K-factor
[15]	2.05 GHz	—	—	MPC, K-factor, PL
[33]	3.1–5.3 GHz	2.2 GHz	−14.5	PL, MPC
[17]	2.4 GHz	—	0	RSSI
[59]	5.7 GHz	—	40	PL
[73–74]	200 MHz–5 GHz	—	—	PL, SF

A2G: air-to-ground MPC: multipath component PL: path loss RSSI: received signal strength indicator SF: shadow fading

statistics functions related to elevation and height with PL expressions through 3D RT experiments.

Ref. [73] modeled the LoS transmission probability based on the shape of the cell building and knife-edge diffraction theory. The model takes into account key statistical parameters such as the building height, building size, building coverage, and street width. In Ref. [74], 3D RT experiments were conducted to characterize the height-dependent attenuation of A2G transmission in suburban environments. Al-HOURANI et al.[75 – 77] implemented environmental terrain based on simulations of statistical parameters recommended by the ITU.

In Ref. [76], a generic PL model was proposed for low-altitude platforms in which the channel model parameters were estimated via 3D RT at 700 MHz, 2 000 MHz and 5 800 MHz. The simulation results show that the elevation angle has a significant effect on multipath path loss.

In the work of DANIEL et al.[74] and FENG et al.[73], channel models are limited to urban and suburban environments and are not generalizable for migration to other environments. In the work of Al-HOURANI et al.[75 – 76], the propagation conditions depend on the height and coverage radius of the UAV. The above three models are applied to different scenarios and have their own advantages and disadvantages, which are summarized in Table 6.

Although the statistical model based on the measured data has low computational complexity, random parameter-based modeling cannot meet the accuracy requirements of actual signal transmission, and the application range is limited to a large extent. The RT-based deterministic model requires precise channel scene parameters to accurately restore the signal propagation process, but the computational effort is too large. The geometry-based stochastic model matches the actual channel scene, but it is difficult to reduce the computational complexity.

3.5 Technical Challenges and Solutions in UAV Channel Measurement

UAV channel measurement requires addressing a series of technical challenges, including low-power consumption and miniaturization, large-bandwidth high-frequency operations, transceiver synchronization, airframe shadowing and dynamic scenarios, as well as the integration of measurement hardware, protocols, and synchronization mechanisms.

1) Low power consumption and miniaturization

Table 6. Comparison of the models proposed in Refs. [73 – 76]

Model	Advantage	Disadvantage
Measurement-based model	Matching actual channel scenarios	Single application scenario
Ray-tracing-based model	Discriminating multipath in the channel	High computational volume and complexity
Geometric random channel model	Matching actual channel scenarios	More complex calculations

Channel measurement systems for UAVs must achieve stringent low-power operation and compact form factors to accommodate deployment on small aerial platforms. Ref. [78] demonstrated that integrating efficient signal processing algorithms and lightweight hardware architectures can substantially reduce both power consumption and physical dimensions. For instance, practical implementations utilize low-power RF front-ends and miniaturized antenna arrays to enable high-precision channel characterization. Such designs adhere to UAV payload constraints while ensuring extended operational durations under limited power budgets.

2) Large bandwidth and high-frequency bands

UAV communications predominantly operate in high-frequency bands such as mmWave spectra, which offer large bandwidth but impose stringent requirements on measurement systems. Ref. [79] addressed these challenges by deploying advanced signal processing techniques to mitigate high-frequency signal attenuation and noise interference. Key strategies include high-sampling-rate analog-to-digital converters (ADCs) and adaptive filtering algorithms to maintain signal integrity across wide bandwidths. Furthermore, Ref. [80] presented empirical results from low-altitude A2G channel measurements in the 915 MHz band, revealing significant spatial diversity even in sparse multipath environments. These insights highlight the potential for high-capacity UAV communication links in practical deployments.

3) Transceiver synchronization

Accurate time and frequency synchronization between transceivers is critical for reliable UAV channel measurements. Ref. [16] emphasized the necessity of GPS-based timing alignment and high-precision frequency references to minimize synchronization errors. For example, GPS synchronization during measurement campaigns reduces timing discrepancies by over 80%, enhancing data reliability. Complementary work in Ref. [81] validated the use of GPS time-stamping to ensure temporal coherence in multi-device measurement systems.

4) Airframe shadowing and dynamic scenarios

UAV airframes and wings introduce signal shadowing and reflection effects, while environmental obstacles and rapid terrain variations further degrade channel stability. Ref. [82] proposed optimized measurement protocols, including multi-antenna configurations and angular diversity techniques, to mitigate shadowing and environmental interference. For instance, deploying omnidirectional antennas reduces polarization mismatch-induced path loss by 35% in scenarios with large roll angles. Additionally, Ref. [83] quantified the impact of UAV attitude dynamics on channel statistics, demonstrating that real-time attitude-aware data correction is essential for accurate measurements in dynamic flight conditions.

5) Integrated measurement systems

The complexity of UAV channel measurements demands holistic solutions integrating hardware innovation, protocol

optimization, and synchronization frameworks. Ref. [16] introduced an FPGA-based real-time processing algorithm for extracting channel impulse responses (CIRs), compensating for system response distortions, recovering power loss, and adaptively identifying MPCs. This approach reduces data storage requirements by 60% while improving processing efficiency. Parallel work in Ref. [81] developed a dedicated channel-sounding system for low-altitude A2G measurements, achieving sub-nanosecond timing resolution through optimized antenna configurations and adaptive measurement protocols. These integrated methodologies not only capture the time-varying and spatially diverse nature of UAV channels, but also provide robust datasets for next-generation channel modeling.

4 UAV Air-to-Ground Channel Measurements in Different Scenarios

As with terrestrial cellular channels, the classification of the various A2G channel types[84] exhibits ambiguity and overlap. The measurement activities of different A2G propagation channels can be broadly categorized based on terrain, terrain coverage, and sounding signal characteristics. The representative environments include deserts, rural areas (plains), forests, suburban areas, and urban neighborhoods. However, these classifications are not always disjoint or exhaustive. In this chapter, we provide a brief overview and comparison of measurement activities in different environments.

4.1 Urban and Semi-Urban Environments

In urban and semi-urban environments, A2G channels are significantly affected by the dense network of buildings and infrastructure. Signals often encounter multiple reflections and scatterings from these structures, leading to complex multipath effects and shadowing. Ref. [85] performed a model-based fading statistical analysis of a narrowband UAV propagation channel in an urban area, with the UAV flying at low elevation angles (1° to 6°) and altitudes of 100 m to 170 m. The study used a 2 GHz continuous wave signal in an urban area with an average building height of 22 m. These data represent the received signal distribution through second-order statistics, power spectral density, and an autocorrelation function with a strong coherent component plus a diffuse reflection contribution under Ricean assumptions. This work is unique because second-order channel fading statistics for A2G propagation via UAVs are rarely available in the literature. The authors of Ref. [85] concluded that the partial shadowing model is best suited for characterizing the dynamics of low-altitude links located between pure terrestrial and land mobile satellite channels. Using the partial shadowing model as a starting point, they developed a narrowband time series generator capable of reproducing the observed signal dynamics, which consists of two main modules: one generating the diffuse reflectance component and the other generating the direct/coherent signal. They also proposed a narrowband channel estimator capable of reproducing the dynamic characteristics of the signal.

The authors of Ref. [20] conducted some related measurement campaigns using a similar device to simulate urban area path loss models for flight altitudes between 150 m and 300 m. They used a new methodology to simulate urban area path loss models. In addition, they obtained measurements in urban and forested areas[31, 85] for the research of spatial diversity techniques and concluded that heavily wooded areas achieved greater diversity gains than open sites. However, at lower elevation angles, the open sites presented significant gains in diversity. Compared with the diversity gain in the urban areas studied in Ref. [85], this gain is approximately 4% lower.

Ref. [13] reported broadband A2G propagation channel measurements in L-band and C-band urban areas. It is observed that the reflection-guided root mean square (RMS) delay extension increases in high-rise buildings. Ref. [86] performed channel measurements using continuous waves with a center frequency of 2 GHz. Received power was measured in different propagation environments, including woods, and significant differences were observed between shadowing effects in the woods and uban buildings.

Studies have shown that the PLE in urban environments typically ranges from 2.5 to 3.5, which is higher than that in other scenarios. For example, measurements in urban areas at 2.4 GHz reveal a PLE of 3.2, indicating increased signal attenuation compared to free space. These conditions necessitate robust channel models that can capture the dynamic changes in signal propagation, making them essential for reliable communication system design.

4.2 Suburban Environment

In the suburban environment, A2G channels exhibit a blend of LoS and NLoS signal paths due to the mix of open spaces and scattered obstacles like trees and low-rise buildings. Measured PLE values here are moderate, typically between 2.0 and 2.5. CAI et al.[52] investigated the scenario of a low-altitude A2G UAV wireless channel on the outskirts of Madrid, Spain. Field experiments of UAVs flying above a cluster of containers with a carrier frequency of 5.76 GHz were conducted, and both narrowband and broadband measurements were performed, as shown in Fig. 5. In the vertical flight test, the UAV flew up and down from 0 to 50 m in altitude, while the UAV performed the horizontal test at a distance of 210 m. The authors investigated the large-scale fading effect in the UAV propagation channel and proposed an improved PL model and power delay profile (PDP). They also computed the PLE in the horizontal and vertical directions using the logarithmic distance path and the double-slope loss model, as shown in Eq. (4). They reported that for a UAV's performance in a particular environment, the delay dispersion increased with height as the UAV rised above the metal structure.

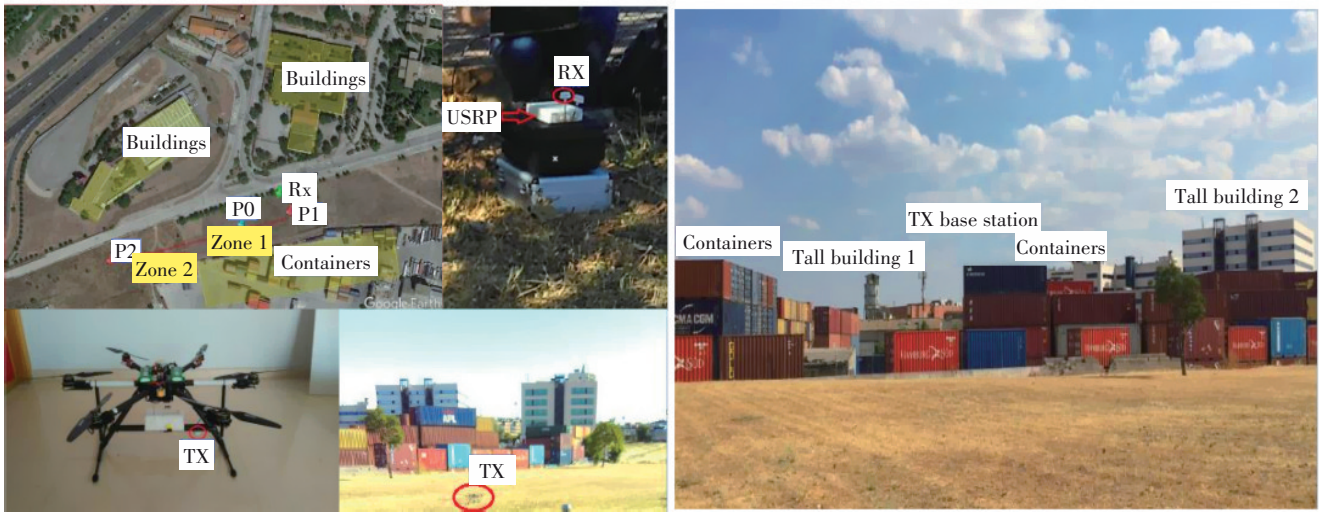

(a) Narrow band measurement scenario

(b) Broadband measurement scenario

RX: receiver TX: transmitter USRP: Universal Software Radio Peripheral

Figure 5. Measurement scenarios and equipment

$$PL(d) = \begin{cases} \alpha_{d_1} 10\log_{10}(d) + \beta_{d_1} + X_\sigma, \ d \leqslant d_1 \\ \alpha_{d_1} 10\log_{10}(d) + \beta_{d_1} + \alpha_{d_1} 10\log_{10}\left(\frac{d}{d_1}\right) + X_\sigma, \ d > d_1 \end{cases} \quad (4),$$

where d_1 is the fitted slope of the distance range between the two links separated by the threshold, α_{d_1} is the slope of the fit for the two link distance ranges separated by the threshold, β_{d_1} is the intercept, and X_σ is the random variable representing the variation in the fit. CHU et al.[79] conducted RT simulations in a simplified environment at ultralow altitudes (0 – 100 m) to analyze A2G channels with path loss, *K*-factors, multipaths, and delay extensions at 1.2 GHz and 4.2 GHz. The *K* factor denotes the power ratio of the LoS path to that of the other paths, as shown in Eq. (5).

$$K = \frac{P_{\text{LoS}}}{P_{\text{NLoS}}} \quad (5).$$

The RMS delay spread is calculated using Eq. (6):

$$\sigma_\tau = \sqrt{\overline{\tau} - \overline{\tau^2}} \quad (6).$$

Experiments show that the multipath component decreases with increasing altitude and eventually stabilizes at high altitude, which can be used to design wireless communication systems for mainstream small UAVs that are restricted to flying at specific altitudes. Ref. [58] presented a detailed measurement analysis of the A2GMIMO propagation channel. It was observed that the spatial decorrelation of the received signals at the GS is quite high due to the interaction of the non-planar wavefront resulting from the near-field effects of the measurement vehicles fitted with the GS antennas. More significant near-field effects are expected from more conventional aerial platforms. Interestingly, the authors suggested that at higher elevation angles, the placement of scatterers near the GS could produce greater spatial diversity.

In Ref. [86], MIMO system performance was tested in different scenarios in outdoor environments, including urban, rural, open field, and forest environments. The effect of terrain coverage on the received power was analyzed for these different scenarios. The results revealed that ground reflections play a central role in affecting the propagation channel model, whereas in forested areas, tree reflections and shadows are the primary factors influencing the propagation channel characteristics. Although there are differences between rural and urban environments, reflections from the walls and surfaces of buildings play an important role. In Ref. [87], a flight measurement campaign was described for an L-band A2G channel with a center frequency of 970 MHz, and the aerial measurements considered a rural environment similar to an airport, featuring a mix of large and small buildings and open grassy areas.

5 Research Directions for Future UAV Air-to-Ground Channel Modeling

In this chapter, we discuss possible future research directions for currently available A2G channel measurements and models. Our goal is to promote more comprehensive propagation

channel models for future UAV communication applications.

5.1 UAV Millimeter-Wave Channel Modeling

UAV mmWave communication, as a promising future communication technology, has received increasing attention in fields such as air base stations, wireless relays, emergency communications, and battlefield communications. UAVs often have LoS paths in the communication process due to their higher flight altitude, while the mmWave frequency band exhibits higher path loss and lower scattering characteristics, leading to higher requirements on LoS propagation conditions for mmWave communication systems. Therefore, UAVs can be an excellent platform for mmWave communication technology. However, there are currently few actual measurement campaigns for UAV A2G channels in the mmWave band. Ref. [69] presented a path loss model for mmWave channels based on measured data in the 28 GHz frequency band, but it did not consider the characteristics of small-scale fading. In UAV communication scenarios, the changes of channel characteristics are extremely sensitive to the variations in narrow beam pointing, and the cluster fading phenomenon is also more obvious, which significantly increases the difficulty and complexity of UAV channel modeling.

Ref. [70] discussed the delay power spectrum and signal angle distribution of UAV mmWave channels by reconstructing city, hill, forest, and ocean scenarios with the RT method. Compared with other types of channel models, the RT-based model has the advantages of high flexibility in scene construction and lower cost of data acquisition, but it faces challenges in analyzing small-scale fading.

Obtaining channel parameters for actual propagation scenarios is one of the key techniques for the accurate operation of UAV mmWave channel models. Although the RT-based prediction of mmWave propagation parameters is accurate, it is difficult to reflect the randomness and non-stationarity of the fast time-varying environment of UAVs. For UAV mmWave channels, the changes in channel characteristics caused by new scenarios are currently unknown. In the future, a large number of channel data can be generated using actual measurements or simulations, and the analysis of large-scale channel data using machine learning methods should be able to make better use of the spatial and angular information of the MPCs and the intrinsic correlation between the model parameters to discover new characteristics.

Combining the analysis with machine learning methods may be an effective means of investigating the stochastic and non-stationary nature of UAV channels. In conclusion, it is certain that the future development of UAV communication will be characterized by multi-scene applications, high mobility, high frequency, and multi-antenna technologies. Therefore, the establishment of suitable UAV mmWave channel modes plays an important role in the scheme design, performance optimization and evaluation verification of future UAV mmWave communication systems. Moreover, Ref. [88] upgraded the existing UAV channel model to an ultra-large-scale MIMO mmWave-terahertz oriented channel model, which is an important research direction in the future. The mmWave-terahertz communication can utilize the huge communication bandwidth to meet the application requirements of high-rate transmission and ultra-low latency.

However, the signal wavelength in the mmWave-terahertz band is extremely short. To mitigate this, Ref. [89] used beamforming to achieve high gain and combined it with massive MIMO technology to compensate for the high propagation loss of terahertz signals in practical applications. Currently, a 3D mmWave-terahertz channel model to support hyperscale MIMO wireless communication systems has been initially proposed in Ref. [90], in which the evolution of clusters in the spatial domain and the actual discrete phase shifts were taken into account.

5.2 Ultra-Wideband Technology

In addition to mmWave, ultra-wideband (UWB) technology is a research priority for future UAV A2G communication systems. The ability of UWB signals to capture MPC with good temporal resolution makes UWB an attractive technology for developing broadband propagation models. The large bandwidth of UWB also promotes high data rates, better penetration through materials, and coexistence with narrowband networks for UAV A2G communications. Although the UAV propagation channel has been studied in the literature, most of the existing work focuses on the path loss characteristics of the A2G channel, and there are almost no comprehensive and dedicated UWB channel models for UAV A2G propagation channels. KHAWAJA et al. developed random path loss and multipath channel models to characterize the A2G UWB propagation channel based on measured data[33]. However, the maximum altitude of UAV flight is only 16 m, and the communication range is short.

Meanwhile, current UWB propagation channel models developed for other scenarios[85, 91] cannot be applied to UAV A2G channels due to different propagation environments. Therefore, establishing a suitable UAV UWB channel model requires prior A2G channel measurements.

5.3 Advanced Modeling and Integration Strategies

Beyond mmWave and terahertz channel modeling, several other promising directions deserve attention. AI and machine learning can enhance the accuracy and efficiency of channel modeling by analyzing large datasets from measurement campaigns. This can help discover new characteristics of UAV channels and improve the predictive capabilities of channel models. Additionally, the integration of advanced antenna technologies like ultra-massive MIMO and intelligent reflecting surfaces (IRS) can significantly improve communication performance and optimize UAV communication

systems. Dynamic and adaptive channel models that incorporate the mobility of UAVs and the time-varying nature of the propagation environment are also crucial for providing more accurate predictions. Furthermore, exploring the integration of UAV communication systems with other technologies such as satellite communications and IoT networks can enhance the overall communication infrastructure and enable more diverse applications.

6 Conclusions

This paper comprehensively reviews the fundamentals and characteristics of UAV A2G channels, emphasizing their unique aspects compared to terrestrial channels, such as fully 3D scattering environments, flight trajectories, and body shadowing effects. We discuss the challenges of UAV channel measurement, including low-power and miniaturized environments, high-frequency bands with large bandwidths, transceiver synchronization, airframe shadowing, and dynamic scenarios. Additionally, we overview UAV channel measurements across different frequency bands and bandwidths and classify UAV A2G channel models based on various environments. Finally, we explore future research directions, including the potential of mmWave and terahertz technologies, ultra-wideband technologies, and the integration of advanced modeling strategies with machine learning to improve UAV channel modeling accuracy.

References

[1] ZENG Y, WU Q Q, ZHANG R. Accessing from the sky: a tutorial on UAV communications for 5G and beyond [J]. Proceedings of the IEEE, 2019, 107(12): 2327 – 2375. DOI: 10.1109/JPROC.2019.2952892
[2] KHAWAJA W, OZDEMIR O, ERDEN F, et al. Ultra-wideband air-to-ground propagation channel characterization in an open area [J]. IEEE transactions on aerospace and electronic systems, 2020, 56(6): 4533 – 4555. DOI: 10.1109/taes.2020.3003104
[3] ZHONG W Z, GU Y, ZHU Q M, et al. A novel spatial beam training strategy for mmWave UAV communications [J]. Physical communication, 2020, 41: 101106. DOI: 10.1016/j.phycom.2020.101106
[4] ZHU Q M, JIANG S, WANG C X, et al. Effects of digital map on the RT-based channel model for UAV mmWave communications [C]//Proc. International Wireless Communications and Mobile Computing (IWCMC). IEEE, 2020: 1648 – 1653. DOI: 10.1109/IWCMC48107.2020.9148461
[5] HUA B Y, ZHOU T T, ZHU Q M, et al. A realistic 3D non-stationary channel model for UAV-to-vehicle communications incorporating fuselage posture [J]. China communications, 2023, 20(6): 277 – 290. DOI: 10.23919/JCC.fa.2021-0290.202306
[6] ZHU Q M, MAO K, SONG M Z, et al. Map-based channel modeling and generation for U2V mmWave communication [J]. IEEE transactions on vehicular technology, 2022, 71(8): 8004 – 8015. DOI: 10.1109/TVT.2022.3174404
[7] LIN X Q, YAJNANARAYANA V, MURUGANATHAN S D, et al. The sky is not the limit: LTE for unmanned aerial vehicles [J]. IEEE communications magazine, 2018, 56(4): 204 – 210. DOI: 10.1109/MCOM.2018.1700643
[8] AMORIM R, NGUYEN H, MOGENSEN P, et al. Radio channel modeling for UAV communication over cellular networks [J]. IEEE wireless communications letters, 2017, 6(4): 514 – 517. DOI: 10.1109/LWC.2017.2710045
[9] ONO F, TAKIZAWA K, TSUJI H, et al. S-band radio propagation characteristics in urban environment for unmanned aircraft systems [C]//2015 International Symposium on Antennas and Propagation (ISAP). IEEE, 2015: 675 – 678
[10] TENG E, DIOGO FALCÃO J, IANNUCCI B. Holes-in-the-sky: a field study on cellular-connected UAS [C]//Proc. International Conference on Unmanned Aircraft Systems (ICUAS). IEEE, 2017: 1165 – 1174. DOI: 10.1109/ICUAS.2017.7991402
[11] KHUWAJA A A, CHEN Y F, ZHAO N, et al. A survey of channel modeling for UAV communications [J]. IEEE communications surveys & tutorials, 2018, 20(4): 2804 – 2821. DOI: 10.1109/COMST.2018.2856587
[12] NI G, DU Z, WANG D, et al. Simulation and analysis of ground and air communication channel characteristics [J]. Radio engineering, 2015, 45(6): 78 – 80+4. DOI:10.3969/j.issn.1003-3106.2015.06.21
[13] MATOLAK D W, SUN R Y. Air-ground channel characterization for unmanned aircraft systems—part III: the suburban and near-urban environments [J]. IEEE transactions on vehicular technology, 2017, 66(8): 6607 – 6618. DOI: 10.1109/TVT.2017.2659651
[14] TAKIZAWA K, KAGAWA T, LIN S, et al. C-band aircraft-to-ground (A2G) radio channel measurement for unmanned aircraft systems [C]// Proc. International Symposium on Wireless Personal Multimedia Communications (WPMC). IEEE, 2014: 754 – 758
[15] NEWHALL W G, MOSTAFA R, DIETRICH C, et al. Wideband air-to-ground radio channel measurements using an antenna array at 2 GHz for low-altitude operations [C]//Proc. IEEE Military Communications Conference. IEEE, 2003: 1422 – 1427. DOI: 10.1109/MILCOM.2003.1290436
[16] YANMAZ E, KUSCHNIG R, BETTSTETTER C. Achieving air-ground communications in 802.11 networks with three-dimensional aerial mobility [C]//Proc. IEEE INFOCOM. IEEE, 2013: 120 – 124. DOI: 10.1109/INFCOM.2013.6566747
[17] AHMED N, KANHERE S S, JHA S. On the importance of link characterization for aerial wireless sensor networks [J]. IEEE communications magazine, 2016, 54(5): 52 – 57. DOI: 10.1109/MCOM.2016.7470935
[18] MATOLAK D W, SUN R Y. Air-ground channel characterization for unmanned aircraft systems: the over-freshwater setting [C]//Proc. Integrated Communications, Navigation and Surveillance Conference (ICNS) Conference. IEEE, 2014. DOI: 10.1109/ICNSurv.2014.6819996
[19] HOLIS J, PECHAC P. Elevation dependent shadowing model for mobile communications via high altitude platforms in built-up areas [J]. IEEE transactions on antennas and propagation, 2008, 56(4): 1078 – 1084. DOI: 10.1109/TAP.2008.919209
[20] SIMUNEK M, PECHAC P, FONTAN F P. Excess loss model for low elevation links in urban areas for UAVs [J]. Radioengineering, 2011, 20(3): 561 – 568
[21] HE R S. Wireless channel measurement and modeling in mobile communication scenario: theory and application [M]. Beijing, China: Posts & Telecom Press, 2018
[22] YANMAZ E, KUSCHNIG R, BETTSTETTER C. Channel measurements over 802.11a-based UAV-to-ground links [C]//Proc. IEEE GLOBECOM Workshops (GC Wkshps). IEEE, 2011: 1280 – 1284. DOI: 10.1109/GLOCOMW.2011.6162389
[23] SUN R Y, MATOLAK D W. Air-ground channel characterization for unmanned aircraft systems part II: hilly and mountainous settings [J]. IEEE transactions on vehicular technology, 2017, 66(3): 1913 – 1925. DOI: 10.1109/TVT.2016.2585504
[24] CHENG X, WANG C X, LAURENSON D I, et al. Second order statistics of non-isotropic mobile-to-mobile ricean fading channels [C]//Proc. IEEE International Conference on Communications. IEEE, 2009: 1 – 5. DOI: 10.1109/ICC.2009.5199438
[25] GAO X J, CHEN Z L, HU Y J. Analysis of unmanned aerial vehicle MIMO channel capacity based on aircraft attitude [J]. WSEAS transactions on information science and applications, 2013, 10(2): 58 – 67
[26] BLANDINO S, KALTENBERGER F, FEILEN M. Wireless channel simu-

lator testbed for airborne receivers [C]//Proc. IEEE Globecom Workshops (GC Wkshps). IEEE, 2015: 1 – 6. DOI: 10.1109/GLOCOMW.2015.7413991
[27] WENTZ M, STOJANOVIC M. A MIMO radio channel model for low-altitude air-to-ground communication systems [C]//Proc. IEEE 82nd Vehicular Technology Conference (VTC2015-Fall). IEEE, 2015: 1 – 6. DOI: 10.1109/VTCFall.2015.7390797
[28] GULFAM S M, NAWAZ S J, AHMED A, et al. Analysis on multipath shape factors of air-to-ground radio communication channels [C]//Proc. Wireless Telecommunications Symposium (WTS). IEEE, 2016: 1 – 5. DOI: 10.1109/WTS.2016.7482050
[29] KSENDZOV A. A geometrical 3D multi-cluster mobile-to-mobile MIMO channel model with Rician correlated fading [C]//Proc. 8th International Congress on Ultra Modern Telecommunications and Control Systems and Workshops (ICUMT). IEEE, 2016: 191 – 195. DOI: 10.1109/ICUMT.2016.7765355
[30] TU H D, SHIMAMOTO S. A proposal of wide-band air-to-ground communication at airports employing 5-GHz band [C]//Proc. IEEE Wireless Communications and Networking Conference. IEEE, 2009: 1 – 6. DOI: 10.1109/WCNC.2009.4917538
[31] SIMUNEK M, FONTÁN F P, PECHAC P. The UAV low elevation propagation channel in urban areas: statistical analysis and time-series generator [J]. IEEE transactions on antennas and propagation, 2013, 61(7): 3850 – 3858. DOI: 10.1109/TAP.2013.2256098
[32] MATOLAK D W, SUN R Y. Air-ground channels for UAS: summary of measurements and models for L- and C-bands [C]//Proc. Integrated Communications Navigation and Surveillance (ICNS). IEEE, 2016. DOI: 10.1109/ICNSURV.2016.7486380
[33] KHAWAJA W, GUVENC I, MATOLAK D. UWB channel sounding and modeling for UAV air-to-ground propagation channels [C]//Proc. IEEE Global Communications Conference (GLOBECOM). IEEE, 2016: 1 – 7. DOI: 10.1109/GLOCOM.2016.7842372
[34] LEMOS CID E, ALEJOS A V, GARCIA SANCHEZ M. Signaling through scattered vegetation: empirical loss modeling for low elevation angle satellite paths obstructed by isolated thin trees [J]. IEEE vehicular technology magazine, 2016, 11(3): 22 – 28. DOI: 10.1109/MVT.2016.2550008
[35] HUANG Z Y, RODRÍGUEZ-PIÑEIRO J, DOMÍNGUEZ-BOLAÑO T, et al. Empirical dynamic modeling for low-altitude UAV propagation channels [J]. IEEE transactions on wireless communications, 2021, 20(8): 5171 – 5185. DOI: 10.1109/TWC.2021.3065959
[36] PINKNEY M F J, HAMPEL D, DIPIERRO S. Unmanned aerial vehicle (UAV) communications relay [C]//Proc. IEEE Military Communications Conference. IEEE, 1996: 47 – 51. DOI: 10.1109/MILCOM.1996.568581
[37] YANG J B, LIU P, MAO H. Model and simulation of narrowband ground-to-air fading channel based on Markov process [C]//Proc. International Conference on Network Computing and Information Security. IEEE, 2011. DOI: 10.1109/ncis.2011.37
[38] KUNISCH J, DE LA TORRE I, WINKELMANN A, et al. Wideband time-variant air-to-ground radio channel measurements at 5 GHz [C]//Proc. 5th European Conference on Antennas and Propagation (EUCAP). IEEE, 2011: 1386 – 1390
[39] BLUEMM C, HELLER C, FOURESTIE B, et al. Air-to-ground channel characterization for OFDM communication in C-Band [C]//Proc. 7th International Conference on Signal Processing and Communication Systems (ICSPCS). IEEE, 2013: 1 – 8. DOI: 10.1109/ICSPCS.2013.6723935
[40] WANG X Y. Analysis and research on channel modelling of low altitude air-ground communication system based on TD-LTE [D]. Shanghai, China: Shanghai Jiao Tong University, 2014
[41] ELNOUBI S M. A simplified stochastic model for the aeronautical mobile radio channel [C]//Proc. Vehicular Technology Society 42nd VTS Conference, Frontiers of Technology. IEEE, 1992: 960 – 963. DOI: 10.1109/VETEC.1992.245268
[42] ZAMAN M A, MAMUN S A, GAFFAR M, et al. Modeling VHF air-to-ground multipath propagation channel and analyzing channel characteristics and BER performance [C]//Proc. IEEE Region 8 International Conference on Computational Technologies in Electrical and Electronics Engineering (SIBIRCON). IEEE, 2010: 335 – 338. DOI: 10.1109/SIBIRCON.2010.5555104
[43] LI Y R, CHENG X. New deterministic and statistical simulation models for non-isotropic UAV-MIMO channels [C]//Proc. 9th International Conference on Wireless Communications and Signal Processing (WCSP). IEEE, 2017. DOI: 10.1109/wcsp.2017.8171101
[44] CHENG X, LI Y R. A 3-D geometry-based stochastic model for UAV-MIMO wideband nonstationary channels [J]. IEEE Internet of Things journal, 2019, 6(2): 1654 – 1662. DOI: 10.1109/JIOT.2018.2874816
[45] CAI X S, RODRÍGUEZ-PIÑEIRO J, YIN X F, et al. An empirical air-to-ground channel model based on passive measurements in LTE [J]. IEEE transactions on vehicular technology, 2019, 68(2): 1140 – 1154. DOI: 10.1109/TVT.2018.2886961
[46] YE X K, CAI X S, YIN X F, et al. Air-to-ground big-data-assisted channel modeling based on passive sounding in LTE networks [C]//Proc. IEEE Globecom Workshops (GC Wkshps). IEEE, 2017: 1 – 6. DOI: 10.1109/GLOCOMW.2017.8269204
[47] CUI Z Z, BRISO-RODRÍGUEZ C, GUAN K, et al. Multi-frequency air-to-ground channel measurements and analysis for UAV communication systems [J]. IEEE access, 2020, 8: 110565 – 110574
[48] QIU Z H, CHU X, CALVO-RAMIREZ C, et al. Low altitude UAV air-to-ground channel measurement and modeling in semiurban environments [J]. Wireless communications and mobile computing, 2017, 2017(1): 1587412. DOI: 10.1155/2017/1587412
[49] GUTIERREZ R M, YU H G, RONG Y, et al. Time and frequency dispersion characteristics of the UAS wireless channel in residential and mountainous desert terrains [C]//Proc. 14th IEEE Annual Consumer Communications & Networking Conference (CCNC). IEEE, 2017: 516 – 521. DOI: 10.1109/CCNC.2017.7983161
[50] RODRÍGUEZ-PIÑEIRO J, DOMÍNGUEZ-BOLAÑO T, CAI X S, et al. Air-to-ground channel characterization for low-height UAVs in realistic network deployments [J]. IEEE transactions on antennas and propagation, 2021, 69(2): 992 – 1006. DOI: 10.1109/TAP.2020.3016164
[51] TENG E, FALCAO J D, DOMINGUEZ C R, et al. Aerial sensing and characterization of three-dimensional RF fields [C]//Second International Workshop on Robotic Sensor Networks. RNS, 2015: 1 – 6
[52] CAI X S, GONZALEZ-PLAZA A, ALONSO D, et al. Low altitude UAV propagation channel modelling [C]//Proc. 11th European Conference on Antennas and Propagation (EUCAP). IEEE, 2017: 1443 – 1447
[53] KUNG H T, LIN C K, LIN T H, et al. Measuring diversity on a low-altitude UAV in a ground-to-air wireless 802.11 mesh network [C]//Proc. IEEE Globecom Workshops. IEEE, 2010: 1799 – 1804. DOI: 10.1109/GLOCOMW.2010.5700251
[54] GODDEMEIER N, WIETFELD C. Investigation of air-to-air channel characteristics and a UAV specific extension to the rice model [C]//Proc. IEEE Globecom Workshops (GC Wkshps). IEEE, 2015: 1 – 5. DOI: 10.1109/GLOCOMW.2015.7414180
[55] HAGUE D, KUNG H T, SUTER B. Field experimentation of cots-based UAV networking [C]//Proc. IEEE Military Communications conference. IEEE, 2006: 1 – 7. DOI: 10.1109/MILCOM.2006.302070
[56] AL-HOURANI A, GOMEZ K. Modeling cellular-to-UAV path-loss for suburban environments [J]. IEEE wireless communications letters, 2018, 7(1): 82 – 85. DOI: 10.1109/LWC.2017.2755643
[57] GAO X J, CHEN Z L, LV J W, et al. The correlation matrix model of capacity analysis in unmanned aerial vehicle MIMO channel [J]. WSEAS transactions on communications, 2012, 11(10/12): 476 – 485
[58] SCHNECKENBURGER N, JOST T, SHUTIN D, et al. Measurement of the l-band air-to-ground channel for positioning applications [J]. IEEE transactions on aerospace and electronic systems, 2016, 52(5): 2281 – 2297. DOI: 10.1109/TAES.2016.150451
[59] MENG Y S, LEE Y H. Measurements and characterizations of air-to-ground channel over sea surface at C-band with low airborne altitudes [J].

IEEE transactions on vehicular technology, 2011, 60(4): 1943 – 1948. DOI: 10.1109/TVT.2011.2136364
[60] AFONSO L, SOUTO N, SEBASTIAO P, et al. Cellular for the skies: exploiting mobile network infrastructure for low altitude air-to-ground communications [J]. IEEE aerospace and electronic systems magazine, 2016, 31(8): 4 – 11. DOI: 10.1109/MAES.2016.150170
[61] ZHU Q M, JIANG K L, CHEN X M, et al. A novel 3D non-stationary UAV-MIMO channel model and its statistical properties [J]. China communications, 2018, 15(12): 147 – 158
[62] JIN K, CHENG X, GE X H, et al. Three dimensional modeling and space-time correlation for UAV channels [C]//Proc. IEEE 85th Vehicular Technology Conference (VTC Spring). IEEE, 2017: 1 – 5. DOI: 10.1109/VTCSpring.2017.8108213
[63] JIANG K L, CHEN X M, ZHU Q M, et al. A geometry-based 3D non-stationary UAV-MIMO channel model allowing 3D arbitrary trajectories [C]//Proc 10th International Conference on Wireless Communications and Signal Processing (WCSP). IEEE, 2018: 1 – 6. DOI: 10.1109/WCSP.2018.8555639
[64] ZENG L Z, CHENG X, WANG C X, et al. A 3D geometry-based stochastic channel model for UAV-MIMO channels [C]//Pro. IEEE Wireless Communications and Networking Conference (WCNC). IEEE, 2017: 1 – 5. DOI: 10.1109/WCNC.2017.7925794
[65] CHENG X, LI Y R, WANG C X, et al. A 3-D geometry-based stochastic model for unmanned aerial vehicle MIMO ricean fading channels [J]. IEEE Internet of Things journal, 2020, 7(9): 8674 – 8687. DOI: 10.1109/JIOT.2020.2995707
[66] MA Z F, AI B, HE R S, et al. Impact of UAV rotation on MIMO channel characterization for air-to-ground communication systems [J]. IEEE transactions on vehicular technology, 2020, 69(11): 12418 – 12431. DOI: 10.1109/TVT.2020.3028301
[67] MA Z F, AI B, HE R S, et al. Three-dimensional modeling of millimeter-wave MIMO channels for UAV-based communications [C]//Proc. IEEE Global Communications Conference. IEEE, 2020. DOI: 10.1109/globecom42002.2020.9322621
[68] LI Y P, WANG W M, GAO H Q, et al. Air-to-ground 3D channel modeling for UAV based on Gauss-Markov mobile model [J]. AEU-international journal of electronics and communications, 2020, 114: 152995. DOI: 10.1016/j.aeue.2019.152995
[69] JIANG S, ZHU Q M, WANG C X, et al. Map-based UAV mmWave channel model and characteristics analysis [C]//Proc. IEEE/CIC International Conference on Communications in China (ICCC Workshops). IEEE, 2020. DOI: 10.1109/icccworkshops49972.2020.9209911
[70] JIANG H, ZHANG Z C, WU L, et al. Three-dimensional geometry-based UAV-MIMO channel modeling for A2G communication environments [J]. IEEE communications letters, 2018, 22(7): 1438 – 1441. DOI: 10.1109/LCOMM.2018.2828110
[71] BAI L, HUANG Z W, CHENG X. A non-stationary model with time-space consistency for 6G massive MIMO mmWave UAV channels [J]. IEEE transactions on wireless communications, 2023, 22(3): 2048 – 2064. DOI: 10.1109/TWC.2022.3208635
[72] MATOLAK D W, SUN R Y. Air-ground channel characterization for unmanned aircraft systems: the near-urban environment [C]//IEEE Military Communications Conference. IEEE, 2015: 1656 – 1660. DOI: 10.1109/MILCOM.2015.7357682
[73] FENG Q X, MCGEEHAN J, TAMEH E K, et al. Path loss models for air-to-ground radio channels in urban environments [C]//Proc. IEEE 63rd Vehicular Technology Conference. IEEE, 2006: 2901 – 2905. DOI: 10.1109/VETECS.2006.1683399
[74] DANIEL K, PUTZKE M, DUSZA B, et al. Three dimensional channel characterization for low altitude aerial vehicles [C]//Proc. 7th International Symposium on Wireless Communication Systems. IEEE, 2010: 756 – 760. DOI: 10.1109/ISWCS.2010.5624356
[75] AL-HOURANI A, KANDEEPAN S, JAMALIPOUR A. Modeling air-to-ground path loss for low altitude platforms in urban environments [C]//Proc. IEEE Global Communications Conference. IEEE, 2014: 2898 – 2904. DOI: 10.1109/GLOCOM.2014.7037248
[76] AL-HOURANI A, KANDEEPAN S, LARDNER S. Optimal LAP altitude for maximum coverage [J]. IEEE wireless communications letters, 2014, 3 (6): 569 – 572. DOI: 10.1109/LWC.2014.2342736
[77] AL-HOURANI A, CHANDRASEKHARAN S, KAANDORP G, et al. Coverage and rate analysis of aerial base stations (Letter) [J]. IEEE transactions on aerospace and electronic systems, 2016, 52(6): 3077 – 3081. DOI: 10.1109/TAES.2016.160356
[78] GODDEMEIER N, DANIEL K, WIETFELD C. Coverage evaluation of wireless networks for unmanned aerial systems [C]//Proc. IEEE Globecom Workshops. IEEE, 2010: 1760 – 1765. DOI: 10.1109/GLOCOMW.2010.5700244
[79] WILLINK T J, SQUIRES C C, COLMAN G W K, et al. Measurement and characterization of low-altitude air-to-ground MIMO channels [J]. IEEE transactions on vehicular technology, 2016, 65(4): 2637 – 2648
[80] ONO F, KAGAWA T, TSUJI H, et al. Measurements on C-band air-to-air channel for coexistence among multiple unmanned aircraft systems [C]//Proc. International Conference on Unmanned Aircraft Systems (ICUAS). IEEE, 2017: 1160 – 1164. DOI: 10.1109/ICUAS.2017.7991486
[81] YU C Y, LIU Y, CHANG H T, et al. AG channel measurements and characteristics analysis in hilly scenarios for 6G UAV communications [J]. China communications, 2022, 19(11): 32 – 46
[82] MAO K, ZHU Q M, QIU Y H, et al. A UAV-aided real-time channel sounder for highly dynamic nonstationary A2G scenarios [J]. IEEE transactions on instrumentation and measurement, 2023, 72: 1 – 15. DOI: 10.1109/TIM.2023.3301592
[83] LYU Y, WANG W, SUN Y Z, et al. Low-altitude UAV air-to-ground multilink channel modeling and analysis at 2.4 and 5.9 GHz [J]. IEEE antennas and wireless propagation letters, 2023, 22(9): 2135 – 2139. DOI: 10.1109/LAWP.2023.3278330
[84] MOLISCH A F, ASPLUND H, HEDDERGOTT R, et al. The COST259 directional channel model-part I: overview and methodology [J]. IEEE transactions on wireless communications, 2006, 5(12): 3421 – 3433. DOI: 10.1109/TWC.2006.256966
[85] SIMUNEK M, FONTAN F P, PECHAC P, et al. Space diversity gain in urban area low elevation links for surveillance applications [J]. IEEE transactions on antennas and propagation, 2013, 61(12): 6255 – 6260. DOI: 10.1109/TAP.2013.2280874
[86] ZELENY J, PEREZ-FONTAN F, PECHAC P. Initial results from a measurement campaign for low elevation angle links in different environments [C]//Proc. 9th European Conference on Antennas and Propagation (EuCAP). IEEE, 2015: 1 – 4
[87] KO J, HUR S, LEE S, et al. 28 GHz channel measurements and modeling in a ski resort town in pyeongchang for 5G cellular network systems [C]//Proc. 10th European Conference on Antennas and Propagation (EuCAP). IEEE, 2016: 1 – 5
[88] ZHU Q M, NI H R, HUA B Y. A survey of UAV millimetre-wave channel measurement and modeling [J]. Mobile communications, 2022, 46 (12): 1 – 11
[89] FAISAL A, SARIEDDEEN H, DAHROUJ H, et al. Ultramassive MIMO systems at terahertz bands: prospects and challenges [J]. IEEE vehicular technology magazine, 2020, 15(4): 33 – 42. DOI: 10.1109/MVT.2020.3022998
[90] SUN Y Z, WANG C X, HUANG J, et al. A 3D non-stationary channel model for 6G wireless systems employing intelligent reflecting surfaces with practical phase shifts [J]. IEEE transactions on cognitive communications and networking, 2021, 7(2): 496 – 510. DOI: 10.1109/TCCN.2021.3075438
[91] CHAIBI H, BELKASMI M, MOHAMMADI Z. UWB outdoor channel characterization and modeling based on measurements [C]//Proc. International Conference on Wireless Networks and Mobile Communications (WINCOM). IEEE, 2015: 1 – 5. DOI: 10.1109/WINCOM.2015.7381298

Biographies

CHEN Peng graduated from the School of Marine Science and Technology, Northwestern Polytechnical University, China in 2013, majoring in information countermeasures technology. He received a PhD degree in underwater acoustic engineering also from Northwestern Polytechnical University in 2019, supervised by Academician MA Yuanliang, a renowned expert in airborne sonar. He then joined Chang'an University for postdoctoral research on civil engineering integrated with advanced acoustic/optical sensing at its wind tunnel laboratory. His research interests include low-altitude drones, marine channels, and highway bridge monitoring, integrating multidisciplinary technologies such as acoustics, radio frequency, optics, and fiber-optic sensing. He has published over 10 SCI/EI papers as the first author in top journals (e.g., *IEEE TVT*, *IEEE SPL*) and led/participated in multiple national/provincial research projects, including the National Natural Science Foundation of China and the China Postdoctoral Science Foundation.

LIU Yajuan received her BS degree in information and communication engineering from Tiangong University, China in 2023. She is currently pursuing a master's degree at Chang'an University, China, focusing on the research of coherent doppler wind lidar research at the School of Information Engineering. Her research interests include optical signal processing, lidar-based atmospheric monitoring, and computational methods for wind profiling.

WEI Wentong received his bachelor's degree in communication engineering from Zhejiang Sci-Tech University, China in 2023. He is currently pursuing a master's degree in information and communication engineering at Chang'an University, China. His research interests include wireless communication, channel modeling, and signal processing, with a focus on channel characteristics, particularly in the context of wireless communication systems. He has presented his research work on channel modeling and analysis at the International Symposium on Antennas and Propagation (ISAPE).

WANG Wei (wei.wang@chd.edu.cn) received his bachelor's degree in communications engineering from Wuhan University, China in 2003, master's degree from the University of Kiel, Germany in 2006, and doctoral degree (summa cum laude) from the University of Erlangen-Nuremberg, Germany in 2014. From 2007 to 2018, he was a scientific staff member with the Institute of Communications and Navigation, German Aerospace Center (DLR). He is currently a professor with the School of Information Engineering, Chang'an University, China. His current research interests include time-variant parameter estimation, channel modeling for localization and navigation, channel measurements, terrestrial radio-based positioning/navigation, and related topics. He received the Best Presentation Paper Award in ION GNSS 2012 and the Best Paper Award in EUCAP 2018 and COTA 2018. He is an associate editor of the *IET Microwave, Antennas and Propagation*. He served as a TPC Member for ICC and VTC conferences and workshops.

LI Na received her master's degree in information and communication engineering from Chang'an University, China in 2024. Her research interests include wireless communication, channel modeling, and UAV communication systems, building on her master's thesis in UAV air-to-ground channel analysis and modeling in campus scenes.

Liquid Neural Networks: Next-Generation AI for Telecom from First Principles

ZHU Fenghao, WANG Xinquan, ZHU Chen, HUANG Chongwen
(Zhejiang University, Hangzhou 310027, China)

DOI: 10.12142/ZTECOM.202502008
https://kns.cnki.net/kcms/detail/34.1294.TN.20250430.1349.002.html, published online April 30, 2025
Manuscript received: 2025-04-01

Abstract: Recently, a novel type of neural networks, known as liquid neural networks (LNNs), has been designed from first principles to address robustness and interpretability challenges facing artificial intelligence (AI) solutions. The potential of LNNs in telecommunications is explored in this paper. First, we illustrate the mechanisms of LNNs and highlight their unique advantages over traditional networks. Then we explore the opportunities that LNNs bring to future wireless networks. Furthermore, we discuss the challenges and design directions for the implementation of LNNs. Finally, we summarize the performance of LNNs in two case studies.

Keywords: artificial intelligence (AI); liquid neural networks (LNNs); telecommunications; wireless networks

Citation (Format 1): ZHU F H, WANG X Q, ZHU C, et al. Liquid neural networks: next-generation AI for telecom from first principles [J]. ZTE Communications, 2025, 23(2): 76 - 84. DOI: 10.12142/ZTECOM.202502008
Citation (Format 2): F. H. Zhu, X. Q. Wang, C. Zhu, et al., "Liquid neural networks: next-generation AI for telecom from first principles," *ZTE Communications*, vol. 23, no. 2, pp. 76 - 84, Jun. 2025. doi: 10.12142/ZTECOM.202502008.

1 Introduction

The 6G wireless communication network is envisioned to revolutionize the telecommunication landscape by incorporating a wide range of advanced communication capabilities. These enhancements are expected to support enriched and immersive experiences, ensure ubiquitous and seamless coverage, and enable innovative collaboration[1]. One of the primary catalysts is incorporating technologies driven by artificial intelligence (AI). By harnessing AI, 6G aims to overcome the limitations of current networks, offering ultra-reliable and low-latency communication, extensive connectivity for massive IoT devices, and significantly improved mobile broadband services[2]. This integration will facilitate groundbreaking applications such as holographic telepresence, tactile internet, intelligent autonomous systems, and smart cities. By leveraging AI, 6G networks will not only optimize performance and enhance data processing efficiency but also ensure adaptive, secure, and robust communication environments[3 - 5]. The synergy between AI and 6G will pave the way for unprecedented connectivity and intelligent communication solutions, fundamentally transforming industries and society as a whole.

The work was supported by the China National Key R&D Program under Grant Nos. 2021YFA1000500 and 2023YFB2904804, National Natural Science Foundation of China under Grant Nos. 62331023, 62101492, 62394292 and U20A20158, Zhejiang Provincial Natural Science Foundation of China under Grant No. LR22F010002, and Zhejiang Provincial Science and Technology Plan Project under Grant No. 2024C01033.

Although AI has exhibited great potential in reshaping the next generation of wireless networks, deploying it in practical communication scenarios remains challenging[6 - 8]. Fig. 1 shows the 6G communication scenarios with AI integration. These challenges arise primarily due to several factors, as outlined below.

1) Robustness: Current AI models often struggle to maintain performance in dynamic and unpredictable environments with varying data distributions[9]. In practical wireless networks, user mobility, signal condition changes, and interference can cause significant variations in the data fed into AI models. This lack of robustness can lead to substantial performance degradation, making it difficult to ensure reliable operation[6]. For instance, an AI model trained under certain static conditions may fail to adapt when deployed in a real-world setting where wireless parameters continuously change. Addressing this issue requires the development of adaptive AI models that can learn and generalize from a wide range of conditions and data patterns.

2) Interpretability: The black-box nature of many AI algorithms poses significant challenges in understanding and explaining their decision-making processes[7]. This lack of interpretability raises concerns about the safety, transparency, and fairness of AI-driven solutions in communication systems. In wireless networks, where decisions can impact a wide range of users and services, it is crucial to ensure that AI models make decisions that are understandable and justifiable. For example, in the context of spectrum resource allocation in com-

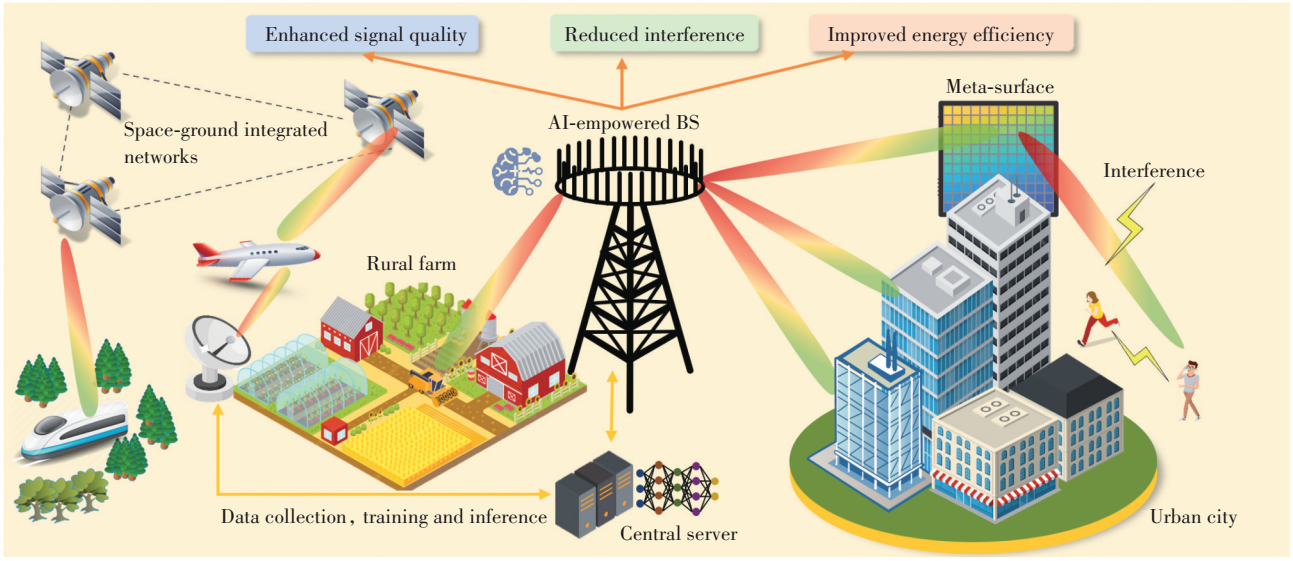

AI: artificial intelligence BS: base station

Figure 1. 6G communication scenarios with AI integration

munications, the AI system should make fair and efficient decisions. Enhancing the interpretability of AI models involves developing methods to provide insights into the inner working and decision criteria of the models.

3) Complexity: AI models, particularly deep learning architectures, require substantial computational resources and complex infrastructure for training and deployment. Training deep neural networks can be computationally intensive and time-consuming, often necessitating specialized hardware such as graphics processing units (GPUs) or tensor processing units (TPUs). Moreover, the deployment of these models in practical wireless networks must contend with constraints such as limited bandwidth, low latency requirements, and the need for real-time processing[8]. This high complexity hinders their practical implementation, especially in edge computing scenarios where computational resources are limited. Simplifying AI models and optimizing their performance to run efficiently on resource-constrained devices are critical areas of research.

Addressing these challenges is crucial for the successful integration of AI into next-generation wireless networks, paving the way for more reliable, transparent, and efficient communication systems. Overcoming these hurdles will allow AI to revolutionize wireless communication, enhancing user experiences and network performance and enabling innovative applications and services. In this article, we provide an overview of the recently proposed liquid neural networks (LNNs)[10–12], which are designed from first principles to be robust, interpretable, and resource-efficient, making them well-suited for the dynamic and complex nature of wireless communication environments. We explore the opportunities that LNNs bring to future wireless networks and discuss the challenges and design directions for their implementation.

The rest of this paper is organized as follows. Section 2 provides an overview of traditional neural networks and their limitations. Section 3 describes the design of LNNs, and Section 4 presents the features and benefits of LNNs. The opportunities that LNNs bring to the future wireless networks are explored in Section 5. Section 6 discusses the main challenges associated with LNN-based communication systems and outlines potential future research directions. Case studies are presented in Section 7 to verify the performance of LNNs. Finally, Section 8 concludes the paper.

2 Overview of Traditional Neural Networks

Traditional neural networks are fundamental in the development of AI technologies, each offering unique strengths for various applications. Below, we discuss four primary types of traditional neural networks: feedforward neural networks (FNNs), convolutional neural networks (CNNs), recurrent neural networks (RNNs), and ordinary differential equation neural networks (ODE-NNs).

2.1 Feedforward Neural Networks

FNNs are the simplest type of artificial neural network architecture. In FNNs, the information moves in one direction: from input nodes, through hidden nodes (if any), to output nodes[13]. There are no cycles or loops in the network. This structure makes FNNs suitable for simple pattern recognition tasks, such as image classification or function approximation. However, they may struggle with tasks requiring memory or temporal dependencies due to their lack of internal hidden states.

2.2 Convolutional Neural Networks

CNNs are specialized for processing structured grid data

like images. They utilize convolutional layers that apply filters to the input data to capture spatial hierarchies of features[14]. CNNs are highly effective in image and video recognition, owing to their ability to learn spatial hierarchies and patterns. The architecture includes convolutional layers, pooling layers, and fully connected layers. CNNs are known for their robustness in handling variations in image data, such as shifts, scales, and distortions.

2.3 Recurrent Neural Networks

RNNs are designed to handle sequential data and capture temporal dependencies. Unlike FNNs, RNNs have connections that form directed cycles, allowing information to persist across different steps in the sequence. This makes RNNs powerful for tasks like time series data, natural language processing, and speech recognition[15]. However, traditional RNNs may suffer from vanishing and exploding gradients, which hinders their performance on long sequences. To address these issues, variants such as long short-term memory (LSTM) networks and gated recurrent units (GRUs) are developed. LSTMs introduce gating mechanisms to manage long-term dependencies, while GRUs simplify the architecture for computational efficiency. Despite these improvements, both LSTMs and GRUs have limitations, including the inability to model continuous-time dynamics and reduced robustness in highly dynamic environments[16].

2.4 Ordinary Differential Equation Neural Networks

ODE-NNs are designed to model continuous-time dynamics, addressing limitations of traditional RNNs[17]. Continuous-time recurrent neural networks (CT-RNNs) and ODE-LSTM networks are key examples. CT-RNNs use ordinary differential equations (ODEs) to capture continuous-time sequences, making them suitable for irregular time intervals, but they are computationally intensive due to the need for numerical solvers. ODE-LSTMs integrate continuous-time modeling into the LSTM framework, enhancing their ability to handle continuous dependencies. Despite these improvements, ODE-LSTMs and CT-RNNs face challenges such as increased computational complexity and potential training instability, which can limit their effectiveness and robustness in highly dynamic environments.

3 Design of LNNs

LNNs are uniquely designed based on first principles, fundamentally differing from other models in neuron operation[10]. First principles derive properties and behaviors directly from fundamental laws of nature, ensuring that the design is grounded in the most essential elements. Inspired by the dynamic and adaptive nature of biological neural systems, LNNs mimic the information transmission mechanisms observed at synapses in the nematode Caenorhabditis elegans. This approach enables LNNs to emulate the flexibility and resilience of natural neural networks. Unlike static architectures, LNNs exhibit dynamic adaptability through continuous self-reconfiguration in real-time input scenarios, maintaining high performance and robustness in dynamic and unpredictable environments. This adaptability makes LNNs particularly well-suited for real-world applications where conditions constantly change. Currently, there are three types of liquid neural networks: liquid time-constant neural networks (LTCs), closed-form continuous-time neural networks (CfCs), and neural circuit policies (NCPs).

3.1 Liquid Time-Constant Neural Networks

Fig. 2 illustrates the basic information flow of a liquid neu-

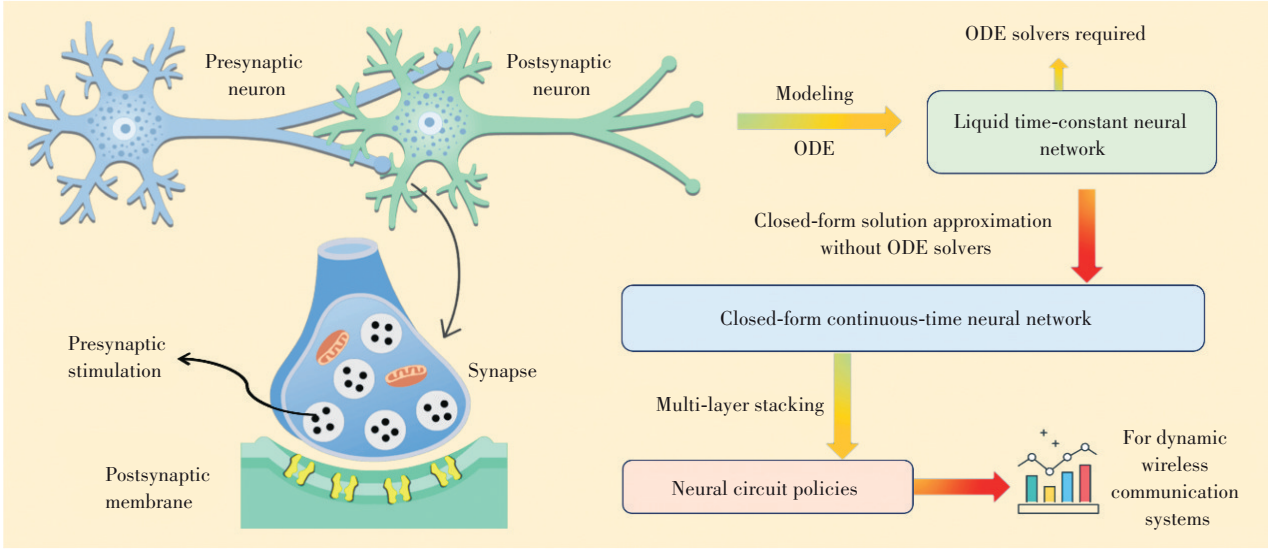

ODE: ordinary differential equation

Figure 2. Liquid neuron and the ODE modeling

ron, which serves as the fundamental building block of LTCs. In this model, a presynaptic neuron transmits information to a postsynaptic neuron via the synapse between them, using presynaptic stimuli. The potential of the postsynaptic membrane acts as a dynamic variable, representing the hidden states in the corresponding neural networks. This entire process is described by an ODE, which captures the dynamic and non-linear interactions between neurons. LTCs have demonstrated exceptional flexibility and generalizability, particularly in applications such as vehicle autopilot and vehicular communications. These networks can adapt to changing external conditions with remarkable efficiency. Notably, LTCs have achieved high-fidelity autonomy in complex autonomous systems with as few as 19 liquid neurons[11]. This capability can be extended to enhance vehicle-to-everything (V2X) communications, where LTCs can optimize data transmission and processing in dynamic, real-time environments. By integrating LTCs into next-generation wireless communication systems, vehicles can achieve seamless connectivity, improve network performance, and attain robust decision-making processes. This enables sophisticated or task-specific operations even under diverse and fluctuating conditions.

3.2 Closed-Form Continuous-Time Neural Networks

While LTCs can adapt to changing environments, their lack of closed-form solutions requires computationally intensive iterative solvers for forward propagation and back propagation. To address this issue, a closed-form solution was proposed to approximate the true solution of the ODE[12], as illustrated in Fig. 2. The closed-form expression successfully circumvents the high overhead of traditional ODE solvers and approximates the solution with a few parameters. To take advantage of existing deep learning tools and theories, CfCs are represented by a specially designed deep neural network structure, as depicted in Fig. 3. This innovative approach significantly reduces computational complexity while maintaining the adaptability and robustness characteristic of liquid neural networks, making CfCs highly suitable for real-time applications in dynamic environments.

3.3 Neural Circuit Policies

To further exploit the potential of LTCs and CfCs, NCPs are designed to integrate multiple CfC or LTC neurons into several layers. An example of an NCP comprising multiple CfC neurons is illustrated in Fig. 3. A typical NCP features four distinct layers: the sensory neuron layer, the inter neurons layer, the command neurons layer, and the motor neurons layer. These layers feature sparse connections both within and between them, mimicking the sparse connectivity observed in biological neural networks. This design reduces computational complexity and accelerates information exchange and fusion. NCPs have demonstrated robust flight navigation capabilities when presented with out-of-distribution data, generalizing effectively to scenarios that were not encountered during training[18]. This ability to handle new and diverse conditions makes NCPs highly valuable for applications requiring high adaptability and real-time processing in dynamic environments.

4 Features and Benefits of LNNs

LNNs stand out due to their unique design and operational principles, which endow them with several distinct features and benefits over traditional neural network models. These characteristics make LNNs exceptionally well-suited for the dynamic and complex nature of modern wireless communica-

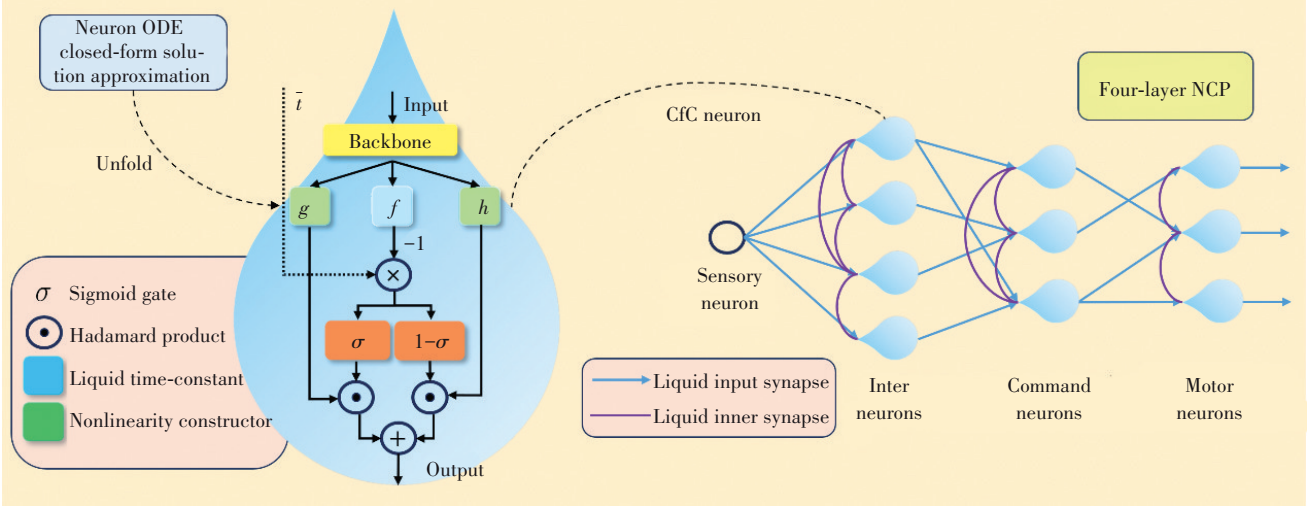

CfC: closed-form continuous-time neural network NCP: neural circuit policy ODE: ordinary differential equation

Figure 3. Structure of a CfC neuron and a four-layer NCP

tion systems. In this section, we delve into the key features and benefits of LNNs as follows.

4.1 Superior Generalizability and Robustness

LNNs exhibit superior generalizability and robustness over traditional neural networks, primarily due to their biologically inspired design that allows continuous adaptation to new and varying inputs[18]. This dynamic and adaptive nature mimics biological neural systems, enabling LNNs to generalize effectively across different conditions and environments. Such adaptability and resilience are particularly valuable in wireless communications, where network conditions and user demands can change rapidly. LNNs maintain high performance even when faced with data that deviate significantly from the training set, making them ideal for real-world applications where unpredictability is the norm. For instance, in dynamic spectrum access and adaptive beamforming, LNNs can adjust to varying spectrum availability and signal conditions in real-time, ensuring optimal communication performance. Moreover, their ability to continuously reorganize and adapt enhances their robustness, allowing them to handle unexpected changes and disturbances effectively. This capability is crucial for maintaining reliable communication links in highly dynamic and unpredictable environments like emergency response scenarios. In such cases, LNNs can adapt to fluctuating network topologies and varying signal conditions, ensuring the delivery of critical information and maintaining robust and resilient communication networks.

4.2 Enhanced Expressivity

LNNs exhibit enhanced expressivity compared with traditional neural networks due to their ability to dynamically adapt to incoming data and capture intricate temporal patterns. This expressivity is evident in their ability to generate complex latent space trajectories when exposed to various input patterns. For example, LNNs produce significantly more detailed and longer trajectories than models like neural ODEs and continuous-time RNNs[10], indicating a higher capacity for nuanced temporal representation. This enhanced expressivity directly contributes to their ability to quickly adapt to changing conditions. The complex internal representations allow LNNs to effectively process and integrate new information, enabling rapid adjustments to new inputs and environments. In wireless communication, this means LNNs can adapt to rapidly changing network conditions and user behaviors, ensuring consistent and reliable performance.Furthermore, the continuous adaptation mechanisms of LNNs, inspired by biological neural systems, support their superior expressivity. This adaptability enables LNNs to maintain high levels of detail and accuracy in their representations, even in dynamic and unpredictable environments, making them ideal for complex and varied tasks in advanced telecommunication applications.

4.3 Improved Interpretability

LNNs also offer significantly improved interpretability, an advantage particularly important for applications requiring transparency and trust. The interpretability of LNNs arises from their ability to disentangle complex neural dynamics into comprehensible and distinct behaviors. By leveraging techniques such as decision trees to analyze neural policies, LNNs can provide clear and logical explanations for their decision-making processes[7]. This enhanced interpretability is essential for understanding and debugging model behavior, especially in safety-critical systems like robotics, autonomous driving, and dynamic wireless communication networks. In the context of telecommunications, interpretability is crucial for ensuring reliable network performance and facilitating troubleshooting. For instance, understanding how LNNs manage spectrum allocation or adjust beamforming in real-time can help network operators optimize resource usage and maintain robust connectivity. Disentangling neural responses into identifiable strategies and behaviors allows for a more precise evaluation of how well these networks capture and represent underlying task dynamics in communication systems. This capability not only boosts the trustworthiness of LNNs but also facilitates their deployment in real-world scenarios where understanding the rationale behind decisions is crucial for maintaining high-performance and reliable wireless communications.

4.4 Lower Complexity

LNNs benefit from lower computational complexity due to their efficient design, arising from several factors. First, the sparse connectivity within and between the layers of NCPs reduces computational overhead, making the networks more efficient without compromising performance. Second, the closed-form solutions used in LNNs eliminate the need for complex iterative solvers typically required for solving ODEs, further lowering computational complexity. Additionally, LNNs possess strong expressive power, enabling them to perform complex tasks with fewer neurons, significantly reducing the overall size of the network. This combination of factors is particularly beneficial in applications requiring real-time processing and decision-making, such as V2X communications and dynamic wireless networks. In telecommunications, lower complexity translates to faster processing speed and reduced energy consumption, which are critical for the scalability and sustainability of next-generation networks[19]. Efficient resource allocation, real-time traffic management, and rapid handovers in mobile networks all benefit from the lower complexity of LNNs, leading to more efficient and robust communication systems. Moreover, the low complexity and efficient design of LNNs contribute to energy savings and environmental sustainability. This makes LNNs suitable for deployment in environments with limited computational and energy resources, including edge devices and IoT sensors, where computational power and battery life are constrained. By reducing

energy consumption, LNNs support a wide range of applications, from smart cities to remote monitoring systems, without overwhelming the network infrastructure, thereby promoting greener and more sustainable technology solutions.

4.5 Continuous-Time Modeling

One of the distinctive features of LNNs is their continuous-time modeling capability. Unlike traditional neural networks that operate in discrete time steps, LNNs leverage ODEs to model the dynamic interactions between neurons. This allows LNNs to capture the continuous and fluid nature of real-world processes more accurately. Continuous-time modeling is particularly advantageous in scenarios requiring high temporal resolution and precision, such as real-time autonomous systems and adaptive communication networks[16]. In telecommunications, continuous-time modeling enables more precise channel estimation, interference management, and adaptive modulation schemes. By modeling the system dynamics in continuous time, LNNs can respond more naturally and effectively to the ever-changing conditions of the environment, ensuring optimal performance in rapidly varying communication scenarios[20].

In summary, LNNs offer distinct features and benefits that make them exceptionally suitable for next-generation wireless communication systems. Their superior generalizability, interpretability, lower complexity, continuous-time modeling, enhanced robustness, and efficient resource utilization position them as a transformative technology. By integrating LNNs into telecommunications, we can achieve more adaptive, reliable, and efficient networks that meet the demands of future wireless communication environments.

5 LNNs for Wireless Communications

In this section, we unveil the opportunities that LNNs bring to the evolution and enhancement of future wireless networks. Specifically, we introduce two key topics: integrated sensing and communication (ISAC) and self-organizing networks (SONs).

5.1 ISAC

ISAC represents a paradigm shift in wireless network design, merging communication and sensing functionalities into a unified framework to enhance spectral efficiency (SE) and reduce hardware costs[21 - 22]. With the biologically inspired architecture and low computational complexity, LNNs are ideally suited for ISAC systems. Their ability to learn and adapt in real time, handle complex and dynamic environments, and generalize effectively makes them ideal for optimizing resource allocation between communication and sensing functions, thus improving SE without extensive computational resources. The adaptability and interpretability of LNNs are crucial for applications like autonomous driving, where precise and reliable sensing is critical for safety, as they can learn from historical data and adapt to new conditions, enhancing sensing accuracy and reliability. In wireless communication, LNNs manage interference, optimize transmission parameters, and ensure robust links, maintaining high quality of service (QoS) even in challenging environments. Their low computational complexity shortens processing time and reduces energy consumption, which is essential for scalable and sustainable next-generation green networks. It is promising to develop joint sensing and communication algorithms, real-time learning and adaptation frameworks, and ensure compatibility with existing network infrastructure and protocols with LNNs. These advancements can lead to more efficient, reliable, and versatile wireless networks.

5.2 SONs

SONs represent a kind of wireless network characterized by their ability to adapt and evolve autonomously in response to changing environmental conditions, network demands, and user behaviors. Unlike traditional static network configurations, these networks can dynamically reconfigure themselves, optimize resource allocation, and maintain robust performance without human intervention. With the continuous adaptation and learning capabilities, LNNs are uniquely suited for implementing SONs. Their biologically inspired architecture allows them to learn and adjust in real time, providing seamless adaptability to varying network conditions. This is particularly crucial in wireless environments where factors such as signal interference, user mobility, and fluctuating demand can significantly impact network performance. For instance, in SONs, LNNs can be employed to predict and address potential network congestion in advance by reallocating resources or adjusting transmission parameters. They can also enhance QoS by dynamically adapting to the quality of the communication links and optimizing handovers in mobile networks. Moreover, LNNs can facilitate proactive maintenance of the communication systems by identifying and mitigating faults or anomalies before they escalate into significant issues. To sum up, SONs powered by LNNs are envisioned to revolutionize wireless communication by enabling networks that are not only more resilient and efficient but also capable of autonomously evolving to meet the ever-changing demands of users and applications. This represents a significant step towards the realization of truly intelligent and adaptive wireless networks.

6 Challenges and Future Research Directions

In this section, we present some of the main challenges associated with LNN-based communication systems and outline potential future research directions. The following subsections delve into specific areas where advancements are needed to fully realize the potential of LNNs in wireless communication.

6.1 Zero Shot Learning

Zero-shot learning (ZSL) describes a model's ability to recognize and categorize data from classes it has never seen be-

fore. This feature is fundamental for LNNs operating in ever-changing and uncertain wireless communication environments. Traditional machine learning approaches often rely on vast numbers of labeled data for every new scenario, a requirement that is not always practical. Although LNNs have the capacity to handle out-of-distribution data, a deeper understanding of the principles behind this ability is necessary. Enhancing these principles enables models to effectively generalize from sparse data and transfer insights gained from past experiences to novel situations. Moreover, combining LNNs with data augmentation strategies holds promise for boosting overall performance, ensuring that the knowledge acquired remains applicable to new challenges without significant degradation. Finally, establishing rigorous evaluation frameworks is essential for accurately measuring the ZSL capabilities of LNNs in real-world wireless communication settings.

6.2 Distributed LNNs

Distributing LNNs across various devices and nodes is vital for modern large-scale wireless communication systems. This approach not only boosts scalability, fault resilience, and efficient resource use but also introduces challenges in effective coordination and synchronization. To harness the full potential of distributed LNNs, it is crucial to develop specialized learning algorithms that reduce both communication overhead and latency while implementing robust fault tolerance and dynamic resource management strategies. Federated learning presents an attractive solution by enabling multiple devices to collaboratively train LNNs locally, thereby slashing communication costs and enhancing data privacy. Focusing research on these areas will significantly improve the practical deployment of distributed LNNs in complex wireless environments.

6.3 Multi-Modality Fusion

Combining data from multiple modalities (such as sensor data, audio, video, and text) in wireless communication systems can significantly improve the performance and reliability of LNNs. By drawing on these diverse information sources, LNNs develop a richer perspective of the communication environment. However, designing architectures that effectively handle and integrate multi-modal data poses both a challenge and an opportunity. Achieving this goal involves tackling data synchronization and fusion issues across different modalities while ensuring that incorporating multi-modal data enhances overall performance without adding excessive complexity[23].

6.4 Training and Inference Latency

A critical area demanding focused future investigation for LNN deployment in 6G is the operational latency, a factor paramount for practical feasibility. Specifically, while LNNs offer unique continuous-time processing, their inference speed must be carefully evaluated. The computational time for numerically solving the underlying ODEs needs direct measurement and comparison against the stringent, often sub-millisecond, real-time response requirements of demanding 6G applications like ultra-reliable low latency communications (URLLC) or real-time network control. Achieving the necessary inference speeds may require dedicated research into optimized numerical solvers tailored for LNNs, exploring model simplification or approximation techniques, and leveraging hardware acceleration platforms. Equally important and currently underexplored, is the comprehensive evaluation of the end-to-end training latency. This encompasses the time consumed by the training algorithm itself, the necessary steps of data collection and processing, and the subsequent phase of model evaluation. Understanding this complete time cycle is vital, as the highly dynamic nature of 6G environments will likely necessitate frequent model retraining or adaptation to maintain optimal performance. Therefore, future research must dedicate significant effort to quantifying both the inference speed on relevant hardware and the practical duration of the full training pipeline for typical 6G tasks, thereby validating the viability of LNNs within next-generation telecommunication systems.

7 Case Studies

In this section, we summarize the performance of LNNs in two typical application scenarios.

7.1 Channel Prediction with LTCs

We assume an urban microcell scenario where an outdoor base station (BS) serves both outdoor and indoor users[24]. A user is connected to the BS and moves in a random walk with a speed of 2 m/s, with the direction uniformly distributed between 0 and 2π radians from its initial position. Historical channel state information (CSI) feedback with a length of 20 is utilized to predict future CSI with a length of 5. The test was conducted in a real-world scenario using practical CSI. The field test simulation parameters are summarized in Table 1. Fig. 4 illustrates the mean squared error (MSE) versus CSI prediction length in channel prediction. It is evident that the MSE of all schemes increases with prediction length, indicating that longer prediction lengths introduce more uncertainty. Among all schemes, the proposed LTCs-based approach consistently outperforms other baselines, achieving lower MSE, with the performance gap widening as the prediction length increases, particularly when it exceeds 6. This highlights the po-

Table 1. Simulation parameters in Figs. 4 and 5

Parameters	Fig. 4	Fig. 5
BS Antenna number	4	64
BS Antenna spacing	0.5λ	0.5λ
User number	1	4
User antenna number	1	2
Central frequency	6 GHz	28 GHz
Liquid neuron number	/	30

BS: base station

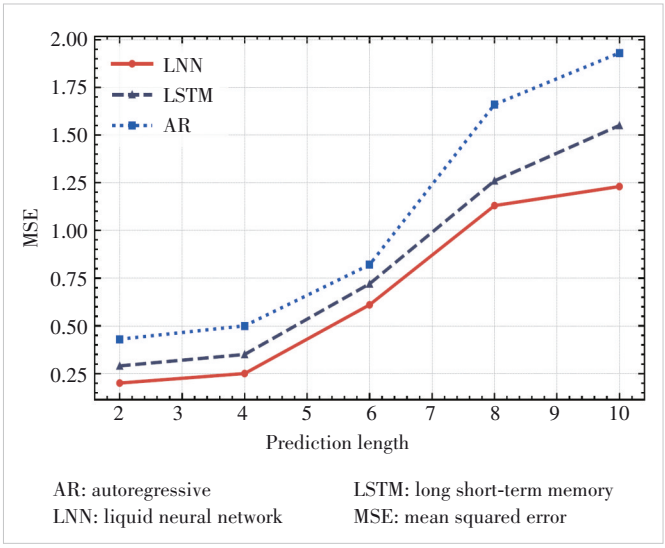

Figure 4. MSE versus prediction length with real-world channel state information

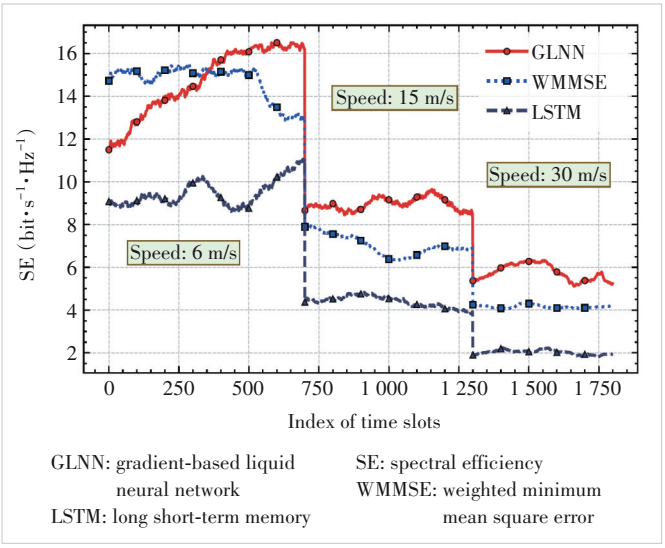

Figure 5. Average SE in a dynamic beamforming scenario

tential of LTCs in achieving more accurate channel prediction in practical and dynamic scenarios.

7.2 Beamforming with NCPs

We consider a multiple-input multiple-output (MIMO) beamforming system[25]. A BS furnished with M antenna elements concurrently provides service to K users. Each user device possesses N_r antennas. The users experience a range of velocities: 6 m/s, 15 m/s, and 30 m/s. Each of these phases encompasses 700, 600, and 500 discrete time intervals, respectively. Key simulation settings are enumerated in Table 1. The average SE achieved under this dynamic condition, contrasted against alternative benchmark schemes, is illustrated in Fig. 5. The gradient-based liquid neural network (GLNN) approach, leveraging NCPs, rapidly surpasses the weighted minimum mean square error (WMMSE) algorithm after a short initial learning period. It then maintains a superior level of SE when juxtaposed with all other reference systems. This behavior underscores its remarkable capacity for adaptation and its efficacy in environments characterized by temporal variations.

8 Conclusions

In this article, we investigate LNNs that are designed from first principles. We delve into their structure, features, and distinct advantages compared with traditional neural networks, as well as their recent applications. LNNs demonstrate remarkable potential as a key enabling technology in next-generation wireless communications due to their superior generalizability, interpretability, lower complexity, continuous-time modeling capabilities, and robust performance in dynamic environments. By leveraging their adaptive nature and efficient design, LNNs can enhance scalability, fault tolerance, and resource utilization efficiency in wireless networks. However, several challenges remain to be addressed to fully realize the potential of LNNs in practical applications, including improving zero-shot learning capabilities, developing distributed LNN frameworks, integrating multi-modality data, and optimizing cross-layer interactions. Future research is expected to focus on overcoming these challenges to ensure that LNNs can effectively adapt to varying conditions and deliver reliable performance in real-world scenarios. By addressing these issues, LNNs can drive the evolution and enhancement of future wireless networks, paving the way for more adaptive, reliable, and efficient communication systems.

References

[1] WANG C X, YOU X H, GAO X Q, et al. On the road to 6G: visions, requirements, key technologies, and testbeds [J]. IEEE communications surveys and tutorials, 2023, 25(2): 905 – 974. DOI: 10.1109/COMST.2023.3249835
[2] SHAHID A, KLIKS A, AL-TAHMEESSCHI A, et al. Large-scale AI in telecom: charting the roadmap for innovation, scalability, and enhanced digital experiences [EB/OL]. [2025-02-16]. https://arxiv.org/abs/2503.04184v1
[3] O'SHEA T, HOYDIS J. An introduction to deep learning for the physical layer [J]. IEEE transactions on cognitive communications and networking, 2017, 3(4): 563 – 575. DOI: 10.1109/TCCN.2017.2758370
[4] ZHU F H, WANG X Q, HUANG C W, et al. Beamforming inferring by conditional WGAN-GP for holographic antenna arrays [J]. IEEE wireless communications letters, 2024, 13(7): 2023 – 2027. DOI: 10.1109/LWC.2024.3402102
[5] DAI L L, JIAO R C, ADACHI F, et al. Deep learning for wireless communications: an emerging interdisciplinary paradigm [J]. IEEE wireless communications, 2020, 27(4): 133 – 139. DOI: 10.1109/MWC.001.1900491
[6] ZHU F H, WANG X Q, HUANG C W, et al. Robust beamforming for RIS-aided communications: gradient-based manifold meta learning [J]. IEEE transactions on wireless communications, 2024, 23(11): 15945 – 15956. DOI: 10.1109/TWC.2024.3435023
[7] WANG T H, XIAO W, SEYDE T, et al. Measuring interpretability of neu-

ral policies of robots with disentangled representation [EB/OL]. (2023-12-11) [2025-02-16]. https://arxiv.org/pdf/2210.06650v2
[8] JIANG W, HAN B, HABIBI A M, et al. The road towards 6G: a comprehensive survey [J]. IEEE open journal of the Communications Society, 2021, 2: 334 – 366. DOI: 10.1109/OJCOMS.2021.3057679
[9] ZHU F H, WANG B H, YANG Z H, et al. Robust millimeter beamforming via self-supervised hybrid deep learning [C]//The 31st European Signal Processing Conference (EUSIPCO). IEEE, 2023: 915 – 919. DOI: 10.23919/EUSIPCO58844.2023.10289989
[10] HASANI R, LECHNER M, AMINI A, et al. Liquid time-constant networks [J]. Proceedings of the AAAI conference on artificial intelligence, 2021, 35(9): 7657 – 7666. DOI: 10.1609/aaai.v35i9.16936
[11] LECHNER M, HASANI R, AMINI A, et al. Neural circuit policies enabling auditable autonomy [J]. Nature machine intelligence, 2020, 2(10): 642 – 652. DOI: 10.1038/s42256-020-00237-3
[12] HASANI R, LECHNER M, AMINI A. Closed-form continuous-time neural networks [J]. Nature machine intelligence, 2022, 4(11): 992 – 1003. DOI: 10.1038/s42256-022-00556-7
[13] ELDAN R, SHAMIR O. The power of depth for feedforward neural networks [C]//The 29th Annual Conference on Learning Theory. PMLR, 2016: 907 – 940
[14] KRIZHEVSKY A, SUTSKEVER I, HINTON G E. ImageNet classification with deep convolutional neural networks [C]//The 26th International Conference on Neural Information Processing Systems. ACM, 2012: 1097 – 1105. DOI: 10.1145/3065386
[15] YU Y, SI X S, HU C H, et al. A review of recurrent neural networks: LSTM cells and network architectures [J]. Neural computation, 2019, 31 (7): 1235 – 1270. DOI: 10.1162/neco_a_01199
[16] MA K, ZHANG F, TIAN W Q, et al. Continuous-time mmWave beam prediction with ODE-LSTM learning architecture [J]. IEEE wireless communications letters, 2023, 12(1): 187 – 191. DOI: 10.1109/LWC.2022.3221159
[17] CHEN R T, RUBANOVA Y, BETTENCOURT J, et al. Neural ordinary differential equations [C]//The 32nd International Conference on Neural Information Processing Systems. ACM, 2018: 6572 – 6583
[18] CHAHINE M, HASANI R, KAO P, et al. Robust flight navigation out of distribution with liquid neural networks [J]. Science robotics, 2023, 8 (77): eadc8892. DOI: 10.1126/scirobotics.adc8892
[19] WANG X Q, ZHU F H, ZHOU Q Y, et al. Energy-efficient beamforming for RISs-aided communications: gradient based meta learning [C]//International Conference on Communications. IEEE, 2024: 3464 – 3469. DOI: 10.1109/ICC51166.2024.10622978
[20] ZHU F H, WANG X Q, HUANG C W, et al. Robust continuous-time beam tracking with liquid neural network [C]//IEEE Global Communications Conference. IEEE, 2024: 4878 – 4883. DOI: 10.1109/GLOBECOM52923.2024.10900942
[21] WEI Z Q, ZHANG Y J, JI D N, et al. Sensing and communication integrated fast neighbor discovery for UAV networks [J]. ZTE Communications, 2024, 22(3): 69 – 82. DOI: 10.12142/ZTECOM.202403009
[22] DU R L, WEI Z Q, YANG Z. Integrated sensing and communication: who benefits more? [J]. ZTE Communications, 2024, 22(3): 37 – 47. DOI: 10.12142/ZTECOM.202403006
[23] WANG B H, ZHU F H, LIU M B, et al. Multi-sources information fusion learning for multi-points NLOS localization [C]//The 99th Vehicular Technology Conference (VTC2024-Spring). IEEE, 2024: 1 – 6. DOI: 10.1109/VTC2024-Spring62846.2024.10683036
[24] YIN H, ZHOU Y H, CAO L, et al. Channel prediction with liquid time-constant networks: an online and adaptive approach [C]//The 94th Vehicular Technology Conference (VTC2021-Fall). IEEE, 2021: 1 – 6. DOI: 10.1109/vtc2021-fall52928.2021.9625323
[25] WANG X Q, ZHU F H, HUANG C W, et al. Robust beamforming with gradient-based liquid neural network [J]. IEEE wireless communications letters, 2024, 13(11): 3020 – 3024. DOI: 10.1109/lwc.2024.3436576

Biographies

ZHU Fenghao received his BE degree in information engineering from Zhejiang University, China in 2023, and he is currently pursuing his MS degree with the College of Information Science and Electronic Engineering, Zhejiang University. His current research interests include massive MIMO, signal processing, and machine learning. He is a recipient of 2024 IEEE ComSoc Conference Travel Grant.

WANG Xinquan is currently pursuing his BE degree at Zhejiang University, China. His current research interests include 6G, beamforming and machine learning. He is a recipient of 2024 IEEE ComSoc Student Travel Grant.

ZHU Chen received his BS degree from North University of China in 2010, and MS degree from Zhejiang University of Technology, China in 2013. He is currently engaged in teaching and researching at the College of Engineering, Zhejiang University, China. His main research interests include general sense computing integration, machine learning, image processing, and cloud-edge collaborative computing.

HUANG Chongwen (chongwenhuang@zju.edu.cn) obtained his BS degree in 2010 from Nankai University, China and MS degree from the University of Electronic Science and Technology of China in 2013, and PhD degree from Singapore University of Technology and Design (SUTD) in 2019. From Oct. 2019 to Sep. 2020, he is a Postdoc at SUTD. Since Sep. 2020, he joined Zhejiang University as a tenure-track young professor. Prof. HUANG is the recipient of 2021 IEEE Marconi Prize Paper Award, 2023 IEEE Fred W. Ellersick Prize Paper Award and 2021 IEEE ComSoc Asia-Pacific Outstanding Young Researcher Award. He has served as an editor of *IEEE Communications Letter*, *Elsevier Signal Processing*, *EURASIP Journal on Wireless Communications* and *Networking and Physical Communication* since 2021. His main research interests focus on holographic MIMO surface/reconfigurable intelligent surface, B5G/6G wireless communications, mmWave/THz Communications, deep learning technologies for Wireless communications, etc.

Overview of Cross-Component In-Loop Filters in Video Coding Standards

LI Zhaoyu[1], MENG Xuewei[1], ZHANG Jiaqi[1], HUANG Cheng[2,3], JIA Chuanmin[1], MA Siwei[1], JIANG Yun[1]

(1. National Engineer Research Center of Visual Technology, Peking University, Beijing 100871, China;
2. ZTE Corporation, Shenzhen 518057, China;
3. State Key Laboratory of Mobile Network and Mobile Multimedia Technology, Shenzhen 518055, China)

DOI: 10.12142/ZTECOM.202502009

https://kns.cnki.net/kcms/detail/34.1294.TN.20250512.1043.002.html, published online May 13, 2025

Manuscript received: 2024-07-09

Abstract: In-loop filters have been comprehensively explored during the development of video coding standards due to their remarkable noise-reduction capabilities. In the early stage of video coding, in-loop filters, such as the deblocking filter, sample adaptive offset, and adaptive loop filter, were performed separately for each component. Recently, cross-component filters have been studied to improve chroma fidelity by exploiting correlations between the luma and chroma channels. This paper introduces the cross-component filters used in the state-of-the-art video coding standards, including the cross-component adaptive loop filter and cross-component sample adaptive offset. Cross-component filters aim to reduce compression artifacts based on the correlation between different components and provide more accurate pixel reconstruction values. We present their origin, development, and status in the current video coding standards. Finally, we conduct discussions on the further evolution of cross-component filters.

Keywords: cross-component in-loop filter; adaptive loop filter; sample adaptive offset; video coding

Citation (Format 1): LI Z Y, MENG X W, ZHANG J Q, et al. Overview of cross-component in-loop filters in video coding standards [J]. ZTE Communications, 2025, 23(2): 85 - 95. DOI: 10.12142/ZTECOM.202502009

Citation (Format 2): Z. Y. Li, X. W. Meng, J. Q. Zhang, et al., "Overview of cross-component in-loop filters in video coding standards," *ZTE Communications*, vol. 23, no. 2, pp. 85 - 95, Jun. 2025. doi: 10.12142/ZTECOM.202502009.

1 Introduction

With the development of video capture, storage, compression, and display technologies, numerous video applications continue to emerge, such as video communications, online conferences, cloud gaming, and immersive video experiences. The advancement brings forth new challenges to video coding technologies. To meet the increasing demand for video compression, various video coding tools and technologies have been proposed, leading to continuous evolution in video coding standards. A significant milestone in this progression was the finalization of the high efficiency video coding (HEVC)[1] standard in 2013, which achieved approximately 50% bitrate savings compared with its predecessor, the advanced video coding (AVC) standard[2]. The latest video coding standard, versatile video coding (VVC)[3], has further improved upon HEVC by achieving roughly 50% bitrate reduction. While H.266/VVC demonstrates excellent video compression capabilities, there remains significant potential in further enhancing video coding efficiency. In the pursuit of exploring advanced video encoding tools, a software model named the enhanced compression model (ECM) has been introduced to explore the potential of video compression further[4].

As a result of the prevalent utilization of block-based operations and coarse quantization within contemporary video coding standards, artifacts such as blocking and ringing have become inherent in compressed frames, thereby markedly diminishing both objective and subjective qualities. To mitigate these compression artifacts, extensive exploration has been conducted on in-loop filter algorithms during the evolution of video coding standards. These filters enhance the quality of reconstructed frames while furnishing high-fidelity reference frames for subsequent images, thereby facilitating more accurate motion compensation.

There are four kinds of in-loop filters in VVC[5], i.e., the deblocking filter (DBF)[6], the sample adaptive offset (SAO)[7], the adaptive loop filter (ALF)[8], and luma mapping with chroma

This work was supported in part by National Science Foundation of China under Grant No. 62031013, PCL-CMCC Foundation for Science and Innovation under Grant No. 2024ZY1C0040, New Cornerstone Science Foundation for the Xplorer Prize, and High performance Computing Platform of Peking University.

scaling (LMCS)[9]. The bilateral filter (BIF)[10] has been newly adopted in ECM. These filters are depicted in Fig. 1. DBF aims to remove the blocking artifact by applying low-pass filters to the boundaries of the coding unit, the prediction unit, and the transform unit. SAO is conducted by conditionally adding an offset to the reconstructed samples after DBF, which shows promising performance in reducing the mean sample distortion and the ringing artifacts. ALF is a Wiener-based spatial filter. It enhances reconstructed video fidelity by taking the weighted average of reference samples as the filtered samples. The weighting coefficients are derived by minimizing the mean square error between the original and decoded samples in the encoder, and then they are transmitted to the decoder. LMCS does not particularly focus on artifact reduction but aims to boost coding efficiency by better utilizing the dynamic range. BIF is a nonlinear, edge-preserving, and noise-reducing filter that has been newly introduced to ECM. Similar to the ALF, it also replaces the intensity of each pixel with a weighted average of intensity values from nearby pixels. While the difference lies in that the weights of BIF depend on the Euclidean distance of pixels and the radiometric differences, which preserves sharp edges. These weights can be calculated both in the encoder and decoder.

In addition to the above-mentioned local filters adopted in the ECM, some other in-loop filters based on the image non-local similarity have been studied, such as a structure-driven adaptive non-local filter (SANF)[11], a non-local structure-based loop filter (NLSF)[12-14], a novel adaptive loop filter utilizing image non-local prior knowledge[15], a parametric non-local loop filter (PNLF)[16], and a deformable Wiener filter (DWF)[17]. Some of these methods were also discussed in the joint video experts team (JVET) meetings[18-21].

Though the aforementioned in-loop filters effectively reduce compression artifacts, these conventional methodologies, characterized by hand-crafted designs, exhibit constraints in addressing more intricate artifacts. In response to this constraint, in-loop filters leveraging convolutional neural networks (CNNs) have been developed, demonstrating superior performance over conventional filtering methods[22-25]. Various neural network-based loop filtering tools have been proposed and adopted by ECM, achieving significant performance improvement[26-29].

While the coding techniques mentioned above only focus on single-component in-loop filtering, ignoring the correlation between different components. Extensive research has demonstrated a high correlation between luma and chroma components in the YUV format[30-33]. Based on this correlation, some prediction techniques were proposed, such as cross-component prediction (CCP)[34] supported in the HEVC range extensions and cross-component linear model (CCLM)[35]. Besides, cross-component techniques are also applied in end-to-end image compression[36], which effectively improves compression performance. Recently, the correlation among different components was also considered in in-loop filters.

Several cross-component in-loop techniques were proposed and adopted in H.266/VVC and the audio video coding standard (AVS3), an independently developed Chinese audio-video coding standard. Continuous studies have been carried out on these methods during the development of ECM. In the ECM-12.0, there are two cross-component filters, namely the cross-component adaptive loop filter (CCALF) and the cross-component sample adaptive offset (CCSAO). CCALF was initially proposed and adopted during the development of H.266/VVC and was optimized and improved in ECM. Similar to ALF, CCALF is also a Wiener filter. The difference is that it only applies to chroma samples, and it utilizes luma samples as the reference samples and corrects the target chroma pixel by applying a linear filter to these selected luma samples. The filter parameters are trained following the principle of minimizing the mean square error (MSE) in the encoder and transmitted to the decoder. CCSAO is adopted by AVS3 and ECM. Specifically, it uses the correlation between luma and

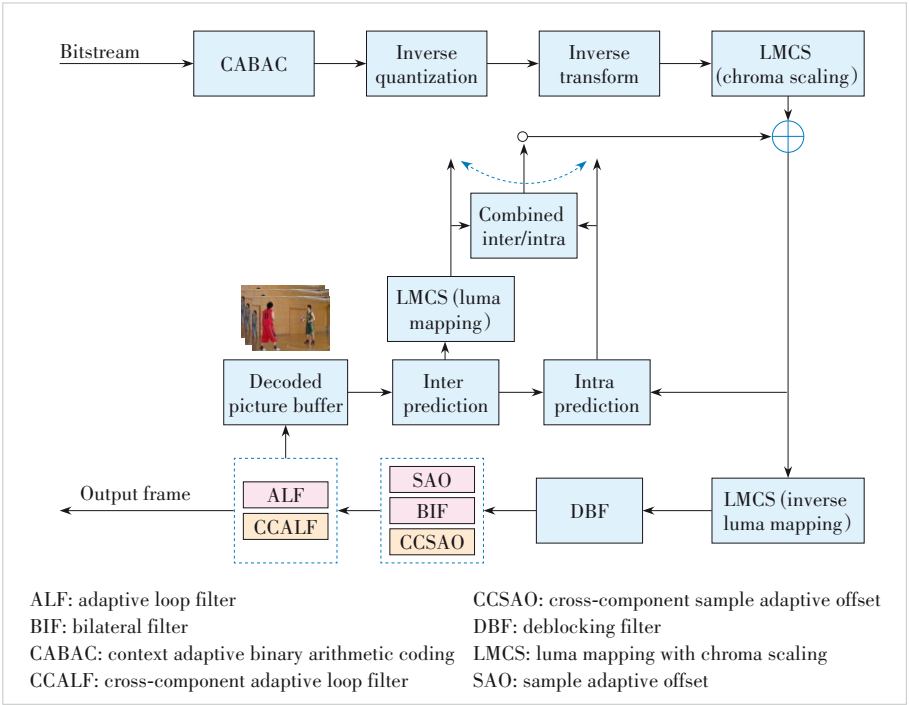

ALF: adaptive loop filter
BIF: bilateral filter
CABAC: context adaptive binary arithmetic coding
CCALF: cross-component adaptive loop filter
CCSAO: cross-component sample adaptive offset
DBF: deblocking filter
LMCS: luma mapping with chroma scaling
SAO: sample adaptive offset

Figure 1. Illustration of the ECM video decoder diagram, with golden boxes corresponding to cross-component filters

chroma components to classify the reconstructed samples into different categories and assigns each category an offset value for sample adjustment.

Compared with ECM-12.0 without CCALF[4], ECM-12.0 with CCALF achieves 2.49% and 2.90% coding gains for the Cb and Cr components under All Intra (AI) configuration, and 1.48% and 2.12% coding gains for Cb and Cr components under random access (RA) configuration. While in VTM-10.0, CCALF can achieve 13.88% and 13.73% coding gains under AI configuration, and 9.69% and 8.55% coding gains under RA configuration for Cb and Cr components respectively[37]. The decrease in the coding gain may be caused by the new cross-component techniques introduced in the prediction process of ECM. For CCSAO, 1.28% and 1.08% coding gains can be achieved for Cb and Cr components under AI configuration, and 3.02% and 2.79% coding gains for Cb and Cr components can be achieved under RA configuration, respectively.

The remainder of this paper is organized as follows. Section 2 introduces the theory of CCALF and summarizes its development. Section 3 introduces the fundamental principles and the proposals about CCSAO. Experimental results and discussions are shown in Section 4. Section 5 concludes this paper.

2 CCALF

CCALF is fundamentally a Wiener filter[38]. Specifically, CCALF derives a correction signal for chroma samples based on the weighted average of luma reference samples. These reference samples are the neighboring samples of the collocated luma sample. The coordinate of the collocated luma sample is derived based on the chroma format of the video. Both the ALF and CCALF use the reconstructed sample of SAO as input, while CCALF only calculates the offsets for chroma components as shown in Fig. 2. The filtering operation can be represented using the conditions below, and we assume the following for 2D images.

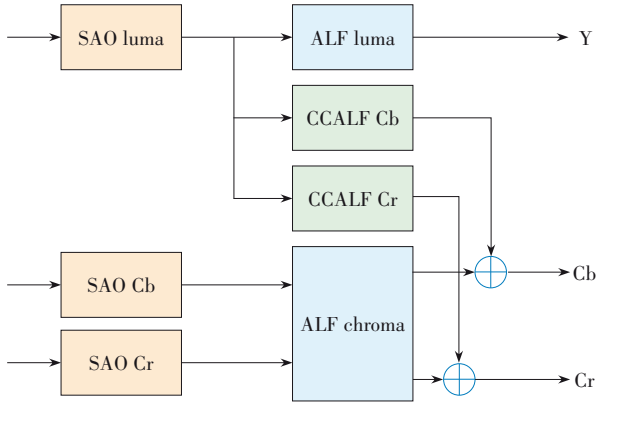

ALF: adaptive loop filter SAO: sample adaptive offset
CCALF: cross-component adaptive loop filter

Figure 2. Illustration of CCALF

$$I'(r) = I(r) + \sum_{i=0}^{N-1} c_i p_i \tag{1}$$

$$p_i = L(r' + \boldsymbol{d}_i) - I(r) \tag{2}$$

where sample location $r = (x, y)$ belongs to the to-be-filtered region R, and $r' = (x', y')$ means the collocated luma sample position of the to-be-filtered chroma sample; $s[r]$ is the original sample, $I[r]$ is the to-be-filtered sample, and $L(r')$ is the collocated luma samples of $[r]$; $\boldsymbol{c} = [\boldsymbol{c}_0, \boldsymbol{c}_1, \boldsymbol{c}_2, \cdots, \boldsymbol{c}_{N-1}]$ means N-tap filter coefficients; $\{\boldsymbol{d}_0, \boldsymbol{d}_1, \boldsymbol{d}_2, \cdots, \boldsymbol{d}_{N-1}\}$ is the filter tap position offset, where $\boldsymbol{d}_i$ denotes the sample location offset to $L(r')$ of the i-th filter tap; $\boldsymbol{p} = [p_0, p_1, p_2, \cdots, p_{N-1}]$ shows the difference values between neighboring reference luma samples and the to-be-filtered chroma sample; $I'(r)$ is the filtered chroma sample.

The coefficients of CCALF are derived by minimizing the mean square error between the reconstructed chroma component after SAO and the original chroma sample, similar to the parameter derivation process of chroma-ALF. Specifically, a correlation matrix is derived, and the coefficients are calculated using the Cholesky decomposition solver to minimize the mean square error.

The coefficient values at different positions are obtained from the bitstream. The filter coefficients are derived by solving the optimization problem shown in Eq. (3).

$$\min_{\boldsymbol{c}} \sum_{r \in R} \left(\boldsymbol{c} \odot \boldsymbol{p} - s[r]\right)^2 \tag{3}$$

$$\boldsymbol{c} = \boldsymbol{R}_{r,r}^{-1} \boldsymbol{R}_{r,s} \tag{4}$$

where $\odot$ is the inner product. By solving the Wiener-Hopf equation as in Eq. (4), the filter coefficients can be calculated. $\boldsymbol{R}_{r,r}^{-1}$ denotes the auto-correlation matrix of the to-be-filtered samples, and $\boldsymbol{R}_{r,s}$ is the cross-correlation matrix of the to-be-filtered and the original samples.

2.1 Filter Shape

The filter shape of CCALF was a 5 × 6 diamond-shaped filter with 14 filter coefficients and 18 taps when it was initially proposed[39]. Considering the trade-off among performance, line buffer, and computational complexity, several reduced filter shapes were proposed[40-43]. Finally, the 3 × 4 diamond filter shape was adopted in H.266/VVC. Fig. 3 illustrates the relative location of the chroma sample being filtered and its support region in the luma sample when CCALF is adopted in H.266/VVC. Consequently, each CCALF filter has only 8 filter coefficients, and the filtering operation is shown in Eq. (1), where $N = 8$.

To improve the performance of CCALF, numerous propos-

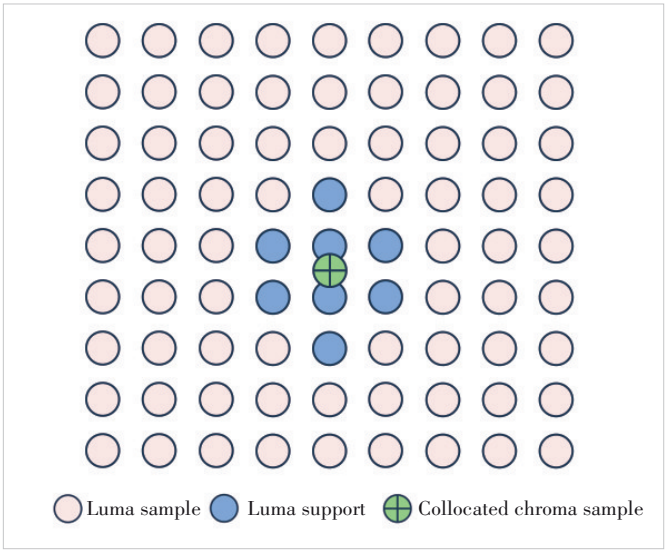

Figure 3. Illustration of the relative location of filtered chroma sample of CCALF and its support in the luma channel for 4∶2∶0 chroma format in H.266/VVC

als have been put forward, considering the trade-off between performance and running time, complexity, and other factors. However, some of these proposals were not adopted.

In Ref. [44], an extension to CCALF was proposed. This contribution suggests extensions to CCALF in both the number and size of filters. While this extension can enhance chroma components, it may lead to some loss in the luma component. Additionally, CCALF could introduce artifacts in chroma components, which is why certain constraints are set in high quantization parameter (QP) regions. Therefore, proposals regarding CCALF must avoid reintroducing these artifacts.

Considering that the correlation between neighboring pixels may depend on the characteristics of the video content, a single filter shape may not be optimal for different video content. A coding tree block (CTB) level filter shape selection scheme was proposed to optimize the CCALF framework[45]. This contribution introduces two filter shapes shown in Fig. 4. Within each adaptation parameter set (APS), multiple filters and their corresponding shapes with coefficients are signaled.

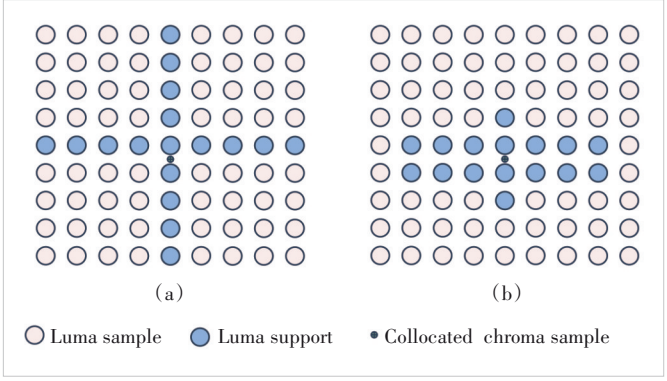

Figure 4. Illustration of the two filter shapes of CCALF in Ref. [45]

For each CTB, the decoder specifies which filter shapes or coefficients are used based on the signaled index.

This contribution demonstrates significant gains in chroma components. However, the necessity of adaptively selecting CCALF shapes is questioned. In a subsequent exploration experience[46], in addition to the adaptive selection of the two filter shapes[45], another scheme involving larger-size filters was proposed. Specifically, a 25-tap long-tap CCALF was introduced. This long-tap filter was considered a simpler scheme to achieve better gain. After joint tests of the modified CCALF and other in-loop filters[47], the long-tap CCALF scheme was eventually adopted. The new shape of CCALF in ECM is illustrated in Fig. 5, and the filtering operation is shown in Eq. (1) where $N = 25$.

Because residual values have been stored and used in luma ALF, the concept of residual-based taps in chroma ALF and CCALF was proposed[48]. Before this contribution, CCALF only had one online-trained CCALF filter with a cross-like filter shape mentioned above, as depicted in Fig. 5. Since the residual values are utilized in the unfixed luma filter of ALF, there is no need to store luma residual values additionally. In this contribution, only one luma-residual-based tap was added. Furthermore, chroma residual values were incorporated into the chroma online-trained filter of ALF, while luma residual values were employed in CCALF. However, considering that chroma residual values were not stored previously and the additional memory required, the resulting gain was comparatively low. Therefore, this proposal is recommended for further study.

At the 31st JVET meeting, luma residual taps in chroma ALF and CCALF were introduced[49]. Five luma residual taps in a cross 3×3 shape were added. These extended taps took the collocated and neighboring luma residual values as input. The inclusion of the luma residual taps in CCALF was adopted due to its relatively higher standalone gain[50]. The filter shape of CCALF in ECM-12.0 is illustrated in Fig. 6.

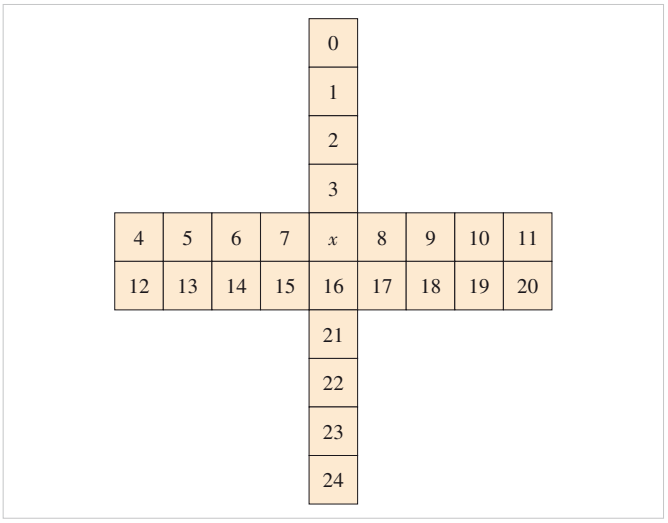

Figure 5. Illustration of the filter shape of CCALF with 25 taps

The coefficients that need to be calculated are divided into two parts: spatial luma sample-based taps and luma residual-based taps. The linear filtering operation can be represented using Eq. (5).

$$I'(x,y) = I(x,y) + \sum_{i=0,12} c_i\left(f_{i,0} + f_{i,1}\right) + \sum_{i=1}^{21} c_i f_i + \sum_{i=22}^{26} c_i g_i \tag{5},$$

$$f_{i,j} = L\left(x' + x_i, y' + y_i\right) - I(x,y) \tag{6},$$

$$g_i = \mathrm{Clip}\left(R\left(x' + x_i, y' + y_i\right)\right) \tag{7},$$

where (x, y) is the coordinate of the center sample, and (x', y') is the coordinate of collocated luma sample; $(x' + x_i, y' + y_i)$ and $(x' + x_{i,j}, y' + y_{i,j})$ are the coordinates of the reconstructed samples corresponding to coefficient c_i; $f_{i,j}$ and f_i show the difference between neighboring luma samples $L(x', y')$ and current sample $I(x, y)$; g_i is the clipped value of luma residual samples $R(x', y')$, which is the residual between prediction samples and reconstructed samples; Clip is the function that limits the values within a certain range to reduce the impact of significant differences in sample values, and the value of the clipping operation depends on the clipIdx of APS and bitDepth.

2.2 Filter Coefficient Calculation and Representation

Except for the filter shape of the CCALF, the optimization of coefficient calculation and signaling[39, 51–54] is important to improve the performance of CCALF.

When CCALF was proposed, each filter had 14 filter coefficients and 18 taps, and every coefficient had an 8-bit dynamic range and was signaled with a third-order exponential-Golomb code[39]. However, it would increase complexity with additional multiplications per chroma pixels. To simplify the computation overhead, a bit shifting scheme was proposed to replace the multiplications[51]. The results show that this scheme can reduce the complexity of the CCALF filter with an accepted loss, so it was adopted. Besides, a contribution was proposed to reduce memory access, encoding latency, and power consumption[54]. It proposes a method to estimate CCALF filtering distortion without conducting real filter operations. With this proposal, the number of encoding passes can be reduced from 152 to 1 without affecting the coding performance. As a desirable simplification, this proposal was adopted.

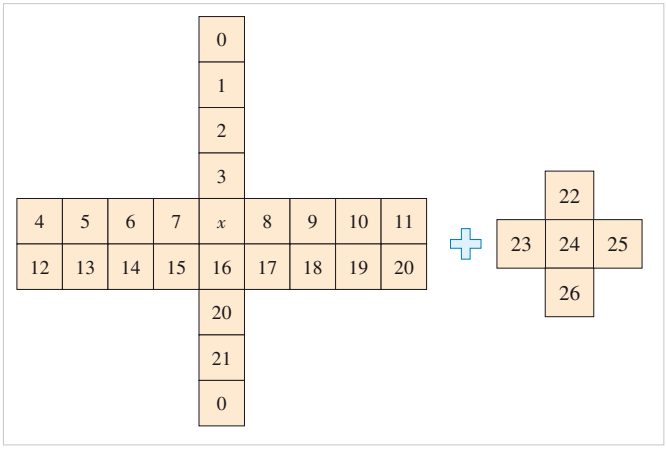

Figure 6. Illustration of CCALF's shape at ECM-12.0 (the left cross-like filter uses the reconstructed spatial sample of luma sample adaptive offset as input with 23 taps, and the right one uses luma residual samples as input)

At the 32nd JVET meeting, coefficient precision adjustment for ALF was proposed, demonstrating promising coding performance with negligible increases in encoding and decoding time[55]. Similarly, at the 33rd JVET meeting, adaptive coefficient precision for CCALF was introduced[56–57]. Since CCALF involves different coefficient derivations compared with ALF, removing the power of 2 constraints was also proposed in this context. This adjustment can enhance the accuracy of coefficients, though a 2-bit syntax element needs to be signaled for per luma filter set to indicate the number of bits. These two contributions have been further investigated.

2.3 Syntax Design

Compared with H. 266/VVC, ECM-12.0 utilizes luma residual samples additionally, as shown in Fig. 6. The residual correction is generated for chroma samples according to Eq. (5). For each picture, two types of information need to be coded for CCALF, i.e., filter coefficient parameters and filter control on/off flags. The filter coefficient parameters include the number of cross-component filters and the coefficients of the corresponding filter. CCALF can transmit up to 8 CCALF filters, with the resulting filters being indicated for each of the two chroma channels on a CTU basis. Each slice only has one APS, and the Cb component and Cr component can have different APSs, which are signaled separately at the slice header. Similar to luma ALF, to reduce bit overhead, filter coefficients of different classifications can be merged. The filter control on/off flags enable better local adaptation, with hierarchical control at the sequence-level, picture-level, slice-level and CTU-level. When the value of sequence-level and picture-level control flags is not present, it is inferred to be equal to 0. When the slice-level on/off control flag is not present, it is inferred to be equal to picture-level on/off control flags. If the slice-level on/off control flag indicates ALF-on, CTU-level filter on/off control flags are interleaved in slice data and coded with CTUs; otherwise, no additional CTU-level filter on/off control flags are coded and all CTUs of the slice are inferred as ALF-off.

Due to the abundant texture features of the luma component, CCALF may introduce artifacts with overly abundant chroma texture, thereby reducing the subjective quality of the

image, especially at high QP. Therefore, the H.266/VVC reference encoder can achieve subjective tuning through configuration file adjustments. Specifically, it can attenuate the application of CCALF in high QP encoding and areas with high-frequency luminance. Algorithmically, CCALF is deactivated on CTUs when any of the following conditions is true:

1) The slice QP value minus 1 is less than or equal to the base QP value;

2) The number of chroma samples exhibiting local contrast exceeding $\left(1 \ll \left(\text{bitDepth} - 2\right)\right) - 1$ surpasses the CTU height, where the local contrast is the difference between the maximum and minimum luma sample values within the filter support region;

3) More than a quarter of chroma samples are in the range between $\left(1 \ll \left(\text{bitDepth} - 1\right)\right) - 16$ and $\left(1 \ll \left(\text{bitDepth} - 1\right)\right) + 16$.

3 CCSAO

CCSAO is conceptually similar to SAO, as it initially classifies the samples to be filtered into different categories, then derives an offset value for each category, and finally corrects the pixels in that category with the corresponding offset value. It uses the reconstructed sample of DBF, which is the same as SAO, and the offsets are derived for three channels respectively. The reconstruction operation of CCSAO can be represented by the equation below.

$$C'_{\text{rec}} = \text{Clip}\left(C_{\text{rec}} + \text{offset}_i\right) \tag{8},$$

where C_{rec} and C'_{rec} are the reconstructed samples after DBF and CCSAO, respectively, i represents the class index of the corresponding sample, and offset_i is the corresponding offset value.

The difference between SAO and CCSAO lies in CCSAO's utilization of the strong correlation between the luma and chroma components in the classification process. It optimizes the reconstruction of one component of the sample by leveraging the information contained in the other component of the sample[58].

3.1 Classifier Extension

The original CCSAO includes only a classification based on band information to avoid a significant increase in complexity. Corresponding band offsets are obtained by minimizing the sum of squared error (SSE) between the original sample and the corrected reconstruction sample. This approach keeps computational complexity low while enabling CCSAO to handle certain encoded artifacts. It should be noted that the offsets need to be signaled in the bitstream.

CCSAO is applied to the output of DBF reconstructed samples, and the offset calculated for each category is added to the output sample from the SAO process. Therefore, CCSAO can be parallelized with SAO, as shown in Fig. 7.

The band information-based classification of CCSAO utilizes the reconstructed sample of three components to process the classification for each component. Specifically, the collocated samples for each component are first selected. Then, an index representing a category is calculated based on the band number of the three components and their collocated samples. The offset value of a sample depends on its category. Regarding the collocated samples for each component, the collocated luma sample can be chosen from 9 candidates, while the collocated chroma samples have fixed positions, as shown in Fig. 8.

CCSAO was first proposed and adopted[59] in the AVS3 video coding standard, in which collocated luma component samples are classified by equally dividing the range of the sample values. For each category, an offset value is derived and used for the chroma samples whose collocated luma sample belongs to the category.

Although cross-component tools in in-loop filters always act on chroma components, regarding cross-component proposals, attention should not only be given to the gain of chroma components but also to the effects on the luma component. Furthermore, subjective quality improvement needs to be considered as well. Considering these reasons, CCSAO was introduced to ECM. This proposal showed great performance im-

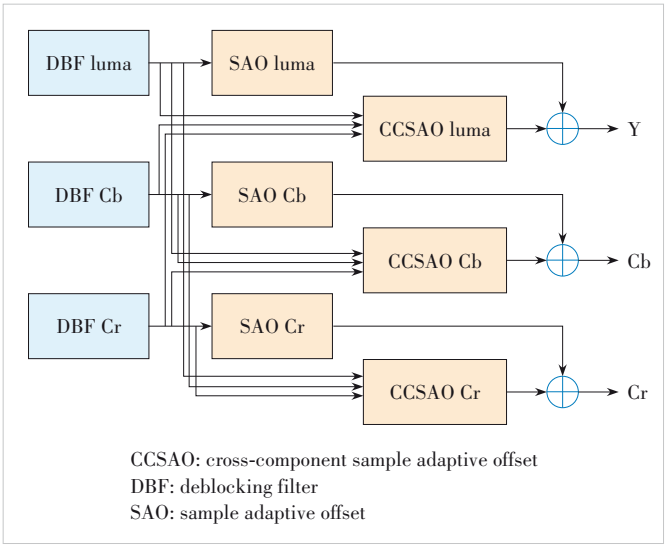

Figure 7. Illustration of SAO process when CCSAO is applied

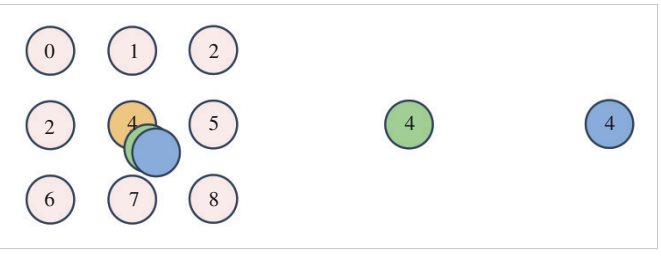

Figure 8. Illustration of the collocated sample used for the CCSAO classification. The left graph shows the 9 locations of the luma component (one of the 9 samples will be chosen based on rate-distortion optimization) and the green and blue samples show the two collocated chroma samples

provement in chroma components while introducing minimal loss in the luma component. Initially, CCSAO only used the band classifier when it was adopted in ECM[60], and the category index is calculated using the equations below.

$$\text{classIndex} = \text{BandNum} \times \left(N_{\text{Cb}} \times N_{\text{Cr}}\right) + \text{band}_{\text{Cb}} \times N_{\text{Cr}} + \text{band}_{\text{Cr}} \tag{9},$$

$$\text{band}_L = P\left(x_{\text{Y}}, y_{\text{Y}}\right) \times N_{\text{Y}} \gg \text{BitDepth} \tag{10},$$

$$\text{band}_{\text{Cb}} = P\left(x_{\text{Cb}}, y_{\text{Cr}}\right) \times N_{\text{Cb}} \gg \text{BitDepth} \tag{11},$$

$$\text{band}_{\text{Cr}} = P\left(x_{\text{Cr}}, y_{\text{Cr}}\right) \times N_{\text{Cr}} \gg \text{BitDepth} \tag{12},$$

where $P\left(i,j\right)$ is the sample value of different components at position $\left(i,j\right)$, N_i is the number of band for each component, $\left(x_{\text{Cb}},y_{\text{Cb}}\right)$ and $\left(x_{\text{Cr}},y_{\text{Cr}}\right)$ are the current chroma sample positions, and $\left(x_Y,y_Y\right)$ is the collocated luma sample position.

As a new in-loop filter tool, several schemes have been proposed to optimize the original CCSAO. An extension of CCSAO was proposed at the 24th JVET meeting, where the proponents extended the design of CCSAO by adding the edge-based classifier[61 - 62]. Similar to the edge-based classification method in SAO, the edge-based classification of CCSAO also uses four 1-D directional patterns, including horizontal, vertical, 45°, and 135°, as shown in Fig. 9. The best direction mode is determined at the encoder through rate-distortion optimization (RDO). Edge information used for classification is derived by calculating the difference between the center pixel and its two adjacent pixels, and then comparing the difference with a predefined threshold value to derive the final class index. The best threshold values are also selected from an array of predefined threshold values based on RDO. If the edge-based classifier is selected, the category index will be calculated as follows, given the chroma sample and the collocated luma samples.

$$\text{classIndex} = \text{BandNum} \times 16 + q_a \times 4 + q_b \tag{13},$$

$$q_i = \begin{cases} 0 & d_i < -Th \\ 1 & -Th < d_i < 0 \\ 2 & 0 < d_i < Th \\ 3 & Th < d_i \end{cases} \tag{14},$$

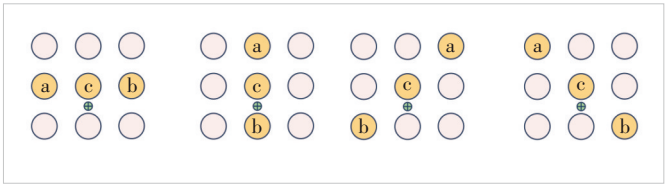

Figure 9. Illustration of the edge-based classification of CCSAO. Four graphs show four different directions, where the yellow samples are the locations used for calculating the class index at different directional patterns

$$\text{BandNum} = \text{cur}_i \times N_i \gg \text{BitDepth} \tag{15},$$

where i can be chosen from the two co-located samples based on RDO, d_i is the delta value between the center sample c and the neighboring sample a or b. q_i is the quantized value of d_i. The position of neighboring sample a or b depends on the best 1-D directional pattern selected from the four 1-D directional patterns. Besides, the offset value is constrained to the range of [−15, 15] and these offsets need to be transmitted to the decoder.

Unlike SAO, the edge-based classifier in CCSAO combines the luma edge and the band index of the sample at the corresponding collocated position to determine the final classification of a given sample. Additionally, CCSAO uses collocated luma samples to derive edge information for chroma samples, while SAO uses neighboring samples of the same component to derive edge information.

A similar contribution was introduced to AVS[63], where the enhanced cross-component sample adaptive offset (ECCSAO) method further improves encoding performance, which extends the edge-based classification by using the edge information of collocated luma samples to classify chroma samples. Moreover, a four-layer quad-tree structure was proposed. The former method has been adopted by AVS.

In the ECM, the edge classifier was further optimized with more edge/band combinations, and the component used for edge classification can be selected from any of the three components[64 - 65]. The new edge-based classification scheme, a subset of the original one with fewer edge range divisions, was added. This allows for more flexible edge/band combinations to adapt to the local characteristics of video sequences. This contribution was adopted at the 31st JVET meeting. The second edge-based classifier is formulated as follows.

$$\text{classIndex} = \text{BandNum} \times 4 + q_a \times 2 + q_b \tag{16},$$

$$q_i = \begin{cases} 0 & d_i < Th \\ 1 & d_i \geqslant T \end{cases} \tag{17}.$$

3.2 Signaling Overhead Reduction

Similar to the APS design in H.266/VVC, the inheritance scheme of CCSAO was also proposed[64 - 65]. There is a strong correlation between the CCSAO offsets and classifier parameters of different pictures. To reduce signaling overhead, the offsets/parameters of some coded pictures can be stored at both the encoder and decoder, allowing them to be used by future pictures. This contribution has also been adopted.

4 Performance Evaluation

To improve the coding performance, both CCALF and CCSAO are integrated into ECM-12.0 seamlessly. A comparative analysis is conducted to evaluate the efficiency and effec-

tiveness of the cross-component in-loop filter tools. With continuous development, both CCSAO and CCALF have achieved remarkable performance gains. To evaluate the coding performance of CCALF and CCSAO, ECM-12.0 without CCALF and CCSAO are regarded as the anchor respectively[66].

As shown in Table 1, CCALF can achieve 2.49% and 2.90% coding gains for Cb and Cr components under AI configuration. For RA configuration, 1.48% and 2.12% coding gains for Cb and Cr components can be achieved. In VTM-10.0, CCALF can achieve 13.88% and 13.73% coding gains for Cb and Cr components under AI configuration, and 9.69% and 8.55% coding gains for Cb and Cr components under RA configuration. The decrease in gain may be caused by the newly proposed and optimized cross-component techniques in the prediction process. For CCSAO, as shown in Table 2, 1.28% and 1.08% coding gains can be achieved for Cb and Cr components under AI configuration. For RA configuration, 3.02% and 2.79% coding gains for Cb and Cr components can be achieved. It can be noted that the Y component coding performance of CCSAO on screen content sequences is significantly greater than that of natural sequences. This may be caused by the more obvious relationship between the texture and directional features of luma and chroma components in screen content videos.

Table 1. Experimental results of ECM-12.0 (anchor: ECM-12.0 without CCALF)

Class	AI			RA		
	Y	Cb	Cr	Y	Cb	Cr
A1	0.09%	−1.21%	−3.32%	0.07%	−1.00%	−3.96%
A2	0.11%	−2.78%	−3.23%	0.13%	−2.62%	−4.94%
B	0.12%	−3.35%	−3.22%	0.15%	−4.31%	−3.41%
C	0.10%	−1.67%	−1.91%	0.03%	−1.48%	−2.12%
E	0.15%	−3.12%	−2.96%	-	-	-
Average	0.11%	−2.49%	−2.90%	0.10%	−2.56%	−3.48%
D	0.02%	−0.42%	−0.18%	-0.01%	−0.94%	−0.53%
F	0.10%	−1.77%	−1.07%	0.15%	−1.08%	−0.32%
TGM	0.12%	−1.19%	−0.72%	0.16%	−1.26%	−1.03%

AI: All Intra
CCALF: cross-component adaptive loop filter
ECM: enhanced compression model
RA: random access
TGM: text and graphics with motion

Table 2. Experimental results of ECM-12.0 (anchor: ECM-12.0 without CCSAO)

Class	AI			RA		
	Y	Cb	Cr	Y	Cb	Cr
A1	−0.28%	−0.83%	−1.36%	−0.42%	−1.89%	−2.42%
A2	0.01%	−0.99%	−1.15%	−0.06%	−1.88%	−2.01%
B	0.08%	−1.94%	−1.63%	−0.16%	−3.76%	−4.07%
C	0.11%	−0.83%	−0.41%	0.00%	−2.10%	−1.20%
E	0.02%	−1.55%	−0.68%	-	-	-
Average	0.01%	−1.28%	−1.08%	−0.15%	−2.57%	−2.56%
D	0.03%	−0.02%	−0.31%	0.10%	−1.56%	−1.05%
F	-0.23%	−1.99%	−1.74%	−0.15%	−2.99%	−1.54%
TGM	-0.73%	−1.64%	−1.81%	−1.01%	−2.72%	−3.38%

AI: All Intra
CCSAO: cross-component sample adaptive offset
ECM: enhanced compression model
RA: random access
TGM: text and graphics with motion

Furthermore, we compare the subjective performance under different configurations. The subjective testing materials consist of the sequences mentioned in the common test conditions (CTC), with each sequence encoded using four QPs (QP = 22, 27, 32, and 37) under the RA configuration. Partial visual quality comparison results of reconstructed sequences are shown in Fig. 10, where the first column displays decoded images with both CCALF and CCSAO applied, the second column shows decoded images without CCALF, and the last column presents reconstructed images without CCSAO. Red boxes highlight regions with significant subjective improvement. The lines on the clothes are clearer in Fig. 10a, whereas the color and lines in Figs. 10b and 10c appear slightly blurry. Compared with Fig. 10e, the boundaries of the clothes in Fig. 10d are more distinct. The lines in Fig. 10d are cleaner than those in Fig. 10f. Additionally, the wires in Fig. 10g are more coherent and clearer compared with Figs. 10h and 10j.

Building upon the demonstrated performance gains of CCALF and CCSAO, it's important to consider the broader context of loop filter development. Loop filters are designed to correct artifacts introduced prior to loop filtering. Different types of loop filters address various artifacts such as blocking, ringing, blurring, and mosquito noise. In VVC, there are three primary loop filters: DBF, SAO, and ALF. Moreover, the CCALF is integrated with ALF to fully utilize the relationship between luma and chroma components. To further exploit the cross-component relationship, an additional cross-component loop filter, CCSAO, has been proposed during the ECM exploration. CCSAO operates in parallel with SAO. With the advancement of ECM, the classifiers of CCSAO have become more refined and diverse[61 – 65]. Concurrently, the structure of CCALF has evolved to be more complex and comprehensive, incorporating a wider variety of samples into its filters[48 – 49]. Moreover, the shape and calculation methods of the filters are continuously optimized[40 – 43, 51, 56]. In addition, other in-loop filters based on image non-local similarity have been studied[11 – 12, 15 – 16]. Traditional loop filters in existing video coding standards primarily focus on local correlations. While non-local loop filters can offer performance gains, their high computational demands and hardware limitations make it challenging to implement in video coding standards. Therefore, methods to optimize non-local filters are proposed[13 – 14]. Overall, many new filtering tools are currently being explored. However, further investigation into the relationship among different components remains a crucial direction for video coding.

Figure 10. Illustration of subjective quality comparison. (a) – (c): BasketballDrill, RA configuration and QP22; (d) – (f): BQMall, RA configuration and QP22; (g) – (i): MarketPlace, random access configuration and QP32

5 Conclusions

Cross-component filters play a crucial role in future video coding standards. By leveraging the correlation between luma and chroma components, cross-component filters can achieve substantial coding performance improvement, leading to the adoption of various video coding standards such as VVC and AVS3. Compression distortion can be effectively mitigated, thereby improving the accuracy of the reconstructed pixel. Nevertheless, the philosophy of current cross-component filters primarily emphasizes utilizing luma information to refine chroma pixels, which neglects the potential impact of chroma information on luma pixels and the correlation between two chroma components. In some scenarios, the chroma texture information and edge details can also contribute to correcting luma inaccuracies. Therefore, cross-component filters still have the potential to achieve substantial performance improvement by delving into the filtering manner and relationship among different channels.

References

[1] SULLIVAN G J, OHM J R, HAN W J, et al. Overview of the high efficiency video coding (HEVC) standard [J]. IEEE transactions on circuits and systems for video technology, 2012, 22(12): 1649 – 1668. DOI: 10.1109/TCSVT.2012.2221191
[2] WIEGAND T, SULLIVAN G J, BJONTEGAARD G, et al. Overview of the H.264/AVC video coding standard [J]. IEEE transactions on circuits and systems for video technology, 2003, 13(7): 560 – 576. DOI: 10.1109/TCSVT.2003.815165
[3] BROSS B, WANG Y K, YE Y, et al. Overview of the versatile video coding (VVC) standard and its applications [J]. IEEE transactions on circuits and systems for video technology, 2021, 31(10): 3736 – 3764
[4] COBAN M, LIAO R L, NASER K, et al. Algorithm description of enhanced compression model 12 (ECM 12) [R]. Joint Video Experts Team (JVET), document JVET-AG2025, 2024
[5] KARCZEWICZ M, HU N, TAQUET J, et al. VVC in-loop filters [J]. IEEE transactions on circuits and systems for video technology, 2021, 31 (10): 3907 – 3925. DOI: 10.1109/tcsvt.2021.3072297
[6] ANDERSSON K, MISRA K, IKEDA M, et al. Deblocking filtering in VVC [C]//Picture Coding Symposium (PCS). IEEE, 2021: 1 – 5. DOI: 10.1109/pcs50896.2021.9477477
[7] FU C M, ALSHINA E, ALSHIN A, et al. Sample adaptive offset in the HEVC standard [J]. IEEE transactions on circuits and systems for video technology, 2012, 22(12): 1755 – 1764. DOI: 10.1109/

TCSVT.2012.2221529
[8] TSAI C Y, CHEN C Y, YAMAKAGE T, et al. Adaptive loop filtering for video coding [J]. IEEE journal of selected topics in signal processing, 2013, 7(6): 934 – 945. DOI: 10.1109/JSTSP.2013.2271974
[9] LU T R, PU F J, YIN P, et al. Luma mapping with chroma scaling in versatile video coding [C]//Data Compression Conference (DCC). IEEE, 2020: 193 – 202. DOI: 10.1109/DCC47342.2020.00027
[10] STRÖM J, WENNERSTEN P, ENHORN J, et al. Bilateral loop filter in combination with SAO [C]//Picture Coding Symposium (PCS). IEEE, 2019: 1 – 5. DOI: 10.1109/PCS48520.2019.8954554
[11] ZHANG J, JIA C M, ZHANG N, et al. Structure-driven adaptive non-local filter for high efficiency video coding (HEVC) [C]//Data Compression Conference (DCC). IEEE, 2016: 91 – 100. DOI: 10.1109/DCC.2016.105
[12] MA S W, ZHANG X F, ZHANG J, et al. Nonlocal in-loop filter: the way toward next-generation video coding? [J]. IEEE multimedia, 2016, 23 (2): 16 – 26. DOI: 10.1109/MMUL.2016.16
[13] MENG X W, JIA C M, WANG S S, et al. Optimized non-local in-loop filter for video coding [C]//Picture Coding Symposium (PCS). IEEE, 2018: 233 – 237. DOI: 10.1109/PCS.2018.8456299
[14] JIA C M, LUO F L, ZHANG X F, et al. Fast non-local adaptive in-loop filter optimization on GPU [J]. IEEE transactions on multimedia, 2020, 23: 39 – 51. DOI: 10.1109/TMM.2020.2981185
[15] ZHANG X F, XIONG R Q, LIN W S, et al. Low-rank-based nonlocal adaptive loop filter for high-efficiency video compression [J]. IEEE transactions on circuits and systems for video technology, 2017, 27(10): 2177 – 2188. DOI: 10.1109/TCSVT.2016.2581618
[16] MENG X W, JIA C M, ZHANG X F, et al. Parametric non-local in-loop filter for future video coding [C]//Data Compression Conference (DCC). IEEE, 2022: 474. DOI: 10.1109/DCC52660.2022.00085
[17] MENG X W, JIA C M, ZHANG X F, et al. Deformable Wiener filter for future video coding [J]. IEEE transactions on image processing, 2022, 31: 7222 – 7236. DOI: 10.1109/TIP.2022.3221278
[18] WANG Z, MENG X, JIA C, et al. Description of SDR video coding technology proposal by DJI and Peking University [R]. Joint Video Experts Team (JVET), document JVET-J0011, 2018
[19] MENG X, JIA C, WANG Z, et al. CE2: non-local structure-based filter [R]. Joint Video Experts Team (JVET), document JVET-K0160, 2018
[20] CHERNYAK R, Victor S, Ikonin S, et al. CE2: noise suppression filter [R]. Joint Video Experts Team (JVET), document JVET-K0053, 2018
[21] LAI C Y, CHEN C Y, HUANG Y W, et al. CE2.5.2: nonlocal mean in-loop filter [R]. Joint Video Experts Team (JVET), document JVET-K0236, 2018
[22] ZHANG K, ZUO W M, CHEN Y J, et al. Beyond a Gaussian denoiser: residual learning of deep CNN for image denoising [J]. IEEE transactions on image processing, 2017, 26(7): 3142 – 3155. DOI: 10.1109/TIP.2017.2662206
[23] WANG M Z, WAN S, GONG H, et al. Attention-based dual-scale CNN in-loop filter for versatile video coding [J]. IEEE access, 2019, 7: 145214 – 145226
[24] CHEN S J, CHEN Z Z, WANG Y B, et al. In-loop filter with dense residual convolutional neural network for VVC [C]//IEEE Conference on Multimedia Information Processing and Retrieval (MIPR). IEEE, 2020: 149-152. DOI: 10.1109/mipr49039.2020.00038
[25] HUANG Z J, GUO X P, SHANG M Y, et al. An efficient QP variable convolutional neural network based in-loop filter for intra coding [C]//Data Compression Conference (DCC). IEEE, 2021: 33 – 42. DOI: 10.1109/DCC50243.2021.00011
[26] LI Y, ZHANG K, LI J, et al. EE1-1.6: deep in-loop filter with fixed point implementation [R]. Joint Video Experts Team (JVET), document JVET-AA0111, 2022
[27] LI J, LI Y, ZHANG K, et al. EE1-1.6: RDO considering deep in-loop filtering [R]. Joint Video Experts Team (JVET), document JVET-AB0068, 2022
[28] LIU D, STRÖM J, DAMGHANIAN M, P. et al. EE1-1.5: combined intra and inter models for luma and chroma [R]. Joint Video Experts Team (JVET), document JVET-AC0089, 2023
[29] LI Y, ZHANG K, ZHANG L. EE1-1.7: deep in-loop filter with additional input information [R]. Joint Video Experts Team (JVET), document JVET-AC0177, 2023
[30] GOFFMAN-VINOPAL L, PORAT M. Color image compression using inter-color correlation [C]//International Conference on Image Processing. IEEE, 2002: II. DOI: 10.1109/ICIP.2002.1039960
[31] SONG B C, LEE Y G, KIM N H. Block adaptive inter-color compensation algorithm for RGB 4 : 4 : 4 video coding [J]. IEEE transactions on circuits and systems for video technology, 2008, 18(10): 1447 – 1451. DOI: 10.1109/TCSVT.2008.2002827
[32] LEE S H, CHO N I. Intra prediction method based on the linear relationship between the channels for YUV 4 : 2 : 0 intra coding [C]//The 16th IEEE International Conference on Image Processing (ICIP). IEEE, 2009: 1037 – 1040. DOI: 10.1109/icip.2009.5413727
[33] LI J R, WANG M, ZHANG L, et al. Sub-sampled cross-component prediction for emerging video coding standards [J]. IEEE transactions on image processing, 2021, 30: 7305 – 7316. DOI: 10.1109/TIP.2021.3104191
[34] FLYNN D, MARPE D, NACCARI M, et al. Overview of the range extensions for the HEVC standard: tools, profiles, and performance [J]. IEEE transactions on circuits and systems for video technology, 2016, 26(1): 4 – 19
[35] PFAFF J, FILIPPOV A, LIU S, et al. Intra prediction and mode coding in VVC [J]. IEEE transactions on circuits and systems for video technology, 2021, 31(10): 3834 – 3847
[36] DUAN W H, CHANG Z, JIA C M, et al. Learned image compression using cross-component attention mechanism [J]. IEEE transactions on image processing, 2023, 32: 5478 – 5493. DOI: 10.1109/TIP.2023.3319275
[37] CHIEN W J, BOYCE J, CHEN W, et al. JVET AHG report: tool reporting procedure (AHG13) [R]. Joint Video Experts Team (JVET), document JVET-T0013, 2020
[38] MISRA K, BOSSEN F, SEGALL A. On cross component adaptive loop filter for video compression [C]//Picture Coding Symposium (PCS). IEEE, 2019: 1 – 5. DOI: 10.1109/PCS48520.2019.8954547
[39] MISRA K, BOSSEN F, SEGALL A. Cross-component adaptive loop filter for chroma [R]. Joint Video Experts Team (JVET), document JVET-O0636, 2019
[40] HU N, DONG J, SEREGIN V, et al. CE5-related: reduced filter shape for cross component adaptive loop filter [R]. Joint Video Experts Team (JVET), document JVET-P0558, 2019
[41] KOTRA A M, ESENLIK S, WANG B, et al. AHG16/CE5-Related: simplifications for cross component adaptive loop filter [R]. Joint Video Experts Team (JVET), document JVET-P0106, 2019
[42] LI J Y, LIM C S. AHG16/Non-CE5: cross component ALF simplification [R]. Joint Video Experts Team (JVET), document JVET-P0173, 2019
[43] ZHAO Y, YANG H T. CE5-related: simplified CCALF with 6 filter coefficients [R]. Joint Video Experts Team (JVET), document JVET-P0251, 2019
[44] KEATING S, BROWNE A, SHARMAN K. AHG12: extensions to CCALF [R]. Joint Video Experts Team(JVET), document JVET-V0080, 2021
[45] SARWE M G, LIAO R L, CHEN J, et al. AHG12: CTB level filter shape selection of CCALF [R]. Joint Video Experts Team (JVET), document JVET-W0079, 2021
[46] SARWER M G, LIAO R L, CHEN J, et al. EE2-4.2, EE2-4.3: on CCALF filter [R]. Joint Video Experts Team (JVET), document JVET-X0045, 2021
[47] HU N, SEREGIN V, KARCZEWICZ M, et al. EE2-4.8: joint tests of chroma BIF, ALF and CCALF [R]. Joint Video Experts Team (JVET), document JVET-X0071, 2021

[48] YIN W B, ZHANG K, ZHANG L. Non-EE2: extensions of residual-based taps in ALF and CCALF [R]. Joint Video Experts Team (JVET), document JVET-AD0234, 2023
[49] YIN W B, ZHANG K, DENG Z P, et al. Non-EE2: luma residual taps in chroma-ALF and CCALF [R]. Joint Video Experts Team (JVET), document JVET-AE0121, 2023
[50] OHM J R. Meeting report of the 32nd Meeting of the Joint Video Experts Team (JVET) [R]. Joint Video Experts Team (JVET), document JVET-AF1000, 2023
[51] HU N, DONG J, SEREGIN V, et al. CE5-related: multiplication removal for cross component adaptive loop filter [R]. Joint Video Experts Team (JVET), document JVET-P0557, 2019
[52] STRÖM J, ANDERSSON K. CE5-related: on the CCALF filtering process [R]. Joint Video Experts Team(JVET), document JVET-Q0165, 2020
[53] MENG X W, ZHENG X Z, WANG S S, et al. CCALF virtual boundary issue for 4:4:4 and 4:2:2 format [R]. Joint Video Experts Team (JVET), document JVET-R0322, Oct. 2019
[54] MENG X W, ZHENG X Z, WANG S S, et al. AHG 10: One-pass CCALF [R]. Joint Video Experts Team (JVET), document JVET-R0327, Oct. 2019
[55] YIN W B, ZHANG K, ZHANG L. Non-EE2: coefficient precision adjustment for ALF [R]. Joint Video Experts Team (JVET) document JVET-AF0198, Oct. 2023
[56] HU N, KARCZEWICZ M, SEREGIN V, et al. EE2-related: adaptive precision for CCALF coefficients [R]. Joint Video Experts Team (JVET), document JVET-AG0233, 2024
[57] SONG N, YU Y, YU H P, et al. Non-EE2: adaptive coefficient precision for CCALF [R]. Joint Video Experts Team (JVET), document JVET-AG0065, 2024
[58] KUO C W, XIU X Y, CHEN Y W, et al. Cross-component sample adaptive offset [C]//Data Compression Conference (DCC). IEEE, 2022: 359 – 368. DOI: 10.1109/DCC52660.2022.00044
[59] KUO C W, XIU X Y, CHEN W, et al. Cross-component sample adaptive offset [R]. Joint Video Experts Team (JVET), document AVS-M5595, 2020
[60] KUO C W, XIU X Y, CHEN Y W, et al. EE2-5.1: cross-component sample adaptive offset [R]. Joint Video Experts Team (JVET), document JVET-W0066, 2021
[61] KOTRA A M, HU N, SEREGIN V, et al. AHG12: edge classifier for cross-component sample adaptive offset (CCSAO) [R]. Joint Video Experts Team (JVET), document JVET-X0105, 2021
[62] KUO C W, XIU X, CHEN W Y, et al. AHG12: CCSAO classification with edge information [R]. Joint Video Experts Team (JVET), document JVET-X0152, 2021
[63] JIAN Y R, ZHANG J Q, LI J R, et al. Enhanced cross component sample adaptive offset for AVS3 [C]//International Conference on Visual Communications and Image Processing (VCIP). IEEE, 2021: 1 – 5. DOI: 10.1109/VCIP53242.2021.9675321
[64] KUO C W, XIU X Y, CHEN W, et al. AHG12: CCSAO with extended edge classifiers and history offsets [R]. Joint Video Experts Team (JVET), document JVET-AD0218, 2023
[65] KUO C W, XIU X Y, CHEN W, et al. EE2-5.1: CCSAO with extended edge classifiers and history offsets [R]. Joint Video Experts Team (JVET), document JVET-AE0151, 2023
[66] KARCZEWICZ M, YE Y. Common test conditions and evaluation procedures for enhanced compression tool testing [R]. Joint Video Experts Team (JVET), document JVET-AF2017, 2023

Biographies

LI Zhaoyu received her BE degree in computer science and technology from Chang'an University, China in 2023. She is currently pursuing her MS degree in computer application technology with Peking University, China. Her research interests include video coding and video coding standard.

MENG Xuewei received her BE degree in communication engineering from Beijing University of Posts and Telecommunications, China in 2017 and PhD degree in computer application technology from Peking University, China in 2022. She is currently a senior software engineer with Core Media Technology, Disney Streaming. Her research interests include video processing, video compression, and video coding standard. She is actively participating in the research of versatile video coding (VVC) standard.

ZHANG Jiaqi received his BS degree from the School of Software Technology, Dalian University of Technology, China in 2017 and PhD degree in computer science from the Institute of Computing Technology, Chinese Academy of Sciences in 2023. He is currently a postdoctoral researcher with the School of Computer Science, Peking University, China. His research interests include data compression and image/video coding.

HUANG Cheng (huang.cheng5@zte.com.cn) received his MS degree from the School of Computer Science and Engineering, Southeast University, China. He is currently a senior system architect and the project manager of video technology research at ZTE Corporation. His research interests include visual coding, storage, transport, and multimedia systems.

JIA Chuanmin received his BE degree in computer science from Beijing University of Posts and Telecommunications, China in 2015 and PhD degree in computer application technology from Peking University, China in 2020. He was a visiting student in New York University, USA in 2018. He is currently an assistant professor with the Wangxuan Institute of Computer Technology, Peking University. His research interests include video compression and multimedia signal processing. He received the Best Paper Award of PCM 2017, Best Paper Award of IEEE MM 2018, and Best Student Paper Award of IEEE MIPR 2019.

MA Siwei received his BS degree from Shandong Normal University, China in 1999, and PhD degree in computer science from the Institute of Computing Technology, Chinese Academy of Sciences, China in 2005. He held a postdoctoral position with the University of Southern California, USA from 2005 to 2007. He joined the School of Electronics Engineering and Computer Science, Institute of Digital Media, Peking University, China where he is currently a professor. He has authored more than 300 technical articles in refereed journals and proceedings in image and video coding, video processing, video streaming, and transmission. He served/serves as an associate editor for the *IEEE Transactions on Circuits and Systems for Video Technology* and *Journal of Visual Communication and Image Representation*.

JIANG Yun received his BE degree in 2000 and ME degree in 2003 in information science and technology from Peking University, China. He is the director of Zhejiang Province Advanced Institute of Information Technology, Peking University. He serves as a senior engineer at the School of Computer Science, Peking University, where he is a master's supervisor. His primary research interests focus on image processing and video coding standards.

GaN-Based Optoelectronic Impact Force Sensor

RUAN Junhui, JIANG Chengxiang, XU Shengli, WANG Yongjin, SHI Fan

(GaN Optoelectronic Integration International Cooperation Joint Laboratory of Jiangsu Province, Nanjing University of Posts and Telecommunications, Nanjing 210003, China)

DOI: 10.12142/ZTECOM.202502010

https://kns.cnki.net/kcms/detail/34.1294.TN.20250520.1401.005.html, published online May 20, 2025

Manuscript received: 2024-10-20

Abstract: A monolithic integration of the light emitting diode (LED) and photodetector (PD) based on III-nitride is designed and fabricated on a sapphire substrate to act as a transceiver. Due to the coexistence of light emission and detection phenomenon of the multi-quantum well (MQW) structure, the monolithic transceiver can effectively sense environmental changes. By integrating a deformable Polydimethylsiloxane (PDMS) film on the transceiver chip, external force variation can be effectively detected. As the thickness of the PDMS reduces, the sensitivity significantly improves but at the expense of the measuring range. A sensitivity of 2.968 3% per newton for a range of 0–11 N is obtained when a 2 mm-thick PDMS film is packaged. The proposed monolithic GaN transceiver-based sensing system has the advantages of compactness, low cost, and simple assembly, providing an optional method for practical applications.

Keywords: monolithic integration; III-nitride; transceiver

Citation (Format 1): RUAN J H, JIANG C X, XU S L, et al. GaN-based optoelectronic impact force sensor [J]. ZTE Communications, 2025, 23 (2): 96 - 102. DOI: 10.12142/ZTECOM.202502010

Citation (Format 2): J. H. Ruan, C. X. Jiang, S. L. Xu. et al., "GaN-based optoelectronic impact force sensor," *ZTE Communications*, vol. 23, no. 2, pp. 96 - 102, Jun. 2025. doi: 10.12142/ZTECOM.202502010.

1 Introduction

Miniaturized force sensors have attracted a lot of attention in structural health monitoring[1-2], human motion measurement[3], and rail transit monitoring[4]. To date, different kinds of force sensors have been reported such as piezoelectricity, capacitance, and optics[5-9]. Compared with electric-based methods, optical sensors have advantages in immunity to electromagnetic interference, fast response and high stability. In terms of optical means, using all-fiber structures as the sensing unit is the most popular strategy. A variety of fiber sensing structures have been developed for force sensing including Mach-Zehnder interferometer[10-12], fiber Bragg grating[13-14], Fabry-Perot interferometer[15-16], etc. Although the wavelength interrogation-based sensing mechanism has the merits of high sensitivity, fast response, and high stability, the system is usually composed of a light source and a spectrometer, which is bulky and complicated to assemble. To miniaturize the system configuration, the integration of the light source, sensing unit and the detector is highly desired.

Recently, GaN and its alloy have been widely used in illumination[17], power electronics[18], display[19], and optical communications[20-22] because of their long lifespan, fast response and good optoelectronic properties. Thanks to the ability of light emission and detection of the multi-quantum well (MQW) diode, many GaN-based monolithic devices have been proposed and demonstrated for angle, humidity, pressure, and liquid concentration measurement[23-26]. To measure the pressure, microdome-patterned polydimethylsiloxane (PDMS) film and sponges are normally used as the reflection boundary to modulate the reflected light[27-29]. However, the common problem facing these microstructure-based PDMS sensing units is that the preparation is relatively complex, and it is difficult to accurately control the shape and distribution of the microstructures.

In this work, a compact design of a GaN optoelectric chip with an Al reflection layer coated PDMS structure for force sensing is proposed. The chip-scale GaN device is composed of a light emitting diode (LED) and a photodetector (PD), which are monolithically integrated on a single wafer, acting as the light emitter and the detector, respectively. The Al-coated PDMS sensing unit is packaged with a gap of 2 mm to the chip. When a force is applied to the surface of the PDMS

This work was supported by the National Key Research and Development Program under Grant No. 2024YFE0204700, Natural Science Foundation of Jiangsu Province under Grant No. BG2024023, and Higher Education Discipline Innovation Project under Grant No. D17018.

structure, the distance between the Al reflection film and the GaN chip changes, which in turn alters the amount of reflected light from the Al film and, consequently, the light received by the PD changes. In this way, the impact force can be effectively detected.

2 GaN-Based Device Design and Fabrication

The schematic diagram of the force sensor is presented in Fig. 1a, which integrates a GaN device with an Al-coated PDMS film. The manufacturing process of the sensing device begins with the mold pouring, using 3D printing to fabricate the molds with controllable thicknesses. The PDMS gel is prepared by mixing the prepolymer and curing agent in a 10:1 ratio, followed by a vacuum processing to eliminate air bubbles. Then the mixture is poured into the printed molds and placed into a heating furnace for 40 min with a curing temperature of 80 °C. After curing, the PDMS film is peeled off from the molds and then attached with a piece of Al reflection membrane in the center. The GaN device is fabricated on a 4-inch GaN wafer, which consists of c-plane sapphire substrates, 3.5 μm thick undoped GaN, 2.2 μm thick Si-doped GaN (n-GaN), 400 nm thick MQW and 0.25 μm thick Mg-doped GaN (p-GaN) from the bottom to the top. To fabricate the GaN device, a 230 nm thick transparent indium tin oxide (ITO) current spreading layer is deposited over p-GaN as a p-contact layer. Two circular regions of a diameter of 210 μm are defined as the active regions of LED and PD by photolithography, and the unmasked areas are etched to the n-GaN surface by inductively coupled plasma (ICP) etching. Subsequently, a deep etching to the sapphire substrate is then performed to realize the device isolation between LED and PD. A 1 μm thick SiO_2 is deposited to form the electrical isolation, and then a window is opened, followed by the deposition of Ni/Al/Ti/Pt/Ti/Pt/Au/Ti/Pt/Ti metal stacks on the n-GaN and ITO surfaces. The physical encapsulation of the sensor is displayed in Fig. 1b, which consists of an optoelectronic chip fixed on a printed circuit board (PCB) and a PDMS film. A manometer is mounted on a linear moving stage and moves axially towards the sensor. As the impact force increases, a larger PDMS deformation directs more light to the PD, thus establishing a relationship between force and photocurrent.

3 Results and Discussion

The electrical and optical characteristics of the device are measured. The current-voltage (I-V) characteristic curve of the LED is presented in Fig. 2a. The turn-on voltage of the device is about 2.2 V, and the inset graph shows the relationship between the output optical power of the LED and the injection current. As shown in Fig. 2b, without illumination, the produced photocurrent level is from 10^{-11} A to 10^{-9} A. As the current starts at 10 mA, the photocurrent level increases dramatically to the order of 10^{-6} A. Fig. 2c illustrates a linear relationship between the PD's photocurrent response and the LED biased currents. To characterize the MQW diode's transceiver capability, the electroluminescence (EL) spectrum of the LED and the response spectrum (RS) of the photodetector are tested, as shown in Fig. 2d. The overlapping regions near 480 nm confirm that the MQW diode can detect light emitted by another MQW diode of the same structure.

To verify the detection ability of the MQW diode, proximity sensing is performed to estimate the distance-dependent photocurrent response. A piece of Al film is placed in front of the

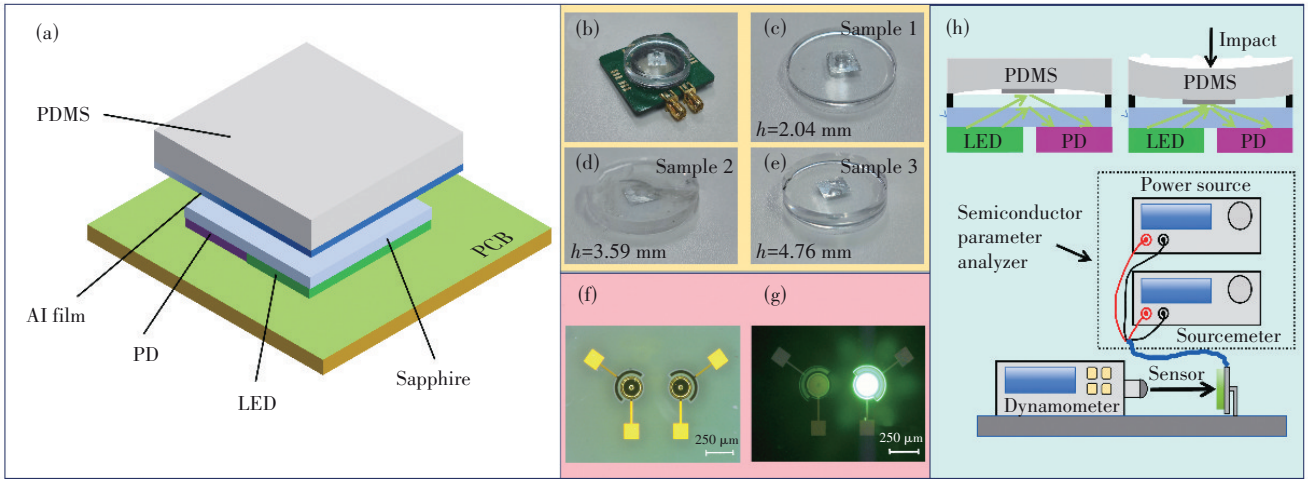

LED: light emitting diode PCB: printed circuit board PD: photodetector PDMS: polydimethylsiloxane

Figure 1. (a) Schematic diagram of the sensor; (b) microphotographs of the physical encapsulation: three kinds of packaged PDMS structures with a thickness of (c) 2.04 mm, (d) 3.59 mm and (e) 4.76 mm, respectively; (f) optical images of the device; (g) LED with biased current at 10 mA; (h) diagram of the experimental setup

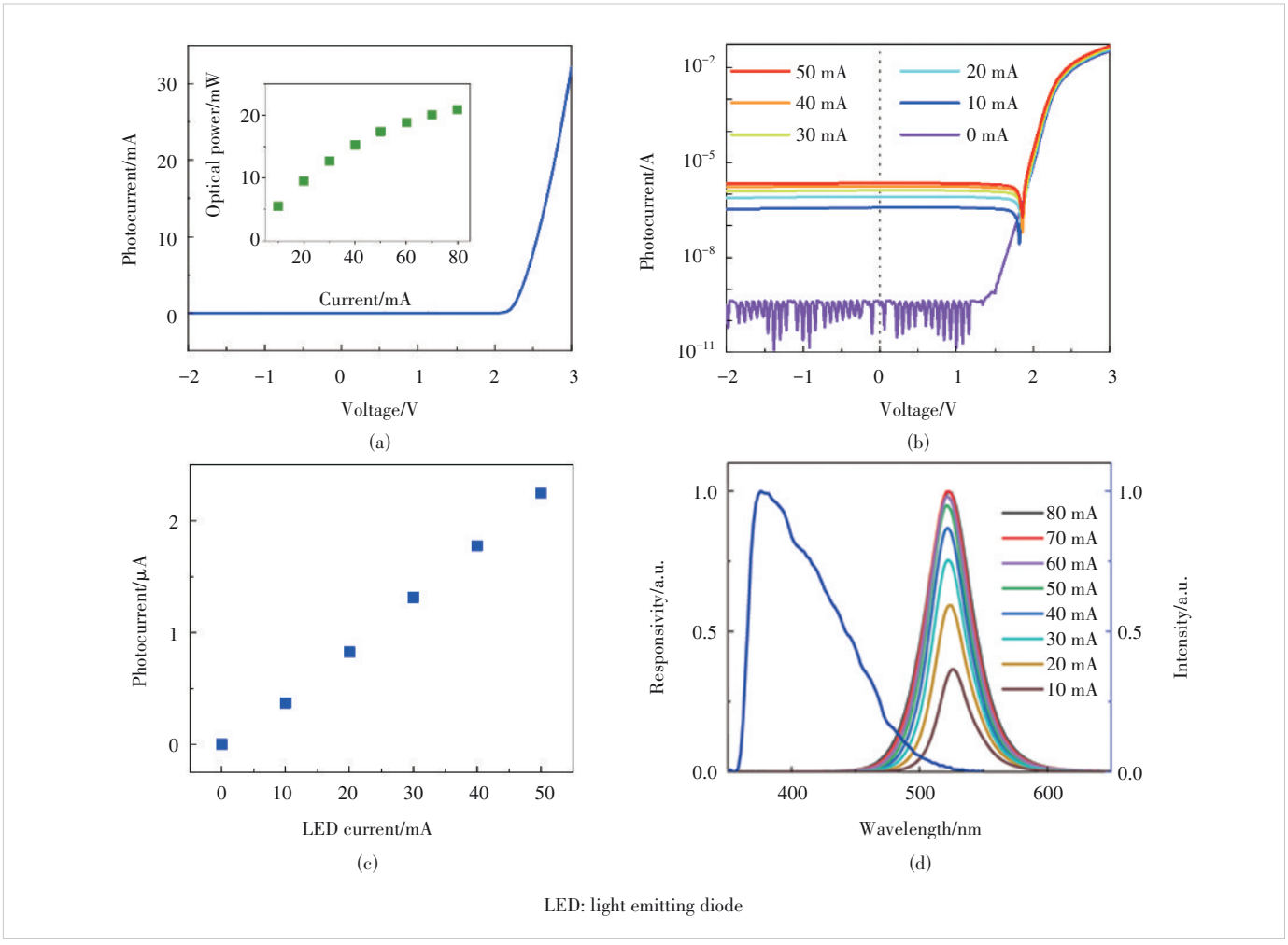

Figure 2. (a) I-V characteristic of the LED, where the inset shows the output power versus the driven current; (b) I-V curve of PD at different injection currents of LED; (c) Photocurrent response of PD under different currents of LED; (d) RS spectra of PD and the electroluminescence spectra of LED

transceiver chip and moves continuously relative to it. Fig. 3a shows the photocurrent response of the on-chip PD when the distance between the Al film and the transceiver changes from 0 to 12 mm with a step of 2 mm. From the given photocurrent response, it resembles a step-like response curve and exhibits a distinguished detection ability over a wide range, especially at the distance within 2.4 mm. These results suggest that the distance should be optimized around 2 mm to achieve a good sensitivity. Subsequently, the photocurrent response at a spacing distance of 2 mm and a step of 200 μm is studied, as plotted in Fig. 3b, showing a significant change in photocurrent at each step.

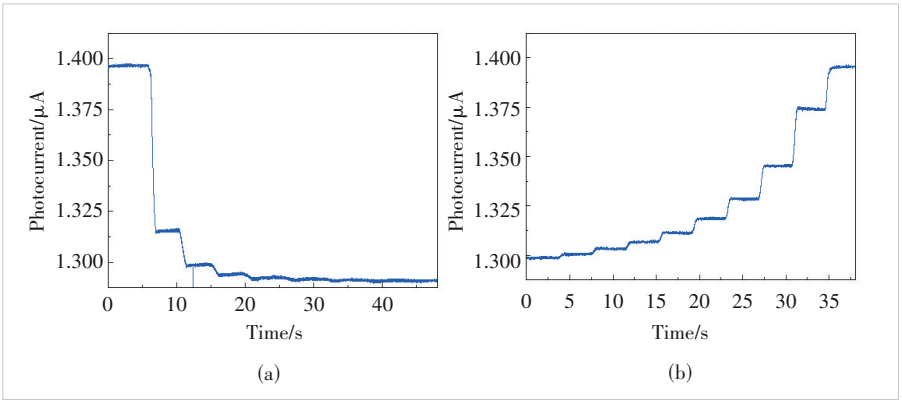

Figure 3. Photocurrent response measured under Al foil moving from (a) 0 to 12 mm, and (b) 0 to 2 mm

In addition to the proximity measurements, a communication performance test of the MQW diode is also carried out to verify the PD's ability to detect transient signal change. The

pseudo-random binary sequence (PRBS) data applied to the external light source are generated with a Keysight 33600A series waveform generator. The measured voltages of the PD with a 1 MΩ oscilloscope under incident PRBS data of 100 bit/s, 200 bit/s, 500 bit/s, and 1 000 bit/s are presented in Figs. 4a – 4d, respectively. The received response rate can easily reach 1 000 bit/s without serious signal distortion. The measured fast response rate indicates that the PD can guarantee sufficient resolution for detecting the instantaneous impact signal.

The photocurrent responses of PDMS samples with varying thicknesses under different forces are tested, as illustrated in Fig. 5. The green, blue and red curves represent PDMS with thicknesses of 2.04 mm, 3.59 mm and 4.76 mm, defined as Samples #1, #2, and #3. For Sample #1, it can respond to impact forces in the range of 0 – 11 N, and the instantaneous photocurrent responses at 3.8 N, 7.3 N and 11 N are recorded and plotted. From the given response curves, a better signal-to-noise ratio (SNR) of the photocurrent response is observed at a larger impact force. At a small force of 3.8 N, a jitter of the baseline is observed, which is caused by the limited PDMS deformation, leading to a small varying photocurrent and a small SNR. When the external force increases to 7.3 N and 11 N, as shown in Figs. 5b and 5c, a smooth photocurrent baseline appears and a better photocurrent response can be seen. Similarly, for Sample #2, as depicted in Figs. 5d, 5e, and 5f, the detectable impact force is larger than that of Sample #1, ranging from 12.5 N to 20.5 N, as the sample thickness increases. Sample #3 has a maximum detection ability of 35 N. However, the detection sensitivity is limited due to the relatively thick PDMS.

The stability test for Sample #1 under an 11 N impact force is shown in Fig. 6a. It shows a consistent photocurrent change of approximately 250 nA over 2 000 s, with the photocurrent profile remaining stable throughout the cycle. Fig. 6b depicts the relative photocurrent response to the impact force and the corresponding data for these three samples. The relative photocurrent is defined as $\Delta I/I$, where I is the initial photocurrent and ΔI is the varying photocurrent caused by the impact.

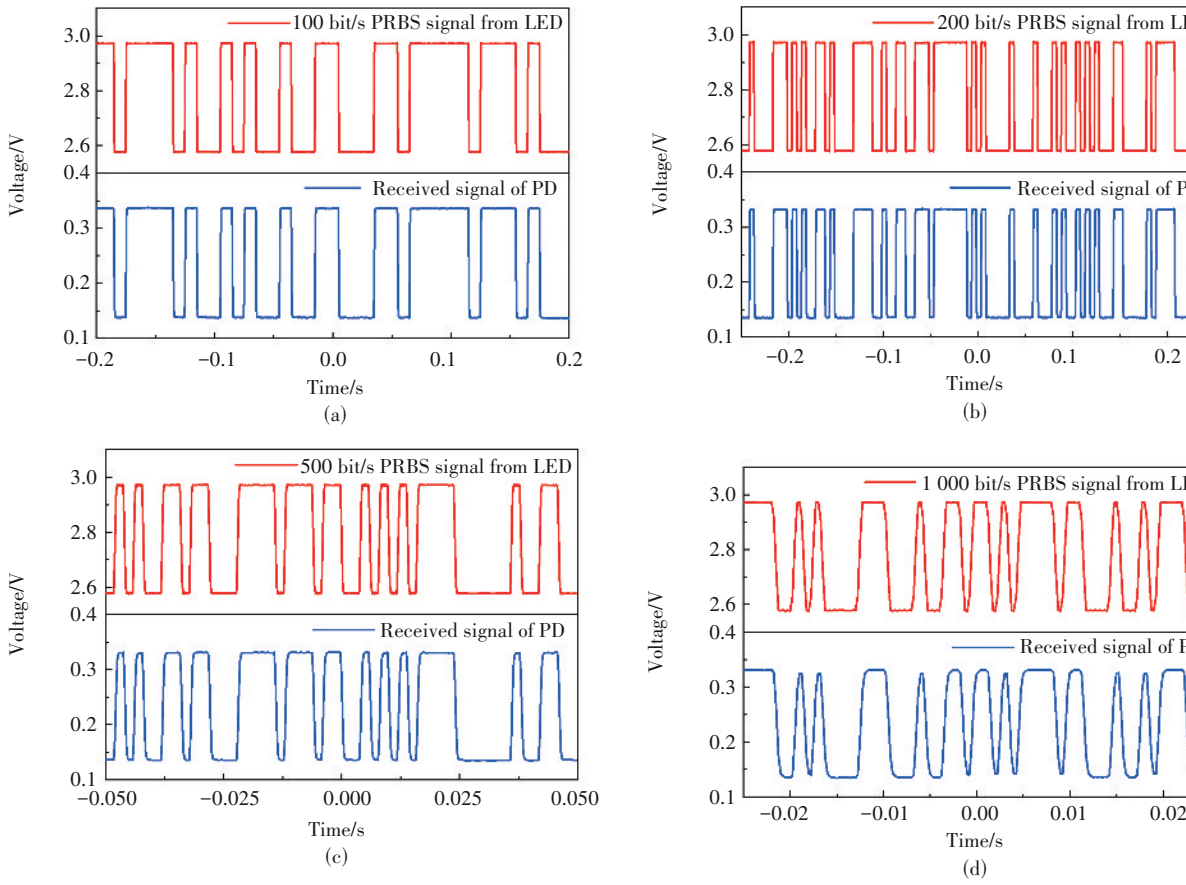

LED: light emitting diode PD: photodetecto PRBS: pseudo-random binary sequence

Figure 4. Measured voltages of the PD under incident PRBS data rates of (a) 100 bit/s, (b) 200 bit/s, (c) 500 bit/s, and (d) 1 000 bit/s

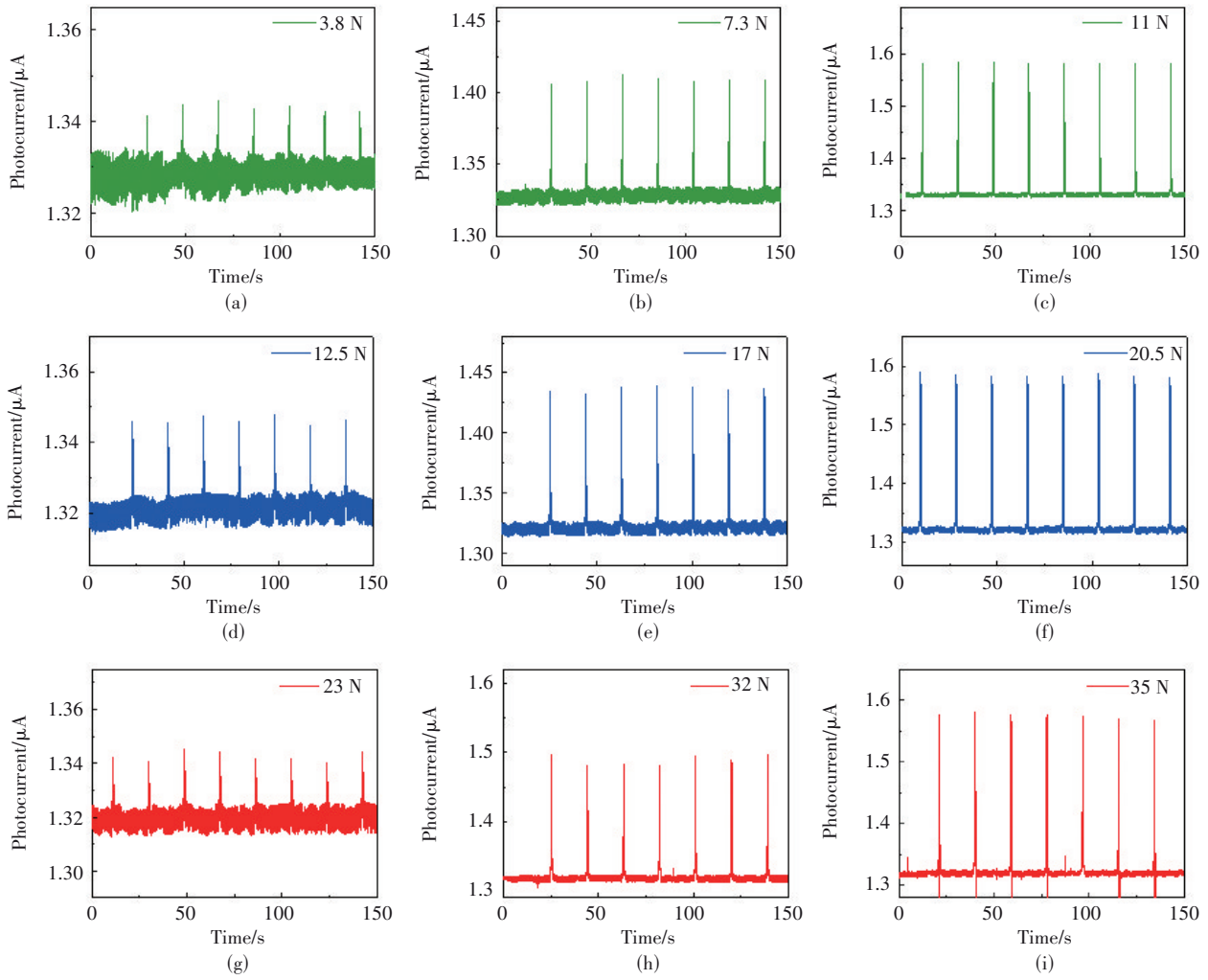

Figure 5. Photocurrent response for Sample #1 under impact forces of (a) 3.8 N, (b) 7.3 N, and (c) 11 N; for Sample #2 under impact forces of (d) 12.5 N, (e) 17 N, and (f) 20.5 N; for Sample #3 under impact forces of (g) 23 N, (h) 32 N, and (i) 35 N

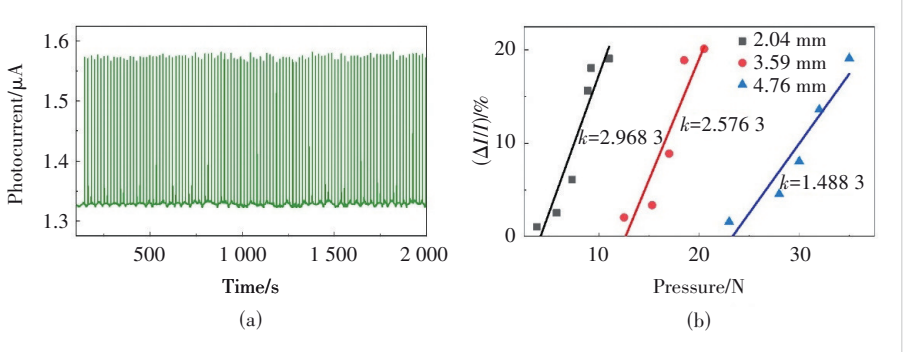

Figure 6. (a) Long-time photocurrent monitor of the sensor with Sample #1; (b) relative photocurrent response of the sensors as functions of impact forces

From the data fitting, Sample #1, the thinnest one, has the highest sensitivity with a slope of 2.968 3% per newton. Sample 2 exhibits a medium sensitivity with a slope of 2.576 3 per newton, while Sample 3, the thickest one, has the lowest sensitivity with a slope of 1.488 3 per newton. Despite the difference in sample thicknesses, the distance between the Al reflector and the chip is set to the same spacing, resulting in the maximum relative photocurrents for all three samples keeping around 20%. The above results reveal that the detection range for impact force can be arbitrarily tailored by selecting PDMS membranes of different thicknesses. In addition, as the thickness of the film increases, the ability to detect the magnitude of the force in-

Table 1. Performance comparison with other force sensors

Method	Linear Range	Sensitivity	Structure Size
Piezoelectric[6]	0.2 – 1.4 N	1.2 V/N	4×4 sensor array (each one: 6×6 mm^2)
Capacitive[7]	0.1 – 1N	0.42 V/N	122×70 mm^2
Capacitive[8]	0.5 – 2 N	N/A	3×0.6×20 mm^3
Capacitive[9]	0 – 9 N	2.8% per newton	22×22×2 mm^3
Fabry-Perot interferometer[15]	0 – 215.4 μN	0.221 pm/μN	20 – 40 mm
Optoelectronic[29]	0 – 40 kPa	0.2 kPa^{-1}	50×50 mm^2
Current work	0 – 35 N	2.96% per newton	2.7×1.8×0.2 mm^3

creases, but the sensitivity decreases. The performance comparisons with other force sensors are summarized in Table 1. The detection range and sensitivity of our current method are comparable to those of piezoelectric and capacitive-based sensors. Notably, the monolithic integration design of our proposed force sensor not only reduces its size to the millimeter scale but also offers advantages in large-scale production and high-density deployment.

4 Conclusions

In summary, a miniature GaN-based impact force sensor is proposed and demonstrated. With a piece of AI attached PDMS film as the force-sensitive unit, deformation of the PDMS induced by the external impact is transformed into the photocurrent changes produced by the transceiver chip. Three PDMS films with different thicknesses are packaged with the transceiver chip to construct impact sensors, and their sensing performances are thoroughly studied. The thickness of PDMS greatly influences the force sensitivity and measurable range. A thin PDMS film is ideal for a low-force and high-sensitivity testing requirement, while a thicker one is better suited for a larger force measurement.

References

[1] CHENG M, ZHU G T, ZHANG F, et al. A review of flexible force sensors for human health monitoring [J]. Journal of advanced research, 2020, 26: 53 – 68. DOI: 10.1016/j.jare.2020.07.001
[2] KENRY, YEO J C, LIM C T. Emerging flexible and wearable physical sensing platforms for healthcare and biomedical applications [J]. Microsystems and nanoengineering, 2016, 2: 16043. DOI: 10.1038/micronano.2016.43
[3] PHAM T H, CARON S, KHEDDAR A. Multicontact interaction force sensing from whole-body motion capture [J]. IEEE transactions on industrial informatics, 2018, 14(6): 2343 – 2352
[4] GAO L, ZHOU C Y, XIAO H, et al. Continuous vertical wheel-rail force reconstruction method based on the distributed Acoustic sensing technology [J]. Measurement, 2022, 197: 111297. DOI: 10.1016/j.measurement.2022.111297
[5] CURRY E J, KE K, CHORSI M T, et al. Biodegradable piezoelectric force sensor [J]. Proceedings of the national academy of sciences of the United States of America, 2018, 115(5): 909 – 914. DOI: 10.1073/pnas.1710874115
[6] EMAMIAN S, NARAKATHU B B, CHLAIHAWI A A, et al. Screen printing of flexible piezoelectric based device on polyethylene terephthalate (PET) and paper for touch and force sensing applications [J]. Sensors and actuators A: physical, 2017, 263: 639 – 647. DOI: 10.1016/j.sna.2017.07.045
[7] GAO S, ARCOS V, NATHAN A. Piezoelectric vs. capacitive based force sensing in capacitive touch panels [J]. IEEE access, 2016, 4: 3769 – 3774
[8] KIM K, PARK J, SUH J H, et al. 3D printing of multiaxial force sensors using carbon nanotube (CNT)/thermoplastic polyurethane (TPU) filaments [J]. Sensors and actuators A: physical, 2017, 263: 493 – 500. DOI: 10.1016/j.sna.2017.07.020
[9] ZHU Y L, CHEN X, CHU K M, et al. Carbon black/PDMS based flexible capacitive tactile sensor for multi-directional force sensing [J]. Sensors, 2022, 22(2): 628. DOI: 10.3390/s22020628
[10] SU H, IORDACHITA I I, TOKUDA J, et al. Fiber optic force sensors for MRI-guided interventions and rehabilitation: a review [J]. IEEE sensors journal, 2017, 17(7): 1952 – 1963. DOI: 10.1109/JSEN.2017.2654489
[11] YUAN W H, YANG Z R, CUI M J, et al. A ring core fiber sensor based on Mach-Zehnder interferometer for transversal force sensing with solvable temperature cross sensitivity [J]. IEEE sensors journal, 2023, 23(4): 3615 – 3622. DOI: 10.1109/JSEN.2023.3234906
[12] LEE C W, LEE J H, SEOK H. Squeezed-light-driven force detection with an optomechanical cavity in a Mach-Zehnder interferometer [J]. Scientific reports, 2020, 10: 17496. DOI: 10.1038/s41598-020-74629-1
[13] XIONG L, JIANG G Z, GUO Y X, et al. A three-dimensional fiber Bragg grating force sensor for robot [J]. IEEE sensors journal, 2018, 18 (9): 3632 – 3639. DOI: 10.1109/JSEN.2018.2812820
[14] LAI W J, CAO L, LIU J J, et al. A three-axial force sensor based on fiber Bragg gratings for surgical robots [J]. IEEE/ASME transactions on mechatronics, 2022, 27(2): 777 – 789. DOI: 10.1109/TMECH.2021.3071437
[15] GONG Y, YU C B, WANG T T, et al. Highly sensitive force sensor based on optical microfiber asymmetrical Fabry-Perot interferometer [J]. Optics express, 2014, 22(3): 3578 – 3584. DOI: 10.1364/OE.22.003578
[16] DASH J N, LIU Z Y, GUNAWARDENA D S, et al. Fabry-Perot cavity-based contact force sensor with high precision and a broad operational range [J]. Optics letters, 2019, 44(14): 3546 – 3549. DOI: 10.1364/OL.44.003546
[17] XIE E Y, CHEN C, OUYANG C S, et al. GaN-based series hybrid LED array: a dual-function light source with illumination and high-speed visible light communication capabilities [J]. Journal of lightwave technology, 2024, 42(1): 243 – 250. DOI: 10.1109/JLT.2023.3303779
[18] FLACK T J, PUSHPAKARAN B N, BAYNE S B. GaN technology for power electronic applications: a review [J]. Journal of electronic materials, 2016, 45(6): 2673 – 2682. DOI: 10.1007/s11664-016-4435-3
[19] ZHU S J, SHAN X Y, LIN R Z, et al. Characteristics of GaN-on-Si green micro-LED for wide color gamut display and high-speed visible light communication [J]. ACS photonics, 2023, 10(1): 92 – 100. DOI: 10.1021/acsphotonics.2c01028
[20] CHANG Y H, HUANG Y M, LIOU F J, et al. 2.805 Gbit/s high-bandwidth phosphor white light visible light communication utilizing an InGaN/GaN semipolar blue micro-LED [J]. Optics express, 2022, 30(10): 16938 – 16946. DOI: 10.1364/OE.455312
[21] YU H B, MEMON M H, WANG D H, et al. AlGaN-based deep ultraviolet micro-LED emitting at 275 nm [J]. Optics letters, 2021, 46(13): 3271 – 3274. DOI: 10.1364/OL.431933
[22] MEMON M H, YU H B, LUO Y M, et al. A three-terminal light emitting and detecting diode [J]. Nature electronics, 2024, 7(4): 279 – 287. DOI: 10.1038/s41928-024-01142-y
[23] YIN J H, YANG H Y, LUO Y M, et al. III-nitride microsensors for 360° angle detection [J]. IEEE electron device letters, 2022, 43(3): 458 – 461. DOI: 10.1109/LED.2022.3148232
[24] YU B L, LUO Y M, CHEN L, et al. An optical humidity sensor: a compact photonic chip integrated with artificial opal [J]. Sensors and actuators B: chemical, 2021, 349: 130763. DOI: 10.1016/j.snb.2021.130763

[25] YU B L, LUO Y M, LI J, et al. Interface engineering in chip-scale GaN optical devices for near-hysteresis-free hydraulic pressure sensing [J]. ACS applied materials & interfaces, 2022, 14(33): 38351 – 38357. DOI: 10.1021/acsami.2c09291
[26] QIN F F, LU X Y, CHEN Y, et al. Concentration sensing system with monolithic InGaN/GaN photonic chips [J]. Chinese optics letters, 2024, 22(6): 062501. DOI: 10.3788/col202422.062501
[27] AN X S, LUO Y M, YU B L, et al. A chip-scale GaN-based optical pressure sensor with microdome-patterned polydimethylsiloxane (PDMS) [J]. IEEE electron device letters, 2021, 42(10): 1532 – 1535. DOI: 10.1109/LED.2021.3103891
[28] ZHAN J, ZHU L, HE Z, et al. Impact force sensors based on GaN optical devices with micropatterned PDMS sponges [J]. IEEE sensors journal, 2023, 23(17): 19226 – 19231. DOI: 10.1109/JSEN.2023.3295931
[29] RAMUZ M, TEE B C, TOK J B, et al. Transparent, optical, pressure-sensitive artificial skin for large-area stretchable electronics [J]. Advanced materials (Deerfield Beach, Fla.), 2012, 24(24): 3223 – 3227

Biographies

RUAN Junhui is currently pursuing his bachelor's degree at the School of Communications and Information Engineering, Nanjing University of Posts and Telecommunications, China. His research interests include optical fiber sensing, GaN optoelectronics sensors, and analog circuit design.

JIANG Chengxiang is currently pursuing his master's degree at the School of Communications and Information Engineering, Nanjing University of Posts and Teleommunications, China. His research interests include GaN devices and visible light communications.

XU Shengli is currently pursuing his bachelor's degree at the School of Communications and Information Engineering, Nanjing University of Posts and Teleommunications, China. His research interests focus on digital signal processing and hardware circuit design.

WANG Yongjin received his PhD degree in microelectronics and solid-state electronics from Shanghai Institute of Microsystem and Information Technology, Chinese Academy of Sciences, China in 2005. He was engaged in the research work with the University of Freiburg, Germany, Tohoku University, Japan, Forschungszentrum Jülich, Germany, and the University of Bristol, UK. Since 2011, he has been a professor with the Nanjing University of Posts and Telecommunications, China, where he is currently the chief investigator of National Innovation Base for Micro-Nano Device and Information System. His research interests include III-nitride monolithic photonic circuit for visible light communication and the Internet of Things. He was the recipient of many scholarships, including the Humboldt Foundation Scholarship, the JSPS Special Researcher Scholarship, and the Royal Society for Engineering Scholarship.

SHI Fan (sf123@njupt.edu.cn) received his PhD degree from the School of Communications and Information Engineering, Shanghai University, China in 2020. He has joined the School of Communications and Information Engineering, Nanjing University of Posts and Telecommunications, China as a lecturer since 2020. His research interests include GaN devices, visible light communication, and mode-locked fiber lasers.

Intelligent AP Clustering and Receiver Design for Uplink Cell-free Networks

AN Zhenyu[1,4], HE Shiwen[1,2], YANG Li[3], ZHAN Hang[1], HUANG Yongming[1,4]

(1. Purple Mountain Laboratories, Nanjing 211111, China;
2. School of Computer Science and Engineering, Central South University, Changsha 410083, China;
3. ZTE Corporation, Shenzhen 518057, China;
4. National Mobile Communications Research Laboratory, School of Information Science and Engineering, Southeast University, Nanjing 210096, China)

DOI: 10.12142/ZTECOM.202502011

https://kns.cnki.net/kcms/detail/34.1294.TN.20250520.0957.002.html, published online May 20, 2025

Manuscript received: 2024-09-26

Abstract: Cell-free networks can effectively reduce interference due to diversity gain. Two key technologies, access point (AP) clustering and transceiver design, play key roles in cell-free networks, and they are implemented at different layers of the air interface. To address the issues and obtain global optimal results, this paper proposes an uplink joint AP clustering and receiver optimization algorithm, where a cross-layer optimization model is built based on graph neural networks (GNNs) with low computational complexity. Experimental results show that the proposed algorithm can activate fewer APs for each user with a small performance loss compared with conventional algorithms.

Keywords: AP clustering; cell-free networks; cross-layer optimization; graph neural network

Citation (Format 1): AN Z Y, HE S W, YANG L, et al. Intelligent AP clustering and receiver design for uplink cell-free networks [J]. ZTE Communications, 2025, 23(2): 103 - 108. DOI: 10.12142/ZTECOM.202502011

Citation (Format 2): Z. Y. An, S. W. He, L. Yang, et al., "Intelligent AP clustering and receiver design for uplink cell-free networks," *ZTE Communications*, vol. 23, no. 2, pp. 103 - 108, Jun. 2025. doi: 10.12142/ZTECOM.202502011.

1 Introduction

The 6G mobile communication system[1-4] will introduce new application scenarios including immersive cloud extended reality (XR), holographic communication, sensory interconnection, etc. As a result, extremely high transmission metrics have been proposed, including Terabit per second level throughput, microsecond level time delay, 10^7 per square kilometer connection density, and 99.999 9% block error rates (BLERs). The increased number of devices in the network presents a series of challenges for a smaller coverage area of a single base station operated at higher frequency bands. Interference at cell boundaries and frequent switching can result in poor service quality and high deployment costs. Fortunately, cell-free architecture can serve as a potential solution to these problems.

Fig. 1 shows a typical cell-free architecture[5], which consists of a central processing unit (CPU) and a large number of distributed access points (APs) that serve a small amount of user equipment (UE). Each AP is connected to the CPU through a fronthaul link and sends the data received from the users in the uplink to the CPU. The CPU transmits the downlink data and power control parameters to the APs. Due to the short distance between AP and UE, the system can achieve high spatial macro-diversity gain and reduce the path loss.

In the early studies[6-7] on cell-free networks, the concept of

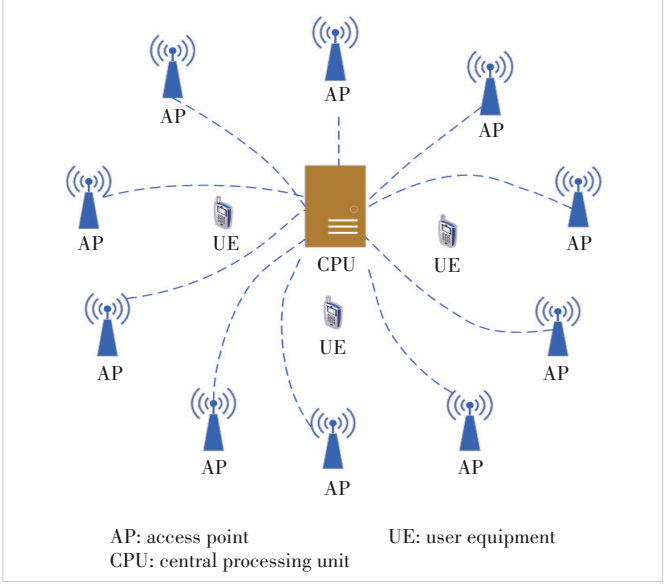

Figure 1. Architecture of cell-free multiple-input multiple-output

This work was supported in part by National Natural Science Foundation of China under Grant No. 62171474.

max-min fairness was emphasized, and it was assumed that all APs would provide almost uniform high-quality services to all UE, which would inevitably increase the CPU signal processing complexity and fronthaul overhead. To address this issue, the authors of Ref. [8] proposed a user-centric virtual cell approach to cell-free massive multiple-input multiple-output (MIMO), where each user is served by a limited number of APs, but using a complex approach. In a user-centric cell-free system, how to assign APs to each user, that is AP clustering, and simultaneously perform the beamforming task is the key to improving network performance. A new distributed and scalable algorithm[9] for a user-centric approach in cell-free large-scale MIMO systems is proposed, which jointly addresses initial access, pilot assignment, cooperation cluster formation, precoding, and combining issues. Better results were obtained compared with regularized zero-forcing (RZF), but the issues were individually considered. The authors of Ref. [10] proposed an AP selection algorithm that combines initial access and pilot selection with a complex algorithm. In Ref. [11], a new framework was proposed for the structured massive access in cell-free massive MIMO systems, which comprises one initial access algorithm, a partial large-scale fading decoding (P-LSFD) strategy, two pilot assignment schemes, and one fractional power control policy. New closed-form spectral efficiency (SE) expressions with maximum ratio (MR) were also obtained. The authors of Ref. [12] proposed a joint power allocation and AP selection algorithm, which selected AP through continuous convex optimization. The simulation results showed that the algorithm had significant energy savings, but at the cost of high computational complexity.

Recently, graph neural networks (GNNs) have also been applied in wireless networks[13]. The authors of Ref. [14] proposed an AP selection algorithm based on GNN, which can predict the connection between UE and APs. However, when the number of APs is large, the prediction accuracy decreases. Ref. [15] considered the joint user scheduling and beamforming optimization algorithm based on the GNN algorithm, but it was limited to the downlink system.

Under the premise of considering the maximum linked APs for a single user device, this paper studies and solves the problem of joint optimization of cell-free uplink AP clustering and combining based on historical data and GNN. The main contributions are summarized as follows:

• Aiming to maximize the system rate while considering the maximum active AP number for a user device, this paper constructs a joint optimization model of cell-free uplink AP clustering and combining;

• An intelligent optimization algorithm based on GNN, including problem transformation, two loops of iterative process, etc., is designed to solve the above joint optimization problems;

• Experiment results show that the proposed algorithm has competitive advantages in performance and computational efficiency compared with the traditional clustering optimization ideas.

2 System Model

We consider an uplink cell-free system with B APs and K users, where each AP is equipped with N_t antennas, while each user has a single antenna. The K users are randomly distributed, and the channel coefficient vector between the b-th AP and the k-th user is denoted as $\boldsymbol{h}_{b,k} \in \mathbb{C}^{N_t*1}, b \in \{1,\cdots,B\}, k \in \{1,\cdots,K\}$. $\boldsymbol{w}_{b,k} \in \mathbb{C}^{N_t*1}$ is the corresponding combining beam vector. The transmitting power of the k-th user is $p_k \in \mathbb{C}^{1*1}$. The stacked combining beam vector and channel coefficient vector of the k-th user could be respectively denoted as $\boldsymbol{w}_k = \left[\boldsymbol{w}_{1,k}^{\mathrm{T}},\cdots,\boldsymbol{w}_{B,k}^{\mathrm{T}}\right]^{\mathrm{T}} \in \mathbb{C}^{BN_t*1}$, $\|\boldsymbol{w}_k\| = 1$ and $\boldsymbol{h}_k = \left[\boldsymbol{h}_{1,k}^{\mathrm{T}},\cdots,\boldsymbol{h}_{B,k}^{\mathrm{T}}\right]^{\mathrm{T}} \in \mathbb{C}^{BN_t*1}$. Assuming that $x_l \in \mathbb{C}^{1*1}$ is the uplink transmitting signal of the l-th user, the received signal could be denoted as follows.

$$\boldsymbol{y} = \sum_{l=1}^{K} p_l \boldsymbol{h}_l x_l + \boldsymbol{n} \tag{1}$$

where $\boldsymbol{n} \in \mathbb{C}^{BN_t \times 1}$ is the complex additive white Gaussian noise with zero mean value and variance σ^2. For convenience, let $\bar{\boldsymbol{h}}_k = \boldsymbol{h}_k/\sigma$ (channel estimation is another topic in wireless networks[19]).

As shown in Fig. 2, several AP clusters are formed in an uplink cell-free network, in which each user is served by various APs, and one AP may link various users. Here, an auxiliary variable $u_{b,k} \in \{0,1\}$ is introduced to represent the link status between the b-th AP and the k-th user. $u_{b,k} = 1$ means that the b-th AP serves the k-th user, otherwise not. Then, we have

$$\bar{x}_k = \bar{\boldsymbol{w}}_k^H \boldsymbol{y} \tag{2}$$

where

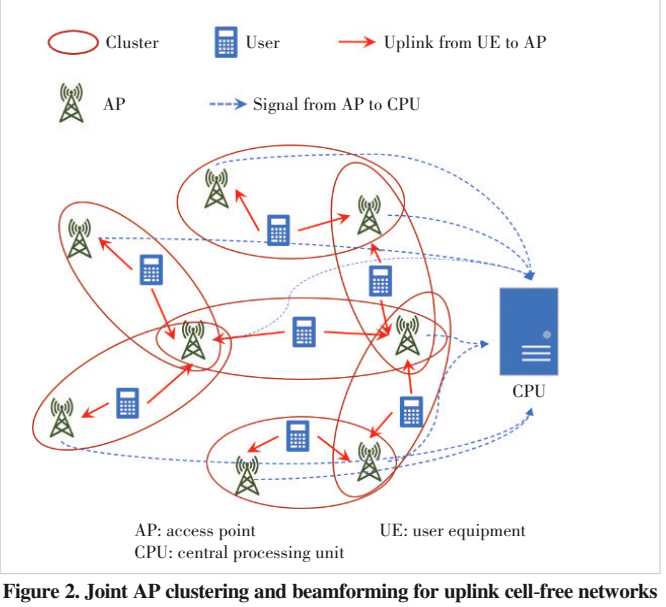

Figure 2. Joint AP clustering and beamforming for uplink cell-free networks

$$\bar{\boldsymbol{w}}_k = \boldsymbol{Q}_k \boldsymbol{w}_k \tag{3}$$

$$\boldsymbol{Q}_k = \begin{bmatrix} u_{1,k}\boldsymbol{I}_{N_t \times N_t} & \cdots & 0 \\ \vdots & \ddots & \vdots \\ 0 & \cdots & u_{B,k}\boldsymbol{I}_{N_t \times N_t} \end{bmatrix} \tag{4}$$

Thus, the signal-to-noise-ratio (SINR) of the k-th user is formulated as follows:

$$\mathrm{SINR}_k = \frac{\Re_k}{I_k + 1} \tag{5}$$

where $\Re_k = p_k \sum_{b=1}^{B} u_{b,k} \left| \boldsymbol{w}_{b,k}^H \bar{\boldsymbol{h}}_{b,k} \right|^2$ and $I_k = \sum_{b=1}^{B} u_{b,k} \sum_{l=1, l \neq k}^{K} p_l \left| \boldsymbol{w}_{b,k}^H \bar{\boldsymbol{h}}_{b,l} \right|^2$.

In this work, the joint optimization problem of uplink clustering and combining design is considered, which is formulated as:

$$\begin{aligned} &P1: \max_{u_{b,k}, \boldsymbol{w}_k} \sum_{k \in \{1,2,\cdots,K\}} \log\left(1 + \mathrm{SINR}_k\right) \\ &\text{s.t. } C1: \sum_{b \in \{1,\cdots,B\}} u_{b,k} \leqslant N, \forall k \in \{1,\cdots,K\} \\ &C2: \left\| \boldsymbol{w}_k \right\|_2 = 1, \forall k \in \{1,\cdots,K\} \\ &C3: u_{b,k} \in \{0,1\}, \forall b \in \{1,\cdots,B\}, k \in \{1,\cdots,K\} \end{aligned} \tag{6}$$

In the above problem, constraint $C1$ assumes that the maximum number of linked APs for each user is N, where $N \leqslant B$. Constraint $C3$ specifies that there are only two states between the user and each AP, i.e., linked and non-linked. Constraint $C2$ ensures that the beam vectors are normalized. It is noted that $P1$ is a non-convex integer programming problem, which is difficult to solve directly. Inspired by the experimental result that GNN outperforms convolutional neural networks in handling wireless network topology information in Ref. [15], we adopt GNN to accomplish the above task in the following section.

3 Optimization Method

3.1 Problem Transformation

To simplify the integer programming problem, constraint $C3$ is first equivalently transformed into the following form:

$$C4: 0 \leqslant u_{b,k} \leqslant 1, \forall b \in \{1,\cdots,B\}, k \in \{1,\cdots,K\} \tag{7}$$

$$C5: \sum_{b \in \{1,\cdots,B\}, k \in \{1,\cdots,K\}} \left(u_{b,k} - u_{b,k}^2\right) \leqslant 0 \tag{8}$$

Introducing the nonconvex constraint $C5$ into the objective function of $P1$ using a Lagrange multiplier μ, the original problem $P1$ is transformed into the following max-min problem $P2$.

$$\begin{aligned} &P2: \max_{\mu} \min_{u_{b,k}, \boldsymbol{w}_k} -\sum_{k \in \{1,2,\cdots,K\}} \log(1 + \mathrm{SINR}_k) + \\ &\mu \chi_C^{\geqslant} \sum_{b \in \{1,\cdots,B\}, k \in \{1,\cdots,K\}} \left(u_{b,k} - u_{b,k}^2\right) \\ &\text{s.t. } C1, C2, C4 \end{aligned} \tag{9}$$

where $\chi_C^{\geqslant}(a) = \max(a, 0)$ is a penalty function to measure the violation degree of constraint $C5$, which adopts an element-wise operation form. In Problem $P2$, constraints $C1$ and $C4$ are convex, and objective function is nonconvex with a complex form. To solve this problem, a two-loop iterative approach is designed. In the outer loop, $u_{b,k}$ and $\boldsymbol{w}_k$ are fixed, and we update μ using the formula:

$$\mu = \mu + \varepsilon_u \chi_C^{\geqslant} \sum_{b \in \{1,\cdots,B\}, k \in \{1,\cdots,K\}} \left(u_{b,k} - u_{b,k}^2\right) \tag{10}$$

where ε_u represents the step size. In the inner loop, μ is fixed, and we aim at obtaining $u_{b,k}$ and $\boldsymbol{w}_k$ by solving the following problem.

$$\begin{aligned} &P3: \Psi \triangleq \min_{u_{b,k}, \boldsymbol{w}_k} \Bigg(-\sum_{k \in \{1,2,\cdots,K\}} \log(1 + \mathrm{SINR}_k) + \\ &\mu \chi_C^{\geqslant} \sum_{b \in \{1,\cdots,B\}, k \in \{1,\cdots,K\}} \left(u_{b,k} - u_{b,k}^2\right) \Bigg) \\ &\text{s.t. } C1, C2, C4 \end{aligned} \tag{11}$$

To solve Problem $P3$, $\boldsymbol{w}_k$ could be estimated with the minimum mean square error (MMSE) approach as follows.

$$\boldsymbol{w}^*_k = \frac{\left(\boldsymbol{I} + \sum_{l \in K} p_l \tilde{\bar{\boldsymbol{h}}}_l \tilde{\bar{\boldsymbol{h}}}_l^H\right)^{-1} \tilde{\bar{\boldsymbol{h}}}_k}{\left\| \left(\boldsymbol{I} + \sum_{l \in K} p_l \tilde{\bar{\boldsymbol{h}}}_l \tilde{\bar{\boldsymbol{h}}}_l^H\right)^{-1} \tilde{\bar{\boldsymbol{h}}}_k \right\|} \tag{12}$$

where $\tilde{\bar{\boldsymbol{h}}}_k = \boldsymbol{Q}_k \bar{\boldsymbol{h}}_k$. Then, given $\boldsymbol{w}_k$, we solve Problem $P2$ using GNN to obtain $u_{b,k}$.

3.2 Intelligent Optimization Framework

In this section, an intelligent optimization framework using GNN is proposed to solve Problem $P2$. As shown in Fig. 3, the framework consists of inner and outer loops. In the outer loop, $u_{b,k}$ and $\boldsymbol{w}_k$ are fixed, and we update μ using Eq. (10). In the inner loop, $u_{b,k}$ is first fixed and we obtain $\boldsymbol{w}_k$ using Eq. (12). Then, $\boldsymbol{w}_k$ is fixed and a GNN based approach is designed to obtain $u_{b,k}$ in the inner loop. Four parts comprise the inner loop. Specifically, the graph representation layer builds a graph that can be applied for subsequent processing; the graph convolution neural network (GCN) layer extracts features from the constructed graph, and outputs optimal $u_{b,k}$; the projection layer projects the output results into the feasible region to meet constraints $C1$ and

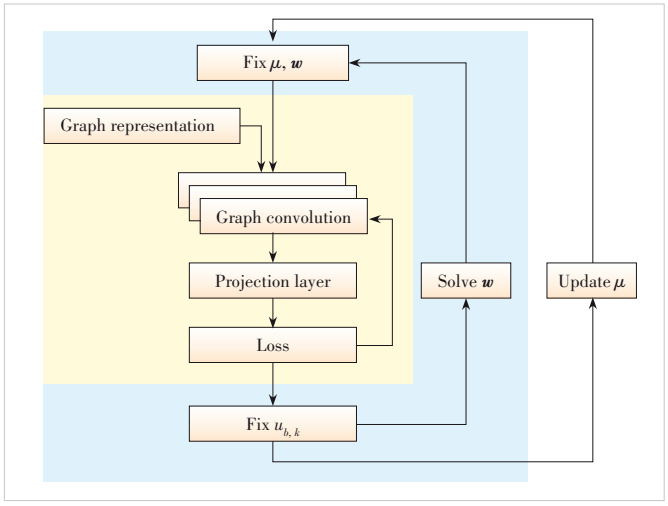

Figure 3. Intelligent iterative optimization framework

*C*4; the loss function layer calculates the loss of the network. These parts are discussed in detail in the following sections.

3.3 Knowledge Graph Representation

The foundation for using GNNs in wireless communication networks is to model the network as a graph, where nodes and edges are assigned feature information. This graph can then be processed by GCN[16-17]. The key step in constructing a knowledge graph representation is to define the triples in wireless networks, which consist of head entities, tail entities, and their relationships.

The knowledge graph can be denoted as $G=(V,E)$, where V is the set of nodes and E is the set of edges. In the paper, the communication links between APs and users are regarded as nodes, while the interference links between users are regarded as edges. The features of nodes and edges are characterized by channel vectors and other state information, as shown in Fig. 4. Specifically, for the i-th node $v_i \in V$, its node feature is defined as $\boldsymbol{x}_i = \left(\left|\bar{\boldsymbol{h}}_{i,1}^H \bar{\boldsymbol{h}}_{i,1}\right|,\cdots,\left|\bar{\boldsymbol{h}}_{i,B}^H \bar{\boldsymbol{h}}_{i,B}\right|\right) \in \mathbb{C}^{B*1}$, and the edge feature of $\boldsymbol{e}_{ij} = \left(v_i,v_j\right) \in E$ is defined as $\boldsymbol{e}_{i,j} = \left|\bar{\boldsymbol{h}}_i^H \bar{\boldsymbol{h}}_j\right| \in \mathbb{C}^{1*1}, j \in \mathcal{N}_i$, where $\left(v_i,v_j\right) \in E$ means the edges of nodes v_i and v_j, and $\mathcal{N}_i$ is the set of adjacent nodes of v_i. From the definition, we can see that a node represents the communication link between a user and an AP, while an edge represents the interference link between users. In the inner iteration process, we initialize the constructed graph G and the objective solution $u_{b,k}$, and then use them as the input to GNN.

3.4 Structure of GCN

Fig. 5 shows the structure of GCN, which comprises message generation, message aggregation, and node updating. Inspired by Ref. [18], we update the rule of the i-th node in layer l as follows.

$$\begin{aligned}\boldsymbol{g}_i^{(l)} &= \boldsymbol{G}\left(\left\{\boldsymbol{M}_\theta^{(l)}\left(\boldsymbol{\beta}_j^{(l-1)},\boldsymbol{x}_j,\boldsymbol{e}_{j,i}\right), j \in \mathcal{N}_i\right\}\right) \\ \boldsymbol{\beta}_i^{(l)} &= \boldsymbol{T}_\theta^{(l)}\left(\boldsymbol{\beta}_i^{(l-1)},\boldsymbol{x}_i,F_{\text{norm}}\left(\boldsymbol{x}_i,\boldsymbol{g}_i^{(l)}\right)\right), i \in \mathcal{V}\end{aligned} \tag{13}$$

In Eq. (13), $\boldsymbol{M}_\theta^{(l)}(\cdot)$ is a message generation function, $\boldsymbol{T}_\theta^{(l)}$ is an updating function, and they are realized using different deep neural networks. $\boldsymbol{G}(\cdot)$ is a message aggregation function and it is applied to aggregate information of nodes. $\boldsymbol{\beta}_i^{(l)} \triangleq \left[u_{:,i},p_i\right] \in \mathbb{R}^{B+1}$ represents the input vector of the i-th node in the l-th layer GCN. $F_{\text{norm}}(\cdot)$ is applied to normalized $\boldsymbol{g}_i^{(l)}$ with the following form:

$$F_{\text{norm}}\left(\boldsymbol{x}_i,\boldsymbol{g}_i^{(l)}\right) = \left\|\boldsymbol{x}_i\right\|_2 \frac{\boldsymbol{g}_i^{(l)}}{\left\|\boldsymbol{g}_i^{(l)}\right\|_2}, i \in \mathcal{V}. \tag{14}$$

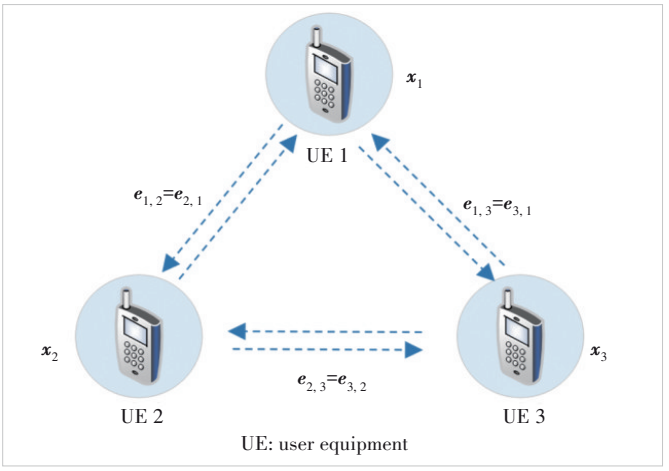

Figure 4. Knowledge graph representation of uplink transmission

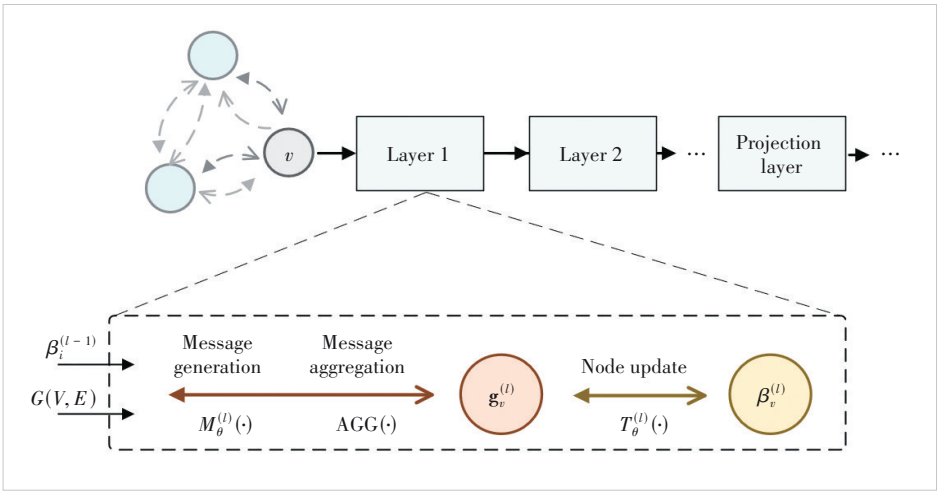

Figure 5. Structure of the proposed graph neural network

3.5 Projection Layer

GNN could obtain $u_{b,k}$ from optimizing $P3$ in the above subsections, without considering the convex constraint $C1$ or $C4$. In this section, an individual projection layer is considered for post-processing $u_{b,k}$ to satisfy constraints $C1$ and $C4$. A projection operator is designed as shown in Eq. (15). It can be easily found that $u_{b,k}$ takes values in the interval [0, 1] (Constraint $C4$), and its summation value is less than N (Constraint $C1$).

$$\Omega_1 \triangleq \left\{ u_{b,k}^{(*)} = \frac{N}{\max\left\{ \sum_{b=\{1,\cdots,B\}} u_{b,k}', N \right\}} u_{b,k}' \right\} \tag{15},$$

where $u_{b,k}' = \min\left(\max\{u_{b,k}, 0\}, 1\right)$.

4 Experiment

4.1 Parameter Settings

This section reports simulated experimental results using the proposed algorithm. In the experiment, users are randomly distributed and they share the same noise variance, namely, $\sigma_k^2 = \sigma^2, \forall k \in \{1,\cdots,K\}$. The radius of the cell is 300 m, and the minimum distance between the user and AP is 200 m. The signal-to-noise ratio (SNR) of the AP is designed as SNR = $10\log(\frac{P}{\sigma^2})$ dB. Updating the step size of ε_u is 1×10^{-5}. The maximum iteration epoch is 200, and the iteration stopping threshold is 1×10^{-3}. An Adam optimizer is adopted, and the learning rate is 1×10^{-4}. The Monte Carlo method is used and the average sum rate is the final value. Besides the proposed algorithm, two approaches are also applied as the baselines. In Baseline 1, for each user, N APs with the optimal channels will be chosen as a cluster. In Baseline 2, all APs will be applied to serve all users.

4.2 Experiment Results

1) Experiment 1: small-scale experiment results

In the small-scale experiment, experiment simulation parameters are shown in Table 1.

In Tables 2 and 3, Baseline 2 applies all seven APs to serve users, thus obtaining the optimal results. In contrast, Baseline 1 selects the four APs with the best channel condition for one user, resulting in a performance loss of less than 2% while reducing linked APs. Moreover, fewer APs are linked using the proposed algorithm, with a performance loss of less than 7% compared with Baseline 1.

2) Experiment 2: large-scale experiment results

In the large-scale experiment, AP number B is 21, user number K is 10, and the maximum linked AP number N is 2. Other simulation parameters are the same as in Table 1.

In the large-scale experiment, all 21 APs are applied to serve 10 users for Baseline 2, which brings the best sum rate performance. Baseline 1 chooses 2 APs for each user device, and it obtains about 5% performance loss when SNR is 20 dB, but the performance loss increases if SNR is 0 dB. The proposed method tends to apply fewer APs to serve UE, but at the cost of about 5% performance loss compared with Baseline 1.

Table 1. Default experiment simulation parameters

Default System Parameter	Value
AP number, B	7
Antenna number of AP, N_t	4
User number, K	3
Antenna number of user	1
SNR/dB	0, 10, 20
Transmitting power of UE, p_k	1 W
Training number	20 000
Testing number	2 000
Maximum link AP number of UE, N	4
Noise variance, σ	1

AP: access point SNR: signal-to-noise ratio UE: use equipment

Table 2. Average sum rate in Experiment 1

	SNR/dB	Proposed/ (bit·s^{-1}·Hz^{-1})	Baseline 1/ (bit·s^{-1}·Hz^{-1})	Baseline 2/ (bit·s^{-1}·Hz^{-1})
$N = 4$	0	4.279 9	4.585 3	4.613 7
	10	20.344 5	21.088 6	21.398 4
	20	40.108 5	41.182 2	41.256 3

SNR: signal-to-noise ratio

Table 3. Average linked access point number in Experiment 1

	SNR/dB	Proposed	Baseline 1	Baseline 2
$N = 4$	0	3.039	4	7
	10	3.055	4	7
	20	3.045	4	7

SNR: signal-to-noise ratio

4.3 Computational Complexity

In Tables 4 and 5, the average sum rate and average linked access point are respectively listed. The computational complexity of the proposed algorithm, and Baselines 1 and 2 are shown in Table 6. The results show that the proposed method has competitive computational complexity compared with Baselines 1 and 2. In small-scale networks, the computational complexity of the proposed method is about 80% and 72% of Baselines 1 and 2, respectively. The advantage increases in large-scale networks, and the ratios are about 52% and 42%.

5 Conclusions

This paper proposes an intelligent optimization algorithm based on GNNs to solve the joint optimization problem of AP clustering and beamforming in uplink massive cell-free networks. We first construct an optimization model with the goal of maximizing the system's sum rate, and solve it under the con-

Table 4. Average sum rate in Experiment 2

	SNR/dB	Proposed/ (bit·s^{-1}·Hz^{-1})	Baseline 1/ (bit·s^{-1}·Hz^{-1})	Baseline 2/ (bit·s^{-1}·Hz^{-1})
N = 2	0	5.065 7	5.535 6	7.116 7
	10	40.438 0	42.832 3	47.354 0
	20	99.548 2	105.068 7	110.738 1

SNR: signal-to-noise ratio

Table 5. Average linked access point number in Experiment 2

	SNR/dB	Proposed	Baseline 1	Baseline 2
N = 2	0	1.428	2	21
	10	1.241	2	21
	20	1.225	2	21

SNR: signal-to-noise ratio

Table 6. Comparison of computational complexity

Algorithms	Experiments	Proposed	Baseline 1	Baseline 2
Computational complexity	Experiment 1	76 512	95 296	106 624
	Experiment 2	1 249 600	2 404 736	2 935 296

straint of considering the maximum number of APs linked with a single user. This paper transforms the wireless network resource optimization problem into a graph optimization problem and leverages GNN to solve it. Simulation experiments show that the proposed algorithm allocates fewer APs to serve a single user than traditional methods at the cost of a small performance loss.

References

[1] YOU X H, WANG C X, HUANG J, et al. Towards 6G wireless communication networks: vision, enabling technologies, and new paradigm shifts [J]. Science China information sciences, 2020, 64(1): 110301. DOI: 10.1007/s11432-020-2955-6
[2] WU Y, WANG D M, YOU X H. Cell-free radio access network technology for 6G [J]. ZTE technology journal, 2024, 30(4): 14 – 25. DOI: 10.12142/ZTETJ.202404004
[3] LI W J, YU P, ZHANG P. Architecture and key technologies of 6G intelligent endogenous network [J]. ZTE technology journal, 2023, 29(5): 2 – 8. DOI: 10.12142/ZTETJ.202305002
[4] HUANG Y H, WANG Q X, LI N. Intelligent and lean 6G network [J]. ZTE technology journal, 2024, 30(4): 3 – 9. DOI: 10.12142/ZTETJ.202404002
[5] WANG D M. Wireless transmission techniques of cell-free massive MIMO for 6G mobile communications [J]. Mobile communications, 2021, 45(4): 10 – 15
[6] NGO H Q, TRAN L N, DUONG T Q, et al. Energy efficiency optimization for cell-free massive MIMO [C]//The 18th International Workshop on Signal Processing Advances in Wireless Communications (SPAWC). IEEE, 2017: 1 – 5. DOI: 10.1109/SPAWC.2017.8227722
[7] YANG H, MARZETTA T L. Capacity performance of multicell large-scale antenna systems [C]//The 51st Annual Allerton Conference on Communication, Control, and Computing (Allerton). IEEE, 2013: 668 – 675. DOI: 10.1109/Allerton.2013.6736589
[8] BUZZI S, D'ANDREA C. Cell-free massive MIMO: user-centric approach [J]. IEEE wireless communications letters, 2017, 6(6): 706 – 709. DOI: 10.1109/LWC.2017.2734893
[9] BJÖRNSON E, SANGUINETTI L. A new look at cell-free massive MIMO: making it practical with dynamic cooperation [C]//The 30th Annual International Symposium on Personal, Indoor and Mobile Radio Communications (PIMRC). IEEE, 2019: 1 – 6. DOI: 10.1109/PIMRC.2019.8904101
[10] BJÖRNSON E, SANGUINETTI L. Scalable cell-free massive MIMO systems [J]. IEEE transactions on communications, 2020, 68(7): 4247 – 4261. DOI: 10.1109/TCOMM.2020.2987311
[11] CHEN S F, ZHANG J Y, BJÖRNSON E, et al. Structured massive access for scalable cell-free massive MIMO systems [J]. IEEE journal on selected areas in communications, 2021, 39(4): 1086 – 1100. DOI: 10.1109/JSAC.2020.3018836
[12] VU T X, CHATZINOTAS S, SHAHBAZPANAHI S, et al. Joint power allocation and access point selection for cell-free massive MIMO [C]//IEEE International Conference on Communications (ICC). IEEE, 2020: 1 – 6. DOI: 10.1109/ICC40277.2020.9148948
[13] HE S W, XIONG S W, OU Y Y, et al. An overview on the application of graph neural networks in wireless networks [J]. IEEE open journal of the communications society, 2021, 2: 2547 – 2565
[14] RANASINGHE V, RAJATHEVA N, LATVA-AHO M. Graph neural network based access point selection for cell-free massive MIMO systems [C]//IEEE Global Communications Conference (GLOBECOM). IEEE, 2021: 1 – 6. DOI: 10.1109/GLOBECOM46510.2021.9685221
[15] HE S W, YUAN J, AN Z Y, et al. Joint user scheduling and beamforming design for multiuser MISO downlink systems [J]. IEEE transactions on wireless communications, 2023, 22(5): 2975 – 2988. DOI: 10.1109/TWC.2022.3215666
[16] HE S W, OU Y Y, WANG L P, et al. Representation learning of knowledge graph for wireless communication networks [C]//IEEE Global Communications Conference. IEEE, 2022: 1338 – 1343. DOI: 10.1109/GLOBECOM48099.2022.10001185
[17] CHEN T R, ZHANG X R, YOU M L, et al. A GNN-based supervised learning framework for resource allocation in wireless IoT networks [J]. IEEE Internet of Things journal, 2022, 9(3): 1712 – 1724. DOI: 10.1109/JIOT.2021.3091551
[18] HE S W, XIONG S W, AN Z Y, et al. An unsupervised deep unrolling framework for constrained optimization problems in wireless networks [J]. IEEE transactions on wireless communications, 2022, 21(10): 8552 – 8564. DOI: 10.1109/TWC.2022.3166964
[19] HE S W, HUANG F Q, AN Z Y, et al. An intelligent channel prediction method in mobile scenarios [J]. Journal of signal processing, 2022, 38(8): 1579 – 1591. DOI: 10.16798/j.issn.1003-0530.2022.08.003

Biographies

AN Zhenyu (anzhenyu_155@126.com) is currently a senior engineer with Purple Mountain Laboratories, China. His research interests include optimization theory and ultra-reliable and low latency communications.

HE Shiwen is a professor in the School of Computer Science and Engineering, Central South University, China. His research interests include wireless communication networks, distributed learning and optimization theory of computation, intelligent Internet of Things, etc.

YANG Li is a senior engineer of ZTE Corporation. He is also an expert in the State Key Laboratory of Mobile Network and Mobile Multimedia Technology, China. His research interests include 3GPP protocol design, intelligent wireless networks, etc.

ZHAN Hang is an engineer with Purple Mountain Laboratories. His research interests include knowledge graph theory of wireless communication networks, big data analysis and artificial intelligence algorithms.

HUANG Yongming is a professor in the School of Information Science and Engineering, Southeast University, China. His current research interests include MIMO wireless communications, cooperative wireless communications and millimeter wave wireless communications.

Integrated All-Light Network for Air, Space, Land, and Sea

LIANG Yingze[1,2], WANG Linning[1,2], QI Ziqian[1], LIU Pengzhan[1], WANG Yongjin[1]

(1. GaN Optoelectronic Integration International Cooperation Joint Laboratory of Jiangsu Province, Nanjing 210003, China;
2. Nanjing University of Posts and Telecommunications, Nanjing 210003, China)

DOI: 10.12142/ZTECOM.202502012

https://kns.cnki.net/kcms/detail/34.1294.TN.20250512.1406.004.html, published online May 13, 2025

Manuscript received: 2024-12-10

Abstract: To meet the demands of high-speed communication under strong electromagnetic interference, an all-light network (ALN) based on a multi-band optical communication system is proposed. It is designed for cross-scenario interconnection and networking, covering air, space, land, and sea. The ALN integrates four types of optical links: underwater blue light communication, white light illumination communication, solar-blind deep ultraviolet communication, and long-distance laser communication systems. These links are interconnected via Ethernet switches with the Transmission Control Protocol (TCP). Any ALN node supports both wired and wireless device access. The data transmission performance between network nodes was tested, with a maximum transmission delay of 73.3 ms, a maximum packet loss rate of 6.1%, and a maximum jitter of 15 ms. This comprehensive all-light network with all-scenario coverage lays the foundation for the future development of network technologies and the digital economy.

Keywords: all-light network; multi-band optical communication system; Ethernet switches

Citation (Format 1): LIANG Y Z, WANG L N, QI Z Q, et al. Integrated all-light network for air, space, land, and sea [J]. ZTE Communications, 2025, 23(2): 109 - 114. DOI: 10.12142/ZTECOM.202502012
Citation (Format 2): Y. Z. Liang, L. N. Wang, Z. Q. Qi, et al., "Integrated all-light network for air, space, land, and sea," *ZTE Communications*, vol. 23, no. 2, pp. 109 - 114, Jun. 2025. doi: 10.12142/ZTECOM.202502012.

1 Introduction

In the contemporary field of communications, optical communication, as an emerging and rapidly advancing technology, is increasingly becoming an integral component of future communication networks[1-8]. Wireless optical communication offers high-speed and low-latency data transmission and unique advantages in complex and denied environments as a complementary communication method.

An all-light network (ALN) represents the culmination of optical communication technologies. It integrates white light illumination communication (WLC), underwater blue light communication (BLC), solar-blind deep ultraviolet communication (DUVC), and long-distance laser communication (LC). This work focuses on the ALN and aims to develop a highly efficient optical communication network with multispectral capabilities and comprehensive scene coverage.

This work was supported by the National Natural Science Foundation of China under Grant No. U21A20495, Research and Development Program of China under Grant No. 2022YFE0112000, and Higher Education Discipline Innovation Project under Grant No. D17018.
The authors contributed equally to this work.

Compared to radio frequency (RF) networks, the ALN demonstrates significant performance advantages. Firstly, it offers excellent anti-interference capability, as optical signals are unaffected by electromagnetic environments[9]. With high directionality, interference resistance, and enhanced security, the ALN is particularly suitable for complex or constrained environments. Secondly, its bandwidth is far superior to that of RF networks, enabling large-capacity data transmission to meet the demands of future ultra-high-speed networks. Lastly, its low latency characteristics make it exceptionally well-suited for scenarios requiring high real-time performance. Leveraging these features, the ALN not only extends the application scope of communication networks but also provides a substantial performance boost to traditional communication methods. It can be employed in disaster emergency communications, deep-sea and space communications, and industrial automation, among other scenarios.

As shown in Fig. 1, there are four main practical application scenarios for full-spectrum optical communication: illumination communication, underwater communication, solar-blind communication, and long-distance communication. We develop subsystems for each scenario using light-emitting di-

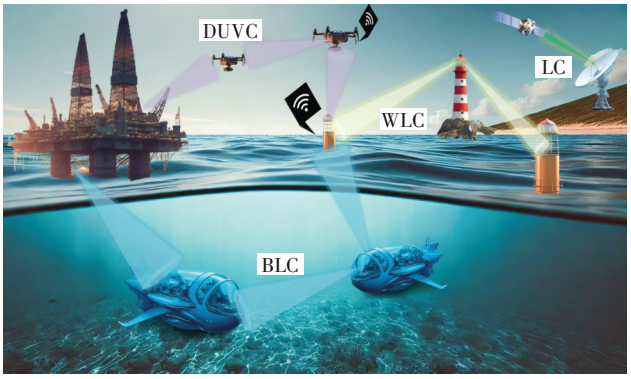

BLC: blue light communication
DUVC: deep ultraviolet communication
LC: laser communication
WLC: white light illumination communication

Figure 1. All-light network (ALN) applications spanning air, space, land and sea

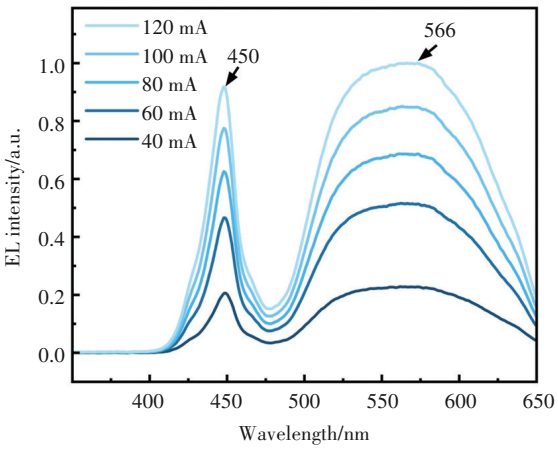

EL: electroluminescence

Figure 2. Electroluminescence spectra variation of white LED in white light illumination communication with increasing injection currents

odes (LEDs) or laser diodes (LDs) operating across four distinct spectral bands. WLC provides efficient data transmission and serves a dual role in illumination. For instance, WLC between buoys and lighthouses enables simultaneous information transmission. Blue and green light exhibit minimal loss in pure seawater, allowing for long-range data transmission[10–13]. BLC facilitates reliable data transfer in underwater environments, enabling control of uncrewed underwater vehicles or establishing communication between underwater sensors and buoys. Due to the ozone layer's absorption, background noise in the deep ultraviolet spectrum is extremely low at the Earth's surface, making DUVC suitable for environments with strong light or electromagnetic interference[14]. Meanwhile, long-distance LC, with its high-power directed beams, provides robust support for long-range, high-bandwidth communication, such as point-to-point communication in space[15]. By using Ethernet switches (ESes) combined with Wireless Fidelity (Wi-Fi) technology or optical fiber technology to connect various optical communication links, the ALN enables information sharing among different network nodes.

2 Experiments and Discussion

In our experiments, we characterized the white LED's electroluminescence (EL) spectra for WLC using a Keithley 2636B SourceMeter and an Ocean Optics HR4000 spectrometer. A multimode optical fiber with a diameter of 200 μm was used to collect the light emitted by the white LED under different injection currents and transmit it to the HR4000 spectrometer. The results are shown in Fig. 2. The EL spectrum of the white LED exhibits a distinct dual-peak profile, with the blue emission peak and excitation peak appearing from left to right. As the injection current increases from 40 mA to 120 mA, the blue emission peak shifts from 449.1 nm to 448 nm, corresponding to a blue shift of 1.1 nm. Meanwhile, the excitation peak remains stable at 566 nm.

We utilized a Keysight E5080A network analyzer to pulse the white LED using an alternating current (AC) signal, generating a bias voltage through a bias-tee module. The modulated light was captured by a Hamamatsu C12702-11 photodiode module and fed back to an Agilent Technologies PNA-LN5203C network analyzer for 3 dB processing. The results are shown in Fig. 3a. When the bias voltage increases from 10.5 V to 12 V, the 3 dB bandwidth expands from 0.55 MHz to 1.13 MHz. However, at a bias voltage of 12.5 V, the bandwidth decreases to 1.02 MHz, likely due to thermal effects in the white LED during actual operation. Therefore, we selected a bias voltage of 12 V to achieve a higher communication rate. This method was also applied to LEDs or LDs operating in other spectral bands. As shown in Fig. 3b, the 3 dB bandwidth of the blue LED reaches a maximum of 4.68 MHz under a driving voltage of 12 V. Fig. 3c presents the 3 dB performance characterization of the green LD device, which achieves a 3 dB bandwidth of 20.2 MHz at a bias voltage of 6 V, indicating that the green LD can achieve a higher modulation rate. As shown in Fig. 3d, the 3 dB bandwidth of the deep-ultraviolet (DUV) LED reaches 25.2 MHz at an operating voltage of 5.6 V. This indicates that the DUV LED theoretically achieves the highest modulation rate among the four types of devices.

We constructed an all-light communication network spanning space, air, and ocean using four different spectral bands: 278 nm, 450 nm, 520 nm, and 566 nm, as shown in Fig. 4. The WLC system is suitable for indoor and outdoor environments. The underwater BLC system addresses the challenges of underwater communication. The DUVC system ensures stable communication under strong illumination conditions, while the long-distance LC system meets the requirements for long-range, high-bandwidth communications.

The testing results showed that WLC achieved a communication rate of at least 2 Mbit/s over a 200 m ground communica-

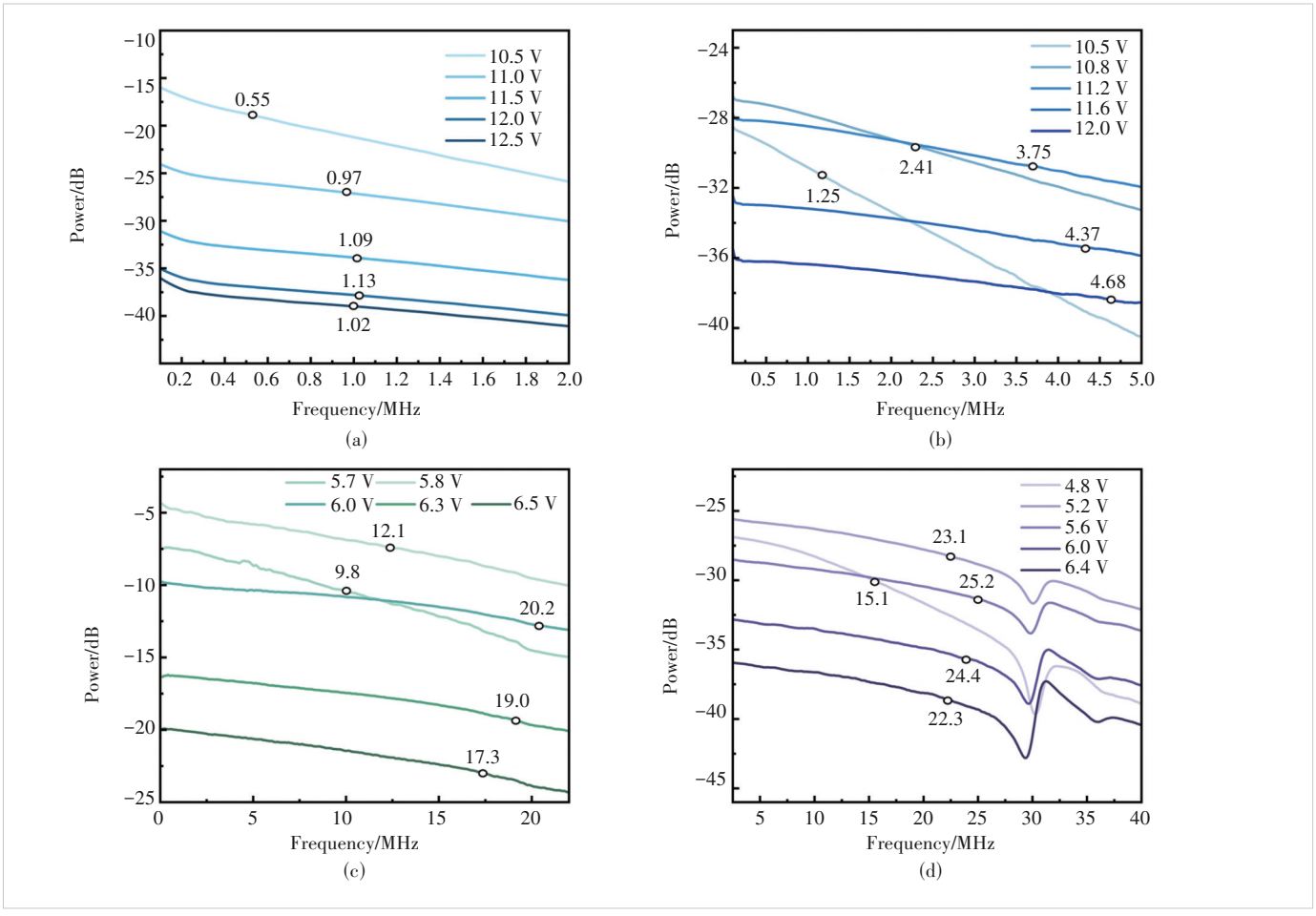

Figure 3. (a) 3 dB bandwidth variation of the white LED with increasing offset voltages; (b) 3 dB bandwidth variation of the blue LED with increasing offset voltages; (c) 3 dB bandwidth variation of the green LD with increasing offset voltages; (d) 3 dB bandwidth variation of the deep-ultraviolet LED with increasing offset voltages

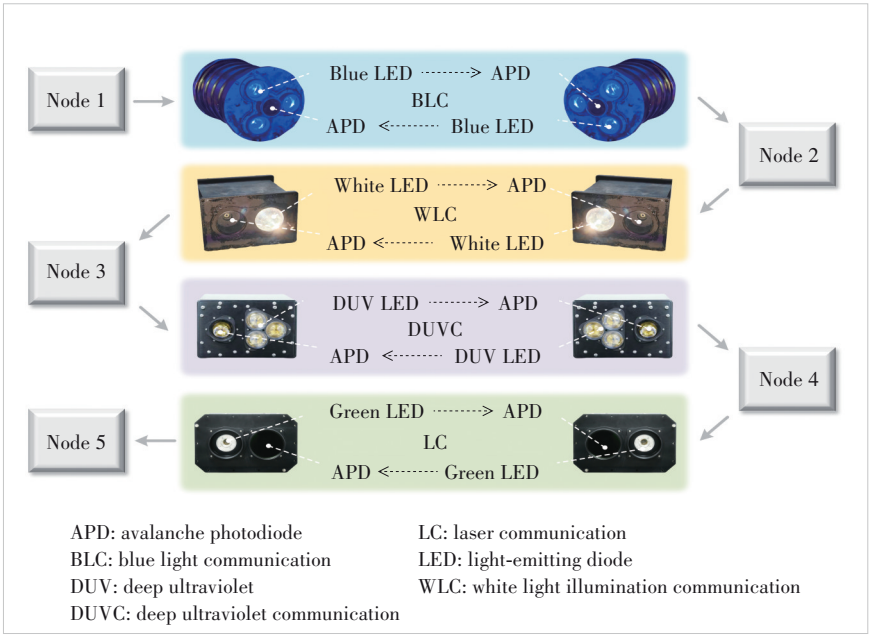

Figure 4. Schematic of the proposed all-light network (ALN) framework

tion distance. Underwater conditions featuring an attenuation coefficient of 0.4 dB/m, BLC supported full-duplex optical communication over distances of at least 50 m, with a communication rate of at least 4 Mbit/s. Both DUVC and LC achieved a communication rate of 10 Mbit/s, with tested distances of 10 m and 120 m, respectively.

By integrating multiple technologies, the ALN system enables flexible configurations and robust adaptability across diverse environments. Whether encountering extreme weather conditions, complex terrains, or specialized application scenarios, the ALN system delivers stable and reliable communication services.

ALN comprises four full-duplex wireless optical communication links connected in series through five nodes. These nodes are formed by ESes, enabling communication systems operating in different spectral bands

to establish networks with optical fibers, even in denied environments with heavy electromagnetic interference. Devices such as sensors, cameras, and PCs can access the ALN at any node through ESes. Additionally, Wi-Fi modules can be integrated into the nodes to provide wireless data access services for PCs and mobile devices, further expanding the ALN's connectivity options. The ESes can be expanded to accommodate multiple devices at the same node. To standardize transmission, all nodes in the wireless optical communication link use Registered Jack-45 (RJ45) network interfaces.

All four optical communication links operate in the full-duplex mode. The demonstration of the signal flow is shown in Fig. 5. When the underwater network camera captures video and sends it to Node 1 (N1), the video signal is encoded into a blue light signal by the BLC transmitter. At the BLC receiver, the light is filtered through a lens using a narrowband filter with a central wavelength of 450 nm, a half-bandwidth of 10 nm, and 45% transmittance, isolating the communication signal from ambient light. Each receiving end of the optical communication systems in different spectral bands is equipped with a corresponding narrowband filter. The optical signal is converted into an electrical signal by an avalanche photodiode (APD), then decoded by the BLC receiver and transmitted to N2. Subsequently, the signal is transmitted via the WLC link using illumination communication with a central wavelength of 566 nm. The signal at N3 is then transmitted to the next node via DUVC. Finally, the LC system converts the signal from N4 into a laser signal, and after transmission through the laser link, the original video stream is restored.

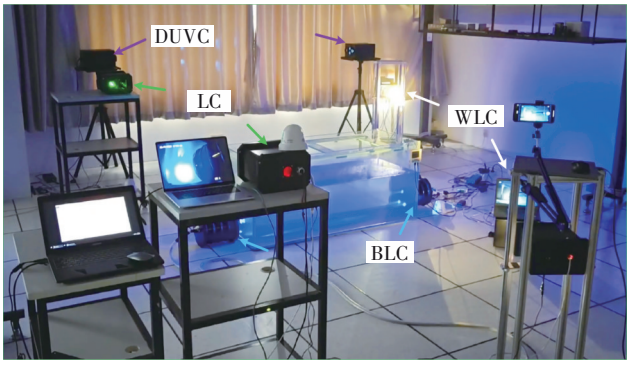

BLC: blue light communication
DUVC: deep ultraviolet communication
LC: laser communication
WLC: white light illumination communication

Figure 5. Demonstration of signal flow in all-light network (ALN)

The full-duplex optical communication system comprises a transmitter (TX) and a receiver (RX). The schematic diagram of the transmission and reception principles is shown in Fig. 6. In the transmission processing chain, a network camera or other sensor using the Transmission Control Protocol (TCP) is connected to the ES via an RJ45 interface. The video stream is then progressively converted into an optical signal. The core components of the TX are LEDs or LDs operating in different spectral bands. The direct current (DC) signal is supplied by an external LM2587 module, while the RF signal is synchronously generated by a transistor-transistor logic (TTL) signal using on-off keying (OOK) modulation within the field-programmable gate array (FPGA) main processing unit (Xilinx Spartan 6). The TTL signal drives the metal-oxide-semiconductor field-effect transistor (MOSFET) or bias tee via the PMD2001D driver. Finally, the modulated optical signal is emitted by the LED or LD.

The RX utilizes a high-sensitivity APD as the core component in the reception processing chain. The APD receives the optical signal under high voltage and converts it into a photocurrent. After amplification and filtering, the signal is re-

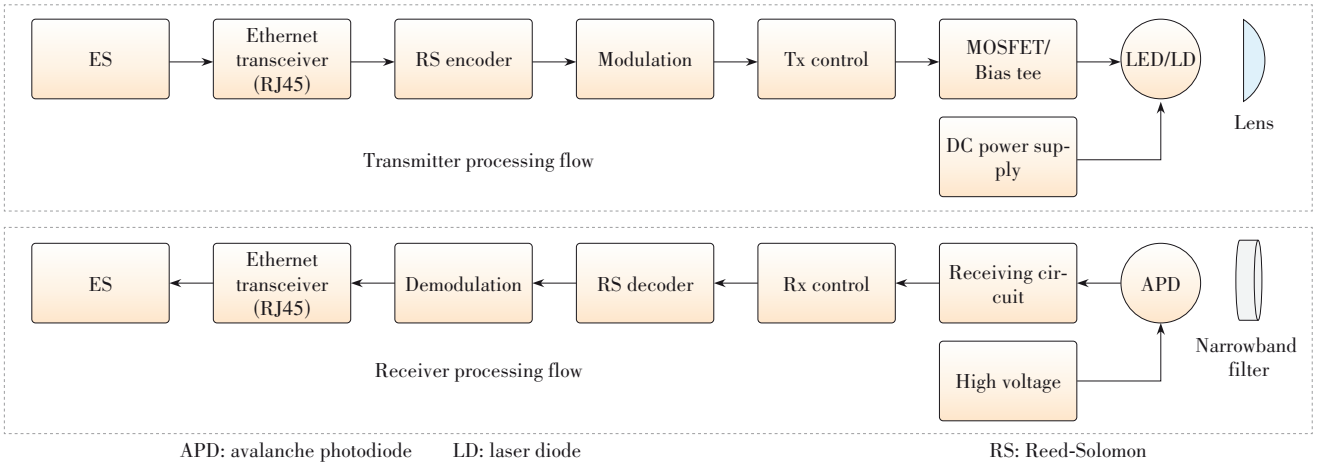

APD: avalanche photodiode
DC: direct current
ES: Ethernet switch
LD: laser diode
LED: light-emitting diode
MOSFET: metal-oxide-semiconductor field-effect transistor
RS: Reed-Solomon
Rx: receiver
Tx: transmitter

Figure 6. Transmission and reception principles of full-duplex optical communication systems

turned to the FPGA for decoding and demodulation. Subsequently, the processed signal is displayed on an external monitor through an RJ45 interface or transmitted to a Wi-Fi module for sharing.

As shown in Fig. 7a, a 20 Mbit/s pseudo-random binary sequence (PRBS) signal generated by an arbitrary waveform generator (AWG) replaces the FPGA signal at the TX to access the LC. After the signal decision at the RX, the output signal matches the original transmitted signal. The amplified analog signal from the first stage of the transimpedance amplifier (TIA) is captured, and the oscilloscope (Keysight, DSOS604A) generates the corresponding eye diagram, as depicted in Fig. 7b. This clear and open eye diagram confirms the accuracy of the received signal in Fig. 7a. The time and amplitude scales of the eye diagram are 20 ns and 500 mV, respectively, as shown in Fig. 7b. This method can also be applied to assess the communication performance of other optical communication system links.

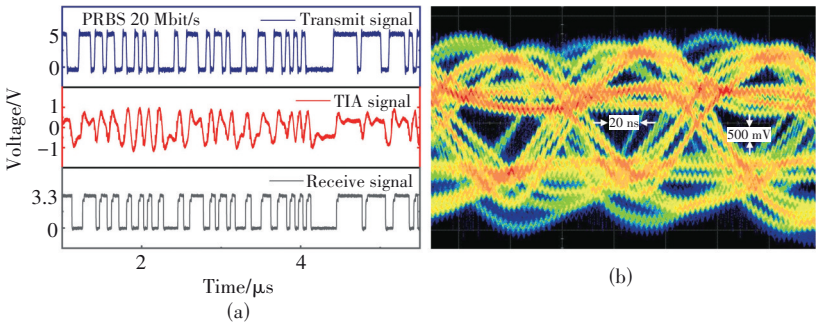

PRBS: pseudo-random binary sequence TIA: transimpedance amplifier

Figure 7. (a) 20 Mbit/s PRBS signals from Rx of the system; (b) eye diagram of the analog signal output from TIA

In the WLC system, interference from ambient light is a primary challenge. To address this, we designed a bandpass filter tailored to the EL spectral peak of the white light LED lamp beads. This effectively suppresses background light interference, ensuring stable signal transmission.

In an underwater BLC system, rapid attenuation of light in water poses the greatest challenge. To mitigate this, we developed a specialized optical structure at the transmitter and adopt a three-window array design. These enhancements improve light transmission efficiency and signal coverage, significantly reducing signal attenuation in underwater environments.

For the DUVC system, the low light output efficiency of DUV LEDs is a major difficulty. To resolve this, we implemented sapphire substrate stripping technology and precise thinning of nitride films, enabling the production of submicron-level DUV LEDs. These advancements greatly enhance light output efficiency. Additionally, sunlight interference presents challenges for solar-blind communication. To address this, we designed a 275 nm bandpass filter at the receiver end, combined with an optical anti-reflection lens, which strengthened signal reception and effectively reduced signal attenuation during daytime communication in solar-blind regions.

Moreover, the primary challenge for LC systems lies in beam collimation. To overcome this, we optimized the optical system preceding the laser, ensuring precise beam alignment. This reduces the impact of atmospheric turbulence and beam divergence, enhancing communication stability and long-distance transmission capabilities.

Delay, packet loss rate (PLR), and jitter are three key metrics for evaluating the performance of an ALN. Delay refers to the time required for data to travel from one end of the network to the other. Increased delay may lead to stuttering during network interactions. PLR represents the proportion of data packets lost during transmission and reception. An increased PLR results in higher network delay and inefficient bandwidth utilization. Jitter refers to the inconsistency in packet delay during transmission, i.e., the arrival time variations of different data packets. Excessive jitter can disrupt data flow continuity, thereby compromising the smoothness of real-time communication.

The ALN contains five nodes. A PC is used as the accessing terminal, and a network camera serves as the accessed terminal. The delay measured under 25 different node access scenarios is shown in Fig. 8a by swapping their connection points. We used a maximum transmission unit of 1 514 bytes for testing. Due to the lower transmission rates of the BLC and WLC, these optical communication links introduced approximately 30 ms of delay, while the higher-speed DUVC and LC links resulted in a lower delay of around 6 ms. The same access setup was used to test the PLR and jitter of the ALN. As shown in Fig. 8b, as the number of nodes traversed increases,

Delay/ms		ALN accessed node				
		N1	N2	N3	N4	N5
ALN accessing node	N1	1.05	31.1	61.2	66.5	73.3
	N2	30.9	1.04	30.9	37.1	43.4
	N3	61.2	30.9	1.04	7.79	13.9
	N4	66.9	37.1	7.8	1.05	7.66
	N5	73.1	43.2	13.4	7.24	1.02

(a)

PLR/%		ALN accessed node				
		N1	N2	N3	N4	N5
ALN accessing node	N1	0	1	2.4	3.9	5.4
	N2	0.6	0	0.9	3	4.6
	N3	2.5	1.1	0	1.8	3.9
	N4	3.9	2.4	1.8	0	1.7
	N5	6.1	4.5	2.8	1.4	0

(b)

Jitter/ms		ALN accessed node				
		N1	N2	N3	N4	N5
ALN accessing node	N1	1	6	10	11	14
	N2	4	1	3	6	11
	N3	10	4	1	3	6
	N4	12	6	2	1	3
	N5	15	10	6	3	1

(c)

ALN: all-light network PLR: packet loss rate

Figure 8. (a) Delay, (b) PLR, and (c) jitter results of five nodes accessing each other

PLR accumulates steadily, with an average rise of 1.435% per optical link and a maximum PLR of 6.1%. Fig. 8c shows that the maximum jitter of 15 ms is measured when N5 accesses N1. Our testing results confirmed uninterrupted, high-quality real-time video transmission when the signal traveled along the longest path in the ALN (from N1 to N5).

3 Conclusions

By establishing an integrated communication network spanning space, air, and sea environments, we achieve full-duplex real-time video communication between network nodes, with a maximum PLR of 6.1% and transmission delay below 73.3 ms. The ALN system is designed to enable wireless internet access via the TCP/IP protocol. For Internet of Things (IoT) applications involving multi-terminal and multi-service interconnections, developing ALN-based mobile communication networks and integrating advanced modulation techniques to enhance network throughput will be crucial.

References

[1] SHAY T M, MACCANNELL J A, GARRETT C D, et al. First experimental demonstration of full-duplex communication on a single laser beam [C]// Proc. Free-Space Laser Communication and Active Laser Illumination III. SPIE, 2004. DOI: 10.1117/12.508511
[2] O'BRIEN D, TURNBULL R, MINH H L, et al. A 280 Mbit/s infra-red optical wireless communications system [C]//Proc. Free-Space and Atmospheric Laser Communications XI. SPIE, 2011. DOI: 10.1117/12.895092
[3] WANG K, NIRMALATHAS A, LIM C, et al. Experimental demonstration of a full-duplex indoor optical wireless communication system [J]. IEEE photonics technology letters, 2012, 24(3): 188 – 190. DOI: 10.1109/LPT.2011.2175912
[4] WANG K. Quasi-passive indoor optical wireless communication systems [J]. IEEE photonics technology letters, 2020, 32(21): 1373 – 1376. DOI: 10.1109/LPT.2020.3026343
[5] ABDALLA I, RAHAIM M B, LITTLE T D C. Interference in multi-user optical wireless communications systems [J]. Philosophical transactions of the royal society a: mathematical, physical and engineering sciences, 2020, 378(2169): 20190190. DOI: 10.1098/rsta.2019.0190
[6] TSONEV D, VIDEV S, HAAS H. Light fidelity (Li-Fi): towards all-optical networking [C]//Proc. Broadband Access Communication Technologies VIII. SPIE, 2013. DOI: 10.1117/12.2044649
[7] LI J, UYSAL M. Optical wireless communications: system model, capacity and coding [C]//Proc. IEEE 58th Vehicular Technology Conference (VTC 2003-Fall). IEEE, 2003: 168 – 172. DOI: 10.1109/VETECF.2003.1285000
[8] OUBEI H M, SHEN C, KAMMOUN A, et al. Light based underwater wireless communications [J]. Japanese journal of applied physics, 2018, 57 (8S2): 08PA06. DOI: 10.7567/JJAP.57.08PA06
[9] ROSHEIM M E, SAUTER G F. Free-space optical communications system pointer [C]//Proc. Free-Space Laser Communication Technologies XV. SPIE, 2003: 126 – 133. DOI: 10.1117/12.501653
[10] LIN A B, TONG Z, SONG Y H, et al. Underwater wireless optical communication system using blue LEDs [J]. Journal of physics: conference series, 2016, 679: 1 – 5. DOI: 10.1088/1742-6596/679/1/012032
[11] ARNON S. Underwater optical wireless communication network [J]. Optical engineering, 2010, 49(1): 1 – 6. DOI: 10.1117/1.3280288
[12] QI Z Q, WANG L N, LIU P Z, et al. Full-duplex underwater wireless blue light communication [J]. Optics express, 2023, 31(6): 9330 – 9338. DOI: 10.1364/oe.483966
[13] ZHOU Z H, YIN H X, YAO Y X. Wireless optical communication performance simulation and full-duplex communication experimental system with different seawater environment [C]//Proc. IEEE International Conference on Signal Processing, Communications and Computing (ICSPCC). IEEE, 2019. DOI: 10.1109/icspcc46631.2019.8960905
[14] WANG L N, BAI M M, QI Z Q, et al. Full-duplex wireless deep ultraviolet light communication [J]. Optics letters, 2022, 47(19): 5064 – 5067. DOI: 10.1364/OL.473369
[15] LIANG Y Z, WANG L N, QI Z Q, et al. Full-duplex wireless light communication using green laser diodes [J]. Optics express, 2024, 32(8): 13543 – 13551. DOI: 10.1364/oe.519815

Biographies

LIANG Yingze received his BS degree in communication engineering from East China Jiaotong University, China in 2022. He is currently working toward a master's degree in electronic information at Nanjing University of Posts and Telecommunications, China. His primary research interest lies in wireless optical communication and its application systems, including embedded development, communication electronics, and signal processing circuits.

WANG Linning received his BS degree in communications engineering and master's degree in electronics and communication engineering from Nanjing University of Posts and Telecommunications, China in 2018 and 2021, respectively. He is currently working toward a PhD degree in communication and information systems at Nanjing University of Posts and Telecommunications. His primary research interest lies in wireless optical communication and its application systems, including embedded development, communication electronics, and signal processing circuits.

QI Ziqian received his BS degree in electronic information engineering from Dalian Jiaotong University, China in 2021 and master's degree in electronics and communication engineering from Nanjing University of Posts and Telecommunications, China in 2024. His primary research interest lies in wireless optical communication and its application systems, including embedded development, communication electronics, and signal processing circuits.

LIU Pengzhan received his MS degree from Nanjing University of Posts and Telecommunications, China. Now he is a PhD student there under the supervision of Prof. WANG Yongjin. His research interests include all-light wireless optical communication networks and integrated GaN optoelectronic devices.

WANG Yongjin (wangyj@njupt.edu.cn) received his PhD degree in microelectronics and solid-state electronics from the Shanghai Institute of Microsystem and Information Technology, Chinese Academy of Sciences in 2005. He was engaged in research work with the University of Freiburg, Germany, Tohoku University, Japan, Forschungszentrum Jülich, Germany, and the University of Bristol, UK. Since 2011, he has been a professor with Nanjing University of Posts and Telecommunications, China. He is currently the chief investigator of the National Innovation Base for Micro-Nano Device and Information System, China. His research interests include III-nitride monolithic photonic circuits for visible light communication and the Internet of Things. He was the recipient of many scholarships, including the Humboldt Foundation Scholarship, the JSPS Special Researcher Scholarship, and the Royal Society for Engineering Scholarship.

The 1st Youth Expert Committee
for Promoting Industry-University-Institute Cooperation

Director	**CHEN Wei,** Beijing Jiaotong University
Deputy Director	**QIN Xiaoqi,** Beijing University of Posts and Telecommunications
	LU Dan, ZTE Corporation

Members (Surname in Alphabetical Order)

CAO Jin	Xidian University
CHEN Li	University of Science and Technology of China
CHEN Qimei	Wuhan University
CHEN Shuyi	Harbin Institute of Technology
CHEN Siheng	Shanghai Jiao Tong University
CHEN Wei	Beijing Jiaotong University
GUAN Ke	Beijing Jiaotong University
HAN Kaifeng	China Academy of Information and Communications Technology
HE Zi	Nanjing University of Science and Technology
HOU Tianwei	Beijing Jiaotong University
HU Jie	University of Electronic Science and Technology of China
HUANG Chen	Purple Mountain Laboratories
LI Ang	Xi'an Jiaotong University
LIU Chunsen	Fudan University
LIU Fan	Southeast University
LIU Junyu	Xidian University
LU Dan	ZTE Corporation
LU Youyou	Tsinghua University
NING Zhaolong	Chongqing University of Posts and Telecommunications
QI Liang	Shanghai Jiao Tong University
QIN Xiaoqi	Beijing University of Posts and Telecommunications
QIN Zhijin	Tsinghua University
SHI Yinghuan	Nanjing University
TANG Wankai	Southeast Univeristy
WANG Jingjing	Beihang University
WANG Xinggang	Huazhong University of Science and Technology
WANG Yongqiang	Tianjin University
WEN Miaowen	South China University of Technology
WU Qingqing	Shanghai Jiao Tong University
WU Yongpeng	Shanghai Jiao Tong University
XIA Wenchao	Nanjing University of Posts and Telecommunications
XU Mengwei	Beijing University of Posts and Telecommunications
XU Tianheng	Shanghai Advanced Research Institute, Chinese Academy of Sciences
YANG Chuanchuan	Peking University
YIN Haifan	Huazhong University of Science and Technology
YU Jihong	Beijing Institute of Technology
ZHANG Jiao	Beijing University of Posts and Telecommunications
ZHANG Yuchao	Beijing University of Posts and Telecommunications
ZHANG Jiayi	Beijing Jiaotong University
ZHAO Yuda	Zhejiang University
ZHAO Zhongyuan	Beijing University of Posts and Telecommunications
ZHOU Yi	Southwest Jiaotong University
ZHU Bingcheng	Southeast University

ZTE COMMUNICATIONS
中兴通讯技术(英文版)

ZTE Communications has been indexed in the following databases:

- Abstract Journal
- China Science and Technology Journal Database
- Chinese Journal Fulltext Databases
- Index Copernicus
- Scopus
- Ulrich's Periodicals Directory
- Wanfang Data
- WJCI 2021–2024

Industry Consultants:

DUAN Xiangyang, GAO Yin, HU Liujun, HUA Xinhai, LIU Xinyang, LU Ping, SHI Weiqiang, TU Yaofeng, WANG Huitao, XIONG Xiankui, ZHAO Yajun, ZHAO Zhiyong, ZHU Xiaoguang

ZTE COMMUNICATIONS
Vol. 23 No. 2 (Issue 91)
Quarterly
First Issue Published in 2003

Supervised by:
Anhui Publishing Group

Sponsored by:
Time Publishing and Media Co., Ltd.
Shenzhen Guangyu Aerospace Industry Co., Ltd.

Published by:
Anhui Science & Technology Publishing House

Edited and Circulated (Home and Abroad) by:
Magazine House of ZTE Communications

Staff Members:
General Editor: WANG Xiyu
Editor-in-Chief: WANG Li
Executive Editor-in-Chief: HUANG Xinming
Deputy Editor-in-Chief: LU Dan
Editorial Director: WANG Pingping
Editor-in-Charge: ZHU Li
Editors: REN Xixi, XU Ye, YANG Guangxi
Producer: XU Ying
Circulation Executive: WANG Pingping
Assistant: WANG Kun

Editorial Correspondence:
Add: 12F Kaixuan Building, 329 Jinzhai Road,
Hefei 230061, P. R. China
Tel: +86-551-65533356
Email: magazine@zte.com.cn
Website: http://zte.magtechjournal.com

Annual Subscription: RMB 120
Printed by:
Hefei Tiancai Color Printing Company
Publication Date: June 25, 2025

China Standard Serial Number: ISSN 1673–5188 / CN 34–1294/TN